

# **Tokamak Edge Plasma Modeling Using an Improved Onion-Skin Method**

**by**

**Wojciech R. Fundamenski**

A thesis submitted in conformity with the requirements  
for the degree of doctor of philosophy (Ph.D.)  
Graduate Department of the Institute of Aerospace Studies  
University of Toronto

© Copyright by Wojciech R. Fundamenski (1999)



National Library  
of Canada

Acquisitions and  
Bibliographic Services  
  
395 Wellington Street  
Ottawa ON K1A 0N4  
Canada

Bibliothèque nationale  
du Canada

Acquisitions et  
services bibliographiques  
  
395, rue Wellington  
Ottawa ON K1A 0N4  
Canada

Your file Votre référence

Our file Notre référence

The author has granted a non-exclusive licence allowing the National Library of Canada to reproduce, loan, distribute or sell copies of this thesis in microform, paper or electronic formats.

The author retains ownership of the copyright in this thesis. Neither the thesis nor substantial extracts from it may be printed or otherwise reproduced without the author's permission.

L'auteur a accordé une licence non exclusive permettant à la Bibliothèque nationale du Canada de reproduire, prêter, distribuer ou vendre des copies de cette thèse sous la forme de microfiche/film, de reproduction sur papier ou sur format électronique.

L'auteur conserve la propriété du droit d'auteur qui protège cette thèse. Ni la thèse ni des extraits substantiels de celle-ci ne doivent être imprimés ou autrement reproduits sans son autorisation.

0-612-45640-4

Canadä

## **Abstract:**

Boundary (edge) plasma phenomena play a crucial role in the development of controlled thermonuclear fusion via magnetic confinement. In this work, the edge plasma are modeled by a coupled set of plasma/neutral transport equations; the neutral transport equations are solved by Monte-Carlo techniques (NIMBUS code), while the plasma transport equations are solved using an improved onion-skin method (OSM) based on the numerical techniques of computational fluid dynamics. The OSM approach, as defined in this thesis, consists of replacing the anomalous cross-field flux terms by (often simplified, always adjustable) cross-field source terms, and taking advantage of available diagnostic data (typically radial profiles of  $\Gamma$  and  $T_e$  from target Langmuir probes), of varying these cross-field sources in order to minimize the error between the solution and the diagnostic data. The OSM approach was shown capable of capturing the transition from attached to detached conditions in a tokamak divertor plasma, an important and timely aspect of present fusion research. The other applications presented in the thesis include a study of the sensitivity of modeling assumptions, a code-code comparison between the OSM and a standard 2D approach (represented by the EDGE2D code), and a code-experiment comparison with reciprocating probe data for Ohmic, L-mode and H-mode shots on the JET tokamak.

## **Acknowledgments:**

I would like to thank my supervisor, Dr. Peter Stangeby, whose inexhaustible enthusiasm and wide knowledge were invaluable from beginning to end. I feel greatly obliged to David Elder for frequent discussions and daily assistance with numerical programming, to Dr. Zingg for his skilled introduction to computational fluid dynamics, to Dr's Haasz and DeLeeuw for providing yearly reviews as part of the doctoral assessment committee, to D.G.Porter for acting as an external examiner and providing a number of valuable suggestions, and finally to everyone at the fusion lab at UTIAS for their constant companionship. The work was supported in part by the National Science and Engineering Research Council of Canada (NSERC), and by the Canadian Fusion Fuels and Technology Project (CFFTP), which is gratefully acknowledged.

## **Table of Contents:**

1. Introduction
2. Tokamak Edge Plasma Model
  - 2.1 Plasma Transport  $\parallel B$
  - 2.2 Plasma-Surface Interaction
  - 2.3 Plasma-Neutral Interaction
  - 2.4 Tokamak Edge Plasma
    - 2.4.1 Limiter edge plasma
    - 2.4.2 Divertor edge plasma
    - 2.4.3 Edge plasma modeling and the onion-skin method
3. Numerical Solution of Model Equations: the OSM2 code
  - 3.1 MHD Equations: Magnetic Grid
  - 3.2 Plasma Equations: Computational Fluid Dynamics
  - 3.3 Neutral Equations: Monte-Carlo simulation
  - 3.4 Iterative stability: Source Relaxation
  - 3.5 Cross-field sources: Diagnostic Variance Minimization
4. Modeling Results: Application of the OSM2/NIMBUS code
  - 4.1 Default model: transition from attached to detached conditions
  - 4.2 Sensitivity to modeling assumptions
    - 4.2.1 Effect of cross-field sources,  $Q_{\perp}$ : the  $Q_{\perp}[U]$  ansatz
    - 4.2.2 Effect of neutral sources,  $Q_3$ ,
    - 4.2.3 Effect of plasma sources,  $Q_p$
    - 4.2.4 Effect of flux expansion sources,  $Q_B$
    - 4.2.5 Effect of kinetic boundary conditions
  - 4.3 Comparison with the EDGE2D/NIMBUS code
  - 4.4 Comparison with experimental data on the JET tokamak
5. Conclusions
6. References

## **Appendices:**

- A.1 Energy in the XXI Century and Nuclear Fusion
- A.2 Plasma Physics
  - A.2.1 Charged Particle Dynamics
  - A.2.2 Statistical Mechanics
  - A.2.3 Kinetic Theory
- A.3 Braginskii and CGL Equations
- A.4 Electrostatic sheath problem
- A.5 Tokamak Core Plasma
  - A.5.1 MHD equilibrium
  - A.5.2 MHD instabilities
  - A.5.3 Kinetic Instabilities and Transport  $\perp B$

## **List of Tables:**

- 4.1.1** Target and upstream conditions for the attached-detached transition results
  - 4.1.2** Comparison of OSM2 and 2PM correction predictions
  - 4.1.3** Comparison of OSM2 and 2PM upstream predictions
  - 4.2.1** Summary of key results for the parametric sensitivity study
- 
- A.4.1** Sheath parameters compared in models

## **List of Figures (results section excepted):**

- 2.1.1** Charged particle orbits and drifts
  - 2.2.1** Plasma-surface and neutral-surface contact
  - 2.2.2** Near sheath regions
  - 2.3.1** H recycling
  - 2.3.2** H atom spectrum
  - 2.3.3** H molecule spectrum
  - 2.3.4**  $P_{rad}$  vs.  $T_e, Z$
  - 2.3.5** Atomic/Molecular Cross-sections
  - 2.4.1** Limiter SOL
  - 2.4.2** Divertor SOL
  - 3.1.1** Typical poloidal grid
  - 3.1.2** Close up of grid near the X-point
- 
- A.1.1** Charged particle orbits and drifts
  - A.2.1** Rosenbluth potentials
  - A.4.1** Shapes of  $f_i(v)$
  - A.5.1** Tokamak schematic
  - A.5.2** Tokamak co-ordinates and flux-surface geometry
  - A.5.3** Typical tokamak fields and currents
  - A.5.4** Magnetic island structure

## 1. Introduction

The objective of the work presented here was to develop an improved *onion-skin method (OSM)* of solving the plasma transport equations in magnetized edge plasmas with the specific aim of studying the phenomenon of divertor plasma detachment in tokamaks. *OSM* is an approach at *interpretive* two-dimensional modeling of a tokamak edge plasma; in this context the term *interpretive* is taken to mean *well suited to interpretation of experiments and closely linked to diagnostic data*. *Onion-skin* interpretive modeling implies an intention of incorporating (as input) as much diagnostic data as possible, while making the fewest possible assumptions about unknown (anomalous) cross-field coefficients. It is based on a standard set of plasma transport equations (used by such 2-D edge plasma codes as UEDGE<sup>[Roa92]</sup>, B2<sup>[Bra97,Bae91]</sup>, and EDGE2D<sup>[Sim92,94]</sup>) which are solved on each flux surface with kinetic boundary conditions at the targets; the cross-field sources are iteratively adjusted to best match the specified (diagnostic) target quantities. An improved *onion-skin* algorithm capable of capturing plasma detachment was developed based on standard numerical methods of *computational fluid dynamics (CFD)*. The formulation, implementation and successful application of this improved *onion-skin method*, taken together, constitute the contribution to knowledge contained in the thesis. Original material may be found in §2.1, §2.4.3, §3.2, §3.4, §3.5 and §4; when presented alongside previous work, original equations will be marked with an asterix, eg. (2.1.17\*).

Previously, the *onion-skin method* had been applied successfully to model *attached* plasma behaviour<sup>[Su97]</sup>, but has been incapable of modeling divertor plasma *detachment*. In addition, due to the steady-state parabolic form of the plasma transport equations required by the previous numerical scheme, this approach could not be made to include parallel viscosity, ion-electron energy exchange or truly continuous transonic mid-flow transition. In the work presented here, these problems were overcome by using the *CFD* methodology to evolve the time-dependent plasma transport equations in parabolic form until convergence (which is equivalent to solving these equations in a steady-state hyperbolic/elliptic form<sup>[Rei92]</sup>); as a result of this modification, stable *detached* plasma solutions were obtained.

In addition, a general method of adjusting the cross-field sources in order to find the best match to selected diagnostic data was developed based on variational techniques. In the present context, this method will be referred to as *Diagnostic Variance Minimization (DVM)*. It consists of a variational scheme to adjust the cross-field particle, momentum and energy sources in order to best match selected diagnostic data (to minimize the statistical variance between selected diagnostic and numerically calculated quantities). The *DVM* approach provides a framework in which the *onion-skin method* could in the future be employed with various types of and multiple sets of diagnostic data (this data need not be located at the target – as for the earlier OSM – provided that it includes radial profiles across the edge plasma, eg. from reciprocating probes, Li-beam diagnostic, Thomson scattering arrays, hydrogen spectroscopy).

Modeling is by definition a theoretical task and must not shy away from mathematical rigor when appropriate; however, excessive attention to detail runs the risk of obscuring rather than clarifying the physical

Modeling is by definition a theoretical task and must not shy away from mathematical rigor when appropriate; however, excessive attention to detail runs the risk of obscuring rather than clarifying the physical content of the model. In addition, the relationship of modeling to experiment generally varies widely from intimate to non-existent. The intention of the OSM-DVM interpretive approach was to achieve a balance between the theoretical and experimental aspects of tokamak edge plasma research, to aid the experimentalist by placing the large amount of diagnostic data in a unifying framework, and hopefully offer insight into these diagnostic measurements. By providing a fast method of estimating the 2-D edge plasma distribution (as compared with the standard 2-D fluid codes which require lengthy parameter searches<sup>[Lo97]</sup>) the OSM-DVM approach is intended to supplement the more laborious 2-D calculations by offering the experimental fusion community an alternative interpretive tool for routine edge plasma modeling. Aside from significant savings in CPU time (ranging from one to two orders of magnitude, with typical solution times of 1 to 10 hours on an IBM RS6000 workstation), the OSM-DVM approach makes fewer assumptions about the physics of cross-field transport, sidestepping the greatest uncertainty in edge plasma modeling.

The presentation which follows is subdivided into sections dealing with theory, numerical methods and computational results. The level of presentation assumes graduate level knowledge of physics and mathematical analysis and some familiarity with plasma physics, fusion research and computational analysis. For the sake of conciseness, only the physics directly relevant to plasma edge modeling is discussed; a number of excellent monograms on plasma physics<sup>[Cha60, Miy78, Kra80, Ros83, Ich92]</sup>, plasma-surface interactions<sup>[Pos84, Sta90]</sup>, plasma-neutral interactions<sup>[Bro66, Jan95]</sup>, fusion technology<sup>[Dol82]</sup> and tokamaks<sup>[Wes97]</sup>, are recommended to the interested reader for further scope in any one of these areas. In addition, the appendices contain brief summaries of the necessary background material and are frequently referred to for the basic concepts and equations. The discussion of numerical methods is broken down into five blocks, corresponding to successive stages in the iterative computational loop, most importantly the CFD and Monte Carlo (MC) methods. The results section deals with several applications of the newly developed OSM2 code (iteratively coupled with the NIMBUS hydrogenic code; this computational loop will be denoted by OSM2/NIMBUS), including an investigation of the attached-detached transition, a sensitivity study with respect to various modeling assumptions, a comparison with an existing 2D edge plasma fluid code EDGE2D/NIMBUS, and a direct confrontation with experimental data from the JET tokamak. Conclusions are drawn from the above results and assessed in light of our present understanding of tokamak edge plasma behaviour.

## 2.1 Plasma Transport || B

The kinetic equation for the single-particle distribution function  $f_a(x, v, t)$  may be written as<sup>[Kra80]</sup>,

$$D_a f_a = \left( \frac{\partial}{\partial t} + \mathbf{v} \cdot \nabla_x + \frac{Z_a e}{m_a} (\mathbf{E} + \mathbf{v} \times \mathbf{B}) \cdot \nabla_v \right) f_a = \sum_{b \in \{i, e, n\}} C_{ab} + S_a \quad a \in \{i, e, n\} \quad (2.1.1)$$

where  $D_a$  is a phase space derivative for species 'a',  $C_{ab}$  represents the change to  $f_a(x, v, t)$  due to collisions with species 'b', and  $S_a$  is a volumetric source of species 'a'; this equation is valid for electrons ( $Z_e = -1$ ), ions ( $Z_i \geq 1$ ) and neutrals ( $Z_n = 0$ ) provided appropriate collision terms are used. Starting with (2.1.1), fluid-like plasma transport equations may be derived. The standard approach adapted in neutral gas dynamics consists of multiplying the kinetic equation by powers of velocity and integrating over velocity space; the resulting velocity moment hierarchy is usually closed on the level of the third moment (the heat flux)<sup>[Cha88]</sup>. This procedure has also been applied to the plasma kinetic equation with the Fokker-Planck collision term<sup>[Lin82]</sup>, yielding expressions for transport coefficients along and across the magnetic field in terms of the ion and electron characteristic times. The final set of moment equations, named after Braginskii who carried out the most complete derivation<sup>[Bra65]</sup>, may be found in §A.3; these are the most widely used equations in edge plasma modeling.

In a strongly magnetized plasma, the above procedure introduces inaccuracies related to the anisotropy of  $f_a(v)$ , which may be significant if collisionality is weak<sup>[Zaw86]</sup>. In the collisionless limit, the Vlasov equation may be expressed in terms of integrals of motion and integrated to yield the Chew-Goldberg-Low (CGL) or double adiabatic equations<sup>[Che56]</sup>, also given in §A.3;. The Braginskii and CGL moment equations may be considered as the asymptotes for high and low collisionality. It is also possible to derive moment equations valid for all degrees of collisionality, reducing to the Braginskii and CGL expressions in their respective limits. This is done by first transforming the kinetic equation into magnetic co-ordinates, next averaging out the rapid gyrating motion to form the drift-kinetic equation, and finally integrating the drift-kinetic equation over powers of velocity. The procedure has first been carried out by Zawaideh, Najmabadi and Conn (ZNC)<sup>[Zaw86,88]</sup>; the following calculation is closely guided by their original paper, but since several minor extensions are introduced, it is presented in some detail.

We first introduce orthogonal magnetic coordinates  $(s_{||}, \alpha, \beta)$  and velocities  $(v_{||}, v_\alpha, v_\beta)$ .

$$\mathbf{B} = \nabla \alpha \times \nabla \beta \quad \hat{i}_{||} = \nabla s_{||} = \frac{\mathbf{B}}{|\mathbf{B}|} = \frac{\mathbf{B}}{B} \quad \hat{i}_\alpha = \frac{\nabla \alpha}{|\nabla \alpha|} \quad \hat{i}_\beta = \frac{\nabla \beta}{|\nabla \beta|} \quad (2.1.2)$$

$$\mathbf{v} \cdot \hat{i}_{||} = v_{||} \quad \mathbf{v} \cdot \hat{i}_\alpha = v_\alpha = v_\perp \cos \varphi \quad \mathbf{v} \cdot \hat{i}_\beta = v_\beta = v_\perp \sin \varphi \quad v_\perp^2 = v_\alpha^2 + v_\beta^2$$

where  $\varphi$  is the gyration angle and  $i_{||}$ ,  $i_\alpha$  and  $i_\beta$  are orthogonal unit vectors. The co-variant phase-space derivative  $D_a$  may be expressed in terms of these variables, ie. for a distribution  $f_a(s, \alpha, \beta, v_{||}, v_\perp, \varphi, t)$ , as

$$D_a \equiv \frac{dx^\xi}{dt} \cdot \frac{\partial}{\partial x^\xi} = \frac{\partial}{\partial t} + \dot{s}_{||} \frac{\partial}{\partial s_{||}} + \dot{\alpha} \frac{\partial}{\partial \alpha} + \dot{\beta} \frac{\partial}{\partial \beta} + \dot{v}_{||} \frac{\partial}{\partial v_{||}} + \dot{v}_\perp \frac{\partial}{\partial v_\perp} + \dot{\varphi} \frac{\partial}{\partial \varphi} \quad (2.1.3)$$

where the dot denotes a convective time derivative. We would next like to average the kinetic equation over a gyration period of a particle, which in a strong  $\mathbf{B}$  field is more rapid than any collision process. Such an average may be carried out for a helical trajectory of a charged particle in a strong magnetic field with slowly varying electric and magnetic fields, §A.2.1, yielding the guiding center drift velocity; the averaging is valid subject to the adiabatic field constraints,  $\delta_v \ll l$  defined in (A.2.6). The convective time derivatives are found by expanding (A.2.3) in powers of  $\delta_v$  retaining the lowest order terms,

$$\begin{aligned}\dot{s}_{||} &= \frac{\partial s_{||}}{\partial t} + v_{||} + \mathbf{v}^{drift} \cdot \nabla s_{||} & \dot{\beta} &= \frac{\partial \beta}{\partial t} + \mathbf{v}^{drift} \cdot \nabla \beta & \dot{\alpha} &= \frac{\partial \alpha}{\partial t} + \mathbf{v}^{drift} \cdot \nabla \alpha \\ \dot{v}_{||} &\approx \frac{e}{m} E_{||} - \frac{v_{\perp}^2}{2B} \frac{\partial B}{\partial s_{||}} & \dot{v}_{\perp} &= \frac{v_{\perp}}{2B} \dot{B} & \dot{\phi} &= \omega_c\end{aligned}\quad (2.1.4)$$

We take the  $\mathbf{B}$ -field itself as constant in time, so that  $(\partial/\partial t)(s_{||}, \alpha, \beta) = 0$ ; drift terms parallel to  $\mathbf{B}$  are small and can be neglected. Inserting the above into the operator  $D_a$  and averaging  $D_a f_a$  over one gyration period,  $\int_0^{2\pi} d\phi / 2\pi$ , we obtain the drift kinetic equation<sup>[Ros83]</sup>. For weak drifts,  $v^{drift}/v = O(\delta_v)$ , the dependence on  $\alpha$  and  $\beta$  may be neglected,  $f_a(\alpha, \beta) \sim O(\delta_v^2)$ . Introducing the relative velocities,  $V_{||} = v_{||} - u_a$ ,  $V_{\perp} = v_{\perp}$ , where  $u_a \equiv \langle v_{||} \rangle_a$  is the average along- $\mathbf{B}$  velocity, the phase-space derivative of  $f_a(s_{||}, V_{||}, V_{\perp}, t)$  becomes,

$$\begin{aligned}D_a &= \frac{\partial}{\partial t} + \dot{s}_{||} \cdot \frac{\partial}{\partial s_{||}} + \dot{V}_{||} \cdot \frac{\partial}{\partial V_{||}} + \dot{V}_{\perp} \cdot \frac{\partial}{\partial V_{\perp}} \\ &= \frac{\partial}{\partial t} + [u_a + V_{||}] \cdot \nabla_{||} + \left[ \frac{Z_a e}{m_a} E_{||} - \frac{V_{\perp}^2}{2B} \nabla_{||} B - \frac{\partial u_a}{\partial t} - (u_a + V_{||}) \cdot \nabla_{||} u_a \right] \cdot \frac{\partial}{\partial V_{||}} + \left[ \frac{V_{\perp}}{2B} (u_a + V_{||}) \nabla_{||} B \right] \cdot \frac{\partial}{\partial V_{\perp}}\end{aligned}\quad (2.1.5)$$

where  $\nabla_{||} \equiv \partial/\partial s_{||}$ . Equation (2.1.1) formed with this operator, valid in the weak drift approximation  $v^{drift}/v \sim O(\delta_v)$ , is accurate to first order in  $\delta_v$ . Multiplying the drift kinetic equation (2.1.5) by  $m n V_{||}^k V_{\perp}^j$  and integrating over velocity space,  $dV = 2\pi V_{\perp} dV_{||} dV_{\perp}$ , we arrive at the (k,j)-moment equation<sup>[Zaw88]</sup>

$$\begin{aligned}\frac{d}{dt} nm \langle V_{||}^k V_{\perp}^j \rangle &+ \nabla_{||} nm \langle V_{||}^{k+1} V_{\perp}^j \rangle - \left[ \frac{eZ}{m} E_{||} - \frac{du}{dt} \right] k \cdot nm \langle V_{||}^{k-1} V_{\perp}^j \rangle \\ &+ \left[ \frac{I}{B} \nabla_{||} B \right] \frac{k}{2} \cdot nm \langle V_{||}^{k-1} V_{\perp}^{j+2} \rangle + \left[ (k+1) \nabla_{||} u - \frac{j+2}{2B} \frac{dB}{dt} \right] \cdot nm \langle V_{||}^k V_{\perp}^j \rangle + \\ &- \left[ \frac{I}{B} \nabla_{||} B \right] \frac{j+2}{2} \cdot nm \langle V_{||}^{k+1} V_{\perp}^j \rangle = \int d^3 V \cdot m V_{||}^k V_{\perp}^j \cdot \left[ \sum_b C_{ab} + S_a \right] \\ n &= \int dV \cdot f_a(s_{||}, V_{||}, V_{\perp}, t) \quad \langle \psi \rangle = \frac{1}{n} \int dV \cdot \psi \cdot f_a(s_{||}, V_{||}, V_{\perp}, t)\end{aligned}\quad (2.1.6)$$

where the 'a' index was dropped for simplicity and  $d/dt = \partial/\partial t + \mathbf{u} \cdot \nabla_{\parallel}$  was introduced. We will denote these moments by the usual fluid-like variables: density  $\rho = nm$ , velocity  $\mathbf{u}$ , pressure  $p$ , heat flux  $\mathbf{q}$ , temperature  $T$ ,

$$\begin{aligned} \begin{pmatrix} \rho \\ \rho \mathbf{u} \\ p_{\parallel} \\ p_{\perp} \\ q_{\parallel} \\ q_{\perp} \end{pmatrix} (s_{\parallel}, t) &\equiv nm \begin{pmatrix} \langle I \rangle \\ \langle v_{\parallel} \rangle \\ \langle V_{\parallel}^2 \rangle \\ \frac{1}{2} \langle V_{\perp}^2 \rangle \\ \langle V_{\parallel}^3 \rangle \\ \frac{1}{2} \langle V_{\parallel} V_{\perp}^2 \rangle \end{pmatrix} & T_{\parallel} &\equiv \frac{p_{\parallel}}{n} & T_{\perp} &\equiv \frac{p_{\perp}}{n} & T &\equiv \frac{p}{n} & (2.1.7) \\ && p &\equiv \frac{1}{3} (p_{\parallel} + 2p_{\perp}) & \delta p &\equiv \frac{2}{3} (p_{\parallel} - p_{\perp}) \\ && \langle V_{\parallel} \rangle &= 0 & \langle V_{\perp} \rangle &\sim v^{drift} & \langle V_{\parallel} V_{\perp} \rangle &= O(\delta_{\psi}) \end{aligned}$$

Similarly, we define symbols for collision and source integrals,

$$\begin{aligned} \begin{pmatrix} R \\ Q_{\parallel} \\ Q_{\perp} \\ H_{\parallel} \\ H_{\perp} \end{pmatrix} (s_{\parallel}, t) &\equiv \int dV \cdot \sum_b \mathbf{C}_{ab} m_a \begin{pmatrix} V_{\parallel} \\ V_{\parallel}^2 \\ \frac{1}{2} V_{\perp}^2 \\ V_{\parallel}^3 \\ \frac{1}{2} V_{\parallel} V_{\perp}^2 \end{pmatrix} & S(s_{\parallel}, t) &\equiv \int dV \cdot \mathbf{S}(s_{\parallel}, v_{\parallel}, v_{\perp}, t) & (2.1.8) \\ && \bar{\psi} &= \frac{1}{S} \int dV \cdot \psi \cdot S(s_{\parallel}, v_{\parallel}, v_{\perp}, t) \end{aligned}$$

From now on, we will neglect cross-field fluxes as first order in  $\delta_{\psi}$  and concentrate on parallel transport alone. There are two incentives for adapting this approach. Firstly, parallel transport is faster by many orders of magnitude, see §A.5.3 and (A.5.15). Secondly, it is found experimentally that cross-field fluxes differ sharply from classical predictions, due to a combination of several physical mechanisms, including electrostatic and magnetic plasma turbulence, and plasma-neutral interaction<sup>[Lie85]</sup>. In fact, no satisfactory model exists to predict their dependence on local plasma conditions<sup>[Cou99]</sup>. We will revisit this question in §2.4.3.

Using the fluid-variable notation, we write down the moment equations up to order three.

$$\frac{d\rho}{dt} + \rho \nabla_{\parallel} \cdot \mathbf{u} - \rho u B^{-1} \nabla_{\parallel} \cdot \mathbf{B} = mS \quad (2.1.9)$$

$$\rho \frac{du}{dt} + \nabla_{\parallel} p_{\parallel} - (p_{\parallel} - p_{\perp}) \mathbf{B}^{-1} \nabla_{\parallel} \cdot \mathbf{B} = Z_{en} E_{\parallel} + R + mS \bar{V}_{\parallel}$$

$$\frac{dp_{\parallel}}{dt} + 3p_{\parallel} \nabla_{\parallel} \cdot \mathbf{u} + B \nabla_{\parallel} \cdot (q_{\parallel} B^{-1}) + (2q_{\perp} - p_{\parallel} u) \mathbf{B}^{-1} \nabla_{\parallel} \cdot \mathbf{B} = Q_{\parallel} + mS \bar{V}_{\parallel}^2$$

$$\frac{dp_{\perp}}{dt} + p_{\perp} \nabla_{\parallel} \cdot \mathbf{u} + B \nabla_{\parallel} \cdot (q_{\perp} B^{-1}) - (q_{\perp} + 2p_{\perp} u) \mathbf{B}^{-1} \nabla_{\parallel} \cdot \mathbf{B} = Q_{\perp} + \frac{1}{2} mS \bar{V}_{\perp}^2$$

$$\begin{aligned} \frac{dq_{\parallel}}{dt} - 3 \left[ \frac{Ze}{m} E_{\parallel} - \frac{du}{dt} \right] p_{\parallel} + \left[ 4 \nabla_{\parallel} \cdot \mathbf{u} - u \mathbf{B}^{-1} \nabla_{\parallel} \cdot \mathbf{B} \right] q_{\parallel} + \nabla_{\parallel} \cdot \rho \langle V_{\parallel}^4 \rangle \\ + \left[ 3\rho \langle V_{\parallel}^2 V_{\perp}^2 \rangle - \rho \langle V_{\parallel}^4 \rangle \right] \mathbf{B}^{-1} \nabla_{\parallel} \cdot \mathbf{B} = H_{\parallel} + mS \bar{V}_{\parallel}^3 \end{aligned}$$

$$\begin{aligned} \frac{dq_{\perp}}{dt} - \left[ \frac{Ze}{m} E_{\parallel} - \frac{du}{dt} \right] p_{\perp} + 2 \left[ \nabla_{\parallel} u - u B^{-1} \nabla_{\parallel} B \right] q_{\perp} + \frac{I}{2} \nabla_{\parallel} \rho \langle V_{\parallel}^2 V_{\perp}^2 \rangle \\ + \left[ \frac{\rho}{4} \langle V_{\perp}^4 \rangle - \rho \langle V_{\parallel}^2 V_{\perp}^2 \rangle \right] B^{-1} \nabla_{\parallel} B = H_{\perp} + \frac{I}{2} m S V_{\parallel} V_{\perp}^2 \end{aligned}$$

where once again the index ' $a$ ' is implied,  $a \in \{i, e\}$ . These equations are not closed, since 4<sup>th</sup> moments appear in the 3<sup>rd</sup> moment equations; closure requires that these be related to lower moments (in gas dynamics, this procedure is usually terminated on the level of the 2<sup>nd</sup> rather than the 3<sup>rd</sup> moment<sup>[Chs58]</sup>; in our case, the 3<sup>rd</sup> moment equations are included in the hope of increasing the accuracy of the heat flux expressions). At this point we can make use of the hierarchy of collision times derived in §A.2.3,  $\tau_{ee} \ll \tau_{ii} \ll \tau_{ei}$ , which suggests that a bi-Maxwellian distribution  $f_a^{2M}(s, V_{\parallel}, V_{\perp}; t; T_{\parallel}, T_{\perp}) \propto \exp[-\beta_{\parallel}(V_{\parallel}-u)^2 - \beta_{\perp}(V_{\perp})^2]$ ,  $\beta = m/2T$ , should provide a good approximation to  $f_a$  for the purpose of evaluating higher moments; with  $f_a = f_a^{2M}$ , 4<sup>th</sup> moments become

$$\langle V_{\parallel}^4 \rangle = 3 \frac{P_{\parallel} P_{\parallel}}{\rho^2} \quad \langle V_{\parallel}^2 V_{\perp}^2 \rangle = 2 \frac{P_{\parallel} P_{\perp}}{\rho^2} \quad \langle V_{\perp}^4 \rangle = 8 \frac{P_{\perp} P_{\perp}}{\rho^2} \quad (2.1.10)$$

To the same accuracy, 3<sup>rd</sup> order collision terms may be approximated by a BGK model<sup>[Bha54]</sup>,

$$\sum_b C_{ab} = \frac{f_a - f_a^{2M}}{\tau_a^H} \quad \frac{I}{\tau_a^{(3)}} \equiv \alpha_a \sum_b \frac{I}{\tau_{ab}} \quad H_{\parallel a} = \frac{q_{\parallel a}}{\tau_a^{(3)}} \quad H_{\perp a} = \frac{q_{\perp a}}{\tau_a^{(3)}} \quad (2.1.11)$$

where  $\tau_{ab}$  are classical collision times (A.2.37) and  $\alpha_a$  is a constant to be determined by comparison with the classical expression for  $q_a$  in the highly collisional limit,  $\tau_{ab} \rightarrow 0$ . Thus, by assuming a bi-Maxwellian distribution for the evolution of the 4<sup>th</sup> moments we have effectively closed the 3<sup>rd</sup> moment equations (2.1.9) which are now valid over the entire range of collisionality subject to the weak drift approximation.

The 2<sup>nd</sup> order (energy exchange) collision terms,  $Q_{\parallel}$  and  $Q_{\perp}$ , contain contributions from like-particle (i-i, e-e) and unlike-particle (i-e) collisions. Once again, based on  $\tau_{ee} \ll \tau_{ii} \ll \tau_{ei}$ , we expect these processes to proceed on different time scales, allowing us to separate them by writing,

$$Q_{\parallel a} = \frac{2(p_{\perp} - p_{\parallel})_a}{\tau_a^{(1)}} + \frac{p_{\parallel b} - p_{\parallel a}}{\tau_{ab}^{(2)}} \quad Q_{\perp a} = -\frac{(p_{\perp} - p_{\parallel})_a}{\tau_a^{(1)}} + \frac{p_{\perp b} - p_{\perp a}}{\tau_{ab}^{(2)}} \quad (2.1.12)$$

Relaxation times may be calculated by isolating each process in turn. The calculation of energy exchange due to like-particle collisions has been carried out for  $f_a = f_a^{2M}$ , and is valid for any degree of anisotropy<sup>[Ich73]</sup>.

$$\tau_a^{(1)} = \frac{5}{2} \tau_a(T_\zeta) \quad T_\zeta = T_{\parallel a} \left\{ \frac{15}{4\zeta^2} \left[ -3 + (\zeta + 3) \left( \frac{g(\sqrt{\zeta})}{\sqrt{\zeta}} \right) \right] \right\}^{-2/3} \quad \zeta = \frac{T_{\perp} - T_{\parallel}}{T_{\parallel}} \quad (2.1.13)$$

where  $g(\sqrt{x}) = \begin{cases} \tan^{-1}\sqrt{x}, & x>0; \\ \tanh^{-1}\sqrt{-x}, & x<0 \end{cases}$ , and  $\tau_a$  refers to the characteristic time (A.2.37) evaluated at the effective temperature  $T_\zeta$ . The calculation of ion-electron energy exchange for bi-Maxwellian electrons,  $f_e = f_e^{2M}$  ( $f_i$  does not effect the result) yields classical collisional times,

$$\tau_{ei}^{(2)} = \tau_{ei}^E \approx \frac{m_i}{2m_e} \tau_e \quad (2.1.14)$$

The final, 1<sup>st</sup> order collision term, vanishes for like particle (i-i, e-e) collisions; hence,  $R_i = -R_e = -R_{ei}$ , a consequence of momentum conservation. We find  $R_e$  by neglecting terms of order  $(m_e/m_i)$  from the 1<sup>st</sup> moment equation for electrons, which we assume are nearly isotropic ( $\delta p_e \ll p_e$ ),

$$\nabla_{\parallel} p_e = -en_e E_{\parallel} + R_e = -(Zen_i E_{\parallel} + R_i) \quad (2.1.15)$$

In the above, we made use of plasma quasi-neutrality,  $n_e = Zn_i$ ; we can thus replace  $Zen_i E_{\parallel} + R_i$ , which occur together in the ion equation, by the electron pressure gradient; in the highly collisional regime, Braginskii's result for  $R_e$  may be used, §A.3. In all the collision terms evaluated above, we neglected the neutral contribution, which will be added separately at a later stage, §2.4.3

As a next step, we form a linear combination of the parallel and perpendicular equations, effecting a transformation to isotropic and non-isotropic quantities,  $\{\psi_1, \psi_{\perp}\} \rightarrow \{\psi, \delta\psi\}$ ,  $\psi \in \{p, q\}$ ,

$$\frac{dp}{dt} + \left[ \frac{5}{3} p + \frac{2}{3} \delta p \right] \nabla_{\parallel} u + B \nabla_{\parallel} (q B^{-1}) - \left[ \frac{5}{3} p - \frac{1}{3} \delta p \right] u B^{-1} \nabla_{\parallel} B = \frac{p_b - p_a}{\tau_{ab}^{(2)}} + \frac{1}{3} m S V^2 \quad (2.1.16)$$

$$\frac{3}{2} \frac{d\delta p}{dt} + \left[ 2p + \frac{7}{2} \delta p \right] \nabla_{\parallel} u + \frac{3}{2} B \nabla_{\parallel} (\delta q B^{-1}) + [p - 2\delta p] u B^{-1} \nabla_{\parallel} B = -\frac{9}{2} \frac{\delta p}{\tau_{ab}^{(1)}} + m S (V_{\parallel}^2 - \frac{1}{2} V_{\perp}^2)$$

$$\begin{aligned} \frac{dq}{dt} + \nabla_{\parallel} \left[ \left( \frac{5}{3} p + \frac{2}{3} \delta p \right) \frac{(p + \delta p)}{\rho} \right] + \left( \frac{8}{3} q + \frac{2}{3} \delta q \right) \nabla_{\parallel} u - \left[ \frac{5}{3} q - \frac{1}{3} \delta q \right] u B^{-1} \nabla_{\parallel} B - \left[ \frac{Ze}{m} E_{\parallel} - \frac{du}{dt} \right] \left( \frac{5}{3} p + \frac{2}{3} \delta p \right) \\ = -\frac{q}{\tau_{ab}^{(3)}} + \left[ \left( \frac{7}{3} p + \frac{1}{3} \delta p \right) \frac{\delta p}{2\rho} \right] B^{-1} \nabla_{\parallel} B + m S V_{\parallel} V^2 \end{aligned}$$

where we used  $\{3\psi, 3\delta\psi/2\} = \{\psi_{||} + 2\psi_{\perp}, \psi_{||} - \psi_{\perp}\}$  and  $\{\psi_{||}, \psi_{\perp}\} = \{\psi + \delta\psi, \psi - \delta\psi/2\}$ ; an expression for  $d/dt(\delta q)$  was omitted for the sake of brevity, since it is not needed below. No information was lost in transforming from  $\{\psi_{||}, \psi_{\perp}\}$  to  $\{\psi, \delta\psi\}$ ; both sets of equations are valid for any anisotropy in  $f_i(V_{||}, V_{\perp})$ . However, by forming isotropic expressions, which dominate for high collisionality ( $\psi_{||} \rightarrow \psi_{\perp} \rightarrow \psi, \delta\psi \rightarrow 0$ ), the non-isotropic contributions may be treated as perturbations to the isotropic equations. For example, a quasi-stationary  $\delta p$  can be obtained by neglecting non-isotropic gradients and external sources in (2.1.16).

$$\begin{aligned} & \left( \frac{7}{2} \nabla_{||} u - \frac{2u}{B} \nabla_{||} B + \frac{9}{2} \frac{1}{\tau^{(1)}} \right) \delta p + \left( 2p \nabla_{||} u + \frac{p}{B} \nabla_{||} B \right) = 0 \\ & \therefore \delta p = -\eta \left( \nabla_{||} u - \frac{u}{2B} \nabla_{||} B \right) \quad \eta \equiv \frac{\frac{4}{9} p \tau^{(1)}}{1 + u \tau [2L_{\nabla u}^{-1} - \frac{10}{9} L_{\nabla B}^{-1}]} \end{aligned} \quad (2.1.17*)$$

where we introduced local gradient scale lengths,  $L_{\nabla \psi} \equiv \psi / \nabla_{||} \psi$ , and expressed our result in the ‘viscous’ form. The non-isotropic nature of the parallel ‘viscosity’  $\eta$ , often obscured in the Braginskii formulation, is here made evident. Our collisional limit,  $\eta = (4/9)\tau^{(1)}p = 1.11\tau p$  is somewhat higher than the classical values of Braginskii (obtained by expanding the pressure equation in terms of the mean-free-path to gradient scale length ratio,  $\lambda / L_{\nabla \psi}$ ):  $\eta_i^{cl} = 0.96\tau p_b, \eta_e^{cl} = 0.73\tau p_e$ . In the opposite limit,  $\tau \rightarrow \infty$ , the ‘viscous’ flux  $\delta p$  saturates to a value of  $-p\mu$ , where  $\mu = (4/L_{\nabla u} + 2/L_{\nabla B})/(7/L_{\nabla u} - 4/L_{\nabla B})$  with  $\mu \rightarrow 4/7$  as  $L_{\nabla u}/L_{\nabla B} \rightarrow 0$ , and  $\mu \rightarrow -1/2$  as  $L_{\nabla B}/L_{\nabla u} \rightarrow 0$ . Transport coefficients of this type are said to be ‘flux limited’.

At this point we would like to write down moment equations for ions and electrons separately, stopping with 2<sup>nd</sup> order moments. We simplify our analysis by assuming quasi-neutrality,  $n_e = Zn_i$ , no net charge production ( $ZS_i = S_e = S_0$ ), negligible parallel currents ( $|j_{||}| = |Zen_i u_i - en_e u_e| \ll len_e u_e|, \therefore u_i \approx u_e = u$ ), and neglecting terms of order  $\tau_e/\tau_i \sim (m_e/m_i)^{1/2}$  or smaller (thus,  $\delta p_e = \delta p_i \cdot O(m_e/m_i)^{1/2}$  will be neglected, while  $\delta p_i$  will follow from (2.1.17); in other words we expect anisotropy in  $f_i(V_{||}, V_{\perp})$  to be much smaller than in  $f_i(V_{||}, V_{\perp})$ ). This allows us to add the 0<sup>th</sup> and 1<sup>st</sup> moment equations for ions and electrons,

$$\begin{aligned} \frac{d\rho}{dt} + \rho \nabla_{||} u - \frac{\rho u}{B} \nabla_{||} B &= mS_0 \quad \rho \equiv n_i m_i \equiv m_i \left( \frac{n_e}{Z} \right) \\ \rho \frac{du}{dt} + \nabla_{||} (\rho_i + p_e + \delta p_i) - \left( \frac{3}{2} \delta p_i \right) \frac{1}{B} \nabla_{||} B &= mS_0 \bar{V}_{||} \end{aligned} \quad (2.1.18)$$

We note that there is no net momentum exchange between ions and electrons:  $(Zn_i - n_e)eE_{||}$  vanishes by quasi-neutrality, while  $R_i + R_e = 0$  by symmetry of the collision operator. To calculate the heat fluxes  $q_i$  and  $q_e$ , we use the isotropic form of the 3<sup>rd</sup> moment equations along with a quasi-stationary, source-free solution of the non-isotropic 2<sup>nd</sup> moment equations. For electrons, we may combine (2.1.16a) and (2.1.16c), and eliminate  $E_{||}$  and  $\nabla_{||} u$  using (2.1.15) and (2.1.18a),

$$q_e \left[ \frac{1}{u\tau_e^{(3)}} + \frac{8}{3u} \nabla_{\parallel} u - \frac{2}{3B} \nabla_{\parallel} B \right] = \frac{5p_e}{3u} \left[ \frac{1}{m_e} \nabla_{\parallel} T_e - \frac{R_e}{m_e n_e} \right] + n_e u \nabla_{\parallel} T_e - \frac{\frac{2}{3} p_e u}{n_e} \nabla_{\parallel} n_e + Q_{ei} \quad (2.1.19^*)$$

$$\therefore q_e = -\frac{n_e \chi_e^{cl}}{\vartheta_e} \left( 1 - \frac{u^2}{c_{\gamma,e}^2} \right) \nabla_{\parallel} T_e - \frac{2}{3} \left( \frac{u^2}{c_{\gamma,e}^2} \right) \frac{T_e \chi_e^{cl}}{\vartheta_e} \nabla_{\parallel} n_e + \frac{\chi_e^{cl}}{\vartheta_e} R_e + \frac{u \tau_e^{(3)}}{\vartheta} \cdot \frac{(p_e - p_i)}{\tau_{ei}^{(2)}}$$

$$\chi_e^{cl} \equiv \frac{5T_e}{3m_e} \tau_e^{(3)} = c_{\gamma,e}^2 \tau_e^{(3)} \quad c_{\gamma,e}^2 = \frac{5}{3} c_e^2 = \frac{5}{3} \cdot \frac{T_e}{m_e} \quad \vartheta_e \equiv 1 + u \tau_e^{(3)} \left( \frac{8}{3L_{\nabla u}} - \frac{2}{3L_{\nabla B}} \right)$$

We find four contributions to  $q_e$ : electron heat conduction, thermo-electric effect, ion-electron collisional momentum and energy transfers (typically  $u \ll c_e$  and the 2<sup>nd</sup> term vanishes). We note that in the collisional limit ( $\lambda_e \ll L_{\nabla u}$ ),  $R_e = R_{ei} = -0.71 n_e \nabla_{\parallel} T_e$ ; comparing with the classical electron heat flux  $q_e^{cl} = n_e \chi_e^{cl} \nabla_{\parallel} T_e$ , where  $\chi_e^{cl} = 3.2 T_e \tau_e / m_e$ , we can estimate  $\tau_e^{(3)} \sim 1.12 \tau_e$ . In the opposite limit ( $\lambda_e \gg L_{\nabla u}$ ),  $q_e$  saturates to a free-streaming value  $q_e^{fs} = k_e p_e c_e$ , with  $k_e \sim 1$  for  $\lambda_e < L_{\nabla B}$ , and  $k_e \ll 1$  for  $\lambda_e > L_{\nabla B}$ . A simple flux-limited expression for  $q_e$ , approaching the above two limits,  $1/q_e = 1/q_e^{cl} + 1/q_e^{fs}$ , shows remarkably good agreement with the more accurate expression (2.1.18), as long as  $k_e(L_{\nabla u}, L_{\nabla B})$  is appropriately chosen<sup>[Zaw88]</sup>. We define a flux-limited electron heat diffusivity in analogy with (2.1.17),

$$\chi_e \equiv -\frac{q_e}{n_e \nabla_{\parallel} T_e} = \chi_e^{cl} \left( 1 + \left| \frac{q_e^{cl}}{q_e^{fs}} \right| \right)^{-1} \quad (2.1.20)$$

A similar procedure may be repeated for the ions. Before commencing, we note that  $\chi_i^{cl} / \chi_e^{cl}$  and  $q_i^{fs} / q_e^{fs} \sim O(m_e/m_i)^{1/2}$  and that the ion contribution to the total heat flux is small (ZNC ignore  $q_i$  entirely). However, in a warm, stagnant plasma ( $u \ll c_i$ ), when  $T_i$  and  $T_e$  are sufficiently de-coupled, ion heat conduction may affect  $T_i(s_{\parallel})$ , and should be included. As before, we combine (2.1.16a) and (2.1.16c), eliminating  $E_{\parallel}$  and  $\nabla_{\parallel} u$  using (2.1.15) and (2.1.18a) and neglect  $\delta p_i$  as an order higher in smallness,

$$q_i = -\frac{n_i \chi_i^{cl}}{\vartheta_i} \left( 1 - \frac{u^2}{2c_{\gamma,i}^2} \right) \nabla_{\parallel} T_i - \frac{2}{3} \left( \frac{u^2}{c_{\gamma,i}^2} \right) \frac{T_i \chi_i^{cl}}{\vartheta_i} \nabla_{\parallel} n_i + \frac{\chi_i^{cl}}{\vartheta_i} \left( \frac{m_e}{m_i} \right) R_e + \frac{u \tau_i^{(3)}}{\vartheta_i} \cdot \frac{(p_i - p_e)}{\tau_{ei}^{(2)}} \quad (2.1.21^*)$$

$$\chi_i^{cl} \equiv \frac{5T_i}{3m_i} \tau_i^{(3)} = c_{\gamma,i}^2 \tau_i^{(3)} \quad c_{\gamma,i}^2 = \frac{5}{3} c_i^2 = \frac{5}{3} \cdot \frac{T_i}{m_i} \quad \vartheta_i \equiv 1 + u \tau_i^{(3)} \left( \frac{8}{3L_{\nabla u}} - \frac{2}{3L_{\nabla B}} \right)$$

The main difference in comparison to  $q_e$ , aside from the smaller magnitude, is the fact that the first term, representing ion heat conduction, is strongly reduced for transonic flow,  $u \sim c_{\gamma,i}$ . Evaluating (2.1.21) for

$\tau_i \rightarrow 0$ , and comparing with  $q_i^d = n_i \chi_i^{cl} \nabla_{\parallel} T_i$  where  $\chi_i^{cl} = 3.9 T_i \tau_i / m_i$ , we estimate  $\tau_i^{(3)} \sim 1.17 \tau_i$ . The flux-limited ion heat diffusivity  $\chi_i$  is defined in complete analogy to (2.1.20).

We next transform the lower moment equations from primitive ( $\rho, u, p_i, p_e$ ) to conservative ( $\rho, \rho u, \rho \epsilon_i, \rho \epsilon_e$ ) variables, better suited to numerical solution, and display the final equation set in vector form,

$$\frac{\partial U}{\partial t} + \nabla_{\parallel} \cdot (\mathbf{F}_{\parallel} + \mathbf{G}_{\parallel}) = \mathbf{Q}_p + \mathbf{Q}_3 + \mathbf{Q}_B \equiv \mathbf{Q}(U) \quad (2.1.22*)$$

$$U = \begin{pmatrix} \rho \\ \rho u \\ \rho \epsilon_i \\ \rho \epsilon_e \end{pmatrix} \quad \mathbf{F}_{\parallel} = \begin{pmatrix} \rho u \\ p_i + p_e + \rho u^2 \\ u(\rho \epsilon_i + p_i) \\ u(\rho \epsilon_e + p_e) \end{pmatrix} \quad \mathbf{G}_{\parallel} = \begin{pmatrix} 0 \\ \delta p_i \\ q_i + u \delta p_i \\ q_e \end{pmatrix} \quad \begin{aligned} \rho \epsilon_i &= \frac{1}{2} p_i + \frac{1}{2} \rho u^2 \\ \rho \epsilon_e &= \frac{1}{2} p_e \\ T_i &= p_i / n_i \\ T_e &= p_e / n_e \end{aligned}$$

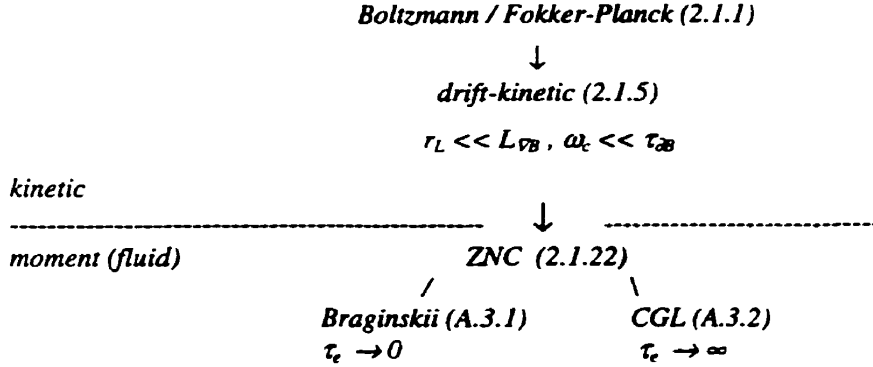
$$\mathbf{Q}_p = \begin{pmatrix} 0 \\ 0 \\ -u \nabla_{\parallel} p_e + \frac{p_e - p_i}{\tau_{ei}^{(2)}} \\ u \nabla_{\parallel} p_e - \frac{p_e - p_i}{\tau_{ei}^{(2)}} \end{pmatrix} \quad \mathbf{Q}_3 = \begin{pmatrix} m_i S_0 \\ m_i v_{\parallel} S_0 \\ \frac{1}{2} m_i v_i^2 S_0 \\ \frac{1}{2} m_e v_e^2 S_0 \end{pmatrix} \quad \mathbf{Q}_B = \left\{ \mathbf{F}_{\parallel} + \mathbf{G}_{\parallel} - \begin{pmatrix} 0 \\ p_i + p_e - \frac{1}{2} \delta p_i \\ 0 \\ 0 \end{pmatrix} \right\} \frac{\nabla_{\parallel} B}{B}$$

where  $\mathbf{U}$  contain the state variables,  $\mathbf{F}_{\parallel}$  the convective fluxes,  $\mathbf{G}_{\parallel}$  are the viscous/conductive fluxes,  $\mathbf{Q}_p$  the plasma source terms (including the collisions between the electron and ion species and their interaction with the net electric field),  $\mathbf{Q}_3$  the neutral source terms (which in addition to sources associated with the creation and destruction of particles, shown in (2.1.22), would also include the change in momentum and energy due to plasma-neutral interactions, not explicitly shown above; the complete neutral sources will be defined in §2.3, cf. (2.3.5)), and  $\mathbf{Q}_B$  the magnetic flux expansion terms;  $\delta p_i, q_i, q_e$  are given by (2.1.17) and (2.1.20). We expect the above set of equations to reduce to those of Braginskii in the high-collisionality limit,  $\tau_e \rightarrow 0$ . Omitting all cross-field terms from (A.3.1), which we have neglected at the outset, we find that the two equation sets are nearly identical, aside from flux limited expressions for  $q_i$  and  $q_e$  and the anisotropic energy exchange term (both reduce, with slight transport coefficient corrections, to the Braginskii expressions as  $\tau_e \rightarrow 0$ ). The flux expansion terms,  $\mathbf{Q}_B$ , are found to agree if the metric is made to reflect the magnetic geometry. In the region of intermediate collisionality, the anisotropy of  $f_i(\mathbf{V}_{\parallel}, \mathbf{V}_{\perp})$  becomes more pronounced affecting,  $\delta p_i, q_i$ , and  $\tau_{ei}^{(2)}$ . The two equation sets progressively diverge in this regime, with differences in their solutions becoming significant beyond  $\lambda_i / L_{VB} > 0.1$ . Finally, in the low collisionality limit ( $\tau_e \rightarrow \infty$ ), the 2<sup>nd</sup> moment equations (2.1.9c,d) reduce to the CGL equations<sup>[Che56]</sup>, see §A.3,

$$\frac{dp_{\perp}}{dt} + p_{\perp} \nabla_{||} u - 2 p_{\perp} u B^{-1} \nabla_{||} B = \frac{d}{dt} \left( \frac{p_{\perp}}{\rho B} \right) = 0 \quad (2.1.23)$$

$$\frac{dp_{||}}{dt} + 3 p_{||} \nabla_{||} u - p_{||} u B^{-1} \nabla_{||} B = \frac{d}{dt} \left( \frac{p_{||} B^2}{\rho^3} \right) = 0$$

We can summarize the various plasma equations by the following schematic:



It is worth emphasizing that the ZNC moment description does not presuppose a perturbed Maxwellian velocity distribution. This assumption, appropriate for high collisionality, is only introduced to close the Braginskii equations. In contrast, the collisionless CGL equations, make no such assumption; the fluid-like primitive variables  $\rho, \mathbf{u}, \mathbf{p}$  represent velocity moments over potentially non-Maxwellian  $f_i(\mathbf{v})$ . The domain of validity of the ZNC or drift-kinetic moment equations presented in this section, which from now on will be referred to simply as the (parallel) plasma transport equations, is given below:

- a) quasi-neutrality,  $n_e = Z n_i$
- b) small parallel currents,  $|Z e n_i u_i - e n_e u_e| \ll |e n_i|$
- c) weak drifts,  $v^{\text{drift}} \ll |v_{||}, v_{\perp}|$
- d) slowly varying fields (A.2.6),  $\delta_v \ll 1$  ( $r_L \ll L_{vB}, \omega_c \ll \tau_{eB}$ )
- e) all collisionality regimes,  $\tau_i, \tau_e \in [0, \infty]$

The extensions to include parallel currents and finite poloidal drifts are straight forward, although non-trivial<sup>[Cha97,Lab97]</sup>; since they do not involve cross-field plasma transport, they will not affect our conclusions regarding the validity of the OSM approach. We shall see presently that in the vicinity of a solid surface, some of the above conditions may be violated; consequently, that region will be considered separately, with the aim of deriving appropriate boundary conditions for the plasma transport equations (2.1.22).

## 2.2 Plasma Surface Interaction

A solid surface has a very different effect on a plasma than on a neutral gas; for the latter, it is a reflecting surface, for the former, an absorbing one (plasma ions and electrons recombine on the surface, and re-enter the plasma volume as neutrals<sup>[Pos84]</sup>). In both cases, massive particles moving towards the surface have an average velocity on the order of their respective sound speeds  $c_a \sim (T_a/m_a)^{1/2}$ ,  $a \in \{i,n\}$ . Neutral particles moving away from the surface have the same average velocity as those moving towards it, producing a zero net flow. There are no plasma ions moving away from the absorbing surface,  $f_i(v_x > 0) = 0$ , hence the plasma flow velocity in front of the surface is equal to the average ion velocity moving towards the surface. Plasma transport equations based on a weakly shifted Maxwellian  $f_i(v_x)$  are thus invalid in the near surface region; their inaccuracy may be estimated by a comparison with a fully kinetic solution. The problem of plasma-solid contact is one of the oldest in plasma physics<sup>[Rie96]</sup>, and it is worth considering it in some detail. We take the  $x = 0$  plane as the location of the absorbing surface, assume symmetry in the  $y$  and  $z$  directions ( $\partial/\partial z = \partial/\partial y = 0$ ,  $\langle v_y \rangle = \langle v_z \rangle = 0$ ), and zero magnetic field; the  $x$  domain is closed by requiring vanishing gradients at infinity,  $L \gg \lambda_D$ ,  $(\partial/\partial x)_L = 0$ . The problem is described by kinetic equations (2.1.1) for ions, electrons and neutrals integrated over  $dv_y dv_z$  and by Poisson's equation for the electrostatic potential  $\phi$  (we assume Maxwellian distributions in  $v_y$  and  $v_z$ , normalized to unity),

$$\begin{aligned} \left( \frac{\partial}{\partial t} + v_{x,i} \frac{\partial}{\partial x} - \frac{eZ}{m_i} \frac{\partial \phi}{\partial x} \frac{\partial}{\partial v_{x,i}} \right) f_i(x, v_{x,i}) &= \sum_{b \in \{i,e,n\}} C_{ib} + S_i \\ \left( \frac{\partial}{\partial t} + v_{x,e} \frac{\partial}{\partial x} + \frac{e}{m_e} \frac{\partial \phi}{\partial x} \frac{\partial}{\partial v_{x,e}} \right) f_e(x, v_{x,e}) &= \sum_{b \in \{i,e,n\}} C_{eb} + S_e \\ \left( \frac{\partial}{\partial t} + v_{x,n} \frac{\partial}{\partial x} \right) f_n(x, v_{x,n}) &= \sum_{b \in \{i,e,n\}} C_{nb} + S_n \\ \frac{\partial^2 \phi}{\partial x^2} &= 4\pi e(n_e - Zn_i) = 4\pi e(\int f_e dv_{x,e} - Z \int f_i dv_{x,i}) \end{aligned} \quad (2.2.1)$$

together with the boundary conditions of no net current and no back flow at  $x = 0$ ,

$$Ze \int f_i v_{x,i} dv_{x,i} - e \int f_e v_{x,e} dv_{x,e} = 0 \quad (2.2.2)$$

$$f_i(x=0, v_{x,i} > 0, t) = f_e(x=0, v_{x,e} > 0, t) = 0$$

The neutrals have been included explicitly in the problem, since they enter both the source and collision terms in the ion and electron equations; they do not, however, interact with the electric field. Plasma-neutral interactions will be discussed in the next section, §2.3.

We begin by observing that since  $c_e \gg c_i$ , an initially neutral surface would quickly become negatively charged,  $\phi(x=0) = \phi_0 < 0$ . The negative floating potential opposes electron flow, until at steady

state the electron and ion currents to the surface are equal,  $Z\langle v_{x,i} \rangle = \langle v_{x,e} \rangle$ . The extent and magnitude of this potential may be estimated by considering the Poisson equation in the near surface region. The smallness of the electron mass, and the consequent high electron self-collisionality, allows us to neglect the first two terms in the electron kinetic equation which leads to (2.1.15); the solution  $f_e(v)$  is easily obtained from (2.2.1) as a shifted Maxwellian distribution reduced by the Boltzmann factor<sup>[Kra80]</sup>,

$$f_e(x, v_{x,e}) = f_e^M(L, v_{x,e}) \exp\left(\frac{e\varphi(x)}{T_e}\right) \quad \varphi(L) = 0 \quad \therefore n_e(x) = n_e(L) \exp\left(\frac{e\varphi(x)}{T_e}\right) \quad (2.2.3)$$

The ion distribution becomes entirely forward shifted at some location  $x_s$ ,  $f_i(0 < x < x_s, v_{x,i} > 0) = 0$ ; the region  $x \in [0, x_s]$  will be referred to as the electrostatic sheath. Since we expect  $x_s$  to be of the order  $\lambda_D$ , which is much shorter than any other length in the plasma, including collisional mean free paths, collisions and sources may be neglected in the sheath,  $C_{ab} = S_a = 0$ . At this point, the kinetic equations may be analyzed in various degrees of sophistication<sup>[Stu90]</sup>; for our analysis, we will adapt an approximate method, which none the less, leads to the same result as the more involved and much lengthier treatments<sup>[Rie96]</sup>. We begin by noting that any trajectory satisfies the collisionless kinetic equation<sup>[Lif92]</sup>, and that conservation of energy gives one such trajectory,  $v_x(x)$ :  $\frac{1}{2}m_i v_x^2 + Ze\varphi(x) = \frac{1}{2}m_i v_{x,s}^2 + Ze\varphi(x_s)$ ; based on this result we can construct a solution to  $f_i(x, v_x)$  from  $v_x(x)$ . In the absence of sources, particle continuity requires that  $f_i(v_1)v_1 = f_2(v_2)v_2$ , where  $v_1 = v_x(x_1)$  and  $v_2 = v_x(x_2)$  are related by  $v_x(x)$ ,

$$f_i(x, v_x) = f(x_s, v_x) \frac{v_{x,s}}{v_x} = f(x_s, v_x) \left( \frac{\frac{1}{2}m_i v_x^2 + Ze(\varphi(x) - \varphi(x_s))}{\frac{1}{2}m_i v_{x,s}^2} \right)^{1/2} \quad (2.2.4)$$

Inserting  $n_e(x)$  and  $n_i(x)$  into Poisson's equation and expanding to first order in  $\Delta\varphi = \varphi(x) - \varphi(x_s)$ , we get

$$\begin{aligned} \frac{\partial^2 \Delta\varphi}{\partial x^2} &= 4\pi e \left\{ n_{e,s} \left( 1 + \frac{e\Delta\varphi(x)}{T_e} \right) - Z \int dv_x f(x_s, v_x) \left( 1 + \frac{Ze\Delta\varphi(x)}{m_i v_x^2} \right) \right\} \\ &= 4\pi e^2 \Delta\varphi(x) \left\{ \frac{n_{e,s}}{T_e} - \frac{Z^2 n_{i,s}}{m_i} \int dv_x f(x_s, v_x) \frac{1}{v_x^2} \right\} = \frac{\Delta\varphi}{\lambda_D^2} \left\{ 1 - \frac{T_e}{m_i} \frac{Z^2 n_{i,s}}{n_{e,s}} \left\langle \frac{1}{v_x^2} \right\rangle \right\} \end{aligned} \quad (2.2.5)$$

Assuming quasi-neutrality at the sheath edge, the condition for a non-oscillatory solution becomes,

$$\left\langle \frac{1}{v_x^2} \right\rangle_{x=x_s}^{-1} \leq \frac{ZT_e}{m_i} \left( \frac{Zn_{i,s}}{n_{e,s}} \right) = \frac{ZT_e}{m_i} \quad (2.2.6)$$

This inequality is referred to as the generalized Bohm criterion<sup>[All76]</sup>. Physically it means that the sheath potential increases until the charge separation within the sheath is reduced sufficiently; this requires (via

continuity) that the ion velocity increase to the order of  $(ZT_e/m_i)^{1/2}$ . The Bohm criterion was first obtained for cold ions<sup>[Rie96]</sup>,  $T_i = 0$  with  $f_i(x, v_x) = n_i(x)\delta(v_x - u(x))$ , for which it becomes  $u(x_s) > (ZT_e/m_i)^{1/2}$ . For cool ions, described by a shifted Maxwellian,  $f_i(x, v_x) = n_i(x)(\beta/\pi)^{1/2}\exp\{-\beta(v_x - u(x))^2\}$ , where  $\beta = m_i/2T_{x,i}(x)$ , such that  $f_i(v_x > 0) = 0$ , and  $f_i(v_x < 0)$  is a broadened delta function of width  $c_i = (T_{x,i}/m_i)^{1/2}$  the Bohm criterion becomes  $1/(u^2(x_s) - c_i^2) < (ZT_e/m_i)^{1/2}$ ; this may be written as  $u(x_s) > ((ZT_e + T_{x,i})/m_i)^{1/2} \equiv c_{s,x}$ , where  $c_{s,x}$  is the parallel plasma sound speed. The flow velocity at the entrance into the sheath is increased by roughly the spread of the ion velocities parallel to the flow. Defining a local Mach number as  $M = u/c_s$ , the Bohm criterion is often stated (with some inaccuracy, since  $T_{i,x}$  need not equal  $T_i$ ) as,

$$M(x_s) = \left( \frac{u}{c_s} \right)_{x_s} \geq 1 \quad c_s = \left( \frac{ZT_e + T_i}{m_i} \right)^{1/2} \quad (2.2.7)$$

From (2.2.5) we see that  $x_s \sim O(\lambda_D)$ , confirming our collisionless ansatz.

We can estimate the floating potential at the wall  $\varphi_0$ , by assuming zero current flow to the wall, sonic ion flow at the sheath edge,  $M(x_s) = 1$ , and Maxwellian electrons throughout,

$$Zen_{i,s}c_s = \frac{I}{4}en_{e,s}\tilde{c}_e \exp\left(\frac{e(\varphi_0 - \varphi_s)}{T_e}\right) \quad \tilde{c}_e = \left(\frac{8T_e}{\pi m_e}\right)^{1/2} = 1.6c_e \quad (2.2.8)$$

We thus obtain an expression for the potential drop across the sheath,

$$-\frac{e(\varphi_0 - \varphi_s)}{T_e} = \frac{I}{2} \ln\left(\frac{1}{2\pi(1+T_i/ZT_e)m_e}\right) \quad (2.2.9)$$

The potential at the sheath edge depends on the flow in the pre-sheath region,  $x > x_s$ , but the pre-sheath potential is generally small in comparison with the potential drop across the sheath<sup>[Stu89]</sup>; typical values for a hydrogenic plasma with  $T_i \sim T_e$  are  $-\varphi_s/T_e \sim 1/2$ , and  $-(\varphi_0 - \varphi_s)/T_e \sim 3$ .

We would also like to estimate the ion and electron power flowing into the sheath, and the total power deposited onto the surface, which may include chemical energies. The electron energy flux at  $x = 0$  is easily calculated with a cut-off-Maxwellian distribution,  $f_e(v_x > 0) = 0$ , while the flux at the sheath edge  $x_s$  must be larger by the value of the sheath potential drop (which is repulsive for the electrons).

$$q_{e,0} = \int \frac{1}{2}m_e v^2 v_x f_e(v_x, v_y, v_z) d^3v = 2T_e \int v_x f_e(v_x) dv_x = 2T_e \Gamma_e \quad (2.2.10)$$

$$q_{e,s} = (2T_e + |e\varphi_s - e\varphi_0|) \Gamma_e$$

If we assume a shifted Maxwellian distribution with  $M(x_s) = 1$  for the ions, we obtain the same result as for the electrons, except the potential drop is reversed,  $q_{i,s} = 2T_i \Gamma_i$ ,  $q_{i,0} = q_{i,s} + Ze|\varphi_s - \varphi_0|$ . In reality the

presence of the **E**-field in the pre-sheath leads to ion flow which distorts  $f_i(x_s, v_x)$ , introducing errors to the above estimate. To progress further the system (2.2.1) would have to be solved on the entire domain,  $x \in [0, L]$ . At present, no such complete solution has yet been obtained (not even when plasma-neutral interactions are neglected); however, a variety of simplified cases are present in the literature<sup>[Rie96]</sup>. These are summarized in §A.4, where they are compared in terms of the predicted normalized fluxes and potentials, Table A.4.1, and the profiles of the ion distributions  $f_i(v)$  at the sheath edge, Fig. A.4.1; the estimated values are strikingly robust with respect to a wide range of assumptions.

In a magnetized plasma, the governing equations (2.2.1) are modified by  $\mathbf{v} \times \mathbf{B}$  terms entering the ion and electron kinetic equations. If  $\mathbf{B}$  is perpendicular to the solid surface, the analysis as presented so far remains valid; otherwise  $\mathbf{E} \times \mathbf{B} \neq 0$  and the geometry of the problem becomes more complicated. The oblique field problem has been considered in some detail<sup>[Cho84]</sup>; the trajectories of the ions and electrons in the near surface region were followed numerically, with the **E**-field determined self-consistently from the Poisson equation using the particle-in-cell method, and the **B**-field taken as constant at an angle  $\vartheta$  to the surface normal. The resulting flow is characterized by two scale lengths: a) within a few Debye lengths of the surface  $x \in [0, 5\lambda_D]$ , the usual electrostatic sheath is formed with flow normal to the surface and strong potential gradients, b) further out, up to a few ion Larmor radii at the local sound speed  $\lambda_\omega = c_s / \omega_c$ ,  $x \in [5\lambda_D, 5\lambda_\omega]$ , a quasi-neutral magnetic pre-sheath region appears in which the net flow is parallel to  $\mathbf{B}$ . The Bohm criterion with an oblique **B**-field becomes,

$$\int \frac{I}{v_{||}^2} f(v_{||}, x) dv_{||} \leq \left( \frac{ZT_e}{m_i} \right)^{1/2} \quad (2.2.11)$$

where  $v_{||}$  is a velocity parallel to  $\mathbf{B}$ . Non-magnetized analysis remains accurate (and insensitive to  $\vartheta$ ), if  $x$  is replaced by  $s_{||}$  and the sheath edge  $x_s$  is taken as the point of entry into the magnetic pre-sheath  $\lambda_\omega$ .

We began the plasma-surface analysis with the express aim of obtaining boundary conditions for the plasma transport equations derived in §2.1; to accomplish this final step we consider the various length scales in the near surface region. These are: the Debye length  $\lambda_D$ , the ion Larmor radius  $r_L$  and the ion collisional mean-free-path  $\lambda_i$ . The evolution of the ion and electron velocity distributions in these regions and the validity of the kinetic and moment equations are shown in Fig. 2.2.2. The fact that kinetic solutions are not valid for  $s_{||} \gg \lambda_i$  expresses the inadequacy of neglecting source and collision terms. For the purpose of modeling, the moment equations are a more efficient tool, with little loss of accuracy for  $s_{||} \gg \lambda_D$ . They must however be constrained by the kinetic solution at some location in the region where both solutions are valid, ie.  $5\lambda_D < s_{||} < 5\lambda_i$ . The sheath edge, taken roughly as the location where Bohm criterion is satisfied, may be chosen as a convenient location to effect this matching of solutions; it is both close enough to the surface that any sources or collisions within the sheath may be neglected, and far enough for quasi-neutrality and moment equations to be valid. In reality, some  $f_i(v)$  distribution exists at this location which

changes continuously into the forward shifted sheath  $f_i(v)$  for  $s_{\parallel} < 5\lambda_D$ , and into gradually less distorted Maxwellian  $f_i(v)$  for  $s_{\parallel} > 5\lambda_D$ ; this distribution is unknown to us. We have instead an approximation to  $f_i(v)$  in the sheath region and again an approximation to its moments in the pre-sheath region. If we denote the former by  $f^S(v)$  and the latter by  $f^P(v)$ , we seek the matching conditions for  $a \in \{i,e\}$ , which assure that  $f^S(v) - f^P(v) = O(\langle v^4 \rangle_S - \langle v^4 \rangle_P)$ . These requirements may be expressed as

$$\langle \psi \rangle_a^S = \langle \psi \rangle_a^P \quad \psi \in \{1, v_{\parallel}, v_{\parallel}^2, v_{\parallel}v^2\} \quad (2.2.12)$$

$$\langle \psi \rangle_a^P = \int \psi_a \cdot f_a^P(v) d^3v \quad \langle \psi \rangle_a^P = \int \psi_a \cdot f_a^P(v) d^3v$$

The right-hand side averages may be related to the density  $n_e$  and fluxes  $\mathbf{F}_e + \mathbf{G}_e$  from the moment equations, (2.1.22); the left-hand side averages require the knowledge of  $f_i^S(v)$  from the kinetic solution. Typically, the energy fluxes are matched by introducing energy sheath transmission coefficients for ions  $\gamma_i$  and electrons  $\gamma_e$ , defined as

$$\langle \frac{1}{2} m_a v_{\parallel} v^2 \rangle_S = (\gamma_a p_a u_a)_S = (\gamma_a T_a F_a)_S \quad (2.2.13)$$

The momentum flux is usually constrained by imposing the Bohm criterion on plasma velocity (since this criterion contains an inequality, the constraint will prevent sub-sonic flow, while allowing supersonic flow). We will adapt both these methods of imposing the kinetic requirements onto the fluid-like moment equations. The effect of boundary conditions on the plasma solution will be studied in §4.2.4

### 2.3 Plasma-Neutral Interaction

Due to proximity of a solid surface, the edge plasma normally contains a significant concentration of neutral species with which it interacts. In this section, we briefly examine the relevant atomic-molecular physics, determine the dominant processes on the basis of their reaction cross-sections, and construct an interaction source term for the moment equations.

Plasma-neutral interactions are normally classified according to the interacting species (neutrals, ions, electrons, photons) and the reaction type (scattering, excitation / emission, dissociation / molecular formation, ionization / recombination, charge exchange, etc.)<sup>[Bro66]</sup>. More generally, we can define  $\mathbf{Y}(n)$  to be a set of all possible, neutral,  $n$ -atom molecules  $X_{Z(1)}X_{Z(2)}\dots X_{Z(n)}$  ( $X_Z$  denotes an atom of nuclear charge  $Z$ ),  $\mathbf{Y}_0$  to be a set of all neutral molecules of any size,  $\mathbf{Y}_+$  to be a set of all molecules (neutral or ionized), and  $\mathfrak{I}$  to be a set of molecules, electrons and photons,

$$\mathbf{Y}(n) = \{X_{Z(i)}X_{Z(i+1)}\dots X_{Z(n)} | Z(i) \in \{1, \dots, N\}; i \in \{1, \dots, n\}\} \quad (2.3.1)$$

$$\mathbf{Y}_0 = \bigcup_{n=1}^{n_{\max}} \mathbf{Y}(n) \quad \mathbf{Y}_+ = \bigcup_{j=0}^{n_{\max}N} \mathbf{Y}_0^{j+} \quad \mathfrak{I} = \{h\nu, e, \mathbf{Y}_+\}$$

Using the above, we can write down all possible  $k$ -body encounters by taking  $k-1$  successive set products of  $\mathfrak{I}$  with itself,  $\mathfrak{R} = \mathfrak{I} \otimes \mathfrak{I} \otimes \dots \otimes \mathfrak{I}$ . Each encounter can lead to several interactions with a probability dependent on the relative energy of the reactants. In the context of fusion research, we are usually interested in hydrogenic plasmas containing small quantities (<10%) of low- $Z$  impurities, originating due to plasma-surface contact at the vessel wall (Be, B, C, O, ...) or injected with the aim of increasing radiation from the plasma (N, Ne, Ar, Xe, ...). We will thus divide our discussion into hydrogen ( $Z=1$ ) and impurity ( $Z>1$ ) reactions. The dominant hydrogen reactions,  $\mathfrak{I} = \{h\nu, e, H, H^+, H_2, H_2^+\}$ , are summarized below<sup>[Jan95]</sup>:

*Atomic hydrogen reactions:  $\mathfrak{I} = \{h\nu, e, H, H^+\}$*  (2.3.2)

$H + H$	$\rightarrow$	$H + H$	<i>atomic scattering</i>
$H + e$	$\rightarrow$	$H^+ + e$	<i>atomic excitation</i>
$H^+$	$\rightarrow$	$H + h\nu$	<i>atomic radiative de-excitation</i>
$H + e$	$\rightarrow$	$H^+ + 2e$	<i>atomic ionization</i>
$H^+ + e$	$\rightarrow$	$H^+ + h\nu$	<i>radiative (two-body) recombination</i>
$H^+ + 2e$	$\rightarrow$	$H^+ + e$	<i>dielectronic (three-body) recombination</i>
$H + H^+$	$\rightarrow$	$H^+ + H$	<i>atomic charge exchange</i>
$H + H$	$\rightarrow$	$H_2 + h\nu$	<i>molecular formation</i>

*Molecular hydrogen reactions:  $\mathfrak{I} = \{h\nu, e, H_2, H_2^+\}$*  (2.3.3)

$H_2 + H_2$	$\rightarrow$	$H_2 + H_2$	<i>molecular scattering</i>
$H_2 + e$	$\rightarrow$	$H_2^+ + 2e$	<i>molecular ionization</i>
$H_2 + e$	$\rightarrow$	$H^+ + H + 2e$	<i>dissociative ionization</i>
$H_2 + e$	$\rightarrow$	$H^+ + H^+ + 3e$	<i>dissociative double ionization</i>
$H_2 + e$	$\rightarrow$	$H + H^-$	<i>dissociative attachment</i>
$H_2 + e$	$\rightarrow$	$H + H + e$	<i>molecular dissociation</i>
$H_2 + e$	$\rightarrow$	$H_2^- + e$	<i>molecular excitation</i>
$H_2^-$	$\rightarrow$	$H_2 + h\nu$	<i>molecular radiative de-excitation</i>
$H_2^-$	$\rightarrow$	$H + H + h\nu$	<i>radiative dissociation</i>
$H_2^+ + e$	$\rightarrow$	$H_2^{++} + e$	<i>molecular excitation</i>
$H_2^{++}$	$\rightarrow$	$H^+ + H + h\nu$	<i>ionized molecule radiative dissociation</i>
$H_2^+ + e$	$\rightarrow$	$H^+ + H + e$	<i>ionized molecule dissociation</i>
$H_2^+ + e$	$\rightarrow$	$H + H$	<i>dissociative recombination</i>
$H_2^+ + e$	$\rightarrow$	$H^+ + H^+ + 2e$	<i>ionized molecule dissociative ionization</i>

Hydrogen atomic and molecular reaction cross sections have been determined experimentally over a wide energy range, and are generally in good agreement with quantum mechanical scattering predictions. Semi-empirical formulations are employed to express experimental data as well as extrapolate to lower energies. For the purpose of the present work, all relevant atomic and molecular data was extracted from the ADAS database<sup>[Sum97]</sup>. The dominant atomic/molecular interaction cross-sections are shown in Fig. 2.3.5.

Let us briefly consider the impact of plasma-neutral interactions on the plasma transport equations. Plasma particle balance is governed by ionization, dissociation and recombination processes (occurring either volumetrically or at the solid surface) leading in the simplest form to the well known Saha equation for the degree of ionization of a gas/plasma mixture, which is obtained by estimating the ionization and recombination cross sections for hydrogen atoms<sup>[Sah21]</sup>,

$$\frac{n_i n_e}{n_n} = \frac{2g_I}{g_0} \left( \frac{m_e T_e}{2\pi} \right)^{3/2} h^{-3} \exp\left(-\frac{E_{iz}}{T_e}\right) \quad (2.3.4)$$

In the above  $n_e$ ,  $n_i$ ,  $n_n$  are the ion, electron and neutral particle densities,  $E_{iz}$  is the ionization potential, and  $g_0$ ,  $g_I$  are statistical factors. For  $T_e \gg E_{iz}$  a hydrogenic plasma becomes fully ionized. A more complete chain of hydrogen reactions including transport and recombination at the vessel walls, is shown schematically in Fig. 2.3.1. In practice, such calculations are carried out numerically using Monte-Carlo transport codes such as EIRENE<sup>[Rei84]</sup>, NIMBUS<sup>[Cup84]</sup>, or DEGAS<sup>[Rom92]</sup>, see §3.3.

The energy spectrum of the hydrogen atom in a field free environment is described by the quantum numbers ( $n, l, s$ ), which determine the orbital electron energies and photon energies for allowed transitions<sup>[Hak87]</sup>. Fig. 2.3.2. The hydrogen atom is most readily ionized by electron impact ( $E_{iz} = 13.6$  eV). Atomic recombination can occur as either a two-body (radiative) or a three-body (dielectronic) process, with the latter becoming significant at higher electron densities. Charge exchange between hydrogen atoms and ions transfer both momentum and energy, but does not effect the particle balance; since the charge exchange cross section is far larger than the ionization and recombination cross sections ( $S_{CX} \gg S_{iz}, S_{rec}$ ), increasingly so as the electron temperature is reduced below  $\sim 5$  eV, this process is important in determining both neutral and ionized hydrogen transport within the plasma (it is also a key mechanism involved in plasma detachment<sup>[Mar95]</sup>). Neutral-neutral scattering collisions begin to effect the plasma momentum balance at higher neutral densities,  $\lambda_n < L$ .

Reactions involving photons generally remove energy from the plasma, producing a local energy sink, provided that the mean-free-path for photon re-absorption is large in comparison with the size of the system,  $\lambda_\gamma > L$  (which fails to be true for a sufficiently dense plasmas). A hydrogen atom emits several photons before being ionized, the number increasing for lower temperatures; typical energy radiated per ionization event varies from  $\sim 30$  eV at  $T_e > 20$  eV to  $\sim 150$  eV at  $T_e = 2$  eV<sup>[Jan95]</sup> (this is usually the dominant cooling process in hydrogenic plasmas).

The energy spectrum of an H<sub>2</sub> molecule is a function of the inter-nuclear distance, electronic configuration, molecular vibration and rotation<sup>[Coh77, Hak87]</sup>. Fig. 2.3.3. Dissociation of H<sub>2</sub> produces two

atoms which share  $\sim 4$  eV of energy (Franck-Condon neutrals<sup>[Jan95]</sup>); these become important for colder plasma ( $T_i < 2$  eV) regions in providing a source of warm neutrals which can heat the plasma and oppose further recombination.

Impurity ( $Z > 1$ ) atomic reactions generally involve more than one orbital electron, which adds complexity to the analysis, and the reactant set  $\mathfrak{I}$  soon becomes intractably large. Dissociation and ionization normally occur in a stepwise manner ( $X_Z^0 \longleftrightarrow X_Z^+ \longleftrightarrow X_Z^{2+} \longleftrightarrow \dots$ ). Each ionization state (except for the fully stripped nucleus) can emit line radiation following excitation. The sum over all states has been calculated as a function of  $T_e$  under the assumption of local thermal equilibrium<sup>[Pso77]</sup>, Fig. 2.3.4. Radiation is seen to gradually increase with atomic number, falling off sharply below some critical  $T_e$ . The latter effect is responsible for a radiation instability encountered in tokamak edge plasmas, leading to MARFE formation<sup>[Neu86]</sup>. The above treatment neglect the transport of impurities, which is of crucial importance for core plasma performance (radiative cooling and plasma dilution<sup>[Sta90]</sup>, see §A.5.3) and edge plasma behaviour (impurity radiative cooling is widely accepted as a key mechanism in plasma detachment<sup>[Pi97]</sup>). Impurity transport may be simulated by Monte-Carlo codes such as DIVIMP<sup>[Sta95]</sup>, or by multi-fluid plasma codes such as B2<sup>[Bra87,Bac91]</sup>, UEDGE<sup>[Roe92]</sup>, or EDGE2D<sup>[Sim92,94]</sup>; we will return to this topic in §3.2.

In the context of edge plasma modeling, we are interested in the plasma-neutral interactions as sources of mass, momentum and energy in the plasma transport equations (2.2.1); for simplicity we will refer to these simply as neutral sources. Using the vector notation of (2.1.22), we can write down the dominant neutral sources as follows,

$$Q_{\mathfrak{I}} = \begin{pmatrix} m_i(S_{iz} - S_{rec}) \\ m_i(\overline{v_{||,H}S_{iz}} - uS_{rec}) - m_i(u - \overline{v_{||,H}})S_{CX} \\ m_i(\frac{1}{2}\overline{v_H^2S_{iz}} - \frac{1}{2}u^2S_{rec}) + Q_{qi} + Q_{zi} \\ m_e(\frac{1}{2}\overline{v_H^2S_{iz}} - \frac{1}{2}u^2S_{rec}) + Q_{qe} + Q_{ze} \end{pmatrix} \quad (2.3.5)$$

where  $S_{iz}$ ,  $S_{rec}$  and  $S_{CX}$  are respectively the local ionization, recombination and charge exchange rates,  $u$  is the plasma flow velocity,  $v_{||,H}$  is the along- $\mathbf{B}$  neutral velocity,  $v_H$  is the neutral birth velocity.  $Q_{qi}$  and  $Q_{qe}$  are the energy sources for ions and electrons due to plasma-neutral interactions, and  $Q_{zi}$  and  $Q_{ze}$  are similar sources due to plasma-impurity interactions. The default  $Q_{qe}$  contains energy gain due photon emission following excitation ( $-\sum E_k S_k$ ), atomic ionization ( $-13.6 \text{ eV} \cdot S_{iz}$ ), fast dissociation ( $-10.4 \text{ eV} \cdot S_{fd}$ ), slow dissociation ( $-5.0 \text{ eV} \cdot S_{sd}$ ), dissociative molecular ionization ( $-8.0 \text{ eV} \cdot S_{dmiz}$ ), and three-body recombination ( $+13.6 \text{ eV} \cdot S_{rec}$ ). The default  $Q_{qi}$  is set to zero, in keeping with a similar assumption in the EDGE2D code. As an option,  $Q_{qi}$  will contain energy gain due to atomic ionization ( $+f_H E_H S_{iz}$ , where  $f_H = n_N / (n_H + n_{H2})$  is the atomic fraction of the neutral density), molecular ionization ( $+f_{H2} E_{H2} S_{iz}$ , with  $E_{H2} \sim 3$  eV which is the Frank-Condon dissociation energy<sup>[Jan95]</sup>), recombination ( $-E_i S_{rec}$ , with  $E_i = 3T_i/2$ ), and charge exchange ( $-(E_i - E_H) S_{cx} - (1/2)mu^2 S_{cx}$ , where  $S_{cx} = n_i n_H \langle \sigma v \rangle_{cx}$ ). The effect of the various energy terms on the edge plasma solution will be discussed in §4.2.2.

## 2.4 Tokamak edge plasma

In the previous sections we examined the general properties of plasmas, as well as their interaction with a solid surface and neutral species. Kinetic and moment equations for ions and electrons were derived, boundary conditions were selected, and dominant source terms were constructed from atomic-molecular considerations. We are now ready to apply these equations to the modeling of edge plasmas, particularly in tokamak experiments. A reader unfamiliar with tokamak research may wish to consult §A.5 or [Gil81, Wes97] for an overview of the tokamak core plasma before continuing further with the present section.

The distinction between core and edge (boundary) plasmas is simple and yet profound: magnetic flux surfaces in the core are topologically closed, while those in the edge are open, in the sense that they penetrate a solid surface ( $\nabla \cdot \mathbf{B} = 0$  is satisfied by closure of field lines within the solid). In other words, the edge plasma is in direct contact with a solid surface and is subject to the behaviour discussed in §2.2. For an overview of edge plasma phenomena in tokamaks the reader is referred to a recent review article<sup>[Sta90]</sup>. The present section draws a distinction between limiter and divertor plasmas, and proceeds to discuss the various methods employed in their modeling. Historically limiters preceded divertors, consequently they are considered first.

### 2.4.1 Limiter edge plasma

By the term *limiter* we mean a solid object protruding into the plasma and determining the *last closed flux surface* (LCFS) at the point of furthest penetration,  $r = r_{LCFS}$ , Fig. 2.4.1. Particles crossing the LCFS carry mass, momentum and energy into the edge plasma,

$$\langle v_\perp \psi \rangle_a^{LCFS} = \int v_\perp \psi_a f_a^{LCFS}(v_\parallel, v_\perp) dv \quad \begin{aligned} \psi &\in \{m, mv, \frac{1}{2}mv^2\} \\ a &\in \{i, e\} \end{aligned} \quad (2.4.1)$$

which in the absence of volumetric sinks are deposited on the limiter targets. Cross-field fluxes decay radially away from the LCFS; for that reason the edge region adjacent to the LCFS is known as the *scrape-off-layer* (SOL). The radial density decay length within the SOL may be estimated by neglecting all volumetric sources within that region and equating the total cross-field particle flow across the separatrix to the total parallel particle flow reaching the targets<sup>[Sta90]</sup>,

$$\int D_\perp \left( \frac{dn}{dr} \right)_{LCFS} ds_\parallel = \int_{SOL} n_e c_s dr \quad \Rightarrow \quad -\frac{d}{dr} \left( D_\perp \frac{dn}{dr} \right) = \frac{n c_s}{2 L_\parallel} \quad (2.4.2)$$

$$\therefore n(r) = n_{LCFS} \exp \left( -\frac{r - r_{LCFS}}{\lambda_n^{SOL}} \right) \quad \lambda_n^{SOL} = \left( \frac{2 D_\perp L_\parallel}{c_s} \right)^{1/2}$$

where  $D_{\perp}$  is a cross-field diffusion coefficient and  $L_{\parallel}$  is a parallel connection length between the targets; in deriving (2.4.2) we have assumed that  $c_s$ ,  $L_{\parallel}$  and  $D_{\perp}$  are independent of  $r$ . Similar expressions may be obtained for  $T_i(r)$ ,  $T_e(r)$  and  $q_i(r)$ , with decay lengths,  $\lambda_{T_i}^{SOL}$ ,  $\lambda_{T_e}^{SOL}$ ,  $\lambda_{q_i}^{SOL}$ . The practical implications are clear: the limiter guards the vessel wall from contact with the hot core plasma ( $T_{core} > 1\text{keV}$ ), provided that  $r_{LCFS} - r_{wall} \gg \lambda_{max}^{SOL}$  (this is especially important during high power transients such as disruptions or runaway electrons); it also localizes plasma-surface interactions to target plates, which are quickly stripped of films and oxides, and appear as pure substrate to the impinging ions<sup>[BeH91]</sup>. There are several disadvantages of the limiter configuration, all linked to the intimate contact of the solid limiter with the core plasma:

- a) high heat fluxes deposited onto the targets near the LCFS lead to melting and sublimation; for this reason, targets are typically made from heat load resistant materials, such as graphite or tungsten<sup>[Gau90]</sup>;
- b) charge exchange collisions between H neutrals and core plasma ions give rise to a flux of energetic H neutrals onto the vessel walls, leading to atomic sputtering and influx of wall material to the plasma<sup>[Pon86]</sup>;
- c) sputtering of limiter target atoms by plasma ions, with several consequences: i) erosion of target material, ii) impurity (mid-Z) atoms leaving the target as neutrals, penetrating directly into the core plasma, and degrading tokamak performance by increasing  $Z_{eff}$ , thus diluting the ions (lower  $P_{fus}$ ) and increasing radiation from the core  $P_{rad}$ , see (A.1.6); iii) cooling of the outer core, which has been linked to the disruptive instability<sup>[Ade81]</sup>. Target sputtering is the main reason why limiters have been replaced by divertors in most tokamaks<sup>[Pio97]</sup>.

#### 2.4.2 Divertor edge plasma

The divertor configuration, as the name indicates, diverts the flow in the edge plasma away from the core region. This is accomplished by altering the magnetic equilibrium with external current carrying coils (magnetic flux surfaces are modified by toroidal coil currents, in such a way as to create a null in the poloidal  $B$ -field at some location in the plasma, called the X-point; the separatrix flux surface passes through the X-point and intersects the targets which are some distance removed from the X-point, and therefore not in direct contact with the core plasma, Fig. 2.4.2). By modulating the coil current, the separatrix may be periodically swept across the target surface, producing a more uniform heat flux profile). The divertor design emerged in direct response to the problems associated with the limiter configuration, above all impurity influx from the targets into the core plasma<sup>[Sta90]</sup>. It was hoped that by removing the targets away from the core, the influx of impurities would be attenuated by ionization of impurity neutrals in the interposing edge layer and by impurity-plasma friction sweeping the impurities back towards the target (an expectation largely fulfilled), that magnetic sweeping and active cooling of target components would allow higher heat fluxes, and that cryogenic pumping of neutrals in the divertor region would

facilitate impurity (as well as helium ash) removal<sup>[Pit97]</sup>. The introduction of a divertor configuration into the tokamak environment had several unforeseen consequences<sup>[Wes97]</sup>:

- a) the appearance of an *enhanced confinement regime* (H-mode), due to a formation of a core transport barrier near the LCFS; H-mode increased confinement by a factor of 2 to 4, leading to higher values of core  $n_e$  and  $T_e$ , and facilitated the first ever achievement of extrapolated energy breakeven at JET<sup>[Sim90]</sup>;
- b) the appearance of *edge localized modes* (ELMs), which are transient bursts of particles and energy into the edge layer<sup>[Asd89]</sup>; two types of ELMs were discovered and linked to steep radial pressure gradients formed by the H-mode transport barrier and to MHD magnetic perturbations; the nature of ELMs is still unclear, but high mode numbers ( $m \sim 10$ ) inferred and  $dp(r)/dr$  estimated suggest a ballooning instability. Although, the transient nature of ELM activity increases the peak target heat flux to potentially dangerous levels, ELMs are also viewed as a desirable stabilizing mechanism against disruptions;
- c) the appearance of a *radiative instability* (MARFE), driven by the inverted temperature dependence of line-radiative power for mid-Z elements (C, O, N, ...), Fig. 2.3.4, producing a region of cold, dense, highly radiating plasma in the vicinity of the X-point<sup>[Neu86]</sup>. The instability saturates for sufficiently low  $T_e$ , when parallel energy transport from the core into the MARFE region can compensate for radiative losses; the resulting state is quasi-stable. Aside from degrading core plasma performance, it normally leads to the disruptive instability and is regarded as an undesirable effect;
- d) the appearance of gradual *plasma detachment* from the target in which the plasma target temperature  $T_{e,0}$  and target plasma flow  $\Gamma_0$  progressively decrease as the upstream density  $n_u \sim n_{LCFS}$  increases<sup>[Mar95]</sup> (in contrast to the behaviour when the plasma is *attached* to the target, in which both  $T_{e,0}$  and  $\Gamma_0$  increase rapidly with  $n_u$ , see the discussion of the two-point model in the following section, §2.4.3). Another diagnostic signature of detachment is the increase of hydrogenic line radiation linked to the divertor neutral density  $n_H$ . Geometry of the divertor chamber exerts a strong influence on detachment, which seems to underline the importance of plasma-neutral interactions in detached plasmas<sup>[Pit97]</sup>. The onset of detachment occurs when  $T_{e,0}$  drops to  $\sim 5$  eV, this is usually accomplished by raising the upstream density or lowering the core power. Comparison of target and upstream conditions reveals a significant drop of the total plasma pressure,  $p_{tot} = p_i + p_e + \mu u^2 = (p_i + p_e)(1 + M^2)$ , indicating volumetric parallel momentum losses; significant departures from total pressure uniformity along a flux surface are the preferred condition for defining detachment; when the pressure drop correction is included, the observed decrease in  $T_{e,0}$  and  $\Gamma_0$  may be explained even by a relatively simple two-point model, see §2.4.3. In the generally accepted explanation, charge-exchange collisions between ion and neutral atoms remove parallel momentum from the plasma flow, leading to the observed pressure drop, while hydrogenic excitation/emission remove most of the energy<sup>[Pit97]</sup>. Detachment is currently viewed, along with the concept of an outer core radiative mantle, as providing the most appealing solution to the problem of reducing the prohibitively high target heat flux in the eventual tokamak fusion reactor, e.g. ITER, to values required by material limits<sup>[Par97]</sup>. From among the proposed designs, spanning a range

of geometries and pumping assemblies, the gas target divertor, in which plasma flow is entirely extinguished by the neutral gas before reaching the target, may be viewed as an asymptote of the divertor concept (the leakage of neutral gas atoms into the core plasma would clearly pose the main constraint in this case). Some uncertainty still remains about the role of volumetric recombination (clearly observed for  $T_{e,0} < 1$  eV, but too weak to account for detachment for  $T_{e,0} \sim 5$  eV), cross-field transport (how are  $D_\perp$  and  $\chi_\perp$  affected by plasma-neutral collisions?), neutral-neutral and photon-neutral interactions (short mean free paths require transport calculations)<sup>[Wes97]</sup>.

A recent review of divertor experiments is recommended for further details<sup>[Pit97]</sup>.

#### 2.4.3 Edge plasma modeling

In modeling the tokamak edge plasma we would like to simulate, as best as possible, all the phenomena observed in limiter and divertor experiments. This is a very ambitious task since much of the underlying physics remains unknown (cross-field plasma transport, low energy plasma/atomic/molecular collisions, electrostatic sheath effects, chemical sputtering and other plasma-surface interactions<sup>[Su90]</sup>). Even the much simpler task of simulating quasi-stationary edge plasma behaviour is far from trivial<sup>[Rei92,Loa97]</sup>. In this section, we focus on the quasi-stationary phenomenon of divertor plasma detachment, and introduce the improved onion-skin method which lies at the very heart of this thesis.

In practice, modeling has an added aim of either prediction or interpretation. The difference is one of approach: predictive modeling relies on established theory to calculate the behaviour of the system (often extrapolating beyond experimentally studied regimes); interpretive modeling places the emphasis on experimental data, which is employed in the modeling framework to supplement available physics and explore the ‘gaps’ in the theory. Clearly, a theory must be sufficiently incomplete for the latter approach to warrant consideration; in edge plasma physics, the most visible ‘gap’ is offered by anomalous (turbulent) cross-field transport. Based on these considerations, the *onion-skin method* of solving the plasma transport equations may be considered as an approach at interpretive modeling of the edge plasma.

The simplest description of the edge plasma, the so called two point model, relates upstream and target quantities, denoted by the subscripts ‘t’ and ‘u’, along a single flux tube. It may be obtained from the parallel transport equations (2.1.22) by retaining only the dominant transport processes: mass and momentum transport by convection (no parallel viscosity), and energy transport by electron thermal conduction. This amounts to neglecting  $Q_B$ ,  $G_\parallel^{(2)}$ ,  $F_\parallel^{(3)}$ ,  $F_\parallel^{(4)}$  in (2.1.22), adding the two energy equations, adapting a classical estimate for  $n_e \chi_e = \kappa_e = \kappa_{e,0} T_e^{5/2}$ , where  $\kappa_{e,0} \sim 2000$  W/(eVm) and using  $\gamma = \gamma_i + \gamma_e$  as target boundary conditions. In addition the two point model neglects volumetric momentum losses  $Q_S^{(2)}$  and flux expansion terms  $Q_B$ . The simplified set of transport equations may be written as<sup>[Su90]</sup>

$$\nabla_{\parallel}(nu) = Q^n \quad \nabla_{\parallel}(p + nm u^2) = 0 \quad \nabla_{\parallel}(K_{e,0} T_e^{5/2} \nabla_{\parallel} T_e) = Q^E \quad T_e = T_i = T = \frac{p}{m} \quad (2.4.3)$$

$$\therefore nu = nu_i + \int_0^{s_{\parallel}} Q^n ds'_{\parallel} \quad p(1+M^2) = p_i(1+M_i^2) \quad T_e^{7/2} = T_{e,i}^{7/2} + \int_0^{s_{\parallel}} \frac{ds'_{\parallel}}{K_{e,0}} \int_0^{s_{\parallel}} Q^E ds''_{\parallel}$$

where  $Q^n$  is the particle source,  $Q^E$  is the sum of ion and electron energy sources, and the bottom expressions are a quadrature form of the simplified transport equations. Evaluating the latter at the target and mid-point locations,  $s_{L,u} = 0$  and  $s_{L,u} = L_{\parallel}/2$ , we obtain the above mentioned two-point model,

$$(1+M_i^2)n_i T_i = (1+M_u^2)n_u T_u \quad T_u^{7/2} - T_i^{7/2} = \frac{7}{4} \frac{q_{\parallel} s_{\parallel,u}}{\kappa_{e,0}} \quad q_{\parallel} = \gamma n_i T_i c_{st} M_i \quad (2.4.4)$$

which is supplemented by the Bohm criterion,  $M_i \geq 1$ . All the energy was assumed to enter the flux-tube uniformly (if all the power entered at the upstream point, the factor  $q_{\parallel} s_{\parallel,u}$  above is doubled); due to the  $\kappa_e \propto T_e^{5/2}$  scaling, upstream quantities are only weakly sensitive to the energy source distribution  $Q^E(s_{\parallel})$ , and due to the absence of convective power, they are independent of the particle source distribution  $Q^n(s_{\parallel})$ . It is instructive to treat  $(q_{\parallel}, n_u)$  as independent variables (these quantities are usually controlled experimentally, although  $q_{\parallel}$  must still be related to the total power deposited into the SOL,  $P_{SOL}$ ) and  $(n_i, T_i, T_u)$  as dependent variables. Rearranging the above equations under the large  $\nabla_{\parallel} T$  assumption  $T_i^{7/2} \ll T_u^{7/2}$ , we find

$$T_u \propto (q_{\parallel} L_{\parallel})^{2/7} \quad T_i \propto \left( \frac{q_{\parallel}}{n_u T_u} \right)^2 \propto \frac{q_{\parallel}^{10/7}}{n_u^2 L_{\parallel}^{4/7}} \quad n_i \propto \frac{n_u^3 L_{\parallel}^{6/7}}{q_{\parallel}^{8/7}} \quad \Gamma_i = n_i c_{st} \propto \frac{n_u^2 L_{\parallel}^{4/7}}{q_{\parallel}^{3/7}} \quad (2.4.5)$$

Target quantities appear to be very sensitive to upstream quantities, especially to the upstream density (this sensitivity arises due to Coulomb scattering (A.2.37) which leads to  $n_e \chi_e \propto T_e^{5/2}$ ); in contrast, the upstream temperature  $T_u$  depends only weakly on  $q_{\parallel}$  and is highly insensitive to the flux-surface distribution of input power  $Q^E(s_{\parallel})$ . We can estimate the effect of volumetric power losses, momentum losses and convective power flow by introducing three new factors  $\delta_p \in [0, 1]$ ,  $\delta_x \in [0, 1]$ , and  $\delta_q \in [0, 1]$  into (2.4.4),

$$(1+M_i^2)n_i T_i = \delta_p \cdot (1+M_u^2)n_u T_u \quad T_u^{7/2} - T_i^{7/2} = \delta_x \cdot \frac{7}{4} \frac{q_{\parallel} s_{\parallel,u}}{\kappa_{e,0}} \quad \delta_q \cdot q_{\parallel} = \gamma n_i T_i c_{st} M_i \quad (2.4.6)$$

These factors propagate accordingly into (2.4.5),

$$T_u \propto \delta_x^{2/7} \quad T_i \propto \frac{\delta_q^2}{\delta_p^2 \delta_x^{4/7}} \quad n_i \propto \frac{\delta_p^3 \delta_x^{6/7}}{\delta_q^2} \quad \Gamma_i \propto \frac{\delta_p^2 \delta_x^{2/7}}{\delta_q} \quad (2.4.7)$$

Target quantities are highly sensitive to volumetric momentum losses  $\delta_p$  and volumetric power losses  $\delta_q$ , and somewhat sensitive to the convective contribution  $\delta_\chi$ . The upstream temperature  $T_u$  is independent of  $\delta_p$  or  $\delta_q$ , and is only weakly sensitive to  $\delta_\chi$ .

The modified two-point model (2.4.6) is sufficient to explain the basic trends of edge plasma behaviour, typically classified in terms of four experimental regimes: sheath limited, conduction limited, high recycling, and detached<sup>[Pis77]</sup>. These regimes correspond, in the above order, to an ascending degree of plasma collisionality ( $1/\tau_e \propto n_e/T_e^{3/2}$ ), also represented by the normalized collisional mean-free-path  $\lambda_e/L_4 \propto T_e^{2/3}/n_e$ . Since collisionality depends on both density and temperature, the above regimes can be traversed by varying either of these quantities. In keeping with the two-point model, we will consider the gradual increase of upstream density  $n_u$  for constant input power (the common experimental situation), which by (2.4.5) decreases  $T_i$  and increases  $n_t$  and  $\Gamma_t$  (note that  $\lambda_e/L_4 \propto T_e^{2/3}/n_e \propto 1/n_u^{1/2}$  at the target).

In the sheath limited regime, which occurs at the highest target temperatures, the collisional mean-free-path is of the order of the flux tube length ( $\lambda_e/L_4 \sim 1$ ), which leads to negligible along-B gradients. In terms of the two-point model, the electron conductivity  $\kappa_e$  is so high that small  $T_e$  gradients are sufficient to carry all the power along the flux tube, leading to flat  $T_e$  profiles; in addition, atomic interactions are ineffective at such high  $T_e$  in removing either momentum or energy from the plasma ( $\delta_p \sim 1$ ,  $\delta_\chi \sim 1$ ,  $\delta_q \sim 1$ ). As a result, upstream conditions are strongly linked to target (or sheath) conditions.

As temperature and the collisional mean-free-path decrease ( $\lambda_e/L_4 \ll 1$ ) the plasma enters the conductively limited regime, characterized by larger along-B gradients; with electron conduction becoming progressively less effective,  $\nabla_t T_e$  increases in order to carry the same power (most pronounced in the near target, colder regions) leading to steeper  $T_e$  profiles. Volumetric energy losses begin to appear as the first corrections to (2.4.4) while total pressure is conserved ( $\delta_p \sim 1$ ,  $\delta_\chi \sim 1$ ,  $\delta_q < 1$ ).

At still lower  $T_e$  (or higher  $n_u$ ) the particle flux to the target, also called the recycling flux, becomes large enough to dominate the power balance, i.e. in the vicinity of the target most of the power is carried by convection, which consequently reduces  $\nabla_t T_e$  over this region. Upstream conditions are thus separated into a convectively limited (transonic, near target) region, and a conductively limited (stagnant, upstream) region. This behaviour is typically referred to as the high recycling regime, emphasizing the role of convection ( $\delta_\chi < 1$ ) although the dividing line between the regimes is somewhat arbitrary.

Finally, for  $T_e < 5$  eV another physical mechanism becomes active, namely ion-neutral charge exchange. This mass conserving interaction, removes both energy and, more importantly, momentum from the plasma flow, creating a net pressure drop along the flux tube ( $\delta_p < 1$ ). The effect on target conditions is visible from (2.4.6): the recycling flux and target density are reduced with increasing  $n_u$  as long as the ratio  $\delta_p n_u$  decreases. This phenomenon is traditionally referred to as plasma 'detachment', for obvious reasons. Two different approaches are used to quantify the degree of plasma detachment: a) the ratio of the actual  $\Gamma_t$  to that predicted by the two point model ( $\Gamma_t \propto n_u^{-2}$ ) based on some reference  $\Gamma_t$  and  $n_u$  in the attached (high-

recycling) regime is used when only target data are available, and rests on the tenuous assumption, recently challenged by experimental results, that  $n_e$  scales linearly with the average core  $n_c$ , b) total pressure ratio  $p_{tot}^u/p_{tot}^t$  measures along- $\mathbf{B}$  momentum losses, which are the physical mechanism at the heart of detachment; this is the preferred quantity when reliable upstream measurements are available, and it will be employed in our study (somewhat arbitrarily we introduce the criterion for detachment as  $p_{tot}^u/p_{tot}^t > 2$ ). Since in the coarse of detachment, the contact between the plasma and the target becomes progressively weaker, another useful quantity is the position of the plasma density peak ( $s_i^{peak}/L_i$ ) and the ratio of peak to target densities ( $n^{peak}/n_t$ ); in the limit of complete detachment (or gas target formation),  $n_t$  and  $\Gamma_t$  are reduced to zero as the ions and electron recombine volumetrically before reaching the target (much as a candle flame is extinguished by the cold gas into which it flows).

It is worth emphasizing the role of neutral particle penetration in the above transition. As the near target plasma cools, the neutral mean-free-path with respect to ionization increases; this pushes the ionization front further away from the target, thereby extending the region of strong plasma flow, which in turn increases convection and flattens the temperature profile. By the same argument, larger target density ( $T_{e,t}$  held constant) would reduce the neutral penetration length, causing steeper near target profiles.

The simplified transport equations (2.4.3) may be integrated from the target to an arbitrary  $s_i$  location, provided target values  $\{T_{e,0}, \Gamma_0\}$  and the spatial source distribution  $\{Q^u(s_i), Q^E(s_i)\}$  are specified; this gives the simplest 1-D edge plasma description,  $\mathbf{U} = \mathbf{U}(s)$ . The original *onion-skin method* (OSM) of estimating 2-D edge plasma profiles,  $\mathbf{U} = \mathbf{U}(r, s_i)$ , consisted of a collection of such 1-D solutions based on radial target information  $\{T_{e,0}(r), \Gamma_0(r)\}$  across the SOL. The quadrature procedure of (2.4.3) remains valid even if simplifications regarding convection, single temperature and momentum losses are removed<sup>[Sta97]</sup>; numerical quadrature may be performed using predictor-estimator methods, such as the fourth order Runge-Kutta technique<sup>[Hil74]</sup>. In this extended form, OSM was previously combined with neutral transport codes, which return  $Q_S[\mathbf{U}(r, s_i)]$ , and iterated until convergence. Attached plasma conditions were modeled successfully, producing good agreement with experimental data and EDGE2D/NIMBUS code results<sup>[Sta97]</sup>. Unfortunately, this earlier version of OSM suffers from serious limitations: a) although it has been used successfully to model high temperature plasmas,  $T_e > 10$  eV (conductively dominated and attached), it becomes unstable for colder target conditions (convectively dominated and detached). b) the quadrature approach requires that the steady-state fluid equations appear in parabolic form, which means that ion viscosity can not be included<sup>[Hir90]</sup>. c) ion-electron energy exchange terms are destabilizing to the quadrature method and must be neglected, d) sonic transition appears as a singularity in the steady-state parabolic form causing a discontinuity in a quadrature solution, e) floating boundary conditions, such as the super-sonic target velocity  $M_t > 1$ , require laborious iterations. For these reasons, the steady-state parabolic form was abandoned, in this thesis, in favour of the steady-state hyperbolic-elliptic form<sup>[Rei92]</sup> (or equivalently the standard time-dependent parabolic form of the Navier-Stokes type<sup>[Hir90]</sup>), and the quadrature method in favour of implicit relaxation grid-based methods; this basic change in the numerical

approach was undertaken only after sufficient familiarity with CFD revealed the reasons for the limitations (b,c,d) of the quadrature method<sup>[Hir90]</sup>.

The nature of the *onion-skin method* is made clearest by a comparison with the standard 2-D modeling approach. Plasma transport equations (A.3.1) may be written in magnetic co-ordinates as

$$\frac{\partial U}{\partial t} + \nabla_{||} \cdot (F_{||} + G_{||}) + \nabla_{\perp} \cdot (F_{\perp} + G_{\perp}) + \nabla_{\wedge} \cdot (F_{\wedge} + G_{\wedge}) = Q[U] \quad (2.4.8)$$

where **U** represents the plasma fluid variables, **F** the convective fluxes, **G** the diffusive fluxes expressed in terms of diffusive transport coefficients of mass, momentum and energy in the parallel, radial and diamagnetic directions, { $D_{||}$ ,  $D_{\perp}$ ,  $D_{\wedge}$ ,  $\eta_{||}$ ,  $\eta_{\perp}$ ,  $\eta_{\wedge}$ ,  $\chi_{||}$ ,  $\chi_{\perp}$ ,  $\chi_{\wedge}$ } and **Q** the interaction source terms. Assuming toroidal symmetry,  $\partial/\partial\phi = 0$ , they may be recast into poloidal co-ordinates ( $r,s$ ), introduced in §A.5.1,

$$\frac{\partial U}{\partial t} + \frac{\partial}{\partial s}(F_s + G_s) + \frac{\partial}{\partial r}(F_r + G_r) = Q[U] \quad (2.4.9)$$

where  $F_s$ ,  $F_r$ ,  $G_s$ ,  $G_r$  are the components of **F** and **G** in the poloidal and radial directions; poloidal fluxes contain the parallel and diamagnetic fluxes with appropriate projections, see (A.3.1). These are the equations, usually written in primitive variables ( $n$ ,  $u$ ,  $p_e$ ,  $p_i$ ), which are most often employed in edge plasma modelling. They are typically solved (using CFD-type numerical techniques) on a poloidal domain bounded by the LCFS, the target and the wall, with boundary conditions of the type discussed in §2.2 at the targets, and the following input<sup>[Rei92]</sup>: a) cross-field flow of power across the separatrix, b) density on the separatrix or particle flow across the separatrix, c) anomalous cross-field transport coefficients for particles and energy ( $D_{\perp}$ ,  $\chi_{\perp}^i$ ,  $\chi_{\perp}^e$ ). The interaction sources **Q**[**U**] are computed in tandem with the plasma variables **U**[**Q**] using a hydrogenic neutral transport code, usually (but not always) based on Monte-Carlo techniques. It is customary to refer to such computational models by the names of the two codes which make up the iterative loop, eg. B2/EIRENE<sup>[Bra87, Rei84]</sup>, EDGE2D/NIMBUS<sup>[Sim92, Cup94]</sup>, UEDGE/DEGAS<sup>[Ron92]</sup>. A discussion of the physics and numerics employed in these codes, and the status of code related research, may be found in [Rei92].

Recently an assessment of divertor edge plasma modelling (using 2D codes described above) has been carried out based on both code-code and code-experiment comparisons<sup>[Loa97]</sup>, finding a large measure of success in modelling quasi-stationary phenomena (divertor plasma detachment, geometry effects, MARFEs) and some success with time-dependent phenomena, notably ELMs. It is worth stressing that the diagnostic signatures of plasma detachment, §2.4.2, have been replicated numerically; the dominant processes have been identified as hydrogenic and impurity radiation, charge-exchange and, indirectly, recombination (it is anticipated that impurity radiation would be necessary as an edge plasma cooling mechanism in high-power tokamaks, such as ITER). Some discrepancy remains in the absolute levels of plasma quantities, especially  $T_e$  which is calculated at  $\sim 1-4$  eV vs. Langmuir probe data of 3-6 eV (this

difference has a pronounced effect on the recombination rate<sup>[Jan95]</sup>). Several assumptions of the 2D models are supported by comparison with experiments:

- a) parallel electron energy transport with classical heat-diffusivity  $\chi_e^e$ , cf. (A.3.2).
- b) diffusive cross-field transport with constant  $(D_\perp, \chi_{\perp}^i, \chi_{\perp}^e)$  in low recycling regimes (Bohm-like  $D_\perp$  in the private flux region, and inward pinch velocity  $v_\perp$  in the high recycling regime; the double peaked structure of  $\Gamma_0$  in this regime is not reproduced and is thought to be linked to classical diamagnetic drifts); typical values of  $\{D_\perp, \chi_{\perp}^{ie}\}$  range over  $\{0.1-0.3, 0.5-2.0\}$  m<sup>2</sup>/s for ohmic discharges,  $\{0.1-0.5, 1.0-5.0\}$  m<sup>2</sup>/s for L-mode discharges, and  $\{0.05-0.2, 0.1-0.5\}$  m<sup>2</sup>/s for H-mode discharges), see §A.5.3.
- c) The transport of impurities using multi-fluid approaches has reinforced the impurity force models, the need to include chemical sputtering of carbon at low target temperatures, and the observed phenomenon of impurity compression in the divertor (the absolute impurity levels are typically calibrated using line radiative intensities from the divertor region)<sup>[Loe97]</sup>.

Significant differences between the various codes have been observed, and linked to the uncertainties in:

- a) determining the position of the separatrix (different methods used in various codes),
- b) measuring upstream  $T_i$  (therefore the ion energy flow across the separatrix),
- c) determining the recycling coefficient at the targets.

Several areas requiring improvements have been identified<sup>[Loe97]</sup>: edge plasma measurements (especially  $T_i$  and impurity/hydrogen radiative losses); more accurate physical models of recombination, charge-exchange, cross-field transport and classical drifts; neutral-neutral (gas dynamic) effects and coupling core transport and edge transport codes.

The 2D code approach, despite showing much success in modelling experimental results, suffers from *practical* disadvantages for interpreting edge data. First of all, it relies on the knowledge of cross-field coefficients  $(D_\perp, \eta_\perp, \chi_\perp)$  which are anomalous (probably governed by turbulence, see §A.5.3) and therefore remain largely unknown<sup>[Com94]</sup>; they are treated as parameters and are adjusted to match experimental results<sup>[Rei92]</sup>. Secondly, diagnostic measurements in the edge (normally near the target) are difficult to impose as boundary conditions, at the risk of ill-posedness (over-constraining the system of equations)<sup>[Rei92]</sup>. Instead, upstream boundary conditions (normally the density  $n_{LCFS}$  and cross-field power  $q_{\perp LCFS}$ ) are imposed; finding the closest match to diagnostic data requires lengthy parameter searches in which both  $(n, q_\perp)_{LCFS}$  and  $(D_\perp, \eta_\perp, \chi_\perp)$  are adjusted<sup>[Loe97]</sup>. Cross-field transport coefficients are probably the least known quantities in a tokamak plasma, and the investigation of mechanisms involved in cross-field transport remains one of the most challenging areas in current fusion effort. Considering the richness of the underlying physics and the complexity of modelling turbulent processes of any kind (cf. Aerodynamics), the situation – namely the lack of sound theoretical basis for cross-field transport – is likely to remain unchanged into the near, if not the distant, future. Fortunately, exhaustive knowledge of the underlying physics is not a necessary condition for the development of a technology, as the aerospace industry will surely attest; rather it motivates empirically based (interpretive) models. Finally, target

quantities are very sensitive to upstream quantities (cf. the two-point model), which introduces numerical stiffness into the parametric search<sup>[Loe97]</sup>.

The above considerations were the primary incentives for developing an alternative solution method for the edge plasma transport equations, broadly referred to as the *Onion Skin Method (OSM)* on account of the flux surface nature of the solution (plasma transport equations are solved on each flux surface in turn). The method consists of replacing the cross field terms in (2.4.8) by source terms  $\mathbf{Q}_\perp$  whose functional dependence on  $\mathbf{U}$  is specified (for now we assume that  $\mathbf{Q}_\perp$  depend on  $\mathbf{U}$  but not on  $\nabla_\perp \mathbf{U}$ ).

$$\frac{\partial \mathbf{U}}{\partial t} + \nabla_{||} \cdot (\mathbf{F}_{||} + \mathbf{G}_{||}) + \nabla_\perp \cdot (\mathbf{F}_\perp + \mathbf{G}_\perp) - \mathbf{Q}_\perp[\mathbf{U}] = \mathbf{Q}[\mathbf{U}] \quad (2.4.10)$$

Ideally, plasma transport along the flux surface as well as the volumetric sources in OSM and 2D codes would contain the same physics, the only difference being the treatment of cross-field plasma transport (diamagnetic drifts are neglected in keeping with §2.1, but could be incorporated without much difficulty in the future; since diamagnetic drifts lead to transport along a flux-surface, they do not affect conclusions regarding the validity of the onion skin approach). OSM, as defined above, rests on the pivotal assumption, referred to from now on as the  *$\mathbf{Q}_\perp[\mathbf{U}]$  ansatz*, that the functional dependence of cross-field sources,  $\mathbf{Q}_\perp[\mathbf{U}]$ , has only a small effect on the plasma solution  $\mathbf{U}(s_{||})$ , given the flux surface average value of  $\langle \mathbf{Q}_\perp \rangle$ . It is somewhat surprising that with so much redundancy in 2D code development (EDGE2D, B2 and UEDGE, despite certain differences, are solving the same set of equations, (2.4.8)) this crucially important postulate has never been properly examined. We may rewrite the  *$\mathbf{Q}_\perp[\mathbf{U}]$  ansatz* as a series of variational conditions<sup>[Wei74]</sup>.

$$\left| \frac{\mathbf{Q}_\perp}{\mathbf{U}} \left( \frac{\partial \mathbf{U}}{\partial \mathbf{Q}_\perp} \right)_{\langle \mathbf{Q}_\perp \rangle} \right| \ll 1 \quad \langle \mathbf{Q}_\perp \rangle = \frac{1}{L_{||}} \int_0^{L_{||}} \mathbf{Q}_\perp(\mathbf{U}(s_{||})) ds_{||} \quad \therefore \delta \langle \mathbf{Q}_\perp \rangle = 0 \quad (2.4.11)$$

to be satisfied for each component of  $\mathbf{U}$  and  $\mathbf{Q}_\perp$ . At this point, the full weight of functional analysis<sup>[Shi74]</sup> could be brought to bear on (2.4.11); it is, however, more instructive, and physically revealing, to adapt a simpler approach by exploiting the hyperbolic/elliptic (convective/diffusive) structure of (2.4.10) and including from the outset the cross-field sources appropriate for tokamak edge plasmas. We begin by noting that if all elements of  $\mathbf{U}$  are non-zero than  $\mathbf{U}$  may be reconstructed given  $\mathbf{F}_{||}(\mathbf{U})$ , (2.1.22); this translates into a series of variational conditions on  $\delta \mathbf{F}_{||} / \delta \mathbf{Q}_\perp$  similar to (2.4.11). Rewriting (2.4.10-11) in steady-state form,

$$\mathbf{F}_{||}^{(j)} = \int_0^{s_{||}} (\mathbf{Q}^{(j)} + \mathbf{Q}_\perp^{(j)}) ds'_{||} - \mathbf{G}_{||}^{(j)} \quad \left| \frac{\mathbf{Q}_\perp^{(k)}}{\mathbf{F}_{||}^{(j)}} \left( \frac{\partial \mathbf{F}_{||}^{(j)}}{\partial \mathbf{Q}_\perp^{(k)}} \right)_{\langle \mathbf{Q}_\perp^{(k)} \rangle} \right| \ll 1 \quad \delta \int_0^{L_{||}} \mathbf{Q}_\perp^{(k)} ds_{||} = 0 \quad (2.4.12)$$

we see that  $F_{\parallel}^{(i)}$  depends explicitly on  $Q^{(i)}$  and  $Q_{\perp}^{(i)}$  and implicitly (via  $U$ ) on  $Q^{(k)}$  and  $Q_{\perp}^{(k)}$ ,  $k \neq j$ . We now investigate (2.4.11) for the mass, momentum and energy equations (2.4.10) in the limits of strong and weak cross-field sources  $Q_{\perp}^{(i)}$  as compared with the neutral sources  $Q^{(i)}$ . Introducing the relative cross-field strength  $f_{\perp}^{(i)} = \langle Q_{\perp}^{(i)} \rangle / \langle Q^{(i)} \rangle$  and the source-target ratio,  $f^{(i)} = \langle Q^{(i)} \rangle L_s / (F^{(i)} + G^{(i)})_{0,N}$ , we note that the  $Q_{\perp}/U$  ansatz (2.4.11) is satisfied when  $f_{\perp}^{(i)} \ll 1$ , for all  $j$ , provided that parallel fluxes dominate  $F_{\parallel} \gg F_{\perp}, G_{\parallel} \gg G_{\perp}$ ; in other words, the validity of the OSM approach should improve with stronger neutral sources. Let us consider the cross-field sources in limiter and divertor edge plasmas:

- a)  $Q_{\perp}^{(1)}$  for limiters arise due to the intimate contact of the limiter with the core plasma, such that most of the particles ionize in the core and diffuse across the LCFS into the SOL, ( $f_{\perp}^{(1)} > 1$ ); although we expect the distribution of particles along the LCFS to be fairly uniform, due to the closed topology of core flux-surfaces, the cross-field fluxes may peak in regions of strong radial density gradients. For divertors,  $Q_{\perp}^{(1)}$  may be similar to the limiter scenario described above (low-recycling) or localized in the near target region (high-recycling). We will consider the high-recycling case, as representative of divertor configurations in general ( $f_{\perp}^{(1)} < 1$ ).
- b)  $Q_{\perp}^{(2)}$  arise due to core plasma rotation or cross-field viscosity; since plasma momentum flow to the targets is determined by the Bohm criterion, these effects are small in comparison to charge exchange losses (typically the cross-field flow of momentum across the LCFS is assumed to be zero in 2D codes for both the limiter and divertor configurations)  $\therefore f_{\perp}^{(2)} \ll 1$ . The  $Q_{\perp}/U$  ansatz for momentum transport is strengthened by the fact that cross-field momentum fluxes transport convective momentum alone; it is easily shown that the maximum amount of momentum which could be transported in this way is smaller than the parallel momentum flux in the plasma.
- c)  $Q_{\perp}^{(3)}$  and  $Q_{\perp}^{(4)}$  arise due to power generation in the core plasma, which then diffuses conductively across the LCFS entering the SOL (the powers deposited into electron and ion channels appear to be roughly equal<sup>[Loa97]</sup>); since the power removed by plasma-neutral interactions is limited to the input power, then  $f_{\perp}^{(3)} > 1, f_{\perp}^{(4)} > 1$  (this situation applies for both limiter and divertor plasmas); as with particle flux, we expect the distribution of radial power along the LCFS to be fairly uniform, increasing with radial temperature gradients: for divertor SOL, there is no power inflow downstream of the X-point.

The above considerations reduce the problem to examining the mass and energy transport equations in two limiting scenarios of core ionization ( $f_{\perp}^{(1)} > 1, f_{\perp}^{(E)} > 1$ ) and SOL ionization ( $f_{\perp}^{(1)} < 1, f_{\perp}^{(E)} > 1$ ). The  $Q_{\perp}/U$  ansatz (2.4.11) is satisfied for the momentum transport equation,  $j = 2$ , in both of these cases.

Core ionization: the  $Q_{\perp}/U$  ansatz may be violated for particle transport ( $j = 1, \nabla_{\parallel} n u = Q_{\perp}^{(1)}$ ) so that the functional dependence of  $Q_{\perp}^{(1)}[U(s_{\parallel})]$  would effect the parallel plasma flow pattern,  $n u(s_{\parallel})$ ; fortunately, in case of dominant core ionization we expect  $Q_{\perp}^{(1)}(s_{\parallel})$  to vary only gradually with  $s_{\parallel}$  due to the closed topology of the core flux surfaces, see (a) above. The  $Q_{\perp}/U$  ansatz is satisfied for the electron energy transport due to the  $\kappa_e \propto T_e^{5/2}$  scaling, as demonstrated by (2.4.3-5), so that the flux-surface profile of

$\mathbf{Q}_{\perp}^E(s_{\parallel})$  has only a small effect on  $T_e(s_{\parallel})$ . The ion energy transport contains both convective and conductive parallel fluxes; the former depend on  $\mathbf{Q}_{\perp}^n(s_{\parallel})$  since  $\mathbf{F}_{\parallel}^{(3)} = (5/2)T_i n \mathbf{u}$ , while the latter are insensitive to  $\mathbf{Q}_{\perp}^E(s_{\parallel})$  due to the  $\kappa_i \propto T_i^{5/2}$  scaling. We expect the energy transport by ion convection  $\mathbf{F}_{\parallel}^{(3)}$  to dominate over electron conduction  $\mathbf{G}_{\parallel}^{(4)}$  only in regions of super-sonic flow, which (by the Bohm criterion) we anticipate only in the vicinity of the targets (ie. downstream of the X-point). Elsewhere in the SOL, electron conduction dominates and the  $\mathbf{Q}_{\perp}/[U]$  ansatz is satisfied. We may conclude that with core ionization dominant, parallel plasma flow and ion convection are indeed sensitive to radial particle diffusion, but due to the location and distribution of the particle and energy sources, the sensitivity to the energy source is weak. The  $\mathbf{Q}_{\perp}/[U]$  ansatz is only violated for the mass transfer equation, affecting  $n_{\parallel}(s_{\parallel})$ .

SOL ionization: the  $\mathbf{Q}_{\perp}/[U]$  ansatz depends in this case on the effect of strong neutral particle sources in the SOL ( $S_{iz}$ ,  $S_{rec}$ ) on the flux tube mass balance. If target particle fluxes are specified as boundary conditions (as is traditionally the case in OSM), then the flux tube integral of  $S_{iz} - S_{rec}$  determines the amount of over/under-ionization with respect to the specified target flux; the cross-field sources are adjusted such that the flux tube integral of  $\mathbf{Q}_{\perp}^n$  offsets this particle imbalance. The  $\mathbf{Q}_{\perp}/[U]$  ansatz is satisfied for the mass transport equation as long as the ratio  $\int \mathbf{Q}_{\perp}^n ds_{\parallel} / \int \mathbf{Q}^n ds_{\parallel} - \langle f_{\perp}^{(1)} \rangle$  remains small (since ion convection is only weakly dependent on  $\mathbf{Q}_{\perp}^n(s_{\parallel})$  while the energy source  $\mathbf{Q}_{\perp}^E(s_{\parallel})$  is largest upstream of the X-point where convection is small, it would be satisfied for energy transport as well). If however  $\langle f_{\perp}^{(1)} \rangle$  approaches unity, the  $\mathbf{Q}_{\perp}/[U]$  ansatz may be violated and the solution may become sensitive to the specified functional dependence of  $\mathbf{Q}_{\perp}^n[U]$ .

The conditions for the validity of the OSM approach are summarized below:

- strong magnetic field ( $\omega_c \tau \gg 1$ ) implying that  $\mathbf{F}_{\parallel} \gg \mathbf{F}_{\perp}$ ,  $\mathbf{G}_{\parallel} \gg \mathbf{G}_{\perp}$ ,
- strong temperature dependence of parallel conductive energy transport,  $\chi_{\parallel} \propto T^{5/2}$ ,
- if dominant core ionization, then nearly uniform influx of particles and power across the LCFS
- if dominant SOL ionization, then only a moderate degree of over-under ionization,  $0.5 < f^{(1)} < 2$ .
- availability of radial information in the divertor (near target) region,  $\mathbf{U}^{\text{diag}} = \mathbf{U}^{\text{diag}}(\mathbf{r})$ .

Condition (a) is necessary in order to introduce the dominant transport directions and impose the flux-surface geometry. Condition (b) satisfies the  $\mathbf{Q}_{\perp}/[U]$  ansatz when near target energy flux is available, cf. the two-point model, which shows that  $T_u$  is weakly dependent on the  $s_{\parallel}$  profile of cross-field energy sources,  $\mathbf{Q}_{\perp}^E(s_{\parallel})$ . Condition (e) assures that sufficient information is available to solve the transport equations on each flux surface. It is worth noting that since this radial information comes from diagnostic measurements, it contains the effects of cross-field fluxes between the different flux surfaces within the SOL.

OSM was initially developed in quadrature form, in which the cross-field sources were renormalized based on the imposed target values<sup>[St97]</sup>. One of the contributions contained in this thesis is the formulation of a more flexible framework for OSM based on variational techniques (applicable for problems in which the integral of a function is known but not its functional dependence; the latter is then specified and the solution satisfying the desired integral value is obtained). In the OSM context, the

variational technique developed will be referred to as Diagnostic Variance Minimization (DVM). It consists of adjusting the cross-field sources in such a way as to minimise the statistical variance  $\|\Xi\|$  between calculated quantities  $\mathbf{U}(r,s)$  and selected diagnosticly obtained quantities  $\mathbf{U}^{\text{diag}}(r,s)$ , where  $\Xi \equiv (\mathbf{U} - \mathbf{U}^{\text{diag}})/\mathbf{U}^{\text{diag}}$ , defined term by term, is a normalized error between  $\mathbf{U}$  and  $\mathbf{U}^{\text{diag}}$ . The variational form of OSM is more general than is needed for the present analysis, which is based only on target Langmuir probe measurements of  $\Gamma$  and  $T_e$ , for which  $\mathbf{U}^{\text{diag}}(r,s) = \mathbf{U}^{\text{diag}}(r) = \{\Gamma_0, \Gamma_L, T_{e,0}, T_{e,L}\}^{\text{diag}}$ . This form is introduced in order to provide a framework for future extension of OSM to other types and larger sets of diagnostic data. At this point, let us digress a little and briefly review the field of edge plasma diagnostics<sup>[Sta65, Loc68, Sta90, Auc89]</sup>. In general, the measurement of edge plasma conditions requires better radial localization in comparison to core measurements; aside from this fact, the same diagnostic methods can be employed. Electron density and temperature are routinely measured by a variety of techniques:

- a) microwave interferometry [ $n_e(r)$ ]
- b) microwave reflectometry [ $n_e(r)$ ]
- c) Thomson scattering (of laser photons by plasma electrons) [ $n_e(r), T_e(r)$ ]
- d) LIDAR (light detection and ranging: time of flight technique) [ $n_e(r), T_e(r)$ ]
- e) ECE (electron cyclotron emission) [ $T_e(r)$ ]
- f) Hydrogen emission spectroscopy ( $H_\alpha, H_\gamma$  lines) [ $n_e(r), T_e(r)$ ]
- g) Impurity emission spectroscopy (eg. He, Li, C lines) [ $n_e(r), T_e(r)$ ]
- h) Langmuir probes (target or reciprocating; single or triple) [ $n_e(r), T_e(r)$ ]

When multiple lines-of-sight are available, tomographic reconstruction is possible, eg. Thomson scattering array on the D-IIID tokamak [ $n_e(r,s), T_e(r,s)$  in the divertor]; this is potentially a very powerful diagnostic tool providing invaluable information about divertor edge plasma phenomena, such as detachment, and offering an ideal opportunity for code-experiment comparisons. The ion temperature, although more difficult to measure, can be obtained via charge-exchange neutral spectroscopy or retarding field ion energy analysis. Plasma flow velocity, or the local Mach number, can be estimated via directional Langmuir probes, Doppler shift spectroscopy, or impurity puff measurements, eg. the carbon plume experiments on Alcator C-mod; unfortunately, due to interpretation errors and scarcity of diagnostic data, the flow velocity is generally unknown. In addition to plasma variables [ $n_e, T_e, T_i, M$ ], a wide range of spectroscopic data, ranging from visible light to soft X-rays, is usually available in the edge region, providing information on neutral hydrogen distribution and various plasma-neutral (atomic/molecular) interactions, eg. two-body recombination rate can be inferred from the associated photon spectrum. All of these diagnostic measurements could potentially be used in conjunction with the OSM-DVM approach; the cross-field sources could be adjusted based on a diagnostic vector  $\mathbf{U}^{\text{diag}}(r,s)$  which would include several diagnostic data sets with specified weight factors. Therein lies part of the appeal of the OSM-DVM approach, which could combine great quantities of disparate diagnostic data into a unified, consistent picture of edge plasma behaviour. Since the OSM-DVM analysis for larger diagnostic sets would follow the same route as for the simpler target Langmuir probe case (provided radial information was available) the present analysis may be

viewed as a preliminary sketch towards a much broader range of OSM-DVM applicability. For the time being, the only claim being made is that the cross-field sources are adjusted according to some diagnostic error  $\Xi$ , ie.  $\mathbf{Q}_\perp = \mathbf{Q}_\perp[\mathbf{U}, \Xi]$ .

The replacement of the radial derivative by cross-field sources allows the transport equations (2.1.22) with an added source term  $\mathbf{Q}_\perp[\mathbf{U}(r,s), \Xi(r,s)]$  to be solved in 1-D sweeps along each flux surface, from which a 2-D plasma solution  $\mathbf{U}(r,s)$  may be constructed (neutral sources  $\mathbf{Q}_3(r,s)$  are obtained from neutral-transport codes, in the present work from NIMBUS<sup>[Cup84]</sup>). It is important to note that although each flux surface is solved independently of the others at each time stage, neutral sources  $\mathbf{Q}_3(r,s)$  depend on the transport of neutral particles and hence on the entire 2-D plasma profile,  $\mathbf{Q}_3[\mathbf{U}] = \mathbf{Q}_3[\mathbf{U}(r,s)]$  and  $\mathbf{Q}[\mathbf{U}] = \mathbf{Q}[\mathbf{U}(r,s)]$ . When  $\mathbf{U}[\mathbf{Q}]$  and  $\mathbf{Q}[\mathbf{U}]$  are iterated in this way, the 2-D nature of the solution becomes apparent.

The sources on the right hand side of (2.4.10) consist of three parts:

- a) Plasma sources,  $\mathbf{Q}_p[\mathbf{U}(r,s)]$  given in (2.1.22), contain the interaction between ions and electrons. With the assumption of equal ion and electron parallel flow velocities, the only contribution comes from ion-electron energy exchange via Coulomb collisions and the interaction with the plasma electric field;
- b) Neutral sources,  $\mathbf{Q}_3[\mathbf{U}(r,s)]$ , include plasma-neutral (atomic/molecular) interactions discussed in §2.3, and have to be calculated based on neutral transport equations. In the work presented here, the volumetric sources of ionization  $S_{iz}$ , recombination  $S_{rec}$ , ion-neutral charge exchange  $S_{CX}$ , electron energy loss due to ionization, dissociation and excitation  $Q_{qe}$ , and ion energy loss due to ionization, recombination and charge exchange  $Q_{qi}$  are calculated using a Monte-Carlo neutral transport code, NIMBUS<sup>[Cup84]</sup>. The effect of impurity cooling is estimated by  $Q_{Ze} = f_{Ze}Q_{qe}$  and  $Q_{Zi} = f_{Zi}Q_{qi}$ . In the default model, the neutral birth velocity along  $\mathbf{B}$  is set to zero,  $v_H = 0$ , which corresponds to an upper limit on the amount of momentum loss due to CX collisions. The effect of ion cooling/heating due to neutral interactions is neglected in the default model in keeping with the EDGE2D code,  $Q_{qi} = 0$ , as is the effect of impurities on the ion energy balance,  $f_{Zi} = 0$ ; an impurity enhancement factor of unity is assumed for the electrons,  $f_{Ze} = 1$ . The default form of  $\mathbf{Q}_3$  is thus (2.3.5) with  $Q_{qi} = 0$ ,  $f_{Zi} = 0$ , and  $f_{Ze} = 1$ ; the sensitivity of the solutions on  $S_{rec}$ ,  $v_H$ ,  $Q_{qi}$ , and  $f_{Ze}$  will be explored in §4.2.2.
- c) Flux expansion sources,  $\mathbf{Q}_B[\mathbf{U}(r,s)]$ , include the effects of magnetic geometry. They are calculated based on the equilibrium  $\mathbf{B}$  field found by solving the Grad-Shafranov equation (A.5.7).

Cross-field sources  $\mathbf{Q}_\perp[\mathbf{U}, \Xi]$  simulate the effect of cross-field plasma transport. Their functional dependence on  $\mathbf{U}$  must be specified, and may be considered as the key modelling assumption. As in all variational approaches, the choice of the test function, here  $\mathbf{Q}_\perp[\mathbf{U}, \Xi]$  should reflect a compromise between content and simplicity, that is between known features of the desired function (in our case, the diffusive nature of cross-field fluxes) and smallest number of free-parameters (a minimum of four per ring are required to impose the four external constraints per ring, two at each target, provided by Langmuir probe data,  $\{\Gamma_0, \Gamma_L, T_{e,0}, T_{e,L}\}^{diag}$ ). Based on these criteria the default form of  $\mathbf{Q}_\perp[\mathbf{U}, \Xi]$  was constructed as follows: the particle source  $\mathbf{Q}_\perp^{(1)}$  was taken proportional to density  $\rho = \mathbf{U}^{(1)}$  (equivalent to  $\nabla_\perp(D_\perp \nabla_\perp n)$  with the same radial length  $\lambda_n^{SOL}$  at all  $s_\parallel$  locations), the momentum source  $\mathbf{Q}_\perp^{(2)}$  to plasma flow  $\rho \mathbf{u} = \mathbf{U}^{(2)}$

(equivalent to  $\nabla_{\perp}(\eta_{\perp}\nabla_{\perp}n_{\perp})$  with the same radial length  $\lambda_u^{\text{SOL}}$  at all  $s_{\parallel}$  locations), while the power sources of ions  $\mathbf{Q}_{\perp}^{(3)}$  and electrons  $\mathbf{Q}_{\perp}^{(4)}$  to double-step functions from inner to outer X-point locations with their value in the inner and outer regions adjusted independently (an approximation of uniform power influx across the LCFS with no influx downstream of the X-points; the division into inner and outer halves is the lowest order refinement necessary to match possible power asymmetries between the two targets); power deposited into the ions and electrons was assumed to be equal (as suggested by experiment)<sup>[Loe97]</sup>. In the future, a more complicated, diffusive form of  $\mathbf{Q}_{\perp}$  involving radial gradients could be introduced:  $\mathbf{Q}_{\perp}^{(1)} \propto D_{\perp}\nabla_{\perp}n$ ,  $\mathbf{Q}_{\perp}^{(2)} \propto \eta_{\perp}\nabla_{\perp}n_{\perp}$ ,  $\mathbf{Q}_{\perp}^{(3)} \propto n\chi_{ie}\nabla_{\perp}T_i$ ,  $\mathbf{Q}_{\perp}^{(4)} \propto n\chi_{ee}\nabla_{\perp}T_e$ ; in which case adjusting  $\mathbf{Q}_{\perp}$  would be equivalent to varying the cross-field coefficients. The default cross-field sources can be summarised in vector form:

$$Q_{\perp}(r, s_{\parallel}) = \begin{pmatrix} \xi^{(1)}(r)U^{(1)}(r, s_{\parallel}) \\ \xi^{(2)}(r)U^{(2)}(r, s_{\parallel}) \\ \Theta(r, s_{\parallel}) \\ \Theta(r, s_{\parallel}) \end{pmatrix} \quad \Theta(r, s) = \begin{cases} 0 & s_{\parallel} \in [0, s_{\parallel}^{X,0}] \\ \xi^{(3)}(r)\gamma_e T_{e,0}^{\text{diag}} \Gamma_0^{\text{diag}} & s_{\parallel} \in [s_{\parallel}^{X,0}, \frac{1}{2}L_{\parallel}] \\ \xi^{(4)}(r)\gamma_e T_{e,L}^{\text{diag}} \Gamma_L^{\text{diag}} & s_{\parallel} \in [\frac{1}{2}L_{\parallel}, s_{\parallel}^{X,L}] \\ 0 & s_{\parallel} \in [s_{\parallel}^{X,L}, L_{\parallel}] \end{cases} \quad (2.4.13)$$

where  $s_{\parallel}^{X,0}$  and  $s_{\parallel}^{X,L}$  are the  $s_{\parallel}$  locations of the X-point and  $\xi(r)$  are parameters adjusted in order to minimise the statistical variance between  $\mathbf{U}(r, s)$  and  $\mathbf{U}^{\text{diag}}(r)$ . Considering only target Langmuir data  $\{\Gamma_0, \Gamma_L, T_{e,0}, T_{e,L}\}^{\text{diag}}$ , we can construct two comparison vectors  $\xi^{\text{diag}}(r)$  and  $\xi(r)$ ,

$$\xi^{\text{diag}}(r) = \begin{pmatrix} \Gamma_0^{\text{diag}}(r) \\ \Gamma_L^{\text{diag}}(r) \\ T_{e,0}^{\text{diag}}(r) \\ T_{e,L}^{\text{diag}}(r) \end{pmatrix} \quad \xi(r) = \begin{pmatrix} \Gamma(r,0) \\ \Gamma(r, L_{\parallel}) \\ T_e(r,0) \\ T_e(r, L_{\parallel}) \end{pmatrix} = \begin{pmatrix} \frac{1}{m}U^{(2)}(r,0) \\ \frac{1}{m}U^{(2)}(r, L_{\parallel}) \\ \frac{2m}{3}U^{(4)}(r,0)/U^{(1)}(r,0) \\ \frac{2m}{3}U^{(4)}(r, L_{\parallel})/U^{(1)}(r, L_{\parallel}) \end{pmatrix} \quad (2.4.14)$$

for which the statistical variance  $\|\Xi\|$  may be defined as some vector norm  $\|\cdot\|$  of the relative error  $\Xi(r)$ , eg. as the sum over all computational rings of the square of the elements of  $\Xi(r)$ .

$$\Xi(r) = \frac{\xi(r) - \xi^{\text{diag}}(r)}{\xi^{\text{diag}}(r)} \quad \|\Xi\| = \sum_r |\Xi(r)|^2 \quad (2.4.15)$$

Finally, we can state the DVM condition for the minimisation of  $\|\Xi\|$  with respect to  $\xi(r)$ .

$$\frac{\partial}{\partial \xi(r)} \|\Xi\| = 0 \quad \frac{\partial}{\partial \xi(r)} \|\Xi\| > 0 \quad r \in [r_{LCFS}, r_{wall}] \quad (2.4.16)$$

Numerical strategies for solving this multivariable optimisation problem are discussed in §3.5. It is worth noting that the DVM technique is not particular to the onion-skin method, and could be included within existing 2D fluid codes to increase their diagnostic content and interpretive ability (in that case the specified cross-field transport coefficients would be adjusted in order to minimize the diagnostic variance).

The case of strong volumetric recombination poses a difficulty for the DVM approach based entirely on target measurements (traditional OSM); the target is no longer at the heart of the active region (of particle, momentum and energy sources) which determines the upstream conditions. In the limit, the recombination front becomes a mobile ‘gas target’ in which nearly all plasma particles are neutralized<sup>[Kra99]</sup>. Let us consider this ‘gas target’ scenario, in which the plasma is entirely extinguished before striking the solid target, such that  $n_0 = \Gamma_0 = 0$ . The standard OSM approach would clearly fail in this case, because no plasma information is available at the target. For finite, but weak, plasma-target contact we expect a wide range of upstream conditions to correspond to a small range of target conditions, an unfavourable situation from the point of view of accuracy. It then becomes useful to seek additional upstream information in order to further constrain the solution. In the present study the upstream (mid-point) separatrix density  $n_u^{sep}$  will serve, when necessary, as this additional constraint; its numerical implementation will be discussed in §3.5.

Possible target boundary conditions have been presented in §2.2. In the default model, they consist of: a) the velocity being limited by the target sound speed according to the Bohm criterion,  $M_0 = u_0 / c_s \geq 1$ , and b) the power fluxes being related to the target temperature by the sheath heat transmission coefficients for ions and electrons,  $q_i = \gamma_i T_{i0} \Gamma_0$ ,  $q_e = \gamma_e T_{e0} \Gamma_0$ ,  $\gamma_e = 5.0$ ,  $\gamma_i = 2.5 + M_0^2 (T_{e0} + T_{i0}) / (2T_{i0})$ . The Mach dependent term of  $\gamma_i$  was added in order to insure that the ion conductive heat flux vanish at the target,  $G_0^{(3)} = 0$  (we can see this by writing  $F_0^{(3)} + G_0^{(3)} = \gamma_i T_{i0} \Gamma_0$ , inserting  $M_0 = u_0 / ((T_{e0} + T_{i0})/m)^{1/2}$  and isolating for  $G_0^{(3)}$ ). The effect of boundary conditions on the final solution is examined in §4.2.5.

Taken together equations (2.1.22), (2.3.5), (2.4.10-16) constitute a self-consistent interpretive model of the edge plasma, which will be referred to from now on as the OSM-DVM default model. The following sections will discuss the numerical implementation of the OSM-DVM model (the OSM2 code) and the extensive application of the OSM2/NIMBUS code package, including a study of the sensitivity of the default model solutions to changes in modelling assumptions.

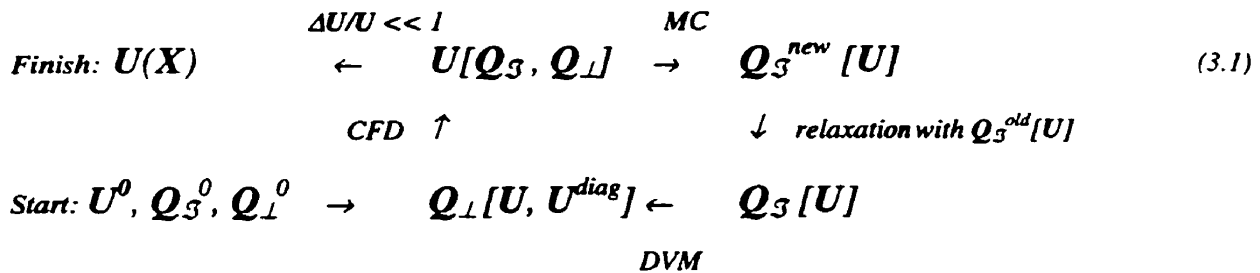
### 3. Numerical Solution of Model Equations: the OSM2 code

The OSM-DVM edge plasma model equations (plasma transport (2.1.22), neutral transport (2.1.1), field equilibrium (A.5.6), cross-field sources (2.4.10-15)) form a self-consistent mathematical system; the present chapter will be devoted to numerical strategies employed in the solution of this system.

The Grad-Shafranov equation (A.5.6) must first be solved in order to obtain the equilibrium magnetic field  $\mathbf{B}(R,Z)$  and construct a corresponding numerical grid  $\mathbf{X}$ . The remaining equations are solved on this grid, that is in magnetic coordinates  $(r,s)$ , using a four step iterative cycle:

- plasma transport equations are solved using the methods of computational fluid dynamics (CFD) for given neutral and cross-field sources:  $\mathbf{U}[\mathbf{Q}_S, \mathbf{Q}_\perp]$
- neutral transport equations are solved using Monte-Carlo (MC) techniques:  $\mathbf{Q}_S^{new} [\mathbf{U}]$
- the new MC sources are relaxed with previous sources  $\mathbf{Q}_S^{old} [\mathbf{U}]$  to assure numerical stability of the MC-CFD iterative cycle:  $\mathbf{Q}_S [\mathbf{U}] = (1-\epsilon_S)\mathbf{Q}_S^{old} [\mathbf{U}] + \epsilon_S \mathbf{Q}_S^{new} [\mathbf{U}], \epsilon_S \ll 1$
- the cross-field sources are calculated according to the DVM technique:  $\mathbf{Q}_\perp [\mathbf{U}, \mathbf{U}^{diag}]$

The above iterative cycle is continued until steady state is reached, that is until  $\mathbf{U}$  no longer changes significantly with further iterations; It may be represented schematically as,



#### 3.1 MHD Equations: Magnetic Grid

As mentioned in §A.5.1, magnetic equilibrium is calculated by numerically solving the elliptic Grad-Shafranov equation in the poloidal plane of the tokamak ( $\partial/\partial\phi = 0$ ), using boundary conditions which include measurements of the edge magnetic field; two typical solvers used for this purpose are EFIT<sup>[Sim94]</sup> and SONNET<sup>[Rei84]</sup>. The calculated magnetic field  $\mathbf{B}(R,Z)$  is used to generate a poloidal grid  $\mathbf{X}$  which conforms to the magnetic geometry (lateral faces of grid cells form magnetic flux surfaces), Fig.3.1.1. At each cell center both poloidal and toroidal components of the magnetic field are stored, from which the field line pitch angle and the connection length between targets  $L_{ij}$  may be calculated,

$$ds_{||} = h_{||} ds = \left( \frac{B}{B_\theta} \right) ds \quad L_{ij} = \int_{outer}^{inner} ds_{||} \quad (3.1.1)$$

The magnetic grid  $\mathbf{X}$  is assumed to contain the following information, Fig. 3.1.2.

$$\mathbf{X} \equiv \left\{ \begin{array}{cccc} s_{i,j} & r_{1,i,j} & r_{i,j} & r_{2,i,j} \\ s_{3,i,j} & r_{3,i,j} & s_{4,i,j} & r_{4,i,j} \\ R_{i,j} & Z_{i,j} & A_{i,j} & \\ B_{\phi,i,j} & B_{\theta,i,j} & & \end{array} \right\} \quad \begin{array}{l} i \in \{1, \dots, N_r\} \\ j \in \{0, \dots, N_s + 1\} \end{array} \quad (3.1.2)$$

where  $s_{i,j}$  and  $r_{i,j}$  are the poloidal and radial co-ordinates of the cell center with indices  $i$  and  $j$ ,  $s_{1,i,j}$  to  $s_{4,i,j}$  and  $r_{1,i,j}$  to  $r_{4,i,j}$  are similar co-ordinates of the four cell corners,  $R_{i,j}$  and  $Z_{i,j}$  are cartesian toroidal co-ordinates of the cell center,  $A_{i,j}$  is the poloidal cell area (cell volume  $\sim 2\pi R_{i,j} A_{i,j}$ ) and  $B_{\phi,i,j}$  and  $B_{\theta,i,j}$  are the toroidal and poloidal components of the magnetic field at the cell center ( $B_{r,i,j} \equiv 0$ , by the definition of the magnetic surface). We will denote a single grid cell by  $\mathbf{X}_{i,j}$ ; all cells with the same  $i$  index lie along a single flux surface forming a computational ring  $\mathbf{X}_i$ . Target locations correspond to the  $j = 0$  and  $j = N_s + 1$  indices.

### 3.2 Plasma Equations: Computational Fluid Dynamics (CFD)

We begin the iterative cycle by specifying neutral and cross-field sources,  $\mathbf{Q}_S(\mathbf{X})$  and  $\mathbf{Q}_\perp(\mathbf{X})$ , and keeping these sources constant, solving the plasma transport equations (2.1.22) to obtain  $\mathbf{U}(\mathbf{X})$ , (since the final solution is insensitive to initial conditions, the exact form of the initial sources is not important; they may be taken from a previously converged solution or prescribed analytically). A solution may be obtained using the standard numerical methods of CFD<sup>[Roe82,Hir90]</sup>, based on replacing temporal and spatial derivatives by corresponding discrete operators,

$$\frac{\partial \psi}{\partial x} \rightarrow \delta_x \psi \quad \frac{\partial \psi}{\partial t} \rightarrow \delta_t \psi \quad (3.2.1)$$

If the relatively coarse, poloidal grid  $\mathbf{X}$  is chosen as a substrate for discrete spatial operations, the grid point locations could not be adjusted to regions of steeper gradients without re-solving the Grad-Shafranov problem. Therefore, for reasons of improved spatial accuracy, we define a series of fine, along- $\mathbf{B}$  grids  $\mathbf{X}_i^H$  (one for each computational ring  $\mathbf{X}_i$ ) of  $N_H$  internal points at locations  $x_k$ ,  $k \in \{1, \dots, N_H\}$ ,  $N_H > N_s$ , and two boundary points  $x_0 = 0$  and  $x_{N_H+1} = L_\phi$ , where  $x$  is a distance along the field line from the outer target,  $x \equiv s_H$ . The two types of grids are linked via (3.1.1), the analytic transformation  $x \longleftrightarrow s$  being isomorphic:  $x = x(s)$ ,  $s = s(x)$ ; the discrete transformation  $\mathbf{T}_i$ :  $\psi_x(\mathbf{X}_i) \rightarrow \psi_s(\mathbf{X}_i^H)$  is however not isomorphic for arbitrary  $\mathbf{X}_i$  and  $\mathbf{X}_i^H$ , that is  $\mathbf{T}_i^{-1}\mathbf{T}_i \neq \mathbf{I}$ , since for  $N_H > N_s$  no general structure exists which would permit complete retrieval of information (a situation analogous to entropy growth and irreversibility in thermodynamics<sup>[Hua87]</sup>). We can however construct  $\mathbf{T}_i$  and  $\mathbf{T}_i^{-1}$  such that  $\int \psi_x(\mathbf{X}_i) dx = \int \psi_s(\mathbf{X}_i^H) ds$  over any region on  $[0, L_\phi]$ , and such transforms will be used to map  $\mathbf{Q}_S$  onto  $\mathbf{X}_i^H$  and  $\mathbf{U}$  onto  $\mathbf{X}_i$ ;  $\mathbf{U}$  and  $\mathbf{Q}$  will be stored on both type of grids to prevent loss of information via repeated application of  $\mathbf{T}_i^{-1}\mathbf{T}_i$ .

We choose  $\delta_x$  to be a three-point, central difference operator, the simplest operator of 2<sup>nd</sup> order accuracy:  $(\delta_x \psi)_k = [\psi_{k+1/2} - \psi_{k-1/2}] / [x_{k+1/2} - x_{k-1/2}]$ , where half-indices indicate mid-point locations,  $x_{k+1/2} = (x_k + x_{k+1}) / 2$ ; similarly,  $(\delta_x \psi)_{k+1/2} = [\psi_{k+1} - \psi_k] / [x_{k+1} - x_k]$ . Plasma variables and sources are defined on the grid points,  $\mathbf{U}_k$  and  $\mathbf{Q}_k$ , and are linearly interpolated from these values to any other location. Fluxes  $\mathbf{F}_{||}$  and  $\mathbf{G}_{||}$ , which we write simply as  $\mathbf{F}$  and  $\mathbf{G}$ , are calculated at the mid-points  $x_{k+1/2}$  in order to give a gradient at the grid points  $x_k$ . Spatial discretisation on  $X_i^H$  may be represented schematically as,

$$\begin{array}{ccccccc} x_0 & x_1 & \dots & x_{k-1} & x_k & x_{k+1} & \dots & x_N & x_{N+1} \\ \bullet & o & \dots & o & o & o & \dots & o & \bullet \\ U_0 & U_1 & & U_{k-1} & U_k & U_{k+1} & & U_N & U_{N+1} \\ Q_0 & Q_1 & & Q_{k-1} & Q_k & Q_{k+1} & & Q_N & Q_{N+1} \\ F_{1/2} & & & F_{k-1/2} & F_{k+1/2} & & & F_{N+1/2} & \\ G_{1/2} & & & G_{k-1/2} & G_{k+1/2} & & & G_{N+1/2} & \end{array} \quad (3.2.2)$$

or emphasizing the non-uniformity of  $X_i^H$ ,

$$\begin{array}{ccccc} x_{k-1} & x_{k-1/2} & x_k & x_{k+1/2} & x_{k+1} \\ o & | & o & | & o \\ U_{k-1} & & U_k & & U_{k+1} \\ Q_{k-1} & & Q_k & & Q_{k+1} \\ F_{k-1/2} & & & F_{k+1/2} & \\ G_{k-1/2} & & & G_{k+1/2} & \end{array} \quad (3.2.3)$$

After discretisation, the system of four coupled partial differential equations is transformed into a system of  $4N$  algebraic equations, which we write in vector form as

$$(\delta_x \mathbf{U})_k = \mathbf{Q}_k - \delta_x (\mathbf{F} + \mathbf{G})_k = \mathbf{Q}_k - \frac{(\mathbf{F} + \mathbf{G})_{k+1/2} - (\mathbf{F} + \mathbf{G})_{k-1/2}}{x_{k+1/2} - x_{k-1/2}} \equiv \mathcal{R}_k \quad k \in \{1, \dots, N_{||}\} \quad (3.2.4)$$

$$\mathbf{F}_{k+1/2} = \mathbf{F}[\mathbf{U}_{k+1/2}] = \mathbf{F}\left[\frac{\mathbf{U}_k + \mathbf{U}_{k+1}}{2}\right] \quad k \in \{0, \dots, N_{||}\}$$

$$\mathbf{G}_{k+1/2} = \mathbf{G}[(\delta_x \mathbf{U})_{k+1/2}] = \mathbf{G}\left[\frac{\mathbf{U}_{k+1} - \mathbf{U}_k}{x_{k+1} - x_k}\right] \quad k \in \{0, \dots, N_{||}\}$$

where we have introduced the residual  $\mathcal{R}_k$  as a measure of local convergence of the solution (in steady state  $\|\mathcal{R}\| = \sum_k |\mathcal{R}_k| \equiv 0$ ). Square brackets in the last two expressions indicate the dependence of the fluxes on  $\mathbf{U}$ : convective fluxes are calculated from interpolated  $\mathbf{U}$  values, while conductive fluxes are obtained from the gradient of  $\mathbf{U}$ , both at the mid-points  $x_{k+1/2}$ .

The temporal derivative may be discretized using a two-point (Euler) discrete operator (2<sup>nd</sup> order accurate):  $(\delta_t \psi)^n = [\psi^{n+1} - \psi^n] / \Delta t$ , where index  $n$  denotes the time stage, so that  $\mathbf{U}^{n+1} = \mathbf{U}^n + (\delta_t \mathbf{U})^n \Delta t$ . Since we are interested only in steady state solutions, time accuracy is not required and time  $t$  may be

viewed as a relaxation variable. Time marching methods are customarily distinguished into explicit ( $\delta_t \mathbf{U}^n = \mathbf{R}^n$ ) and implicit ( $\delta_t \mathbf{U}^n = \mathbf{R}^{n+1}$ ), the former based on already known  $\mathbf{U}^n$ , the latter on next-stage, as yet unknown  $\mathbf{U}^{n+1}$ . Explicit methods are generally far less stable, although the degree of stability depends on the details of the discretization and equation system being solved, eg. the explicit Euler method with central differencing is unconditionally unstable for purely convective fluxes requiring artificial dissipation terms. The stability limitations of explicit methods may be understood as the requirement that information must travel between adjacent grid points during the update time step  $\Delta t$ <sup>[Hir90]</sup>, based on characteristic (eigen-) velocities of convective and conductive fluxes,  $c_F = (u, u \pm c_\gamma)$ ,  $c_G = (q_e/p_e, \delta p_i/\rho u) = (\chi_e/L_{vTe}, \eta_i/\rho L_{vG})$ , two approximate limits are imposed on the update time step  $\Delta t_k < \min(\Delta t_k^F, \Delta t_k^G)$ ,

$$\Delta t_k^F = \frac{x_{k+1/2} - x_{k-1/2}}{(u + c_\gamma)_k} \quad c_\gamma = \left( \frac{5}{3} \cdot \frac{p_i + p_e}{\rho} \right)^{1/2} \quad \Delta t_k^G = \frac{(x_{k+1/2} - x_{k-1/2})^2}{\max(\chi_e, \eta_i / \rho)_k} \quad (3.2.5)$$

In a typical tokamak edge plasma, conductive fluxes would be much more constraining on the explicit updates ( $\Delta t_k^G \ll \Delta t_k^F$ ) due to high values of electron heat diffusivity  $\chi_e$  and the square dependence on grid spacing (very small near the target). In short, the system exhibits a large degree of numerical stiffness and is ill suited to explicit time marching (requiring prohibitively long convergence times). In contrast, the implicit formulation offers greater numerical stability, allows longer time steps, and leads to faster convergence<sup>[Hir90]</sup>; for these reasons, implicit Euler time marching was selected. With implicit updates, infinite time steps are potentially allowed, but are limited in practice by implementation of boundary conditions (often non-implicit) or strong non-linearities in the equations; time steps on the convective time scale  $\Delta t_k^F$  are more appropriate (still a great improvement over  $\Delta t_k^G$ ). We may write the update to  $\mathbf{U}^n$  as

$$(\delta_t \mathbf{U})^n = (\mathbf{Q} - \delta_x \mathbf{F} - \delta_x \mathbf{G} - \delta_x \mathbf{H})^{n+1} = \tilde{\mathbf{R}}^{n+1} \quad (3.2.6)$$

where  $\mathbf{H}$  represent artificial dissipation fluxes, to which we return shortly. In implicit form, the update to  $\mathbf{U}^n$  is expressed in terms of the next stage  $\mathbf{U}^{n+1}$ . The new values may be obtained by expanding  $\mathbf{Q}$ ,  $\mathbf{F}$ ,  $\mathbf{G}$  and  $\mathbf{H}$  to first order in  $\Delta \mathbf{U}^n = \mathbf{U}^{n+1} - \mathbf{U}^n$  and defining Jacobian matrices for each quantity.

$$\psi^{n+1} = \psi^n + \left( \frac{\partial \psi}{\partial \mathbf{U}} \right)^n \Delta \mathbf{U}^n = \psi^n + \mathbf{J}_\psi^n \Delta \mathbf{U}^n \quad \psi = \{\mathbf{Q}, \mathbf{F}, \mathbf{G}, \mathbf{H}\} \quad (3.2.7)$$

Inserting the above into (3.2.6) we obtain,

$$[\mathbf{I} + \Delta t (\delta_x \mathbf{J}_F^n + \delta_x \mathbf{J}_G^n + \delta_x \mathbf{J}_H^n - \mathbf{J}_Q^n)] \Delta \mathbf{U}^n = (\mathbf{Q}^n - \delta_x \mathbf{F}^n - \delta_x \mathbf{G}^n - \delta_x \mathbf{H}^n) \Delta t = \tilde{\mathbf{R}}^n \Delta t \quad (3.2.8)$$

The above is a linear system which may be solved for  $\Delta \mathbf{U}^n$ . The expression in the square brackets is a sparse  $4N \times 4N$  matrix composed of  $4 \times 4$  blocks related to the Jacobian matrices. For the purpose of evaluating these matrices, it is convenient to introduce a shorthand notation for  $\mathbf{U}$ ,

$$\mathbf{U} = \begin{pmatrix} \rho \\ \rho u \\ \rho \epsilon_i \\ \rho \epsilon_e \end{pmatrix} = \begin{pmatrix} a \\ b \\ c \\ d \end{pmatrix} \quad \mathbf{F} = \begin{pmatrix} b \\ \frac{2}{3}(c+d+\frac{b^2}{a}) \\ \frac{b}{a}(\frac{5}{3}c - \frac{1}{3}\frac{b^2}{a}) \\ \frac{b}{a}(\frac{5}{3}d) \end{pmatrix} \quad \mathbf{G} = \begin{pmatrix} 0 \\ -\eta_i \delta_x(\frac{b}{a}) \\ -\frac{2m\kappa_i}{3} \delta_x(\frac{c}{a} - \frac{b^2}{2a^2}) - \eta_i \frac{b}{a} \delta_x(\frac{b}{a}) \\ -\frac{2m\kappa_e}{3} \delta_x(\frac{d}{a}) \end{pmatrix} \quad (3.2.9)$$

and perform the differentiation in this notation:

$$\mathbf{J}_F = \left( \frac{\partial \mathbf{F}}{\partial \mathbf{U}} \right) = \begin{pmatrix} 0 & 1 & 0 & 0 \\ -\frac{2b^2}{3a^2} & \frac{4b}{3a} & \frac{2}{3} & \frac{2}{3} \\ -\frac{5bc}{3a^2} + \frac{2b^3}{3a^3} & \frac{5c}{3a} - \frac{b^2}{a^2} & \frac{5b}{3a} & 0 \\ -\frac{5bd}{3a^2} & \frac{5d}{3a} & 0 & \frac{5b}{3a} \end{pmatrix} \quad (3.2.10)$$

$$\mathbf{J}_G^0 = \left( \frac{\partial \mathbf{G}}{\partial \mathbf{U}} \right) = \begin{pmatrix} 0 & 0 & 0 & 0 \\ \eta_i \delta_x \left( \frac{b}{a^2} \right) & -\eta_i \delta_x \left( \frac{1}{a} \right) & 0 & 0 \\ -\frac{2m\kappa_i}{3} \delta_x \left( \frac{b^2}{a^3} - \frac{c}{a^2} \right) & \frac{2m\kappa_i}{3} \delta_x \left( \frac{b}{a^2} \right) & -\frac{2m\kappa_i}{3} \delta_x \left( \frac{1}{a} \right) & 0 \\ \frac{2m\kappa_e}{3} \delta_x \left( \frac{d}{a^2} \right) & 0 & 0 & -\frac{2m\kappa_e}{3} \delta_x \left( \frac{1}{a} \right) \end{pmatrix}$$

$$+ \begin{pmatrix} 0 & 0 & 0 & 0 \\ 0 & 0 & 0 & 0 \\ \eta_i \frac{b}{a} \delta_x \left( \frac{b}{a^2} \right) + \eta_i \frac{b}{a^2} \delta_x \left( \frac{b}{a} \right) & -\eta_i \frac{1}{a} \delta_x \left( \frac{b}{a} \right) - \eta_i \frac{b}{a} \delta_x \left( \frac{1}{a} \right) & 0 & 0 \\ 0 & 0 & 0 & 0 \end{pmatrix}$$

$$\mathbf{J}_{\nu} = \left( \frac{\partial Q_{\nu}}{\partial \mathbf{U}} \right) = \begin{pmatrix} 0 & 0 & 0 & 0 \\ 0 & 0 & 0 & 0 \\ \frac{2b}{3a^2} \delta_x d & -\frac{2}{3a} \delta_x d & 0 & -\frac{2b}{3a} \delta_x \\ -\frac{2b}{3a^2} \delta_x d & \frac{2}{3a} \delta_x d & 0 & \frac{2b}{3a} \delta_x \end{pmatrix}$$

$$+ \begin{pmatrix} 0 & 0 & 0 & 0 \\ 0 & 0 & 0 & 0 \\ -\frac{b^2}{3a^2 \tau_{ei}^{(2)}} + \frac{5Q_{ei}}{2a} & -\frac{2b}{3a \tau_{ei}^{(2)}} & -\frac{2}{3\tau_{ei}^{(2)}} & -\frac{2}{3\tau_{ei}^{(2)}} - \frac{3Q_{ei}}{2d} \\ \frac{b^2}{3a^2 \tau_{ei}^{(2)}} - \frac{5Q_{ei}}{2a} & -\frac{2b}{3a \tau_{ei}^{(2)}} & \frac{2}{3\tau_{ei}^{(2)}} & -\frac{2}{3\tau_{ei}^{(2)}} + \frac{3Q_{ei}}{2d} \end{pmatrix} \quad Q_{ei} = \frac{p_e - p_i}{\tau_{ei}^{(2)}}$$

$$\mathbf{J}_B = \left( \frac{\partial \mathbf{Q}_B}{\partial \mathbf{U}} \right) = \frac{\nabla_{||} B}{B} (\mathbf{J}_F + \mathbf{J}_G) - \frac{\nabla_{||} B}{B} \begin{pmatrix} 0 & 0 & 0 & 0 \\ \frac{b^2}{3a^2} + \frac{\eta_i}{2} \delta_x \left( \frac{b}{a^2} \right) & -\frac{2b}{3a} - \frac{\eta_i}{2} \delta_x \left( \frac{l}{a} \right) & \frac{2}{3} & \frac{2}{3} \\ 0 & 0 & 0 & 0 \\ 0 & 0 & 0 & 0 \end{pmatrix}$$

$$\mathbf{J}_S = \left( \frac{\partial \mathbf{Q}_S}{\partial \mathbf{U}} \right) = 0 \quad \mathbf{J}_{\perp} = \left( \frac{\partial \mathbf{Q}_{\perp}}{\partial \mathbf{U}} \right) = 0 \quad \mathbf{J}_Q = \left( \frac{\partial \mathbf{Q}}{\partial \mathbf{U}} \right) = \mathbf{J}_B + \mathbf{J}_P$$

A number of comments are in order:

i) in differentiating  $\mathbf{G}$  we treated  $\eta_i$ ,  $\kappa_i = n\chi_i$  and  $\kappa_e = n\chi_e$ , as constants, which greatly simplified calculation of  $\mathbf{J}_G$  (denoted below as  $\mathbf{J}_G^0$ ); this omission does not adversely affect stability, provided that  $\mathbf{J}_G^0$  is evaluated at each time stage using  $\eta_i(\mathbf{U}^n)$ ,  $\kappa_i(\mathbf{U}^n)$  and  $\kappa_e(\mathbf{U}^n)$ . Had we assumed that all three coefficients exhibit the classical (non-flux limited) dependence,  $\eta_\alpha, \kappa_\alpha \propto T_\alpha^{5/2}$ , chain rule differentiation would yield,

$$\mathbf{J}_G^{cl} = \mathbf{J}_G^0 + \frac{5m}{3} \begin{pmatrix} 0 & 0 & 0 & 0 \\ -\frac{\eta_i}{T_i} \left( \frac{b^2}{a^3} - \frac{c}{a^2} \right) \delta_x u & \frac{\eta_i}{T_i} \left( \frac{b}{a^2} \right) \delta_x u & -\frac{\eta_i}{T_i} \left( \frac{l}{a} \right) \delta_x u & 0 \\ -\frac{\kappa_i}{T_i} \left( \frac{b^2}{a^3} - \frac{c}{a^2} \right) \delta_x T_i & \frac{\kappa_i}{T_i} \left( \frac{b}{a^2} \right) \delta_x T_i & -\frac{\kappa_i}{T_i} \left( \frac{l}{a} \right) \delta_x T_i & 0 \\ \frac{\kappa_e}{T_e} \left( \frac{d}{a^2} \right) \delta_x T_e & 0 & 0 & \frac{\kappa_e}{T_e} \left( \frac{l}{a} \right) \delta_x T_e \\ 0 & 0 & 0 & 0 \end{pmatrix} \quad (3.2.11)$$

$$+ \frac{5m}{3} \begin{pmatrix} 0 & 0 & 0 & 0 \\ 0 & 0 & 0 & 0 \\ -\frac{\eta_i}{T_i} \left( \frac{b^2}{a^3} - \frac{c}{a^2} \right) u \delta_x u & \frac{\eta_i}{T_i} \left( \frac{b}{a^2} \right) u \delta_x u & -\frac{\eta_i}{T_i} \left( \frac{l}{a} \right) u \delta_x u & 0 \\ 0 & 0 & 0 & 0 \end{pmatrix}$$

If the flux-limited dependence of  $q_e$  and  $\delta p_i$ , both of the form  $1/\psi = 1/\psi^{cl} + 1/\psi^{fs}$ , is also considered, then the final  $\mathbf{J}_G$  would consist of classical and flux-limited contributions,

$$\mathbf{J}_G = \begin{pmatrix} I & 0 & 0 & 0 \\ 0 & \left( \frac{\delta p_i}{\delta p_i^{cl}} \right)^2 & 0 & 0 \\ 0 & 0 & I & 0 \\ 0 & 0 & 0 & \left( \frac{q_e}{q_e^{cl}} \right)^2 \end{pmatrix} \mathbf{J}_G^{cl} + \begin{pmatrix} I & 0 & 0 & 0 \\ 0 & \left( \frac{\delta p_i}{\delta p_i^{fs}} \right)^2 & 0 & 0 \\ 0 & 0 & I & 0 \\ 0 & 0 & 0 & \left( \frac{q_e}{q_e^{fs}} \right)^2 \end{pmatrix} \mathbf{J}_G^{fs} \quad (3.2.12)$$

$$\mathbf{J}_G^{fs} = \begin{pmatrix} 0 & 0 & 0 & 0 \\ \frac{4}{7} \cdot \frac{b^2}{3a^2} & -\frac{4}{7} \cdot \frac{b}{a} & \frac{4}{7} \cdot \frac{2}{3} & 0 \\ 0 & 0 & 0 & 0 \\ -\frac{1}{2a} q_e^{fs} & 0 & 0 & \frac{3d}{2} q_e^{fs} \end{pmatrix}$$

Since the above Jacobians do not enter the residual  $\mathcal{R}$ , which alone acts as the forcing function for  $\Delta\mathbf{U}$ , they affect stability and rate of convergence, but not the steady state, converged solution  $\mathbf{U}$ . We find that, the removal of Jacobian terms corresponding to calmer source terms, eg.  $\mathbf{J}_B$  or the first matrix in  $\mathbf{J}_P$ , has little effect on either convergence or stability.

- ii) in  $\mathbf{J}_B$ , the  $B$ -field gradient  $\nabla_i B/B$  may be calculated and stored as  $L^{VB}_k = B_k(x_{k+1} - x_{k-1}) / (B_{k+1} - B_{k-1})$ ,
- iii) in  $\mathbf{J}_P$  we treated  $\tau_{ei}^{(2)}$  as a function of  $\mathbf{U}$ ,  $\tau_{ei}^{(2)}[\mathbf{U}] \propto T_e^{3/2} n^{-1} \propto d^{3/2} a^{-5/2}$ ,
- iv) since  $\mathbf{Q}_3$  and  $\mathbf{Q}_1$  do not change in the course of CFD convergence, their Jacobians vanish,
- v) it is important to remember that  $\delta_x$  occurring inside the Jacobian matrices are operators which act on  $\Delta\mathbf{U}$  in (3.2.9), and should not be applied only to their argument in the matrix. This becomes clear is we examine the structure of  $\delta_x \mathbf{J}_G$  in the  $\Delta\mathbf{U}$  basis. A term-operator in  $\mathbf{J}_G$ ,  $(\alpha \delta_x \beta)$ , gives rise to a term-operator in  $\delta_x \mathbf{J}_G$  .  $\delta_x(\alpha \delta_x \beta)$ , which when acting on  $\Delta\mathbf{U}$  produces terms tri-diagonal with respect to the  $\Delta\mathbf{U}$  basis,

$$(\delta_x \mathbf{J}_G)_k = (\delta_x [\alpha \cdot \delta_x \beta])_k = \frac{1}{x_{k+1/2} - x_{k-1/2}} \left[ \alpha_{k+1/2} \frac{\beta_{k+1} - \beta_k}{x_{k+1} - x_k} - \alpha_{k-1/2} \frac{\beta_k - \beta_{k-1}}{x_k - x_{k-1}} \right] \quad (3.2.13)$$

Artificial dissipation fluxes  $\mathbf{H}$  were introduced for reasons of numerical stability. Let us consider the situation without  $\mathbf{H}$ : as a consequence of spatial discretisation, grid related harmonics are introduced into the solution; they are either attenuated or augmented at every time stage, the latter leading to numerical instability (this behaviour depends on the operators  $\delta_x$  and  $\delta_t$ , the grid spacing  $x_k$ , the temporal step size  $\Delta t$ , and the nature of the equations; it has been studied extensively and stability limits for all practical schemes are readily available<sup>[Hir80]</sup>). The case of central two-point differencing  $\delta_x$  and explicit Euler time marching  $\delta_t$  applied to locally hyperbolic (convectively dominated,  $c_F > c_G$  or  $|u| + c_T > \Delta x/\chi_c$ ) equations is destabilized by a decoupling of alternate grid points<sup>[Hir74]</sup>. A number of methods of dealing with this problem may be found in the literature<sup>[Roe82, Hir90]</sup>: a) splitting the convective fluxes according to direction and discretizing using an upwind  $\delta_x$ , then limiting the local flux to prevent oscillating overshoots, the so-called TVD (total variance diminishing) methods, and b) introducing artificial dissipation fluxes which dampen numerical oscillations during convergence, while adding only a small error to the final solution (it has been shown that flux-limiting methods lead to artificial dissipation terms). Accordingly, artificial dissipation fluxes suggested by Jameson were adapted<sup>[Jam82]</sup>,

$$\begin{aligned}
 \mathbf{H}_{k+1/2} &= \boldsymbol{\omega}_{k+1/2}^{(2)} \delta_x \mathbf{U} - \boldsymbol{\omega}_{k+1/2}^{(2)} \delta_x \delta_x \delta_x \mathbf{U} & \mathbf{J}_H = \left( \frac{\partial \mathbf{H}}{\partial \mathbf{U}} \right) &= \boldsymbol{\omega}_{k+1/2}^{(2)} \delta_x - \boldsymbol{\omega}_{k+1/2}^{(4)} \delta_x \delta_x \delta_x & (3.2.14) \\
 \boldsymbol{\omega}_k^{(2)} &= \kappa^{(2)} (|u| + c_\gamma)_k \max(\Psi_{k-1}, \Psi_k, \Psi_{k+1}) & \Psi_k &= \begin{vmatrix} p_{k+1} - 2p_k + p_{k-1} \\ p_{k+1} + 2p_k + p_{k-1} \end{vmatrix} \\
 \boldsymbol{\omega}_k^{(4)} &= (|u| + c_\gamma)_k \max \left[ 0, \kappa^{(4)} - \frac{w_k^{(2)}}{(|u| + c_\gamma)_k} \right] & \kappa^{(2)} \sim 0.25 & \kappa^{(4)} \sim 0.01
 \end{aligned}$$

where  $p_k$  is the pressure,  $c_\gamma = [(5/3)(p_i + p_e)/\rho]^{1/2}$  is the adiabatic sound speed, and  $\kappa^{(2)}$  and  $\kappa^{(4)}$  are constants. In this form,  $\delta_x \mathbf{H}$  contains both 2<sup>nd</sup> and 4<sup>th</sup> order dissipation terms: the 2<sup>nd</sup> order term is largest in regions of strong pressure gradients, (eg. shock waves or detached fronts), while the 4<sup>th</sup> order term, which effectively dampens higher harmonics, is clipped in these regions. The Jacobian matrix is particularly easy to evaluate, leaving the same spatial operators as in  $\mathbf{H}$ .

We now have all the components necessary to find the update  $\Delta \mathbf{U}^n$ . The linear system could be solved using standard LU decomposition<sup>[Pre92]</sup> at a computational cost  $\sim (4N_h)^3$ . We notice however that the matrix expression in the square brackets of (3.2.9) has a highly sparse structure (penta-diagonal, if all terms are retained; tri-diagonal, if 4<sup>th</sup> order terms are neglected from  $\delta_x \mathbf{J}_H$ ). We choose the second variant, a decision justified by later analysis, and write the linear system

$$\begin{pmatrix}
 \mathbf{B}_1 & \mathbf{C}_1 & & & \\
 \mathbf{A}_2 & \mathbf{B}_2 & \mathbf{C}_2 & & \mathbf{0} \\
 \vdots & \vdots & \ddots & & \\
 & \mathbf{A}_k & \mathbf{B}_k & \mathbf{C}_k & \\
 & \vdots & \ddots & \ddots & \\
 \mathbf{0} & & \mathbf{A}_{N_h-1} & \mathbf{B}_{N_h-1} & \mathbf{C}_{N_h-1} \\
 & & \mathbf{A}_{N_h} & \mathbf{B}_{N_h} & 
 \end{pmatrix}
 \begin{pmatrix}
 \Delta \mathbf{U}_1 \\
 \Delta \mathbf{U}_2 \\
 \vdots \\
 \Delta \mathbf{U}_k \\
 \vdots \\
 \Delta \mathbf{U}_{N_h-1} \\
 \Delta \mathbf{U}_{N_h}
 \end{pmatrix}
 =
 \begin{pmatrix}
 \tilde{\mathcal{R}}_1 \Delta t_1 \\
 \tilde{\mathcal{R}}_2 \Delta t_2 \\
 \vdots \\
 \tilde{\mathcal{R}}_k \Delta t_k \\
 \vdots \\
 \tilde{\mathcal{R}}_{N_h-1} \Delta t_{N_h-1} \\
 \tilde{\mathcal{R}}_{N_h} \Delta t_{N_h}
 \end{pmatrix}
 \quad (3.2.15)$$

where each of the  $\mathbf{A}_k$ ,  $\mathbf{B}_k$  and  $\mathbf{C}_k$  represent  $4 \times 4$  matrix blocks. Such a linear system is most efficiently solved using a block tri-diagonal Thomas algorithm<sup>[Hal74, Pre92]</sup>, developed initially for scalar tri-diagonal systems, but easily extended to block tri-diagonal systems by replacing scalar algebra with matrix operations, App.3 (it requires a series of  $4 \times 4$  matrix inversions on the returning sweep for which LU decomposition was used). Computational cost is reduced from  $\sim (4N_h)^3$  to  $\sim 4^3 N_h^2$ , that is by a factor of  $\sim N_h$ . The updates  $\Delta \mathbf{U}^n$  and the new state variables  $\mathbf{U}^{n+1} = \mathbf{U}^n + \Delta \mathbf{U}^n$  are thus obtained. The entire process is repeated until the relative changes to  $\mathbf{U}^n$  are small,  $(\Delta \mathbf{U}^n / \mathbf{U}^n) \ll 1$ .

Boundary conditions discussed in §2.2 and §2.4.3 (the Bohm criterion and energy transmission coefficients for ions and electrons) may be numerically implemented in a number of ways. The key feature is the transition from a hyperbolic to an elliptic system at the target; since  $M_0 > 1$  by the Bohm criterion, the hyperbolic nature of equations at the target is guaranteed. The simplest implementation method is to explicitly update the grid boundary variables,  $\mathbf{U}_0$  and  $\mathbf{U}_{N_h+1}$ , after each sweep of the solution  $\mathbf{U}_k$  on the inner

grid points,  $k \in \{1, \dots, N_{\text{II}}\}$ ; the boundary updates  $\Delta \mathbf{U}_0$  and  $\Delta \mathbf{U}_{N_{\text{II}}+1}$  should reflect both physical and numerical constraints (known as floating or numerical boundary conditions, which involve extrapolations of  $\mathbf{U}$  from the inner grid points in order to assure continuity of  $\mathbf{U}_0$  and  $\mathbf{U}_{N_{\text{II}}+1}$  with the inner  $\mathbf{U}_k$ ) and may be calculated by a method similar to the inner point updates  $\Delta \mathbf{U}_k$ . Let us define the constraint vector as  $\Psi_0(\mathbf{U})$ ; then the desired updates  $\Delta \mathbf{U}_0$  may be obtained by Newton's method<sup>[Hil74]</sup>,

$$\Psi_0^{BC} = \begin{cases} Extr_0(\mathbf{F}_1^{(1)}, \mathbf{F}_2^{(1)}) + Extr_0(\mathbf{G}_1^{(1)}, \mathbf{G}_2^{(1)}) \\ \left\{ \begin{array}{l} (p_i + p_e + \rho c_s^2)_0, \quad M_0 < 1 \\ Extr_0(\mathbf{F}_1^{(2)}, \mathbf{F}_2^{(2)}) + Extr_0(\mathbf{G}_1^{(2)}, \mathbf{G}_2^{(2)}), \quad M_0 > 1 \end{array} \right. \\ (\gamma_i T_i \Gamma)_0 \\ (\gamma_e T_e \Gamma)_0 \end{cases} \quad \Psi_{1/2}^{FG} = \mathbf{F}_{1/2}(\mathbf{U}) + \mathbf{G}_{1/2}(\mathbf{U}) \quad (3.2.16)$$

$$\Psi_0(\mathbf{U}) = \Psi_0^{BC} - \Psi_{1/2}^{FG} \quad \Delta \Psi_0 = \left( \frac{\partial \Psi_0}{\partial \mathbf{U}_0} \right) \Delta \mathbf{U}_0 = \mathbf{J}_{\Psi_0} \Delta \mathbf{U}_0 \quad \Delta \mathbf{U}_0 = \mathbf{J}_{\Psi_0}^{-1} \Delta \Psi_0 = -\varepsilon_{\Psi} \mathbf{J}_{\Psi_0}^{-1} \Psi_0, \quad \varepsilon_{\Psi} = 0.1$$

where  $Extr_0(A_1, A_2)$  denotes a linear extrapolation of  $A(x)$  from the values at  $A(x_1)$  and  $A(x_2)$  to the target  $x_0=0$ . The evaluation and inversion of the Jacobian matrix proceed in exact analogy to (3.2.9-11). As already mentioned, explicit updates may destabilize near target cells. A more stable method, short of the fully-implicit treatment (which for reasons of flexibility we would like to avoid), is to make the updates semi-implicit by solving for  $T_{i,0} \rightarrow \mathbf{U}_0^{(3)}$  from  $\Psi_0^{(3)} = 0$  and for  $T_{e,0} \rightarrow \mathbf{U}_0^{(4)}$  from  $\Psi_0^{(4)} = 0$ , where  $\mathbf{F}_{1/2}$  and  $\mathbf{G}_{1/2}$  were expressed in terms of  $\mathbf{U}_0$  and  $\mathbf{U}_1$  according to (3.2.4) and (3.2.9); the updates to  $\mathbf{U}^{(1)}$  and  $\mathbf{U}^{(2)}$  are made explicitly according to (3.2.16). A further improvement involves a small iterative loop in which the updated values of  $\mathbf{U}_0$  and  $\mathbf{U}_{N_{\text{II}}+1}$  are diffused into the grid by a series of explicit updates of the few near target cells,  $\mathbf{U}_0$  and  $\mathbf{U}_{N_{\text{II}}+1}$  are then updated semi-implicitly, and the cycle repeated until local convergence. In our case, it was found that the one-time semi-implicit method is more efficient for  $T_e < 10$  eV, while the cyclical semi-implicit method is superior for  $T_e > 10$  eV.

The main motivation for introducing the fine grid  $\mathbf{X}^{\text{II}}$  was to eventually adjust grid point locations in order to maximize spatial accuracy. There are two main approaches for adapting the grid to the solution<sup>[Dun90]</sup>: a) introducing more grid points, b) redistributing the grid points according to spring-like, variational, or control function methods. Selecting control function redistribution method of Eiseman<sup>[Eis87]</sup>, which effectively adapts  $\mathbf{X}^{\text{II}}$  to both internal and boundary errors in  $\mathbf{U}$ , we introduce a uniform grid  $\xi_k$ ,  $k \in \{0, \dots, N_{\text{II}}+1\}$ ,  $\xi_{k+1} - \xi_k = 1$ , and treat  $\mathbf{X}^{\text{II}}$  as an isomorphic mapping from  $\xi$ ,  $x_k = x_k(\xi_k)$ . We will induce diffusion of  $x_k$  in  $\xi$ -space in response to a control function  $\Pi(\mathbf{U}(x_k(\xi_k)))$ , which will determine the grid-point density in  $\xi$ -space (grid points are clustered in regions where  $\Pi$  is large). This process may be written as an elliptic differential equation<sup>[Hal95]</sup>, which we discretize using a 2<sup>nd</sup> order, central-difference  $\delta_{\xi}$

$$\delta_\xi \delta_\xi X^{\parallel} + \Pi(U(x_k(\xi_k))) \delta_\xi X^{\parallel} = 0 \quad \Pi = \vartheta^{(1)} \Pi^g + \vartheta^{(2)} \Pi^a \quad (3.2.17)$$

where  $\vartheta$ 's are parametric constants and  $\Pi$  was subdivided into geometric and adaptive contributions. The former constrain the near target cell size (we select  $\Pi^g$  such that  $\|U_0 - U_1\|/\|U_0\| < 10\%$ ); this constraint is relaxed exponentially away from the targets.

$$\Pi^g(\xi_k) = \Pi^g(U_0) \exp[-\vartheta^{(3)}(\xi_k - \xi_0)] + \Pi^g(U_{N_{\parallel}+1}) \exp[-\vartheta^{(3)}(\xi_k - \xi_{N_{\parallel}+1})] \quad (3.2.18)$$

The latter impose changes to inner grid point density in  $\xi$ -space in response to some measure of solution variation  $f_k$ , which we choose as the  $\|\cdot\|_1$  norm of the difference  $U_{k+1} - U_{k-1}$ . These are normalized to the interval  $[0,1]$  and in the form  $w_k$  defined below are subjected to clipping and smoothing operations<sup>[Hal95]</sup>,

$$\begin{aligned} f_k &\equiv \|U_{k+1} - U_{k-1}\| & w_k &= 1 + \vartheta^{(4)} \frac{f_k - f_{\min}}{f_{\max} - f_{\min}} & \bar{w}_k &= \frac{1}{3}(w_{k+1} + w_k + w_{k-1}) \\ \hat{w}_k &= Clip[w_k] = \begin{cases} w_k & , \quad w_k < \vartheta^{(5)} \bar{w}_k \\ \bar{w}_k & , \quad w_k > \vartheta^{(5)} \bar{w}_k \end{cases} & \tilde{w}_k &= Smooth[\hat{w}_k] = \frac{1}{4}(\hat{w}_{k+1} + 2\hat{w}_k + \hat{w}_{k-1}) \end{aligned} \quad (3.2.19)$$

Adaptive control function  $\Pi^a$  measures the relative gradient of  $w_k$  in  $\xi$ -space,

$$\Pi^a(U(x_k(\xi_k))) = \frac{(\delta_\xi \tilde{w})_k}{\tilde{w}_k} = \frac{\tilde{w}_{k+1} - \tilde{w}_{k-1}}{2\tilde{w}_k} \quad (3.2.20)$$

Combining (3.2.17-20) and solving the tri-diagonal system (3.2.23) using the Thomas algorithm, we obtain new values of  $x_k$  of the grid  $\mathbf{X}^{\parallel}$ ; typical parameter choices are  $\vartheta = \{10, 1, 1/3, 10, 2\}$ . The process is repeated with  $\mathbf{U}$  interpolated to the new  $x_k$  values from the input  $\mathbf{U}(x_k)$ , until the relative changes to  $x_k$  are small.  $\Delta X_i^{\parallel}/X_i^{\parallel} \ll 1$ . The final (new) grid is then relaxed with the input (old) grid to assure gentler evolution:  $\mathbf{X}^{\parallel} = \epsilon_x \mathbf{X}_{\text{new}}^{\parallel} + (1-\epsilon_x) \mathbf{X}_{\text{old}}^{\parallel}$ ,  $\epsilon_x \sim 0.03$ .

We can now combine all the above modules, and present an algorithm of the edge plasma solver. Given sources  $\mathbf{Q}(\mathbf{X}) = \mathbf{Q}_3(\mathbf{X}) + \mathbf{Q}_\perp(\mathbf{X})$ , edge plasma variables  $\mathbf{U}(\mathbf{X})$  are obtained by mapping the sources onto the along- $\mathbf{B}$  grids,  $\mathbf{Q}(\mathbf{X}) \rightarrow \mathbf{Q}(\mathbf{X}_i^{\parallel})$ , converging the CFD solver on each  $\mathbf{X}_i^{\parallel}$  grid, and mapping the solution back onto the poloidal grid,  $\mathbf{U}(\mathbf{X}_i^{\parallel}) \rightarrow \mathbf{U}(\mathbf{X}_i)$ . The final algorithm is given below:

(3.2.21)

<b>Solve Edge</b> [ $X, Q(X)$ ]	<b>Solve ring</b> [ $i, X_i^{\text{II}}, Q(X_i^{\text{II}})$ ]	<b>Adapt Grid</b> [ $i, X_i^{\text{II}}, U(X_i^{\text{II}})$ ]
<i>Do</i> $i = i_{LCFS}, i_{\text{wall}}$	<i>Read</i> $U^{\text{old}}(X_i^{\text{II}})$	<i>Loop</i>
$Q(X_i) \rightarrow Q(X_i^{\text{II}})$	<i>Loop</i>	$\{X_i^{\text{II}}, U(X_i^{\text{II}})\} \rightarrow \{\Pi^a, \Pi^s\}$
<b>Solve Ring</b> [ $i, X_i^{\text{II}}, Q(X_i^{\text{II}})$ ]	<b>Sweep Ring</b> [ $i, X_i^{\text{II}}, Q(X_i^{\text{II}})$ ]	$\{\Pi^a, \Pi^s\} \rightarrow X_i^{\text{II}}$
<b>Adapt Grid</b> [ $i, X_i^{\text{II}}, U(X_i^{\text{II}})$ ]	<i>Exit when</i> $\max(\mathcal{R}_k) < \varepsilon_R \ll 1$	<i>Exit when</i> $\Delta X_i^{\text{II}} / X_i^{\text{II}} \ll 1$
<b>Solve Ring</b> [ $i, X_i^{\text{II}}, Q(X_i^{\text{II}})$ ]	<i>End loop</i>	<i>End loop</i>
$Q(X_i^{\text{II}}) \rightarrow Q(X_i)$	<i>Return</i> $U(X_i^{\text{II}})$	$X_i^{\text{II}} = \varepsilon_x X_i^{\text{II}}_{\text{new}} + (1 - \varepsilon_x) X_i^{\text{II}}_{\text{old}}$
<i>End do</i>		<i>Return</i> $X_i^{\text{II}}$
<i>Return</i> $U(X)$		

**Sweep Ring** [ $X^{\text{d}}, Q(X^{\text{d}})$ ]

<b>Find Fluxes:</b>	$\{X^{\text{d}}, U\}$	$\rightarrow$	$\{\Delta, F, G, H\}$
<b>Find <math>Q_p, Q_n</math>:</b>	$\{X^{\text{d}}, U\}$	$\rightarrow$	$\{Q_p, Q_n\}$
<b>Find Jacobians:</b>	$\{X^{\text{d}}, U, Q_p, Q_n\}$	$\rightarrow$	$\{J\}$
<b>Find Residual:</b>	$\{X^{\text{d}}, Q, Q_p, Q_n, F, G, H\}$	$\rightarrow$	$\mathcal{R}$
<b>Find Matrix:</b>	$\{X^{\text{d}}, J, \Delta\}$	$\rightarrow$	$[ABC]$
<b>Invert Matrix:</b>	$[ABC] \Delta U = \mathcal{R} \Delta$	$\rightarrow$	$\Delta U$
<b>Update U:</b>	$\Delta U$	$\rightarrow$	$U$
<b>Update BC:</b>	$U, Q, F, G$	$\rightarrow$	$U_0, U_{N+1}$

**3.3 Neutral Equations: Monte-Carlo simulation**

Having solved the plasma transport equations on the poloidal grid  $\mathbf{X}$ , we proceed to (re)calculate the neutral sources  $\mathbf{Q}_3$ . The kinetic equation describing the transport of neutral species, (2.1.1) with  $Z = 0$ , may be solved using Monte-Carlo simulation<sup>[Van81]</sup>. This numerical technique consists, in the present context, of stochastically generating a large number ( $N_{MC}$ ) of particle trajectories based on a specified plasma background  $\mathbf{U}(\mathbf{X})$  and atomic/molecular cross-sections. As a consequence of the statistical law of large numbers, for  $N_{MC} \gg 1$  the probability distribution obtained by averaging over the simulated trajectories will approach the exact solution of the kinetic equation, with an error proportional to  $1/\sqrt{N_{MC}}$ .

Let us consider one such neutral particle trajectory. A neutral  $H_2$  molecule is created at some location  $\mathbf{x} = (r, s, \phi)$  and velocity  $\mathbf{v} = (v_r, v_s, v_\phi)$  with a probability  $Pr^{H_2}(\mathbf{x}, \mathbf{v})$  determined by: a) the ion flux to the surface  $\Gamma_0(r)$ , b) the rate of volumetric recombination  $S_{\text{rec}}(\mathbf{x})$ , c) the wall, target and plasma temperatures  $T_{\text{wall}}(s), T_0(r), T_i(\mathbf{x}), T_e(\mathbf{x})$  (we will work on a per particle basis, so that  $\int d\mathbf{x} d\mathbf{v} Pr^{H_2}(\mathbf{x}, \mathbf{v}) = 1$ ; to obtain actual magnitudes we would multiply the results by a given source strength). If an atom is launched from (born at) the target,  $|\mathbf{v}|$  is chosen according to  $T_0$  and its direction according to some forward peaked

angular distribution<sup>[Poa85]</sup>, eg.  $\cos^2\theta$ ; if it is launched from the plasma,  $|v|$  is determined by the Franck-Condon energy spectrum and its direction has a nearly isotropic angular distribution<sup>[Jan95]</sup>. The trajectory is constructed by explicitly updating  $\mathbf{x}$  and  $\mathbf{v}$  through small time intervals  $\Delta t$ ,  $\mathbf{x}^{n+1} = \mathbf{x}^n + \mathbf{v}^n \Delta t$ , where  $n$  denotes the time stage. For neutral particles,  $\mathbf{v}$  is only changed by a collision or reaction with another particle (charged or neutral); locally calculated mean free paths determine the probability that a particular interaction takes place in the small interval  $\Delta x$ . At each time stage, this is simulated by a uniform random variable  $\xi \in [0,1]$  with corresponding branching ratios. If a scattering event does occur, the new velocity  $\mathbf{v}'$  is obtained by simulating the kinematics of the collision with appropriate random variables. If the molecule is dissociated into two H atoms, each of these is then followed in turn. A trajectory is terminated when a neutral particle is either ionized or absorbed by the wall.

The final probability  $Pr_{i,j}^a$  that a neutral particle of species 'a' is found in cell  $X_{i,j}$  (sum over grid equals unity,  $\sum_{i,j} Pr_{i,j}^a = 1$ ) and the cell average  $\langle \psi^a \rangle_{i,j}$  of any trajectory related quantity  $\psi^a$ , may be obtained in terms of integrals of a cell based delta function  $\delta[\mathbf{x}_k, X_{i,j}]$  over  $N_{MC}^a$  trajectories of species 'a' which we denote by  $\{\mathbf{x}_k(t), \mathbf{v}_k(t) | k = 1, \dots, N_{MC}^a\}$ ,  $a = \{H_2, H\}$ ,

$$Pr_{i,j}^a = \frac{1}{N_a} \sum_{k=1}^{N_a} \frac{1}{\tau_k} \int_0^{\tau_k} dt \cdot \delta[\mathbf{x}_k(t), X_{i,j}] \quad \delta[\mathbf{x}_k(t), X_{i,j}] \equiv \begin{cases} 1, & \mathbf{x}_k(t) \in X_{i,j} \\ 0, & \mathbf{x}_k(t) \notin X_{i,j} \end{cases} \quad (3.3.1)$$

$$\langle \psi^a \rangle_{i,j} = \frac{1}{Pr_{i,j}^a} \cdot \frac{1}{N_a} \sum_{k=1}^{N_a} \frac{1}{\tau_k} \int_0^{\tau_k} dt \cdot \psi^a[\mathbf{x}_k(t), \mathbf{v}_k(t)] \cdot \delta[\mathbf{x}_k(t), X_{i,j}]$$

Multiplying  $Pr_{i,j}^a$  by a given source strength and dividing by cell volume  $2\pi R_{i,j} A_{i,j}$  we obtain the number density  $n_a(\mathbf{X})$ , velocity  $\mathbf{u}_a(\mathbf{X}) = \langle \mathbf{v}_a \rangle$  and temperature  $T_a(\mathbf{X})$ ,  $3T_a/2 = m_a \langle v_a^2 \rangle / 2$ , for both molecular,  $a = H_2$ , and atomic,  $a = H$ , hydrogen. This approach is equivalent to calculating macroscopic quantities  $\langle \psi_a \rangle$  by integrating over phase-space density  $\rho(\mathbf{x}_k, \mathbf{v}_k | k = 1, \dots, N^a)$ , (A.2.12), since the set of  $N_{MC}^a$  trajectories  $\{\mathbf{x}_k(t), \mathbf{v}_k(t) | k = 1, \dots, N_{MC}^a\}$  is an estimate of  $\rho(\mathbf{x}_k, \mathbf{v}_k | k = 1, \dots, N^a)$ , which becomes exact as  $N_{MC}^a \rightarrow N^a - 10^{23}$ . Line integrals over the step-wise linear trajectories may be replaced by Riemann sums ( $|\Delta x_k / \Delta x_{i,j}| > 1$  is required) at the cost of a reduction in accuracy but with savings in memory storage and quadrature time.

$$Pr_{i,j}^a = \frac{1}{N_a} \sum_{k=1}^{N_a} \frac{1}{\tau_k} \sum_n \Delta t^n \cdot \delta[\mathbf{x}_k(t^n), X_{i,j}] \quad (3.3.2)$$

For the purpose of calculating discrete events, such as excitation or ionization reactions, it is simpler to cumulatively store all the instances of a given event  $\beta$  in a grid-based array  $N^\beta(\mathbf{X})$ , which divided by  $N_{MC}$  gives the average number of events in a given cell per particle launched. Combining event densities  $n_\beta(\mathbf{X})$  with calculated  $n_a(\mathbf{X})$ ,  $\mathbf{u}_a(\mathbf{X})$  and  $T_a(\mathbf{X})$ , the atomic-molecular sources  $\{S_{iz}(\mathbf{X}), S_{cx}(\mathbf{X}), Q_{qe}(\mathbf{X}), Q_{qi}(\mathbf{X})\} \rightarrow Q_S(\mathbf{X})$  may be estimated. Again, as  $N_{MC} \rightarrow \infty$ , all the estimates become exact; in practice  $N_{MC} \sim 10^4$  is usually sufficient to achieve  $\sim 1\%$  error in scalar quantities (vector quantities, such as

$u_s$ , always contain larger errors for the same  $N_{MC}$ ). Several neutral transport codes based on Monte-Carlo techniques are commonly used in the fusion community (EIRENE<sup>[Rei84]</sup>, DEGAS<sup>[Ron92]</sup>, NIMBUS<sup>[Cup84]</sup>). All the results presented here were obtained with the NIMBUS code, although EIRENE has also been run as validation.

The Monte-Carlo technique may also be used to simulate impurity (neutral and ion) transport in the edge plasma, with the aim of calculating the fraction of target impurity atoms reaching the core, their redeposition rate and the role they play in plasma detachment and MARFE formation. The trajectories of neutral impurity species (entering the plasma from the target as a result of physical or chemical sputtering with a probability determined by experimentally obtained yield expressions, and a specified velocity distribution) may be followed in the same way as the hydrogenic neutrals. After ionization, the equation of motion (A.2.3) of an impurity ion (whether atomic or molecular) becomes,

$$m_Z \frac{dv^Z}{dt} = Ze(\mathbf{E} + v^Z \times \mathbf{B}) + \mathbf{F}_{||}^Z + \mathbf{F}_{\perp}^Z \quad (3.3.3)$$

where the forces on an impurity atom due to collisions with hydrogenic (field) ions,  $\mathbf{F}_{||}^Z$  and  $\mathbf{F}_{\perp}^Z$ , may be obtained from plasma kinetic theory<sup>[Rei97]</sup>, cf. (A.2.30-37). Assuming a shifted Maxwellian impurity ion velocity distribution  $f_i^Z(v)$ , the parallel forces may be expressed in a fluid-like form<sup>[Sta95]</sup>,

$$\mathbf{F}_{||}^Z = -\frac{I}{n_Z} \nabla_{||} p_Z + m_Z \frac{u - v_{||}^Z}{\tau_s} + \alpha_e \nabla_{||} T_e + \beta_i \nabla_{||} T_i \quad (3.3.4)$$

The first term of this equation is the impurity pressure gradient force; the second term is the friction force on the impurity ions moving with along- $\mathbf{B}$  fluid velocity  $v_{||,z}$  exerted by the background ions moving with parallel fluid velocity  $u$  ( $\tau_s$  is the stopping time); the final two terms are the electron and ion temperature gradient forces, which arise because Coulomb collisions are more effective for colder particles, (the electrons and H<sup>+</sup> ions striking the impurity ion from the colder side, give it more momentum than do the hotter particles striking from the opposite side). In principle each of the above forces can act in either direction – toward or away from the solid target. However, in the simplest case the plasma flows toward the target at all points and thus the frictional force tends to suppress divertor leakage of impurities. The temperature usually rises away from the target,  $\nabla_{||} T > 0$ , so that the T-gradient forces push the impurity ions in the upstream direction, tending to *increase* divertor leakage. The impurity pressure-gradient force generally acts in both directions, away from the location where the ions are created by neutral ionization. The pressure gradient force can be interpreted on an individual ion basis as *parallel diffusion* and may be treated as a random-walk problem (the parallel velocity of the ion is changed at each time step  $\Delta t$  by  $\pm (T_z/m_z)^{1/2} (2\Delta t/\tau_{||})^{1/2}$ , where  $\tau_{||}$  is the Coulomb parallel collisional diffusion time, and the sign is chosen randomly). The cross-field force  $\mathbf{F}_{\perp}^Z$  may be expressed with the help of an anomalous diffusion coefficient  $D_{\perp}^Z$ , and the update to the ion velocity is also constructed in a Monte-Carlo manner.

$$v_{||} = v_{||,0} + \frac{F_{||}^z}{m_z} \Delta t + \sqrt{\frac{2D_{\perp}^z}{\Delta t}} \xi_{\perp} \quad (3.3.5)$$

The transport of impurity atoms, either sputtered from the wall or injected into the plasma, may be followed in this way through successive ionization stages: eg. for Carbon,  $C^0 \longleftrightarrow C^+ \longleftrightarrow C^{2+} \leftarrow \dots$ . The impurity transport results presented in this thesis use the DIVIMP code<sup>[Sta95]</sup>, based on the principles discussed in this section.

### 3.4 Iterative Stability: Source Relaxation

In §3.2, we saw that numerical stability of the CFD method requires knowledge of the neutral source Jacobian,  $(\partial Q_3 / \partial U)$ . During CFD convergence the sources  $Q_3$  remain constant,  $(\partial Q_3 / \partial U) = 0$ , but change abruptly after a call to the neutral M-C code from which new  $Q_3$  are returned. If the change in  $Q_3$  is too large, instability may result. Since the sources are calculated using a Monte-Carlo method,  $(\partial Q_3 / \partial U)$  is not known a priori. A numerical estimation of this Jacobian requires a differential increment of each spatial variable, and becomes prohibitively expensive. A more efficient method of assuring CFD stability consists in relaxing the sources in such a way that the plasma quantities change sufficiently slowly. In general, having found the new MC sources, we update the next stage sources as,

$$Q_3 = (1 - \epsilon_3) Q_3^{old} + \epsilon_3 Q_3^{new} \quad \epsilon_3 = \epsilon_3[U] \ll 1 \quad (3.4.1)$$

The exact form of  $\epsilon_3[U]$  may be optimized to give the quickest convergence without loss of stability. Clearly, the final solution does not depend on the form of  $\epsilon_3[U]$ , since  $Q_3^{new} - Q_3^{old}$  in steady state. Due to the stochastic nature of Monte-Carlo simulation, we expect some variation ( $-1/\sqrt{N_{MC}}$ ) between successive  $Q_3^{new}$  even if plasma background  $U$  remains constant. In addition, the M-C part of the iterative loop is more computationally expensive than the CFD part. The time efficiency of the iterative loop may be optimized (ie. the ratio  $t_{MC}/t_{CFD} > 1$  reduced), by performing MC runs with fewer particles, and compensating for the larger oscillation in  $Q_3^{new}$  by reducing the relaxation factor  $\epsilon_3[U]$ . The effective number of MC particles used to obtain the final source  $Q_3$  may be estimated as  $N_{MC}/\epsilon_3[U]$ . Typically,  $\epsilon_3[U]$  was found by requiring that  $Q_3^{new}$  change by at most  $\sim 10\%$  per iteration.

### 3.5 Cross-field Sources: Diagnostic Variance Minimization

The final step in the iterative cycle consists of adjusting the cross-field sources  $\mathbf{Q}_\perp$  according to the DVM method, in order to best match given diagnostic data. In §2.5.3, the DVM technique was presented as a multi-variable optimization problem. The radial dependence of  $\mathbf{U}$  and  $\xi$  is discretized when this problem is projected onto the poloidal grid  $\mathbf{X}$ :  $\xi(r) \rightarrow \xi_i$ ,  $\mathbf{U}(r,0) \rightarrow \mathbf{U}_{i,0}$ ,  $\mathbf{U}(r,L_\theta) \rightarrow \mathbf{U}_{i,N_\theta+1}$ , where  $i$  refers to the computational ring  $\mathbf{X}_i$ . Depending on the number of non-degenerate free parameters  $N_\alpha$  and the number of diagnostic constraints  $N_{\text{diag}}$ , this problem may be under ( $N_\alpha < N_{\text{diag}}$ ), well ( $N_\alpha = N_{\text{diag}}$ ) or over ( $N_\alpha > N_{\text{diag}}$ ) constrained<sup>[Zwi89]</sup>. In the first case, there exists a family of  $\{\xi_i\}$  for which  $\|\Xi\| = 0$ , in the second case, only one such  $\xi_i$ , and in the third case, none at all (in all three cases a minimum of  $\|\Xi\|$  may be found, which does not vanish only if the problem is ill posed). We will assume here that the problem is in fact well posed (although the analysis which follows applies regardless of this assumption) as is the default choice of  $\xi_i$  and  $\xi_i^{\text{diag}}$  for target Langmuir probe data. The particular path taken by the control variables  $\xi_i$  should not effect the final state, provided that all components of  $\xi_i$  and  $\xi_i$  are involved in the optimization. We can construct an increment  $\Delta\xi_i$  by expanding  $\xi_i[\Xi_i]$  for small  $\Delta\Xi_i$  and applying the Newton method<sup>[Hui74]</sup>,

$$\Delta\Xi \approx \left( \frac{\partial \Xi}{\partial \xi} \right) \cdot \Delta\xi = \mathbf{J}_\Xi \Delta\xi \quad \Delta\xi = \mathbf{J}_\Xi^{-1} \Delta\Xi \quad \Delta\Xi = -\epsilon_\Xi \Xi_i \quad (3.5.1)$$

with  $\epsilon_\Xi$  acting as a small damping constant. From (2.4.13-16) we note that,

$$\begin{aligned} \left( \frac{\partial |\Gamma_0| + |\Gamma_{N_\theta+1}|}{\partial \xi^{(1)}} \right)_Q &> 0 & \left( \frac{\partial |\Gamma_0|}{\partial \xi^{(2)}} \right)_Q &> 0 & \left( \frac{\partial |\Gamma_{N_\theta+1}|}{\partial \xi^{(2)}} \right)_Q &< 0 \\ \left( \frac{\partial |T_{e,0}|}{\partial \xi^{(3)}} \right)_Q &> \left( \frac{\partial |T_{e,0}|}{\partial \xi^{(4)}} \right)_Q & \left( \frac{\partial |T_{e,0}|}{\partial \xi^{(3)}} \right)_Q &> 0 & \left( \frac{\partial |T_{e,N_\theta+1}|}{\partial \xi^{(4)}} \right)_Q &> 0 \end{aligned} \quad (3.5.2)$$

From which we can construct an approximation to the inverse of  $\mathbf{J}_\Xi$  and write down the final form

$$\Delta\xi_i = \epsilon_\Xi \cdot \xi_i \cdot \begin{pmatrix} -\Xi_i^{(1)} - \Xi_i^{(2)} \\ -\Xi_i^{(1)} + \Xi_i^{(2)} \\ \Xi_i^{(3)} \\ \Xi_i^{(4)} \end{pmatrix} \quad \epsilon_\Xi = \begin{pmatrix} 0.2 \\ 0.02 \\ 0.2 \\ 0.2 \end{pmatrix} \quad (3.5.3)$$

in which departures from  $\Gamma_0^{\text{diag}}$  and  $\Gamma_L^{\text{diag}}$  are used to increment cross-field particle and momentum sources (if  $\Gamma_0^{\text{diag}} = \Gamma_L^{\text{diag}}$ , then  $\mathbf{Q}_\perp^{(2)} = 0$  is expected and observed) and departures from  $T_{e,0}^{\text{diag}}$  and  $T_{e,L}^{\text{diag}}$  to

increment cross-field energy sources (same for electrons and ions). This simple method has proved efficient for the default choice of  $\zeta^{diag}$  for target Langmuir probe data and any norm  $\|\cdot\|$  as long as  $\|\Xi\|$  vanishes at its minimum. The general Newton method may prove superior for larger diagnostic comparison sets.

As mentioned in §2.4.3, for strong volumetric recombination, it is useful to impose an additional upstream constraint, which in this study has been chosen as the upstream density on the separatrix,  $n_u^{sep}$ . To impose this constraint, the growth of the radiative density peak must be controlled, which amounts to limiting the growth of recombination. Due to an exponential dependence of  $\langle\sigma v\rangle_{rec}$  on  $T_e$  and the added effect of  $n \propto 1/T$  due to pressure conservation, the growth of  $S_{rec} = n_e n_i \langle\sigma v\rangle_{rec}$  may be effectively opposed by small changes ( $-0.1$  eV) in the target temperature. This method has been implemented within a feedback loop similar to the one discussed above, with  $\Xi^{(5)}$  measuring the departure from  $n_u^{sep}$  and  $\Delta\zeta^{(5)}$  containing an update to target  $T_e$ . The constraint is one sided, with upstream density not allowed to exceed  $n_u^{sep}$ , but allowed to fall below this limiting value.

#### 4. Results

In the previous two chapters, a model of the edge plasma was developed, and a numerical method of solving the model equations was outlined. In the present chapter, these equations are solved in a variety of scenarios: a) the transition from attached to detached conditions is studied via a series of solutions ranging in target  $T_e$  from 32 eV to 0.5 eV, and  $\Gamma_0 = 10^{23}$  to  $10^{24} \text{ m}^{-2}\text{s}^{-1}$ , b) the sensitivity of the solutions to several modeling assumptions is examined for conductively limited (8 eV) and detached (0.5 eV) conditions, c) the OSM2/NIMBUS solution is compared with a 2-D edge code EDGE2D/NIMBUS by using the target values obtained with the latter code as the diagnostic target data for OSM2, and d) an attempt to model experimental measurements is made by comparing the OSM2 simulation with reciprocating probe data on the JET tokamak. As part of the validation procedure the results of (a) above are examined in detail: the sources are broken down into the neutral, cross-field, plasma and flux-expansion contributions, the flux balances of mass, momentum and energy are divided into their hyperbolic (convective) and elliptic (viscous, conductive) components, and the OSM2 solutions are compared with the two-point model predictions (2.4.6); the comparison with the EDGE2D code, point (d) above, may also be viewed as a validation step. Solutions are displayed on two types of figures: along- $\mathbf{B}$  plots and poloidal contour plots. The former provide target-to-target flux-tube profiles at four radial locations in the SOL and contain electron temperature  $T_e$  [eV], ion temperature  $T_i$  [eV], plasma flow  $n_u$  [ $10^{23} \text{ m}^{-2}\text{s}^{-1}$ ], Mach number  $M$  [-], electron density  $n_e$  [ $10^{20} \text{ m}^{-3}$ ], and total pressure  $p_{tot} = F^{(2)} = p_e + p_i + \rho u^2$  [Pa]; the target-to-target (connection) lengths for the four chosen flux tubes, denoted by their ring numbers (ir=8 is the first SOL ring beyond the separatrix), and the locations of the inner and outer X-points are given below,

	$L_\theta$ [m]	$(s_\theta^X/L_\theta)_{out}$	$(s_\theta^X/L_\theta)_{in}$
ir = 8	119	0.1345	0.843
ir = 10	98	0.0874	0.886
ir = 12	92	0.0706	0.900
ir = 14	88	0.0730	0.893

The latter plots offer a poloidal view of the divertor region showing  $T_e$  [eV],  $T_i$  [eV],  $n_e$  [ $\text{m}^{-3}$ ],  $M$  [-], atomic hydrogen density  $n_H$  [ $\text{m}^{-3}$ ], molecular hydrogen density  $n_{H2}$  [ $\text{m}^{-3}$ ], ionization rate  $S_{iz}$  [ $\text{m}^{-3}\text{s}^{-1}$ ], recombination rate  $S_{rec}$  [ $\text{m}^{-3}\text{s}^{-1}$ ], charge exchange momentum loss rate  $Q_{cx}$  [Pa/m], electron power loss rate  $Q_{qe}$  [ $\text{W m}^{-3}$ ], average H atom energy  $E_H$  [eV], rate of  $H_\alpha$  line emission from neutral hydrogen  $H_\alpha$  [ $\text{m}^{-3}\text{s}^{-1}$ ], densities of neutral carbon and its first four ionization states  $C^0, C^+, \dots, C^{++}$  [ $\text{m}^{-3}$ ] and the total energy radiated by all carbon atoms/ions  $Q_C$  [ $\text{W m}^{-3}$ ] (carbon transport was calculated using the DIVIMP Monte-Carlo code using the hydrogenic plasma/neutral background obtained from the OSM2/NIMBUS calculation; only carbon originating at the targets was considered in order to better isolate the effect of detachment on impurity transport; both physical and chemical sputtering were included). As mentioned in §3.2, two grids were used to generate the solution: the neutral sources are generated on the fixed poloidal (coarse) grid, while the CFD solver is converged on the adjustable, along- $\mathbf{B}$  (fine) grid; since the mapping of sources and plasma variables between the two grids results in partial loss of information, all variables are stored on both grids. In the figures below, the poloidal contour plots refer to the coarse grid while the along- $\mathbf{B}$  plots refer to the fine grid. The largest difference between these two solutions usually occurs within the first cell of the coarse grid, which is too crude to properly resolve the near target gradients (see §4.1 below).

#### 4.1 Attached – Detached Transition

In the first set of solutions, the gradual onset of divertor plasma detachment (discussed in §2.4 in terms of the four experimental regimes) is simulated by fixing the target particle flux  $\Gamma_0 = n_0 u_0 = 10^{23} \text{ m}^{-2}\text{s}^{-1}$  and progressively lowering the target temperature  $T_{e,0} = \{32, 16, 8, 4, 2, 1, 0.5\} \text{ eV}$ ; the magnetic geometry corresponds to an L-mode discharge (shot 34859) on the JET tokamak with a MARK-I divertor configuration. Both  $\Gamma_0$  and  $T_{e,0}$  are specified as radially uniform and equal at both targets (including the private flux region); the uniform radial profiles, obviously not physical for power entering the SOL from the core across the separatrix, were chosen to emphasize that radial variations in the final solution are caused by magnetic geometry and neutral transport rather than by radial variations of target conditions, ie. that the iterated solution is inherently 2-D, rather than a collection of 1-D along- $\mathbf{B}$  solutions. The choice of symmetric boundary conditions was made for similar reasons, in particular to draw attention to asymmetries generated by the magnetic field geometry. The default OSM2 model was used for all cases in §4.1, with two modifications: a) the private flux-region was treated in a simplified manner: plasma variables were linearly interpolated on each flux tube, based on the specified values at the targets, b) the flux-tube integrated input power was not allowed to increase radially away from the separatrix; for some of the cases in this section, this physically motivated constraint, produced radially decaying target temperature profiles.

The first case ( $T_{e,0} = 32 \text{ eV}$ , Fig.4.1.1-5) demonstrates all the features of a sheath limited SOL. The temperature is nearly uniform along each flux tube, with  $T_e$  and  $T_i$  decoupled due to weak collisionality ( $\tau_{ei} \propto T_e^{3/2}$  is too small at these conditions to relax  $T_e$  and  $T_i$  to a common value;  $T_i > T_e$  due to smaller ion conductivity  $\kappa_i \ll \kappa_e$ ); the fact that  $T_{i,0}/T_{e,0} \sim 2$  reflects the difference in the sheath boundary conditions for ions and electrons (same input power for both species). Plasma flow  $nu$  and Mach number  $M$  decay exponentially away from the targets with a characteristic length for ionization,  $\lambda_{iz} \ll L_\parallel$  (the flow turns sonic at the sheath-edge,  $M_0 = 1$ ; since the scale of the sheath is so much smaller than the length of a flux tube, this is not clear on the full scale figures, but can be seen on the close-ups near the inner target, eg. Fig.4.1.10), leveling off upstream to  $\sim 20\%$  of  $\Gamma_0$  in the direction of the outer target; due to the short penetration length, only  $\sim 10\%$  of the neutrals reach the core,  $f_{iz}^{\text{core}} = 0.11$ . The stagnation point occurs near the inner target (not far from the inner X-point,  $s_{ii}^{\Gamma=0}/L_\parallel \sim 0.8$ ) due to poloidal asymmetry in the magnetic field, although the boundary conditions are symmetric (the asymmetry is related to the dominant toroidal  $\mathbf{B}$ -field, which varies with the major radius as  $1/R$ ); this effect can be offset by raising the plasma flow at the inner target (or by inclusion of drift effects) which shifts the stagnation point towards the mid-point. Both  $n_e$  and  $p_{tot}$  reach their maximum values very close to the target ( $s_{peak}/L_\parallel \sim 0.993$ ,  $n_{peak}/n_e \sim 2.15$ ; all values refer to the inner peak on the separatrix flux tube) and remain fairly constant along each flux tube; in solutions with different target pressures at the inner and outer targets (say,  $T_{e,0} = 32 \text{ eV}$  and  $T_{e,L} = 8 \text{ eV}$ , not shown)  $p_{tot}$  changes continuously between the two target values. Along- $\mathbf{B}$  variations in  $n_e$  and  $p_{tot}$ , most noticeable beyond the outer X-point, are caused by an ionization peak in this region, which modifies the  $nu$  profile and gives rise to a local viscous flux gradient,  $\mathbf{G}^{(2)} = -\eta_{||} \nabla_{||} \mathbf{u}$ ; the drop of  $p_{tot}$  away from the targets is due entirely to parallel viscosity. Flux expansion  $Q_B^{(2)}$  plays a relatively small role in the momentum balance; its relative contribution is studied in §4.2. The weak radial gradients seen in Fig.4.1.1, indicate radial uniformity of the neutral sources; thus the presence of a finite  $\nabla_{\perp} T_e = dT_e/dr < 0$  arises due to a radially decaying input (deposited) power

profile,  $dP_{in}/dr < 0$ . The unphysical increase in upstream density away from the separatrix is a consequence of the unphysical choice of uniform radial target profiles (a more physical scenario with radially decaying boundary conditions will be considered in §4.2-4). The relatively low upstream density ( $< 10^{13} \text{ m}^{-3}$ ) as compared with typical experimental values ( $1-3 \times 10^{19} \text{ m}^{-3}$ ) is a consequence of the relatively low  $\Gamma_0$  (the choice of low  $\Gamma_0$  was made to illustrate a particular type of detached transition, in which the detached ionization front reaches the X-point and develops into a MARFE-like radiative region). Higher density cases ( $\Gamma_0 = 3 \times 10^{23}$  and  $10^{24} \text{ m}^{-2}\text{s}^{-1}$ ) for attached (8 eV) and detached (0.5 eV) conditions are presented near the end of §4.1

Source profiles, Fig. 4.1.2, reveal exponential decay away from the targets, characteristic of a short neutral penetration length (the double step function profiles of  $Q_\perp^{(3)}$  and  $Q_\perp^{(4)}$ , which are clearer for lower  $T_e$  cases, eg. Fig.4.1.9, represent the input power and are divided into the inboard and outboard parts; their asymmetry reflects the greater volumetric energy losses  $Q_{qe}$  next to the inner target). The power balance shows the dominance of conduction over convection, especially in the electron channel, while the momentum balance indicates a presence of charge-exchange losses even at  $\sim 70$  eV (although their net effect is no larger than that of the viscous flux). It should be noted that conservation of mass, momentum and energy, is equivalent to convergence of the solution set (2.1.22); typically  $|R_{max}\Delta t/U| < 10^4$ . Poloidal contours, Fig.4.1.3-4, provide a 2-D representation of the along-B profiles, Fig.4.1.1-2. The core density and temperature were specified by assuming a constant radial increment of 250 eV and  $5 \times 10^{18} \text{ m}^{-3}$  per core ring (flux surface). The ionization front  $S_{iz}$  responsible for the majority of the electron cooling  $Q_{qe}$  and the  $H_\alpha$  line emission is clearly ‘attached’ to the target (recombination is negligible); the density of neutral species also peaks in the vicinity of the target (due to short penetration lengths) with atoms penetrating further than molecules. As a result of thermalizing collisions, the average neutral energy  $E_H$  approaches the average ion energy  $3T_i/2$ . In Fig.4.1.5, the Monte-Carlo simulation of carbon transport using the DIVIMP code is displayed. The carbon neutrals originating at the target are quickly ionized such that only the  $C^{4+}$  penetrates significantly beyond the X-point, and only the  $C^{5+}$  and  $C^{6+}$  states (not shown) reach the inner core. Most of the carbon radiation coincides with the  $C^{2+}$  ionization state, peaking next to the target (the default model of  $Q_C = f_z Q_{qe}$  with  $f_z = 1$  gives a rough estimate for the impurity radiation, although  $Q_C$  is less extended than  $Q_{qe}$ ).

The next two cases (16 eV, Fig.4.1.6-7; 8 eV Fig.4.1.8-12) demonstrate a transition to the conductively limited regime, characterized by the presence of strong  $T_e$  gradients in the cool, near target region ( $T_e$  is conductively dominated,  $T_e \propto s_{\parallel}^{2/7}$ , on the entire spatial domain);  $T_e$  and  $T_i$  remain decoupled with  $T_i/T_e \sim 2$ . The plasma flow  $n\mathbf{u}$  and Mach number  $M$  decay less rapidly (with a longer half-length) due to lower ionization rate and stronger neutral penetration (the position of the stagnation point is unaffected, since changes in boundary conditions are symmetric). The density peak separates from the target,  $s_{peak}/L_{\parallel} \sim 0.982$ , with a decrease in the relative peak-to-target density ratio,  $n_{peak}/n_t \sim 1.4$ . In contrast to the sheath-limited case, pressure rises away from the target as a results of charge-exchange collisions overcoming the viscous flux, Fig.4.1.9. Along-B variations in  $p_{tot}$  near the outer X-point are also suppressed by the larger  $Q_{CX}$ . An increase in the radial  $T_e$ ,  $T_i$  and  $p_{tot}$  gradients close to the separatrix indicates stronger plasma-neutral interactions  $Q_S$  on the near-separatrix flux tubes requiring larger input power (this may be explained by a weaker poloidal field in the vicinity of the X-point ( $B_\theta \rightarrow 0$ ,  $B_\phi \rightarrow B$ ), which decreases of the field line pitch angle,  $\tan^{-1}(B_\theta/B)$ ; consequently, field lines must traverse a longer distance to cover the same poloidal interval,  $s_{\parallel} = (B/B_\theta)s$ , and

an ion travelling along such a flux tube has a longer distance in which to interact with the neutral species contained in the region enhancing the plasma-neutral reactivity and producing larger neutral sources for the plasma,  $\mathbf{Q}_3$ ). The asymmetry in the input power is more pronounced due to stronger electron cooling near the inner target. Examining, Fig.4.1.9, we see that the plasma-neutral interaction  $\{S_{iz}, Q_{cx}, Q_{qe}\}$  region is more extended, although most neutral species remain confined to the divertor region with a maximum near the target; neutral species penetrate further due to lower  $S_{iz}$  allowing a larger fraction of neutrals to reach the core,  $f_{iz,core} \sim 0.22$ . The same is true of carbon atoms and ions, Fig.4.1.11, although the penetration of carbon ions is governed primarily by  $\nabla_i T_e$  forces; the radiative power departs somewhat from the  $Q_{qe}$  distribution, but has a comparable integrated value. In Fig.4.1.10-11, which are close-ups of Fig.4.1.8-9 in the vicinity of the inner target, the effect of grid coarseness is examined; it is seen that for attached solutions, the relatively coarse poloidal grid  $X$  is sufficient to resolve the near target gradients (the same will not be true for detached conditions as we will see in Fig.22-23 ahead).

Since the 8 eV case will be the object of a parametric sensitivity study in §4.2, it is worth commenting on the relative contributions of constitutive sources, Fig.4.1.9. In the mass and momentum equations, both  $\mathbf{Q}_\perp$  and  $\mathbf{Q}_B$  are small in comparison with  $\mathbf{Q}_3$ , that is  $S_{iz}$  and  $Q_{cx}$ . In the energy equations, net power enters the flux tube by cross-field transport with equal amounts deposited to each species; in addition, the ions gain energy from the along-B electric field  $E_{||}$ , while being cooled by equipartition collisions with the electrons (the latter effect dominates the plasma source,  $Q_p^{(3)} < 0$ , while  $Q_{qi} = 0$  is specified in the default model); electrons gain energy by equipartition and loose energy to  $E_{||}$  (with a net heating effect  $Q_p^{(4)} > 0$ ) and by atomic interactions,  $Q_{qe} < 0$ . Flux expansion sources redistribute the power along-B according to the variation of the total B-field ( $Q_B > 0$  beyond the outer X-point,  $Q_B < 0$  between the outer and inner mid-planes, and  $Q_B \ll Q_{qe}$  near the targets). As a consequence of the Mach dependent  $\gamma_i$ , the ion conductive flux  $\mathbf{G}^{(3)}$  vanishes at the targets, unlike the electron conductive flux  $\mathbf{G}^{(4)}$  which is comparable to the convective flux  $\mathbf{F}^{(4)}$ ; the dominance of conduction is most pronounced around the stagnation point at which convective fluxes approach zero.

The next three cases (4 eV Fig.4.1.13-14; 2 eV, Fig.4.1.15-17; 1 eV, Fig.4.1.18-19) demonstrate a gradual transition to weakly detached conditions. The separation of the density peak from the target ( $s_{peak}/L_{||} \sim 0.97 \rightarrow 0.96$ ,  $n_{peak}/n_c \sim 1.4 \rightarrow 2.6$ ,  $f_{iz,core} \sim 0.29 \rightarrow 0.44$ ) and total pressure loss become more pronounced ( $p_{tot,u}/p_{tot,l} \sim 1.5 \rightarrow 3.3$ ;  $Q_\perp^{(2)}, Q_B^{(2)} \ll Q_3^{(2)}$ ), especially on the separatrix flux tube. The region of neutral penetration, plasma-neutral interaction and high recycling progressively expands towards the X-point (that is, the ionization front moves away from the target with the consequent extension of the nu profile). The increase of peak density is reflected by a growing degree of over-ionization on the separatrix flux tube, as indicated by  $Q_\perp^{(1)} < 0$  ( $S_{rec}$  increases significantly, but remains small in comparison with  $S_{iz}$ ). This has two consequences: a) since  $Q_\perp^{(1)} \propto n_e$  in the default model,  $Q_\perp^{(1)} < 0$  leads to a net particle sink near the target and a local maximum in the plasma flow nu, b) combined with flux expansion, it also gives rise to a net particle sink in the upstream region, which tends to reduce the plasma flow nu (under more symmetric conditions these effects give rise to flow reversal, in which two additional stagnation points appear, such that plasma flows towards the targets in the innermost and outermost regions, and away from the targets in the upstream regions, cf. the higher density case below; flow reversal has also been predicted by 2-D codes and has been confirmed experimentally<sup>[16,197]</sup>; the potential of flow reversal to enhance impurity leakage into the core makes it important for fusion experiments). The dominant role of convection in the divertor region produces an inflection in the curvature of

the  $T_e$  profile and a transition to supersonic flow at the sheath edge. In the same region,  $T_i$  and  $T_e$  approach a common value due to higher collisionality and more effective energy equipartition at lower temperatures. The transport of carbon also increases due to colder divertor conditions; higher ionization states ( $C^{3+}$ ,  $C^{4+}$ ) concentrate along the divertor legs (extending from the target to the X-point), as does the radiated power density from carbon  $Q_C$  (the ratio of the maximum  $Q_C/Q_{qe}$  rises from 0.61 for the 8 eV case to 1.9 for the 1 eV case). The increase of impurity cooling is very important in detachment, eventually leading to the formation of a MARFE-like radiative region in the vicinity of the X-point ( $Q_Z$  is treated improperly in the default model which uses  $Q_Z = f_z Q_{qe}$ , since  $Q_{qe}$  is spatially much broader than  $Q_Z = Q_C$ ).

The 0.5 eV case, Fig.4.1.20-26, is an example of a detached plasma ( $p_{tot,v}/p_{tot,i} \sim 6$ ) without significant recombination. The trends outlined in the preceding paragraph have progressed further ( $s_{peak}/L_1 \sim 0.93$ ,  $n_{peak}/n_i \sim 8$ ,  $f_{iz,core} \sim 0.65$ ), with the ionization front, the density peak and the recycling region reaching the X-point. The most striking new feature is a plateau region in the  $T_e$  profile, in which conduction is negligible and nearly all the energy is carried by convection. The plateau electron temperature is more than twice the target  $T_e$  because of two physical mechanisms: a) the electrostatic sheath acts as a low energy filter for the electrons, allowing only the more energetic electrons to reach the target, and effectively cooling the near target plasma; this process is represented by the relatively high value of the sheath heat transmission coefficient for the electrons,  $\gamma_e \sim 5$ , in comparison to the purely convective value of  $\sim 2.5$ ; the corresponding kinetic boundary condition,  $F_0^{(4)} + G_0^{(4)} = 2.5 T_{e,0} \Gamma_0 - \kappa_e \nabla_i T_e = \gamma_e T_{e,0} \Gamma_0$  gives rise to a temperature gradient of  $(\nabla_i T_e/T_e)_0 = (\gamma_e - 2.5) \Gamma_0 / \kappa_e$  at the target, which requires  $T_e$  to increase away from the target as long as  $\gamma_e > 2.5$  (note that  $\gamma_e = 5$  results in  $F_0^{(4)} = G_0^{(4)}$ ; in the T-plateau region  $\nabla_i T_e/T_e \ll 2.5 \Gamma_0 / \kappa_e$  and convection dominates); assuming negligible sources in the target-plateau transition region, we have  $\Gamma_1 \approx \Gamma_0$  and  $2.5 T_{e,1} \Gamma_1 \approx \gamma_e T_{e,0} \Gamma_0$  where the subscript 1 denotes the T-plateau value; this leads to an estimate of  $T_{e,1}/T_{e,0} \approx \gamma_e / 2.5$ , which with  $\gamma_e = 5$  predicts a plateau temperature of twice the target value, b) the self-consistent plasma (pre-sheath) electric field  $E_1$ , largest in the near target region, transfers energy from the electrons to the ions, enhancing  $\nabla_i T_e$ . The above near target gradient occurs on a scale much shorter than the ionization length, and comparable to the collisional mean-free-path (for both 8 eV and 0.5 eV); the latter point is reassuring, since in any fluid-like description, the collisional length scale offers the lower limit to the resolution of any plasma quantity. The above arguments also justify the introduction of the adjustable fine grid, since the inadequacy of the coarse grid in resolving the near target gradients becomes evident, cf. Fig.4.1.22. In the T-plateau region, the plasma flow  $nu$  exceeds the target value with a noticeable peak in the  $nu$  profile; an effective particle sink due to over-ionization and cross-field sources is responsible for this inversion in the flow profile (recombination is present but comparatively small,  $\langle S_{rec} \rangle / \langle S_{iz} \rangle \sim 0.02$ , where  $\langle Q \rangle$  denotes a flux tube integral of  $Q$ ; in many early, and some more recent, explanations of detachment, recombination was proposed as the dominant process; this view would be discredited by the above solution (see also §4.2.2 where momentum loss persists even with  $S_{rec} = 0$ ). The creation of a cold, dense, convective, collisional and highly radiative region between the ionization front and the target is characteristic of advanced stages in plasma detachment. Poloidal contours show the extent of this region vis-à-vis the divertor geometry; the ionization front is seen to reach and bend around the X-point (the front can not extend into the core plasma since the neutrals are ionized shortly after entering the core). The refraction of the ionization front at the X-point may be viewed as an asymptote of plasma detachment, with the core

playing an increasingly dominant role henceforth; this interaction culminates in the formation of a dense, radiative (MARFE-like) region at the X-point (It should be emphasized that this thesis contains only steady-state results, with no information about temporal characteristics of the obtained solutions; the term 'evolution', appearing frequently below, refers to numerical convergence, rather than temporal evolution). The carbon atoms and ions are concentrated along the legs of the divertor and the X-point, radially peaking on the separatrix (max.  $Q_c/Q_{qe} = 1.35$ ); the expansion of the radiative region into the core would cause along-B transport on the core flux surfaces, as well as radial transport across the separatrix, neither of which are handled properly by the OSM approach.

A summary of the plasma values at the location of the inner density peak of the separatrix ring,  $ir=8$ ,  $(s_w/L_4)_{n,p}$ , is given below. Progressive separation from the target is accompanied by an extension of the convective region, increased over-ionization and penetration of hydrogen neutrals and carbon ions into the core.

$T_{e,L}$	$(s_w/L_4)_{n,p}$	$n_e/n_{e,L}$	$T_e/T_{e,L}$	$\Gamma/\Gamma_L$	$M/M_L$	$f_{iz}^{core}$	$f_{iz}^{(1)sep}$	$\langle S_{rec} \rangle / \langle S_{iz} \rangle$
32 eV	0.9926	2.16	1.0	0.55	0.25	0.11	0.85	$-10^{-4}$
16 eV	0.987	1.78	1.15	0.64	0.35	0.17	0.88	$-10^{-4}$
8 eV	0.982	1.41	1.27	0.73	0.46	0.22	0.93	$-10^{-4}$
4 eV	0.973	1.40	2.0	0.78	0.45	0.28	1.23	$-10^{-4}$
2 eV	0.965	1.75	2.73	0.92	0.35	0.37	1.50	$-10^{-3}$
1 eV	0.962	2.57	3.16	1.03	0.26	0.44	1.65	$-10^{-3}$
0.5 eV	0.933	7.8	2.6	1.2	0.11	0.65	1.80	0.015

The next four cases examine attached and detached solutions in the higher density range; the target particle flux is increased threefold and tenfold with respect to the 8 eV and 0.5 eV cases. As Fig.4.1.27-28 ( $\Gamma_0 = 3 \times 10^{23} \text{ m}^{-2}\text{s}^{-1}$ ,  $T_{e,0} = 8 \text{ eV}$ ) and Fig.4.1.29-30 ( $\Gamma_0 = 10^{24} \text{ m}^{-2}\text{s}^{-1}$ ,  $T_{e,0} = 8 \text{ eV}$ ) indicate, a warm plasma becomes progressively more attached as the density increases (steeper gradients of  $T_e$ ,  $T_i$ ,  $n_u$ ,  $M$ , and  $n_e$  near the target) due to a linear reduction of the neutral penetration length with density. The higher input power raises the upstream temperature and pressure, but the relative pressure drop remains roughly the same, that is viscous, at all densities. The ionization front, the electron cooling region and the carbon cloud are also pushed closer to the target ( $Q_c/Q_{qe} = 0.35$ ).

Higher density detached solutions are shown in Fig.4.1.31-32 ( $\Gamma_0 = 3 \times 10^{23} \text{ m}^{-2}\text{s}^{-1}$ ,  $T_{e,0} = 0.5 \text{ eV}$ ;  $n_u^{sep} \sim 10^{19} \text{ m}^{-3}$ ) and Fig.4.1.33-34 ( $\Gamma_0 = 10^{24} \text{ m}^{-2}\text{s}^{-1}$ ,  $T_{e,0} = 0.5 \text{ eV}$ ,  $n_u^{sep} \sim 3 \times 10^{19} \text{ m}^{-3}$ ); in both cases, the upstream separatrix density was constrained by the method discussed in §2.4.3 and §4.3.1, although for the  $3 \times 10^{23}$  case this constraint is only necessary during the evolution transient. We note that detachment appears mainly near the separatrix (often seen in experiments<sup>[Mar95, Pit97]</sup>). The increase of near target density has two consequences: a) reduction of neutral penetration, which leads to a translation of the reactive region towards the target, a shortening of the convective  $T_e$  plateau and a suppression of the supersonic flow into the sheath ( $M_0=1$ ), b) the appearance of significant volumetric recombination with  $S_{rec} >> S_{iz}$  at the density peak (the region of maximum  $S_{rec}$  is known as the recombination front) with the flux tube averages approaching unity,  $\langle S_{rec} \rangle / \langle S_{iz} \rangle \sim 0.1$  for  $\Gamma_0 = 3 \times 10^{23}$  and  $\langle S_{rec} \rangle / \langle S_{iz} \rangle \sim 0.5$  for  $\Gamma_0 = 10^{24}$ . The density peak, sometimes referred to as a plasma buffer, evolves due to a synergism of three physical processes: a) hydrogenic and

impurity radiation, which cool the divertor plasma, b) charge-exchange collisions, which remove along- $\mathbf{B}$  momentum from the plasma, and c) volumetric recombination, which increases the recycling rate between the ionization and recombination fronts. Recombination, though not responsible for pressure loss (since  $S_{\text{CX}} \gg S_{\text{rec}}$  nearly all momentum is removed by charge exchange collisions, even when  $\langle S_{\text{rec}} \rangle / \langle S_{\text{ix}} \rangle \sim 1$ ), plays a major role in this 'condensation' process by altering the along- $\mathbf{B}$  flow profile and the plasma energy balance ( $S_{\text{rec}}$  has a net cooling effect at lower density and a net heating effect at higher density). The above synergism has been studied in some detail, both theoretically and numerically, and is believed to be responsible for the experimentally observed unstable translation of the active region towards the X-point<sup>[Kra99]</sup>. It is instructive to note that the relative pressure drop  $p_{\text{tot},w}/p_{\text{tot},i}$  and peak-to-target density ratio  $n^{\text{peak}}/n_i$  increase only moderately with higher density, an increase which can be attributed more to  $S_{\text{rec}}$  than to  $\Gamma_0$ . If we consider that plasma-neutral interactions involve a product of neutral and plasma densities, and scale linearly with  $n_e$ , we would expect only those processes involving  $n_e^2$ , such as recombination, to lead to non-linearities in the degree of plasma detachment. The above two cases confirm this prediction. The appearance of flow reversal on the separatrix flux tube is related to a higher degree of over-ionization,  $Q_{\perp}^{(1)} < 0$ . Although the reversed flow is weak in absolute terms, the along- $\mathbf{B}$  variations of  $\mathbf{n}\mathbf{u}$  would be sufficient to cause strong flow-reversal if the inner particle flux was allowed to increase or if  $Q_{\perp}^{(1)}$  was assumed to have a weaker density scaling (hence a more uniform along- $\mathbf{B}$  profile; as mentioned in §2.4.3, strong over-ionization increases the sensitivity to  $Q_{\perp}^{(1)}$  which could lead to inaccuracies in the OSM2 solution; this point will be explored in §4.2.1 ahead). Finally, we note that the appearance of the peak in the separatrix  $p_{\text{tot}}$  profiles is a numerical rather than a physical effect. It is caused by loss of information while transferring the solution  $\mathbf{U}$  from the fine, along- $\mathbf{B}$  grid  $\mathbf{X}_f$  on which it is converged to the coarse, poloidal grid  $\mathbf{X}$  used for NIMBUS calculations. This is confirmed by comparing  $p_{\text{tot}}$  of Fig.4.1.31 which is based on grid  $\mathbf{X}$  with  $\mathbf{F}^{(2)}$  of Fig.4.1.32 which is based on  $\mathbf{X}_f$ ; the absence of the total pressure peak in the latter case, shows that grid coarseness introduces inaccuracy to the coupled OSM2/NIMBUS cycle. In the future, it would be desirable to refine the coarse Monte-Carlo grid adaptively in order to prevent such behavior (such adaptation is being developed as part of a separate Ph.D. project for the EIRENE poloidal grids generated by the SONNET magnetic code, and may be available for the OSM2/EIRENE code combination within the near future).

The final case in §4.1, Fig.4.1.35, shows an example of non-uniform radial target profiles ( $T_e$  and  $\Gamma_0$  decreasing roughly linearly across the target from 8 eV to 1 eV and  $10^{23} \text{ m}^{-2}\text{s}^{-1}$  to  $10^{22} \text{ m}^{-2}\text{s}^{-1}$ ); these profiles are somewhat more representative of experiment. Radial variations of  $T_e$ ,  $T_i$ ,  $\mathbf{n}\mathbf{u}$ ,  $n_e$  and  $p_{\text{tot}}$  clearly reflect the imposed boundary profiles; it is interesting to note the increase of radial  $\mathbf{n}\mathbf{u}$  gradients with temperature, caused by a shorter neutral penetration length. Carbon impurity transport is enhanced along the hotter separatrix flux tube, with a larger net penetration to the core.

In concluding this section, let us compare the above solutions with the predictions of the two-point model, discussed in §2.4.3. This study may be considered as part of the validation process, which along with procedural transparency and code documentation, is essential for providing the reader/user with a sufficient degree of confidence in code results (the alternative, a black box approach, is rarely conducive to good science, while having the potential to create disastrous mistakes). The modified two-point model equations (2.4.6) with the target and upstream plasma conditions obtained by the OSM2 solution, will be used to calculate the convective, radiative and pressure corrections

$(\delta_x, \delta_q, \delta_p)^{2PM}$ . The same corrections will then be estimated independently by examining the sources and fluxes of the OSM2 solution,  $(\delta_x, \delta_q, \delta_p)^{OSM}$  and the two sets of numbers will be compared for the attached-detached transition of §4.1. Based on (2.4.6) and the implied definitions, we may write the above corrections explicitly as,

$$\begin{aligned} \delta_p^{2PM} &\equiv \frac{P_{tot,s}}{P_{tot,u}} = \frac{[(I+M^2)n_e(T_e+T_i)]_s}{[(I+M^2)n_e(T_e+T_i)]_u} \\ \delta_p^{OSM} &\equiv \left( I + \frac{\int_0^{S_{IL,u}} Q^{(2)} ds_{||}}{P_{tot,s}} \right)^{-1} \quad (4.1.1) \\ \delta_x^{2PM} &\equiv \frac{T_{e,u}^{7/2} - T_{e,s}^{7/2}}{\frac{7}{4}(\frac{L}{2}P_{\perp})S_{||,u}} K_{e,0} \\ \delta_x^{OSM} &\equiv I - \frac{\int_0^{S_{IL,u}} F^{(3)} + F^{(4)} ds_{||}}{\int_0^{S_{IL,u}} F^{(3)} + G^{(3)} + F^{(4)} + G^{(4)} ds_{||}} \\ \delta_q^{2PM} &\equiv \frac{[\gamma_e T_e + \gamma_i T_i] n_e c_s M}{\frac{L}{2} P_{\perp}} \\ \delta_q^{OSM} &\equiv I - \frac{\int_0^{S_{IL,u}} Q^{(4)} ds_{||}}{\frac{L}{2} P_{\perp}} \quad P_{\perp} = \int_0^{L_u} Q_{\perp}^{(3)} + Q_{\perp}^{(4)} ds_{||} \end{aligned}$$

Table 4.1.1 contains a summary of inner target and upstream (mid-point) conditions for the solutions ranging from the sheath limited (32 eV) to detached (0.5) regimes, at four radial locations (the same flux tubes as in the figures,  $ir = 8, 10, 12, 14$ ). The trends already observed in the course of the section are well brought out by this summary: upstream conditions remain rather insensitive to even large changes in target conditions, in agreement with the predictions of the two-point model. Table 4.1.2 shows the input power  $P_{\perp}$ , the inner target heat flux  $q_{IL,L}$  and the comparison between the correction factors as defined in (4.1.1); inverse delta's are shown in order to increase accuracy. The observed trends also agree with the observations made earlier: radiative, charge exchange and convective contributions increase with lower target temperature and the onset of detachment. The agreement between the 2PM and OSM factors is very good for  $\delta_q$  (which indicates energy conservation in the CFD equations), reasonably good for  $\delta_p$  (slight differences can be attributed to viscous fluxes), and least good for  $\delta_x$  (convectional contribution is to be assumed uniform in the modified two-point model, while in fact it is confined to the recycling (divertor) region, so that  $\delta_x^{2PM} < \delta_x^{OSM}$ ; as expected, the discrepancy grows with detachment). The systematic error may also be attributed to the factor 7/4 in the denominator of  $\delta_x^{2PM}$  which corresponds to uniform power deposition: for the default X-point to X-point profile this factor takes on some value between 7/4 (uniform) and 7/2 (upstream). A slightly more direct comparison is shown in Table 4.1.3, where the upstream  $n_e$ ,  $T_e$  and  $(T_e+T_i)/2$  values of the OSM2 solution are compared with the simple (uncorrected,  $\delta_x^{OSM} = \delta_p^{OSM} = 1$ ) and corrected ( $\delta_x^{OSM}, \delta_p^{OSM}$  from Table 4.1.2) two-point model. We can conclude that the OSM2 solver broadly agrees with the corrected two-point treatment across a wide range of SOL conditions.

## 4.2 Sensitivity to Modeling Assumptions

The validation of any model requires an examination of the sensitivity of the solution to pivotal modeling assumptions. In the present context, this pivotal assumption is precisely the  $\mathbf{Q}_{\perp}[U]$  ansatz, discussed in §4.2.1. In addition, by changing a single parameter in a multi-variable problem we are able to isolate the effect of any physical process represented by the model equations, thereby examining its role in the overall behaviour of the system. The division of this section reflects the morphology of sources introduced in §3.4.5: the sensitivity to cross-field sources  $\mathbf{Q}_{\perp}$ , neutral sources  $\mathbf{Q}_3$ , plasma sources  $\mathbf{Q}_p$ , flux-expansion sources  $\mathbf{Q}_B$  and boundary conditions  $\{\gamma_e, \gamma_i\}$  is studied in turn. However, it should be stressed that while the sensitivity to  $\mathbf{Q}_{\perp}$  lies at the very heart of the matter, the sensitivity to the other sources does not (ie. it will not affect our conclusions regarding the validity of the OSM approach). Due to space limitations, only along- $\mathbf{B}$  plots are shown for each case considered, provided that noticeable departure from the default model has occurred; changes of key quantities are also summarized in Table 4.2.1. The study will focus on one attached (case A: 8 eV,  $10^{23} \text{ m}^{-2}\text{s}^{-1}$ ) and two detached cases (case B: 0.5 eV,  $10^{23} \text{ m}^{-2}\text{s}^{-1}$ ; case C: 0.5 eV,  $3 \times 10^{23} \text{ m}^{-2}\text{s}^{-1}$ ).

### 4.2.1 Sensitivity to cross-field sources, $\mathbf{Q}_{\perp}$ : the $\mathbf{Q}_{\perp}[U]$ ansatz

In the context of the OSM approach, as defined by (2.4.10), the crucial assumption is that plasma solution  $\mathbf{U}$  is only weakly sensitive to the formal (user specified) dependence of the cross-field sources on  $\mathbf{U}$ ,  $\mathbf{Q}_{\perp}[U]$ . This assumption which due to its pivotal importance has been named *the  $\mathbf{Q}_{\perp}[U]$  ansatz*, has already been examined in §2.4.3, where it was concluded that spatial distribution of the particle cross-field source  $\mathbf{Q}_{\perp}^{(1)}$  raises the largest question about the validity of the OSM approach. It is therefore appropriate that we begin our analysis at this point. In the default model,  $\mathbf{Q}_{\perp}^{(1)} \propto \mathbf{U}^{(1)} \propto n_e$  was assumed, corresponding to radial diffusion with a constant radial length. In Fig.4.2.1-2 the effect of assuming  $\mathbf{Q}_{\perp}^{(1)} \propto \text{constant}$  is examined. As expected, case A is virtually unaffected, with only slight changes to upstream flow ( $n_{\text{u}} \downarrow 5\%$ ) and density ( $n_{\text{u}} \uparrow 5\%$ ); the arrows indicate increase/decrease and are followed by per-cent changes. Case B is only mildly affected, with small changes in peak ( $n^{\text{peak}} \downarrow 20\%$ ,  $n_{\text{u}}^{\text{peak}} \downarrow 10\%$ ) and upstream ( $n_{\text{u}} \downarrow 20\%$ ,  $T_{\text{u}} \uparrow 20\%$ ) values, stronger along- $\mathbf{B}$  gradients in  $p_{\text{tot}}$  and  $n_{\text{u}}$ , and the appearance of weak flow reversal on the separatrix ring (as expected for a more uniform cross-field particle sink due to over-ionization,  $f_{\text{sep}}^{(1)} > 1$ ,  $\mathbf{Q}_{\perp}^{(1)} < 0$ ). This relative insensitivity, despite strong difference between  $\mathbf{Q}_{\perp}^{(1)} \propto n_e$  and  $\mathbf{Q}_{\perp}^{(1)} \propto \text{constant}$  (note that  $n^{\text{peak}}/n_{\text{u}} \sim 15$ ), is consistent with the conclusion drawn in §2.4.3, that the  $\mathbf{Q}_{\perp}[U]$  ansatz is satisfied for the mass transport equation provided that over/under-ionization is not excessive,  $f^{(1)} < 2$ . For case C, a weaker variation was adapted,  $\mathbf{Q}_{\perp}^{(1)} \propto n_e^{1/2}$ , which changes the max-min along- $\mathbf{B}$  variation of  $n_e$  from  $\sim 20$  to  $\sim 4.5$  (this choice was preferred at higher densities over the highly unphysical  $\mathbf{Q}_{\perp}^{(1)} \propto \text{constant}$ ). The results, Fig.4.2.3, show a pronounced increase in flow reversal and upstream  $T_{\text{i}}$ , accompanied by a reduction in the degree of detachment ( $p_{\text{tot},\text{u}}/p_{\text{tot},\text{c}} \downarrow 25\%$ ) for all SOL rings. Peak values of density and plasma flow remain roughly the same. We must conclude that as the degree of ionization increases beyond  $f^{(2)} > 2$ , the OSM2 solutions become sensitive to the assumed  $\mathbf{Q}_{\perp}^{(1)}[U]$  scaling, a conclusion which

has been anticipated by the earlier analysis of the  $Q_{\perp}[U]$  ansatz. However, we should qualify the above statement with two comments: a) the changes for case C, which are at most a factor of 2, are still within the margin of accuracy of most edge diagnostics, b) the adjustment of the spatial form of  $Q_{\perp}^{(1)}[U]$  has its equivalent in varying the assumed  $D_{\perp}$  values in 2D fluid codes (in both cases, the cross-field transport is the biggest unknown). In keeping with the DVM approach, additional upstream information should be used to adjust this scaling in such a way as to best match all the diagnostic data (both target and upstream); it is clear that for detachment, it is important to have input information both below and above the region of intense atomic interactions; the task of including this extended upstream data will be left for future refinements.

The sensitivity to the  $Q_{\perp}^{(2)}[U]$  dependence was investigated in a similar manner, Fig.4.2.4-6. As the results indicate, the effect of the cross-field momentum source is comparable to that of the particle source: weak for case A and B, and pronounced for case C (since the momentum source is introduced in the default OSM-DVM model in order to match the specified target flow patterns, we may expect its role to increase with the appearance of recombination which directly alters these patterns). We should however note, with self-consistent  $\Gamma_i$  data available at both targets, the cross-field momentum sources should remain relatively small.

The effect of changing the cross-field (deposited) power profile from the default, uniform double-step function (2.4.13) to a pressure dependent ( $Q_{\perp}^{(3)} \propto p_i$ ,  $Q_{\perp}^{(4)} \propto p_e$ ) double-step function is negligible, aside from a slight (<10%) decrease in  $n_e^{\text{peak}}$ , Fig.4.2.7-8. The same was found for a field dependent ( $Q_{\perp}^{(3)} \propto B$ ,  $Q_{\perp}^{(4)} \propto B$ ) double-step function (not shown). In all three cases, the asymmetry remains heavily shifted towards the inner side, with little alteration (<10%). Despite the highly artificial division into inner and outer regions (which could be removed by a linear variation), the plasma solution is remarkably continuous across the upstream mid-point. We can safely conclude that due to the  $\kappa_e \propto T_e^{5/2}$  scaling, the cross-field power scaling  $Q_{\perp}^{(3,4)}[U]$  does not significantly affect the final solution (irrespective of the degree of detachment).

#### 4.2.2 Sensitivity to neutral sources, $Q_S$

The effect of neutral sources, unlike that of cross-field sources, is not an issue touching on the question of the validity of the OSM approach (neutral and along- $B$  physics, including  $Q_S$ ,  $Q_p$ ,  $Q_B$  and  $\{\gamma_e, \gamma_i\}$ , may be progressively refined as superior atomic models become available). As a consequence, the following sections may be viewed as an exploration of the physics represented by the model equations, rather than as validation of the OSM approach as such.

The effect of turning off recombination is shown in Fig.4.2.10-11 (case A is not shown, since the change is imperceptible). Case B is virtually unaffected, with a slight drop of the density and plasma flow peaks ( $n^{\text{peak}} \downarrow 5\%$ ;  $n_u^{\text{peak}} \downarrow 5\%$ ). In contrast, case C shows strong changes on the separatrix ring ( $n^{\text{peak}} \uparrow 50\%$ ;  $n_u^{\text{peak}} \uparrow 80\%$ ;  $P_{\perp} \uparrow 15\%$ ;  $T_{i,u} \uparrow 20\%$ ) and weaker changes elsewhere in the SOL. Notably,  $p_{\text{tot},u}/p_{\text{tot},i}$  is unchanged on the separatrix ring, while being reduced from ~4 to ~3 on outer SOL rings. This behaviour may be explained by noting that even in the presence of significant recombination ( $S_{\text{rec}} \sim S_{iz}$ ), nearly all momentum is removed by CX collisions ( $S_{\text{CX}} \gg S_{\text{rec}}$ , a result dependent solely on the ratio  $\langle \sigma v \rangle_{\text{rec}}/\langle \sigma v \rangle_{\text{CX}} \ll 1$ , see Fig.2.3.1). We may deduce that recombination alters the degree of detachment indirectly, via the particle and energy balances (by cooling/heating the plasma and altering the plasma

flow in the active region). The next step is to consider the degree of over/under-ionization  $f^{(1)}$  and the default  $Q_{\perp}^{(1)} \propto n_e$  scaling (in both the detached cases, the separatrix ring is over-ionized,  $f^{(1)} > 1$ ,  $Q_{\perp}^{(1)} < 0$ , with outer SOL rings under-ionized,  $f^{(1)} < 1$ ,  $Q_{\perp}^{(1)} > 0$ ). Consequently, by setting  $S_{rec} = 0$ , the separatrix ring becomes more over-ionized ( $f^{(1)} \uparrow 30\%$ , from 2.7 to 3.7) and  $Q_{\perp}^{(1)} < 0$  becomes an even stronger sink for plasma particles (this is the reason for the initially surprising increase of  $n_e^{\text{peak}}$  for  $S_{rec} = 0$ ); likewise, the other SOL rings become less under-ionized which decreases the positive  $Q_{\perp}^{(1)}$ . Unfortunately, the effect of  $S_{rec}$  on the energy balance could not be treated properly since only the  $+13.6\text{eV} \times S_{rec}$  term is controlled directly, the other terms (radiative cooling due to recombination into excited atomic states) are returned en-mass from NIMBUS. We may conclude that although recombination contributes to detachment, it is not necessary for its appearance.

The effect of neutral velocity on momentum loss is shown in Fig.4.2.12-14, where  $v_n^H = 0$  of the default model, which represents the maximum amount of momentum removal from the ions, was replaced by  $v_n^H = 0.5u$ , ie. the neutrals were assumed to move everywhere at half the plasma velocity. Both of these assumptions are crude, and more advanced estimates of  $v_n^H$  should be made in the future. Case A is only mildly affected by this reduction in the amount of momentum loss ( $p_{\text{tot},u}/p_{\text{tot},t} \downarrow 10\%$ ,  $f^{(2)} \downarrow 50\%$ ) while the impact on cases B and C is more pronounced ( $n^{\text{peak}} \downarrow 50\%$ ;  $p_{\text{tot},u}/p_{\text{tot},t} \downarrow 50\%$ ,  $f^{(2)} \downarrow 50\%$ ). The results confirm that momentum loss is the dominant physical processes responsible for plasma detachment (ie. the upstream-to-target pressure ratio is directly correlated to the momentum removal rate; the presence of over-ionization and recombination introduce non-linearity into the otherwise linear dependence).

In the default model, ion-neutral energy term  $Q_{qi}$  was set to zero in agreement with the default settings of the EDGE2D code; the effect of non-zero  $Q_{qi}$  (calculated according to the last paragraph in §2.3) is examined below, Fig.4.2.15-16. For case A, ion-neutral energy exchange is much smaller than electron cooling,  $Q_{qi} \ll Q_{qe}$  and the default solution remains virtually unchanged. With  $Q_{qi}$  turned on, there is no solution for case B which would satisfy  $T_{e,t} = 0.5\text{ eV}$  (the reason is simple: in the  $T_e$  plateau region,  $T_e < 2\text{ eV}$ , the ions are heated by charge-exchange collisions with Franck-Condon atoms more effectively than they are cooled by the electrons, which in turn loose energy due to  $Q_{qe} < 0$ ; the target electron temperature can not be reduced to 0.5 eV, even if the input power approaches zero). This observation points to the potential importance of  $Q_{qi}$  for detachment, and we must conclude that the case B (0.5 eV,  $10^{23}\text{ m}^{-2}\text{s}^{-1}$ ) is deficient in physical content with the default setting of  $Q_{qi} = 0$ , and must be treated with caution. A solution may be found for case C because at higher densities electron cooling comes to dominate over CX ion heating ( $Q_{qe} > Q_{qi}$ ) allowing the plateau temperature to drop below the F-C value of  $\sim 2\text{ eV}$ . Input power and upstream temperature increase to compensate for the  $Q_{qi}$  energy losses in the  $T_i > 2\text{ eV}$  region ( $P_{\perp} \uparrow 30\%$ ;  $T_{i,u} \uparrow 30\%$ ). The degree of detachment is reduced ( $p_{\text{tot},u}/p_{\text{tot},t} \downarrow 20\%$ ) for all SOL rings, while on the separatrix ring the degree of over-ionization increases ( $f^{(1)} \uparrow 25\%$ ), leading to flow reversal and partially compensating for the reduction in  $p_{\text{tot},u}/p_{\text{tot},t}$  due to  $Q_{qi}$  heating). A still higher density case (0.5 eV,  $10^{24}\text{ m}^{-2}\text{s}^{-1}$ ), Fig.4.2.17, shows that  $Q_{qi}$  provides a stabilizing mechanism missing from the default model:  $T_{e,t}$  adjustments are no longer necessary to stabilize the solution (ion heating opposes further recombination and density peak growth). The finite  $Q_{qi}$  model is clearly the preferred alternative.

In Fig 4.2.18-20, the effect of neglecting electron cooling due to impurities is shown (this is done by setting  $f_Z = 0$  in  $Q_Z = f_Z Q_{qe} < 0$ , cf. the default value of  $f_Z = 1$ ). Since this reduces the power removed from the plasma, the power deposited into the SOL must also decrease in order to achieve the same target  $T_e$ . This is observed in varying degrees in

the three cases (A:  $P_{\perp} \downarrow 30\%$ , B:  $P_{\perp} \downarrow 50\%$ , C:  $P_{\perp} \downarrow 30\%$ ); due to the  $\kappa_e \propto T_e^{5/2}$  scaling, the decrease of upstream  $T_e$  is smaller for hotter plasmas. The degree of detachment  $p_{\text{tot},u}/p_{\text{tot},i}$  is only marginally altered by setting  $f_Z = 0$ , which is to be expected since the near target conditions, which determine the amount of momentum loss, remain largely unchanged; however in each case the same pressure ratio corresponds to smaller input power. We may therefore conclude that impurity radiation enhances detachment by cooling the plasma. Since the treatment of impurity radiation in the default model is relatively crude, future refinements are strongly advisable (an iterative coupling of the OSM2 and DIVIMP codes would provide the optimum, albeit computationally costly, algorithm).

#### 4.2.3 Sensitivity to plasma sources, $\mathbf{Q}_P$

The effect of plasma sources is confined to transferring energy between the ion and electron channels; however, since energy is transported within and removed from these channels by different physical processes, the energy coupling provided by electron-ion collisions has a strong effect on the overall plasma behaviour. Plasma sources  $\mathbf{Q}_P$  (2.4.14), are composed of a collisional term  $Q_{ei} \equiv (p_e - p_i)/\tau_{ei}$ , which tends to equalize  $T_e$  and  $T_i$ , and an electric field term,  $Q_E \equiv u \nabla_u p_e$ , largest in the vicinity of the target, which transfers energy from the electrons to the ions.

The role of collisional energy equipartition may be examined by setting  $Q_{ei} = 0$ , Fig.4.2.21-22. The ion temperature is seen to rise drastically when the strong ion energy sink is removed (the cross-field input power into the ion and electron channels is assumed to be equal in the default model,  $\mathbf{Q}^{(3)\perp} = \mathbf{Q}^{(4)\perp}$ ). This rise of near target  $T_i$  to values of well over 5 eV, sharply reduces the rate of charge-exchange collisions and the associated momentum loss from the plasma ( $p_{\text{tot},u}/p_{\text{tot},i} < 2$ ); this is not caused by the energy dependence of the charge-exchange cross-section, but rather by the drop of ion and neutral densities (pressure balance with higher  $T_i$  and  $T_H$ ). In short, collisional energy equipartition is necessary for the appearance of detachment, due to its role of cooling the ions in the divertor volume.

#### 4.2.4 Sensitivity to flux expansion sources, $\mathbf{Q}_B$

Flux expansion sources arise in the plasma transport equations due to along- $\mathbf{B}$  variations of the magnetic field (2.1.22). Their effect on the default solutions is best explored by setting  $\mathbf{Q}_B = 0$ , Fig.4.2.23-25. In all cases, the separatrix flux tube is the most affected, the total pressure profile becoming more uniform and symmetrical. For case A, the separatrix density and flow profiles approach the profiles elsewhere in the SOL, suggesting that radial differences present in the default case A are caused by  $\mathbf{B}$ -field variations near the X-point (where the separatrix and outer SOL magnetic geometry differs the most) rather than by neutral source variations. The effect on case B is similar, with only minor changes in the overall plasma solution ( $n^{\text{peak}} \downarrow 20\%$ ;  $p_{\text{tot},u}/p_{\text{tot},i}$  – same). For case C, the effect of  $\mathbf{Q}_B = 0$  becomes more pronounced, increasing the degree of over-ionization and upstream temperature on the separatrix ring ( $f^{(1)} \uparrow 20\%$ ;  $T_{i,u} \uparrow 20\%$ ;  $n^{\text{peak}} \uparrow 20\%$ ;  $n^{\text{peak}} \uparrow 50\%$ ), while decreasing the degree of detachment ( $p_{\text{tot},u}/p_{\text{tot},i} \downarrow 10\%$ ) on the outer SOL rings. It is reassuring that, although a measurable effect, flux expansion does not greatly alter the overall plasma behaviour ( $\mathbf{Q}_B$  is often ignored in simpler treatments of the SOL, such as the two-point model or some of the earlier versions of onion-skin modeling).

#### 4.2.5 Sensitivity to kinetic boundary conditions, $\{\gamma_e, \gamma_i\}$

The kinetic origin of the ion and electron sheath heat transmission coefficients was discussed in some detail in §2.2, and their effect on the near target plasma profile has already been alluded to in §4.1. In this section, this effect is examined by reducing first  $\gamma_e$  and then  $\gamma_i$  by unity.

In Fig.4.2.26-28,  $\gamma_e$  has been reduced from the default value of  $\gamma_e = 5$  to  $\gamma_e = 4$ . Case A is only mildly affected by the smaller power required to satisfy the boundary conditions,  $q_e = \gamma_e T_e \Gamma_0$  ( $P_\perp \downarrow 20\%$ ;  $T_{e,u}$ -same). The most direct effect on Case B is the lowering of the  $T_e$  plateau (since lower  $\gamma_e$  requires a smaller  $\nabla_i T_e$  at the target, see §2.2), which increases  $n_e^{\text{peak}}$  by ~ 30%; the degree of detachment  $p_{\text{tot},u}/p_{\text{tot},l}$  remains unchanged. The effect becomes more pronounced for case C, when the plateau temperature governs the density peak evolution; with lower  $T_e$ ,  $n_e^{\text{peak}}$  increases and the solution is stabilized with the additional constraint  $n_e^{\text{sep}} < 10^{19} \text{ m}^{-3}$ .

Similarly, in Fig.4.2.29-31,  $\gamma_i$  has been reduced from the default value of  $\gamma_i = 2.5 + M_0^2(T_{e,0}+T_{i,0})/(2T_{i,0})$  to  $\gamma_i = 1.5 + M_0^2(T_{e,0}+T_{i,0})/(2T_{i,0})$ . For case A, the near target  $T_i$  increases since a higher ion temperature is necessary to carry the same amount of ion power to the target,  $q_i = \gamma_i T_i \Gamma_0$  (note that, ion convection is much stronger than ion conduction at the target); this carries over into slight changes to  $n_e$  and  $p_{\text{tot}}$ , but since  $T_{e,l}$  and not  $T_{i,l}$  determines the amount of input power,  $P_\perp$  remains virtually unchanged. For case B, the effect of lowering  $\gamma_i$  by unity is nearly the same as that of lowering  $\gamma_e$  by the same amount, (the plateau  $T_e$  decreases and  $n_e^{\text{peak}}$  increases as before), with one notable difference: namely a suppression of the supersonic flow at the target. The similarity between the sensitivity to  $\gamma_e$  and  $\gamma_i$  for lower  $T_e$  is consistent with strong electron-ion energy coupling (via collisional equipartition,  $Q_{ei}$ ) for colder plateau conditions.

#### 4.3 Comparison with the EDGE2D/NIMBUS code

As was mentioned in §2.4.3, the onion-skin method is not intended to replace but to complement the existing 2D fluid codes; it is an interpretive tool designed primarily for experimental use. By the same token existing 2D fluid codes are primarily predictive tools, although they are also frequently used to interpret experiments. A comparison of these two approaches would not only provide an assessment of the onion-skin method, but could tell us a lot about the relative importance of cross-field transport in the edge plasma. In this section, such a comparison is presented based on the OSM2/NIMBUS and EDGE2D/NIMBUS codes (the latter code was selected because of its close association with the JET tokamak). The radial target profiles of  $T_e$  and  $\Gamma_0$  extracted from the EDGE2D solution are passed into OSM2 as the diagnostic target constraints. The two solutions are then compared everywhere in the SOL.

The EDGE2D/NIMBUS solution, shown in Fig.4.3.1-4, was obtained with the following input: power flux across the separatrix  $P_\perp = 1 \text{ MW}$ , separatrix density  $n_{\text{sep}} = 0.5 \times 10^{19} \text{ m}^{-3}$ , cross-field transport coefficients  $D_\perp = 0.15 \text{ m}^2/\text{s}$ ,  $\chi^i_\perp = 1 \text{ m}^2/\text{s}$ ,  $\chi^e_\perp = 1 \text{ m}^2/\text{s}$ , and kinetic boundary conditions  $\gamma_e = 5.0$ ,  $\gamma_i = 2.5 + M_0^2(T_{e,0}+T_{i,0})/(2T_{i,0})$ . The SOL plasma appears to be well attached and conductively limited, with some asymmetry between the inner and outer targets (increasing away from the separatrix) and with significant radial gradients across the SOL ( $n_e$ ,  $T_e$ ,  $T_i$ , and  $p_{\text{tot}}$  decay away from the separatrix).

The OSM2/NIMBUS solution, shown in Fig.4.3.5-8, was obtained by specifying the EDGE2D target values of plasma flow and electron temperature  $\{\Gamma_0, \Gamma_L, T_{e,0}, T_{e,L}\}(r)$  as the diagnostic constraints for the OSM-DVM approach. Special care was taken to insure that OSM2 and EDGE2D modeling equations differed only in the treatment of radial fluxes: a) neutral sources, including  $Q_{cx}$  and  $Q_{qi}$ , were calculated directly by NIMBUS, b) impurity contributions were neglected,  $f_z = 0$ , c) the same kinetic boundary conditions  $\{\gamma_e, \gamma_i\}$  were used, d) flux limited heat conductivities were replaced by classical values, e) the cross-field source scaling  $Q_\perp[U]$  was specified as for the default OSM-DVM model of in §2.4.3. Comparison reveals close agreement between the OSM2 and EDGE2D solutions, both in the along- $\mathbf{B}$  and cross-field directions, Fig.4.3.9-10, with only minor differences: OSM2 predicts slightly larger along- $\mathbf{B}$  gradients near the targets, more extended and asymmetrical flow patterns, and more uniform total pressure profiles. The near target drop of separatrix  $p_{tot}$  in the EDGE2D solution is accompanied by spatial oscillation (perhaps due to the coarseness of the near target cells). The pressure drop on the separatrix in the EDGE2D solution has been linked to cross-field viscous effects; when cross-field viscosity is set to zero in EDGE2D, total pressure becomes more uniform, improving agreement between the two codes. Aside from these relatively small differences, the overall 2D plasma distribution is very closely replicated. It is worth considering the implications of this result, namely that the claim sometimes made against the OSM method as being devoid of cross-field content is misinformed. The radial information enters OSM2 through the radial profiles of the diagnostic target quantities,  $\Gamma_0(r), T_{e,0}(r), \Gamma_L(r), T_{e,L}(r)$ . The cross-field sources  $Q_\perp$  are then adjusted in response to these radial profiles. Replacing  $F_\perp + G_\perp$  (calculated with specified  $D_\perp, \chi_\perp^i, \chi_\perp^e$ ) by the much simpler  $Q_\perp$  has apparently only a minor effect on the final solution (at least for the conductively-limited regime considered here). The only explanation consistent with this result is that the precise flux-tube location of cross-field transport is far less important than its flux-tube integrated value (rapid along- $\mathbf{B}$  transport effectively redistributes both particle and power entering the flux tube, the redistribution of particles being slower due to ion inertia).

#### 4.4 Comparison with experiment: reciprocating probe (RCP) measurements on JET

The final application of the OSM2/NIMBUS code examined in this thesis is perhaps the most important. Since the onion-skin method was repeatedly identified as an interpretive tool, its ultimate test must involve a comparison with experiment. For this purpose, the upstream reciprocating Langmuir probe (RCP) data on the JET tokamak was compared with the results of the OSM2/NIMBUS simulation (target Langmuir probe data was used as the diagnostic constraint); Li-beam and LIDAR measurements are also available for some shots, but the RCP data and the three methods are in rough agreement as to the radial decay lengths of  $n_e$  and  $T_e$ . Five shots were selected from more than twenty examined: an Ohmic shot (48310,  $t = 54.4$  sec), three L-mode shots (45702,  $t = 61$  sec; 45791,  $t = 63$  sec; 45798,  $t = 63.5$  sec), and one H-mode shots (47734, 61 sec). Default modeling assumptions of §2.4.3 were adapted, with the exception of  $Q_{cx}$  and  $Q_{qi}$ , which were obtained directly from NIMBUS.

For the Ohmic shots, the OSM2 solution, Fig.4.4.1-2, exhibits the familiar conductively limited behaviour with strong radial gradients and relatively low upstream densities. The RC probe is inserted and withdrawn from the SOL vertically near the top of the torus ( $R = 3.25$  m). Unfortunately, there is no reliable method of determining the location of the separatrix. Because of the large size of the plasma in comparison to the small SOL thickness, the errors

may be significant. The procedure often employed to relate target and upstream flux tubes relies on total pressure conservation in the absence of detachment. In other words the upstream radial profiles are shifted such that  $p_{\text{tot}}^{\text{up}}/p_{\text{tot}}^{\text{st}} \sim 1$  (in our case this required a shift by 18 mm); flux tubes are then identified by the distance away from the separatrix at the outer mid-plane,  $r_{\text{mid}}$ . The measured and calculated values are plotted as a function of this ordinate in Fig.4.4.3-4 (the RCP data is highly scattered and in the absence of experimental error analysis, 20% error bars were assumed for  $n_e$  and  $T_e$ , and 50% error bars for the Mach number). The measured (RCP) and predicted (OSM) values agree to within the assumed experimental error; slight departures on the separatrix ring are likely caused by loss of accuracy as the probe enters the core plasma. Plasma flow differs substantially for a number of reasons: a) Mach probe interpretation depends on the anomalous cross-field transport coefficients, and may contain a large systematic error, b) drifts in the diamagnetic direction, which are at present not included in the OSM2 code, have been shown to significantly alter along- $B$  flow patterns in the SOL, c) the assumed cross-field particle source may need to be varied in order to match the observed flow. Similar level of agreement is obtained for the L-mode shots, Fig.4.4.5-10, and the H-mode shot for which RCP data was available, Fig.4.4.11-12 (it is difficult to say whether the agreement with the H-mode Mach number is significant or simply fortuitous). It is hoped that the above results illustrate the utility of the OSM-DVM approach (each OSM2/NIMBUS solution required only ~ 6 hrs of CPU time on a typical IBM RS6000 work station): with a modest improvement in microprocessor speed, 2-D SOL plasma distributions may be reconstructed based on target diagnostic data within one hour (this is the closest to real-time/inter-shot analysis which is possible at present).

## 5.0 Conclusions

The improved OSM approach, as defined by (2.4.10), has been successful at modeling all the regimes of tokamak edge plasma behaviour, including plasma detachment. The regions of validity of the above approach have been investigated both theoretically, by investigating the validity of the  $Q_{\perp}/U$  ansatz, and numerically, by examining the sensitivity of the solution on the assumed form of cross-field sources, leading to similar conclusions: a) the solution is highly insensitive to cross-field power sources for all SOL regimes, b) it is only weakly insensitive to cross-field momentum and particle sources for attached SOL conditions, and c) it may become sensitive to cross-field momentum and particle sources for certain detached conditions. Since the amount of cross-field momentum flow plays a relatively smaller role than cross-field particle flow in actual tokamak edge plasmas, the latter effect may be singled out as the key sensitivity; the requirement that over/under-ionization with respect to the targets does not exceed a factor of two on any flux tube may be used as a rough validity criterion of the above OSM approach. As discussed in §4.2.1, this criterion can be mitigated by introducing additional diagnostic data upstream of the ionization front; even in the present form, the sensitivities observed for strong detachment remain within the bounds of accuracy for most edge diagnostics.

Code-code comparison with a standard 2D edge plasma modeling approach (EDGE2D/NIMBUS vs. OSM2/NIMBUS) has shown good agreement between the two codes. This positive result is the best confirmation so far of the predicted correspondence between the OSM and the standard modeling approach, and one of the key results presented in this work. It establishes, at the very least, the practical usefulness of the OSM approach, which produces a nearly identical solution in a much short time (~6 hours) than that required for the EDGE2D parameter scan (~1 week).

Code-experiment comparison between the upstream profiles of  $T_e$  and  $n_e$  obtained by OSM2/NIMBUS and those measured by reciprocating probe data on the JET tokamak for Ohmic, L-mode and H-mode discharges, further reinforce the above conclusions; the profiles agree to within the experimental error of the probe, estimated at 20%.

The improved OSM method could greatly enhance our interpretive capability of edge plasma behaviour. It has the potential for incorporating unlimited number of diagnostic channels, for being used in ‘real time’ for inter-shot analysis, for extraction of flux-surface averaged anomalous cross-field transport coefficients, and for inclusion within existing edge plasma codes such as B2, EDGE2D or UEDGE. It is presently being installed as a routine analysis tool at JET, and further improvements to the OSM2 code (drifts, currents, cross-field source dependence on gradients, upstream diagnostic data) are anticipated.

## 6. References

The approach adapted below to selecting an appropriate source for a given piece of information, is that of referring whenever possible to general and widely available sources (preferably on the text-book level). For example, in case of Maxwell's equations the reader is referred to Jackson's Classical Electrodynamics, rather than to Maxwell's original paper. In some instances, however, an effort is made to preserve scientific chronology, eg. nuclear fusion as the source of stellar energy is referred to the original publication [Atk29].

- [All76] J.E. Allen, *J. Phys. D*, **9**, 2331 (1976).
- [Asd89] ASDEX Team, *Nucl. Fusion*, **29**, 1959 (1989).
- [Ash81] D. Ashby, M. Hughes, *Nucl. Fusion*, **21**, 911 (1981).
- [Atk29] R.d'E. Atkinson, F.G.Houtermans, *Zeitschriften Physik*, **54**, 656 (1929).
- [Arn89] V.I.Arnold, Mathematical Methods of Classical Mechanics, 2<sup>nd</sup> ed., (1989).
- [Auc89] O. Auciello, D.L.Flamm, Plasma Diagnostics, Academic Press (1989).
- [Bae91] M. Baelmans, *Ph.D. Thesis, Ecole Royale Militaire*, Belgium (1991).
- [Bal60] R.Balescu, *Physics of Fluids*, **3**, 52 (1960).
- [Bal63] R. Balescu, Statistical Mechanics of Charged Particles, John Wiley (1963).
- [Bal88] R. Balescu, Transport Process in Plasmas, North-Holland (1988).
- [Bat85] G.Bateman, MHD Instabilities, MIT Press (1985).
- [BeH91] R. Behirsch, (ed.), Sputtering by Particle Bombardment, Berlin (1981-91).
- [Bha54] P.L. Bhatnagar, E.P.Cross, M.Krook, *Phys.Rev.* **95**, 511 (1954).
- [Blo90] E.E.Bloom, *Nuclear Fusion*, **30**, 1879 (1990).
- [Boo90] D.L.Dook, NRL Plasma Formulary, Naval Research (1990).
- [Bor66] M.Born, Atomic Physics, Hafner (1966).
- [Bra87] B. Braams, *NET rep., EUR-FU IXII-80-87-68*, Comm. of E.C. (1987)
- [Bra65] S.I. Braginskii, in *Reviews of Plasma Physics*, edited by M.A.Leontovich, *Consultants Bureau*, New York, (1965) **I**, 205.
- [Bro66] S.C. Brown, Basic Data of Plasma Physics, MIT Press (1966).
- [Bru87] B.Brunelli, G.G.Leotta, ed., Muon-Catalyzed Fusion and Fusion with Polarized Nuclei, Plenum (1987).
- [Cas59] E.D.Cashwell, C.J.Everett, Monte Carlo Method for Random Walk Problems, Pergamon (1959).
- [Cha42] S. Chandrasekhar, Principles of Stellar Dynamics, U.Chicago Press (1942).
- [Cha58] S.Chapman, T.G.Cowling, Mathematical Theory of Non-uniform Gases, Cambridge U. Press (1958)
- [Cha60] S. Chandrasekhar, Plasma Physics, U.Chicago Press (1960).
- [Cha86] C.S.Chang, F.L.Hinton, *Phys. Fluids*, **29**, 3314 (1986).
- [Cha97] A. Chankin, *J. Nucl. Materials*, **241-243**, 199 (1997).
- [Che56] G.F.Cheow, M.L.Goldberger, F.E.Low, *Proc. Roy. Soc.*, **A236**, 112 (1956).
- [Cho84] R. Chodura in [Pos84].

- [Coh77] C.Cohen-Tannoudji, B.Diu, F.Laloe: Quantum Mechanics I & II, 2<sup>nd</sup> Ed., John Wiley (1977).
- [Con77] J.W. Connor, J.B.Taylor, *Nuclear Fusion*, **17**, 1047 (1977).
- [Con78] J.W.Connor, et al., *Phys.Rev.Let.*, **40**, 396 (1978).
- [Con79] E.U. Condon, G.H.Shortley: The theory of Atomic Spectra, Cambridge U. Press (1979).
- [Con90] R.W.Conn et al., *Nuclear Fusion*, **30**, 1919 (1990).
- [Con94] J.W.Connor, H.R.Wilson, *Plasma Phys and Cont. Fusion*, **36**, 719 (1994).
- [Cou99] G.F.Counsell, et al., *J. Nucl. Materials*, **266-269**, 91 (1999).
- [Cow81] R.D.Cowan, The Theory of Atomic Structure and Spectra, UC Press, Berkeley (1981).
- [Cup84] E. Cupini, A. De Matteis, and R. Simonini, *NET Rept. EUR XII* (1984) 324/9.
- [Dan90] J.F.Dannenhoffer, *AIAA Paper 90-1565* (1990).
- [deB94] H.J.de Blank, *Fusion Tech.* **25**, 39 (1994).
- [Dol82] T.J.Dolan, Fusion Research, 3 Vols, Pergamon (1982).
- [Dro89] R.Drouin et al., *14<sup>th</sup> Congress of the World Energy Conference*, Montreal (1989).
- [Eis87] P.R.Eisman, *Comp.Meth. in Appl. Mech and Eng.*, **64**, 321 (1987).
- [Emm80] G.A.Emmert, R.M.Wieland, A.T.Mense, et al. *Phys.Fluids*, **23**, 803 (1980).
- [Ere98] S.K.Erents, P.C.Stangeby, *Nuclear .Fusion*, **38**, 1637 (1998).
- [Fri87] J.P.Friedberg, Ideal magnetohydrodynamics, Plenum Press (1987).
- [Fro89] R.A.Frosh, et al., "Strategies for Manufacturing", *Scientific American* (1989).
- [Fun92] W.R. Fundamenski, "Evolution and Status of D-<sup>3</sup>He Fusion", *Masters. Thesis, McMaster U.* (1992).
- [Fun96] W.R.Fundamenski, *Fusion Tech.*, **28** (1996).
- [Fur73] H.P.Furth, et al., *Phys. Fluids*, **16**, 1054 (1973).
- [Gau90] W.B.Gauster, *Nuclear Fusion*, **30**, 1897 (1990).
- [Gib89] J.H.Gibbons et al., "Strategies for Energy Use", *Scientific American* (1989).
- [Gie90] P.J.Gierszewski, et al., "Alternate Fusion Concepts: Status and Plans", CFFT-G-9009 (1990).
- [Gil81] R.D.Gill (ed.), Plasma Physics and Nuclear Fusion Research, Academic Press (1981).
- [Gla60] S. Glasstone, R.H.Loveberg, Controlled Thermonuclear Reactions, Van Nostrand (1960).
- [Gra57] H.Grad, H. Rubin, 2<sup>nd</sup> *UNICPUAE*, **31**, 190 (1959).
- [Gra88] R.S.Granetz, P. Smeulders, *Nuclear Fusion*, **28**, 457 (1988).
- [Gra89] T.E.Graedel, P.J.Crutzen, "The Changing Atmosphere". *Scientific American* (1989).
- [Gri66] H.R.Griem, Plasma Spectroscopy, Academic Press (1966).
- [Gue60] R. Guensey, Ph.D. dissertation, U. Michigan (1960).
- [Hak87] H. Haken, H.C. Wolf, Atomic and Quantum Physics, 2<sup>nd</sup> Ed., Springer (1987).
- [Hal95] D.J. Hall and D.W. Zingg, *AIAA Journal*, **33** (1995), 1205-1210.
- [Haz92] R.D.Hazeltine, J.D.Meiss, Plasma Confinement, Adison-Wesley (1992).
- [Haz98] R.D.Hazeltine, *Physics of Plasmas*, **6**, 550 (1992).
- [Her44] G.Herzberg, Atomic Spectra and Atomic Structure, Dover (1944).
- [Hil74] F.B. Hilderbrand, Introduction to Numerical Analysis, 2<sup>nd</sup> ed., Dover (1974).

- [Hir90] C. Hirsch, Numerical Computation of Internal and External Flows, John Wiley and Sons (1990).
- [Hor97] L. Horton, private communications (1997).
- [Hua87] K. Huang, Statistical Mechanics, 2<sup>nd</sup> Ed., John Wiley & Sons (1987).
- [Ich73] S. Ichimaru, Basic Principles of Plasma Physics, Benjamin (1973).
- [Ich92] S. Ichimaru, Statistical Plasma Physics, Vol.. 1, Adison-Wesley (1992).
- [Isa66] E. Isaacson, H.B. Keller, Analysis of Numerical Methods, John Wiley & Sons (1966)
- [Isl99] R.C. Isler, et al., *J. Nucl. Materials*, **266-269**, 376 (1999).
- [Jac75] J.D. Jackson, Classical Electrodynamics, 2<sup>nd</sup> Ed., John Wiley & Sons (1975).
- [Jam82] A. Jameson, in [Roe82].
- [Jan95] R.K.Janev, ed., Atomic and Molecular Processes in Fusion Edge Plasmas, Plenum (1995).
- [Kad65] B.B. Kadomtsev, Plasma Turbulence, Academic Press (1965).
- [Kaz84] M.S. Kazimi, *Nuclear Fusion*, **24**, 1461 (1984).
- [Kir74] G. Kirczenow, J. Marro, ed., Transport Phenomena, Springer (1974).
- [Kol74] A.N. Kolmogorov, S.V. Formin, Introductory Real Analysis, Dover (1970).
- [Kov84] L.M. Kovrzhnykh, *Nuclear Fusion*, **24**, 851 (1984).
- [Kra80] N.A. Krall, A.W. Trivelpiece, Principles of Plasma Physics, San Francisco Press (1980).
- [Kra99] S.I. Krashenikov, et al., *J. Nucl. Materials*, **266-269**, 251 (1999).
- [Kuh69] H.G. Kuhn, Atomic Spectra, 3<sup>rd</sup> Ed., Longmans (1969).
- [LaB97] B. LaBombard, et al. *J. Nucl. Materials*, **241-243**, 149 (1997).
- [Lam83] J.R. Lamarsh, Introduction to Nuclear Engineering, 2<sup>nd</sup> ed. Addison-Wesley (1983).
- [Lan37] L.D. Landau, *Zhur. Eksp. i Teoret. Fiz.* **7**, 203 (1973).
- [Lan46] L.D. Landau, *J. Phys.* **10**, 26 (1946).
- [Lan76] L.D. Landau, E.M. Lifshitz, Mechanics, 2<sup>nd</sup> ed., Pergamon (1976).
- [Lan89] L.D. Landau, E.M. Lifshitz, The Classical Theory of Fields, 4<sup>th</sup> ed., Pergamon (1989).
- [Lan82] L.D. Landau, E.M. Lifshitz, Quantum Mechanics, 3<sup>rd</sup> ed., Pergamon (1982).
- [Lan82] L.D. Landau, E.M. Lifshitz, Statistical Physics, 3<sup>rd</sup> ed., Pergamon (1982).
- [Law57] J.D. Lawson, *Proc. Phys. Soc.* **B70**, 6 (1957).
- [Len60] A. Lenard, *Annals of Physics*, **10**, 390 (1960).
- [Lie85] P.C. Liewer, *Nuclear Fusion*, **25**, 543 (1985).
- [Lif82] E.M. Lifshitz, Pinefsky, Physical Kinetics, 3<sup>rd</sup> ed., Pergamon (1982).
- [Loa97] A. Loarte, *J. of Nucl. Materials*, **241-243**, 118 (1997).
- [Loc68] W. Lochte-Holtgreven, ed. Plasma Diagnostics, John Wiley (1968).
- [Mat95] G.F. Matthews, *J. of Nucl. Materials*, **220-222**, 104 (1995).
- [Mer70] E. Merzbacher, Quantum Mechanics, 2<sup>nd</sup> ed., John Wiley (1970).
- [Mes58] A. Messiah, Quantum Mechanics I & II, John Wiley (1958).
- [Mig93] S. Migliuolo, *Nuclear Fusion*, **33**, 1721 (1993).
- [Mil74] G.H. Miley et al., *U.Illinois Nucl. Eng. Report*, **C00-2218-17** (1974).

- [Mil76] G.H.Miley, Fusion Energy Conversion, American Nuclear Society (1976).
- [Miy78] K. Miyamoto, Plasma Physics for Nuclear Fusion, MIT Press (1978).
- [Nak90] S.Nakai et al., *Nucl.Fusion*, **30**, 1779 & 1863 (1990).
- [Neu86] J. Neuhauser, et al., *Nucl. Physics*, **26**, 1679 (1986).
- [Par97] R. Parker, et al., *J. Nucl. Materials*, **241-243**, 1 (1997).
- [Pau60] L.Pauling, The Nature of the Chemical Bond, Cornell U. Press (1960).
- [Pit97] C.S. Pitcher and P.C. Stangeby, *Plasma Phys. and Contr. Fusion*, **39** (1997).
- [Pos77] D.E. Post, et al., Atomic Data and Nuclear Tables, **20**, 397 (1977).
- [Pos84] D.E.Post, R. Behirsch (eds.), Physics of Plasma-Wall Interactions in Controlled Fusion, Plenum Press (1984).
- [Pre92] W.H.Press, et al., Numerical Recipes in Fortran, Cambridge (1992).
- [Ran82] J.Rand McNally, Jr., Physics of Fusion Fuel Cycles, *Nucl.Tech./Fusion*, **2**, 9 (1982).
- [Rec78] A.B.Rechester, M.N.Rosenbluth, *Phys.Rev.Let.*, **40**, 38 (1978).
- [Rei84] D.Reiter, *Julich Report 1947* (1984).
- [Rei92] D. Reiter, *J. Nucl. Materials*, **196-198**, 80 (1992).
- [Rei98] D.Reiser, *Nucl. Fusion*, **38**, 165 (1998).
- [Rie94] K.-U. Riemann, *Phys.Plasmas*, **4**, 4158 (1994).
- [Rie96] K.-U. Riemann, *Contr. Plasma Phys.*, **36**, S16 (1996).
- [Roe82] P.L.Roe (ed.), Numerical Methods in Aeronautical Fluid Mechanics, Academic Press (1982).
- [Ron92] T.D. Ronglien, J.L. Milovich, M.E.Rensink, G.D.Porter, *J. Nucl. Mater.*, **196-198**, 347 (1992).
- [Ros57] M.N.Rosenbluth, et al., *Phys. Rev.* **107**, 1 (1957).
- [Ros83] M.N.Rosenbluth, R.Z. Sagdeev (eds.), Handbook of Plasma Physics, North Holland (1983).
- [Sah21] M.N. Saha, *Proc. Roy. Soc.*, **A99**, 135 (1921).
- [Sea62] M.J.Seaton, Atomic and Molecular Processes, D.R.Bates ed., Academic Press (1962).
- [Sch49] L.I.Schiff, Quantum Mechanics, McGraw Hill (1949).
- [Sch89] S.H.Schneider, ‘The Changing Climate’, *Scientific American* (1989).
- [Sch88] J.T.Scheuer, G.A.Emmert, *Phys.Fluids*, **31**, 1748 (1988).
- [Sch90] J.T.Scheuer, G.A.Emmert, *Phys.Fluids*, **B2**, 445 (1990).
- [Sha57] V.D.Shafranov, *Zh.Exps.Teo.Fiz.* **33**, 710 (1957)..
- [Shi74] G.E.Shilov, Elementary Functional Analysis, Dover (1974).
- [Shk66] I.P.Shkarpofsky et al., The Particle Kinetics of Plasmas, Addison-Wesley (1966).
- [Sim92] R. Simonini, A. Taroni, M.Keilhacker et al., *JNM* **196-198**, 369 (1992).
- [Sim94] R. Simonini et al., *Contrib. Plasma Phys.* **34** (1994), 368-373.
- [Sob79] I.I.Sobelman, Atomic Spectra and Radiative Transitions, Springer (1979).
- [Spa90] K.H.Spatchek, Theoretische Plasmaphysik, Teubner (1990).
- [Spi62] L.Spitzer, Jr., Physics of Fully Ionized Gases, 2<sup>nd</sup> ed., John Wiley (1962).
- [Sta81] W.M.Stacey, Fusion Plasma Analysis, John Wiley (1981).

- [Sta89] P.C. Stangeby, in [Auc89].
- [Sta90] P.C. Stangeby and G. M. McCracken, *Nuclear Fusion*, **30** (1990) 1225-1379.
- [Sta95] P.C. Stangeby and J.D. Elder, *Nuclear Fusion* **35** (1995) 1391-1412.
- [Sta97] P.C. Stangeby, J.D. Elder, W. Fundamenski, et al., *J. Nucl. Mater.* **241-243** (1997) 358.
- [Stm90] R.D. Stambaugh, et al., *Phys. Fluids*, **B2**, 2941 (1990).
- [Sti62] T.H. Stix, The Theory of Plasma Waves, McGraw-Hill (1962).
- [Str65] T.F. Stratton, Plasma Diagnostic Techniques, Academic Press (1965).
- [Syk81] A. Sykes, J.A. Wesson, *Plasma Phys. Cont. Fusion*, **1**, 237 (1981).
- [Tan78] W.M. Tang, *Nuclear Fusion*, **18**, 1089 (1978).
- [Ton29] L. Tonks, I. Langmuir, *Phys. Rev.* **34**, 876 (1929).
- [Tro83] F. Troyon, et al., *Plasma Phys. Contr. Fusion*, **26**, 209 (1984).
- [Van81] N.G. Van Kampen, Stochastic Processes in Physics and Chemistry, North Holland (1981).
- [Vla38] A.A. Vlasov, *Zh. Eksp. Teor. Fiz.* **8**, 291 (1938).
- [Vin89] M. Vinokour, *Journal of Computational Physics*, **81**, 1 (1989).
- [Wei74] R. Weinstock, Calculus of Variations, Dover (1974).
- [Wes78] J. Wesson, *Nuclear Fusion* **18**, 87 (1978).
- [Wes89] J. Wesson, *Nuclear Fusion* **29**, 1695 (1991).
- [Wes98] J. Wesson, Tokamaks, Oxford U. Press (1998).
- [Whi54] H.E. White: An introduction to Atomic Spectra, McGraw-Hill (1954).
- [Whi77] R.B. White, et al., *Phys. Fluids*, **20**, 800 (1977).
- [Woo87] L.C. Woods, Principles of Magnetoplasma Dynamics, Oxford (1987).
- [Woo90] A.J. Wootton, et al. *Phys. Fluids*, **B2**, 2879 (1990).
- [Zaw86] E. Zawaideh, F. Najmabadi, R.C. Conn, *Phys. Fluids* **29** (1986) 463.
- [Zaw88] E. Zawaideh, N.S. Kim, F. Najmabadi, *Phys. Fluids* **31** (1988) 3280.
- [Zwi89] D. Zwillinger, Handbook of Differential Equations, Academic Press (1989).

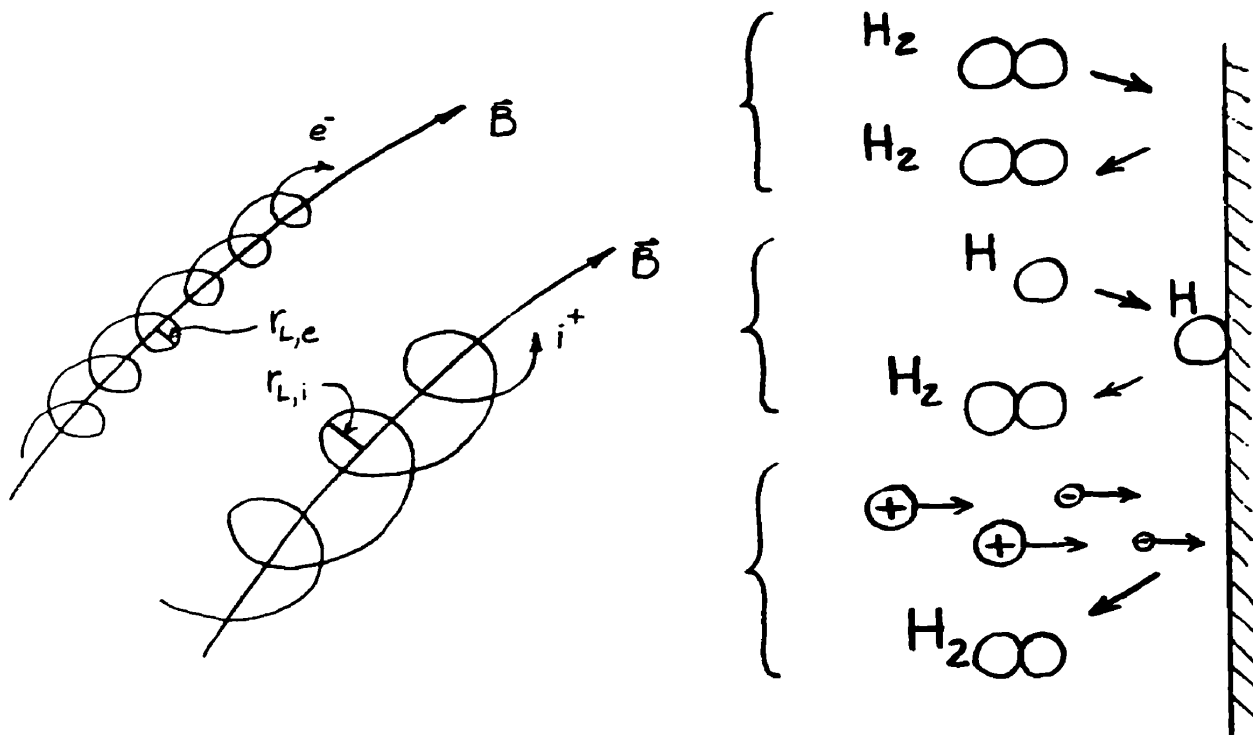


Fig.2.1.1: Charged particle orbits in the presence of a magnetic field  $\mathbf{B}$

Fig.2.2.1: Plasma-surface vs. neutral-surface interactions

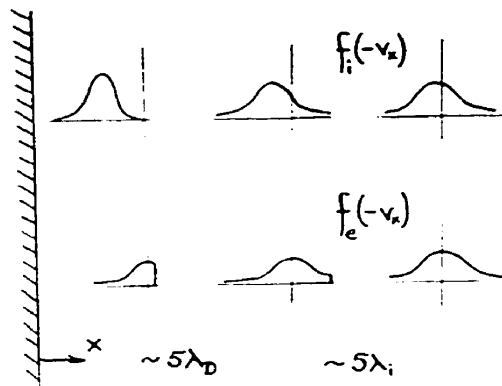


Fig.2.2.2: Ion and electron velocity distributions in the collisional plasma, the collisionless pre-sheath and the electrostatic sheath.

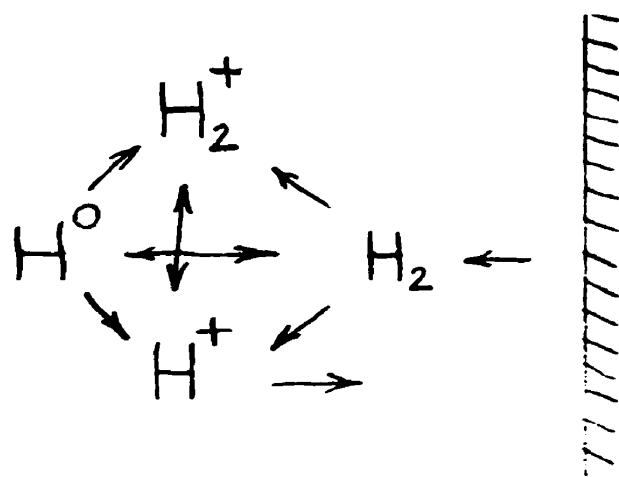
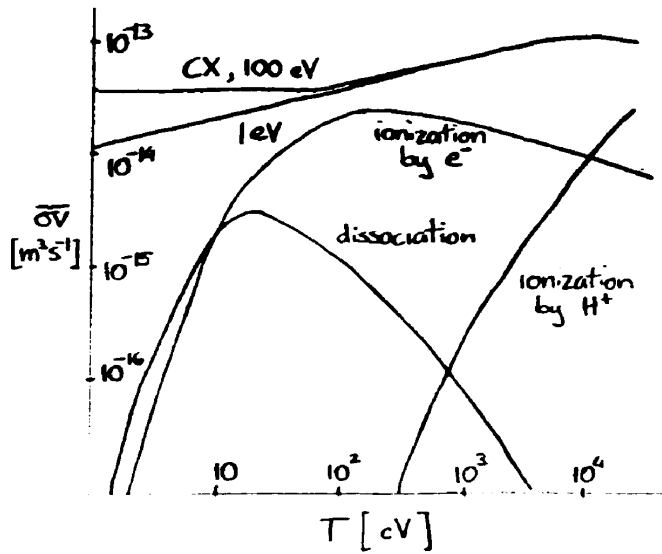
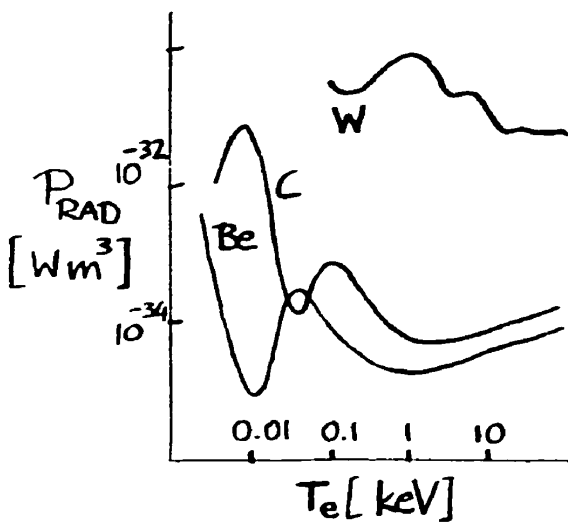
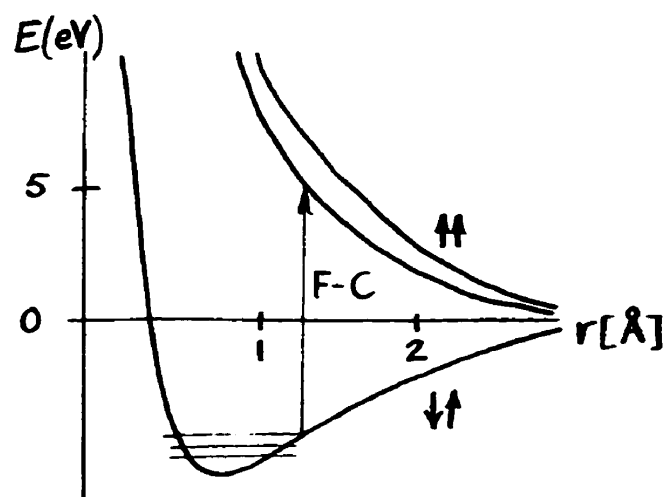
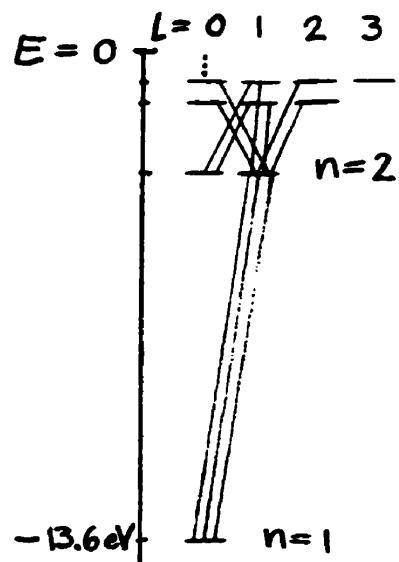


Fig.2.3.1: A schematic of hydrogen recycling including both volumetric and wall interactions.



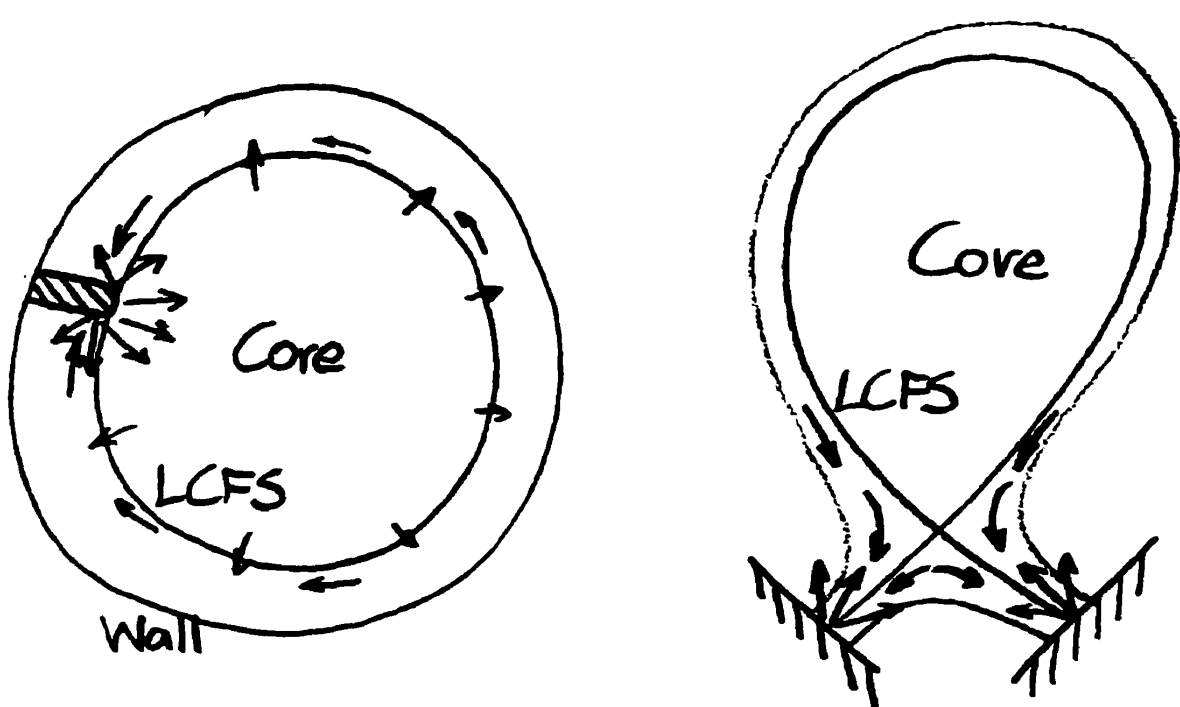


Fig.2.4.1: Schematic representation of limiter SOL

Fig.2.4.2: Schematic representation of divertor SOL

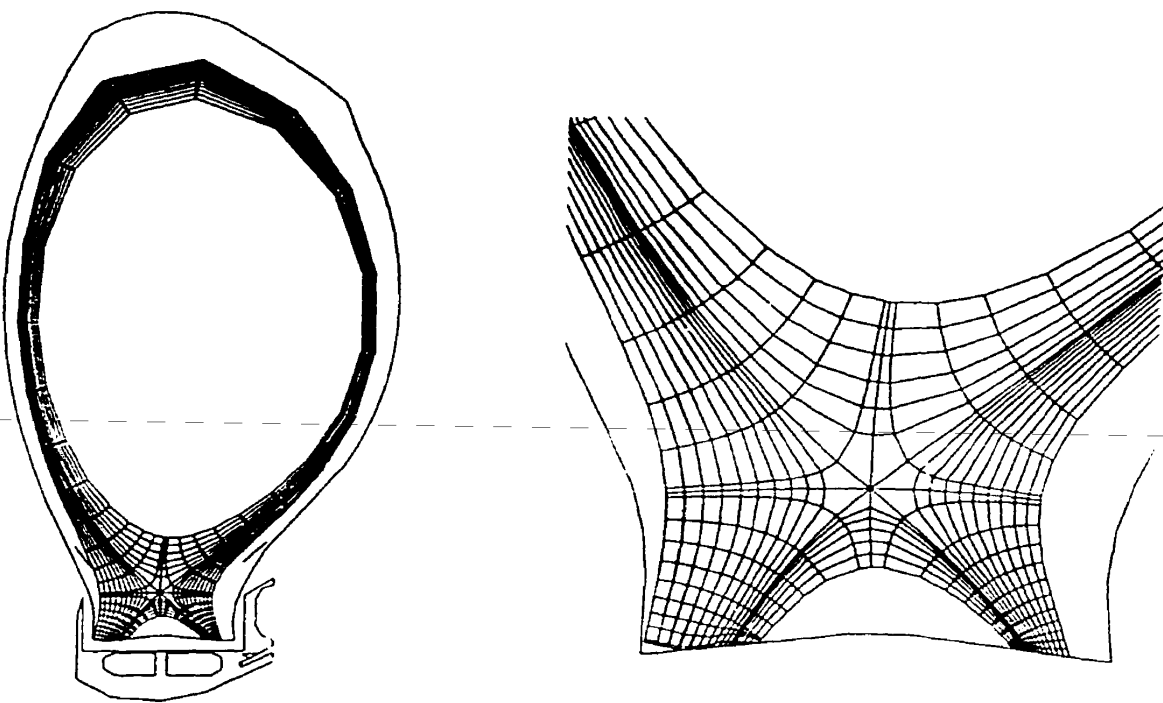


Fig.3.1.1: A typical poloidal grid used for divertor edge plasma modeling on the JET tokamak. This grid was used for majority of the results in §4.

Fig.3.1.2: A close up of the same grid in the vicinity of the X-point, including the divertor volume.

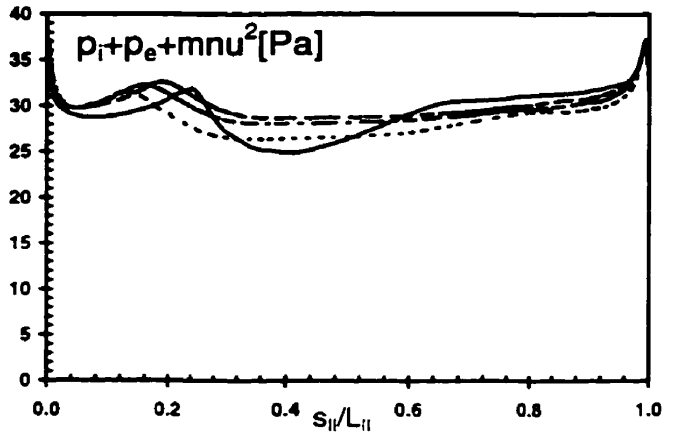
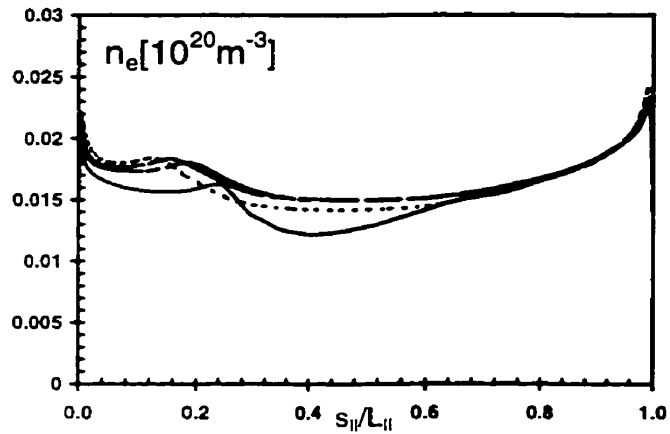
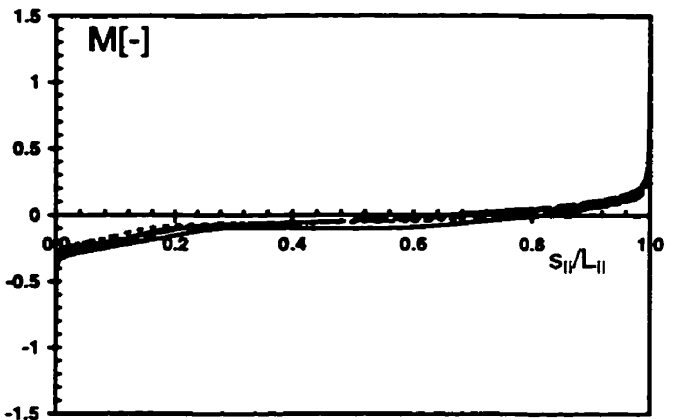
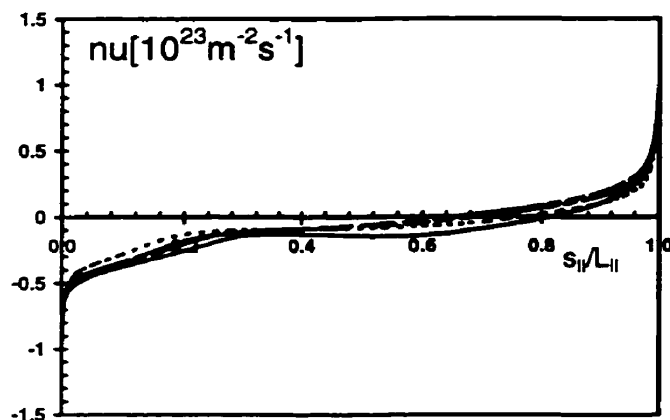
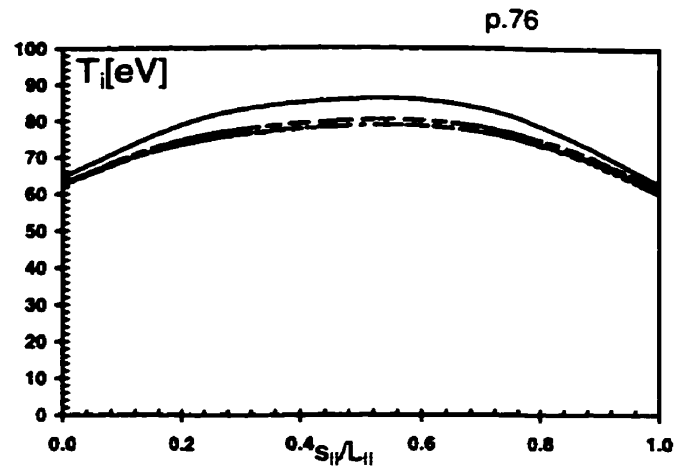
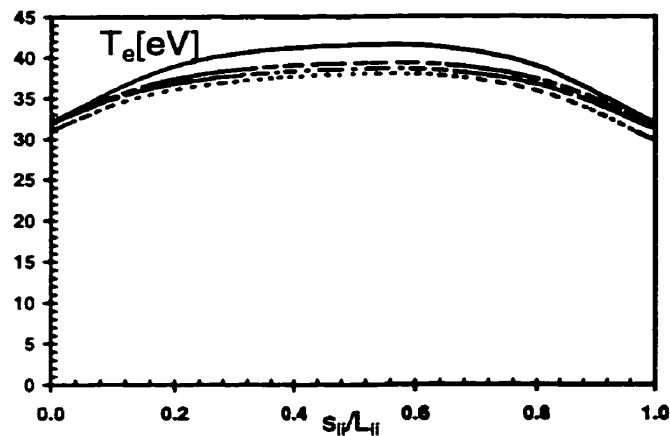


Fig. 4.1.1: Along-B plots of plasma variables for the 32 eV,  $10^{23} \text{ m}^{-2} \text{s}^{-1}$  case at four radial locations in the SOL (solid line, separatrix ring, ir=8; dashed line, ir=10; dot-dashed line, ir=12; dotted line, ir=14).

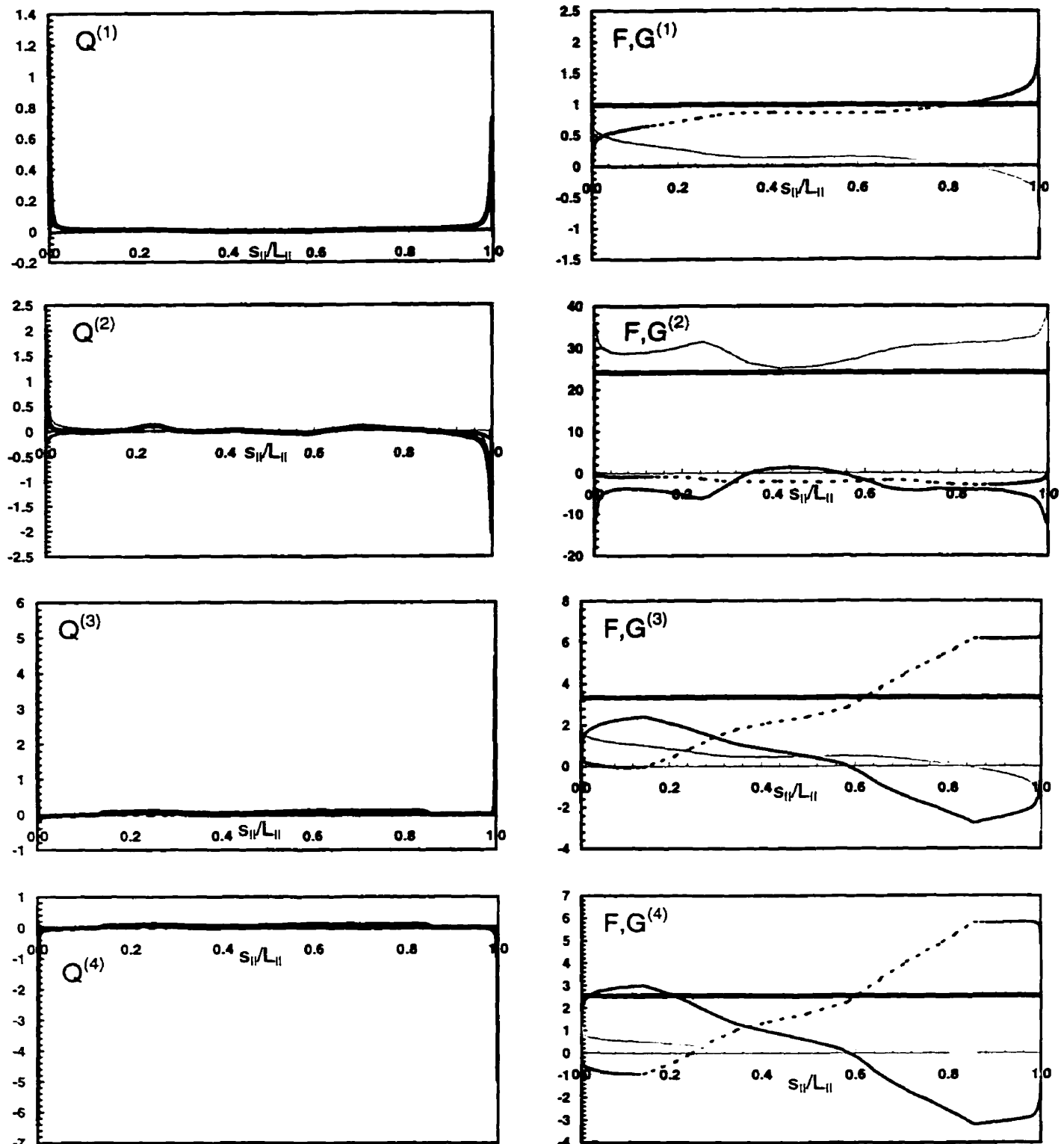


Fig.4.1.2: Along- $\mathbf{B}$  plots of sources and fluxes for the 32 eV,  $10^{23} \text{ m}^{-2} \text{s}^{-1}$  case on the separatrix ring,  $\text{ir}=8$ . Sources: light grey line, cross-field; dark grey line, neutral; black line, flux expansion; dotted line, plasma; thick line, total  $\mathbf{Q}$ . Fluxes: grey line,  $\mathbf{F}$ ; black line,  $\mathbf{G}$ ; dotted line,  $\mathbf{Q}$  integrated from 0 to  $s_{\parallel}$ ; thick line, sum.

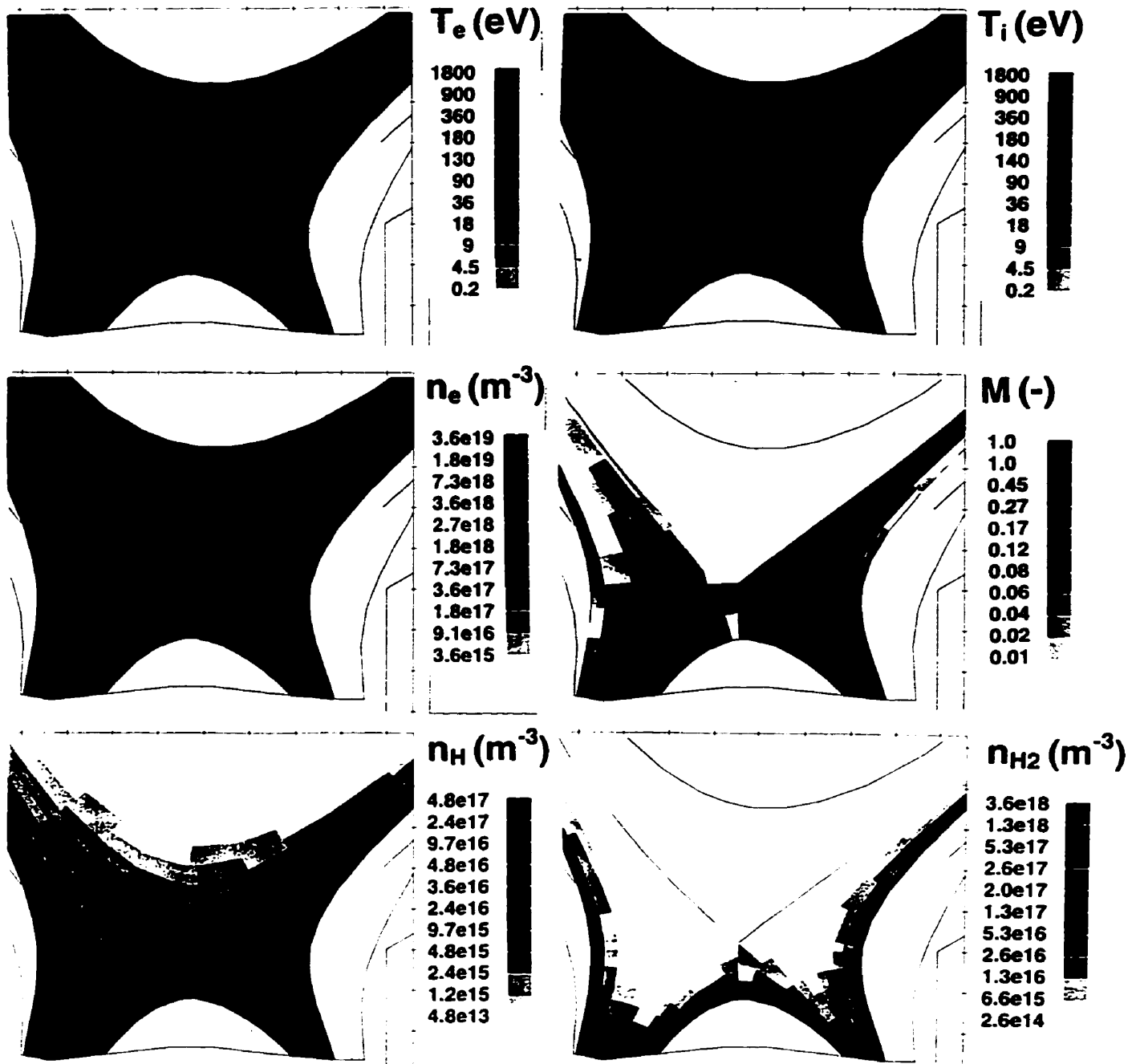


Figure 4.1.3: Poloidal contour plots of plasma variables and neutral densities for the 32 eV case (absolute value of the Mach number is shown).

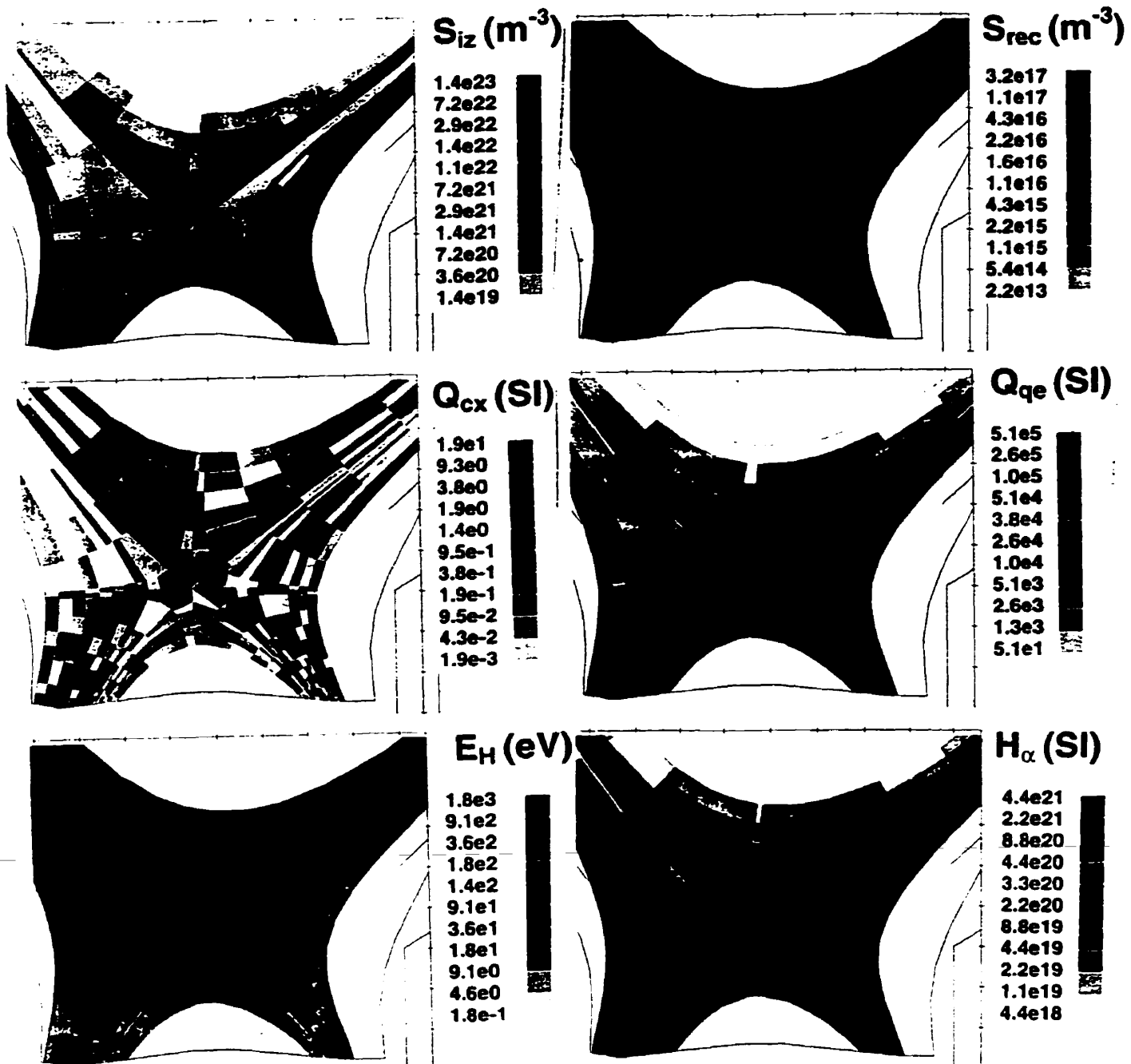


Figure 4.1.4: Poloidal contour plots of neutral sources for the 32 eV case: ionization  $S_{iz}$  [m<sup>-3</sup>s<sup>-1</sup>], recombination  $S_{rec}$  [m<sup>-3</sup>s<sup>-1</sup>], momentum removal  $Q_{cx} = m(u - v_{LH})S_{cx}$  [Pa/m] and electron cooling  $Q_{qe}$  [Wm<sup>-3</sup>] (absolute value of  $Q_{qe}$  is shown). Also included is the average atom energy  $E_H$  [eV] and intensity of H<sub>α</sub> line emission [m<sup>-3</sup>s<sup>-1</sup>].

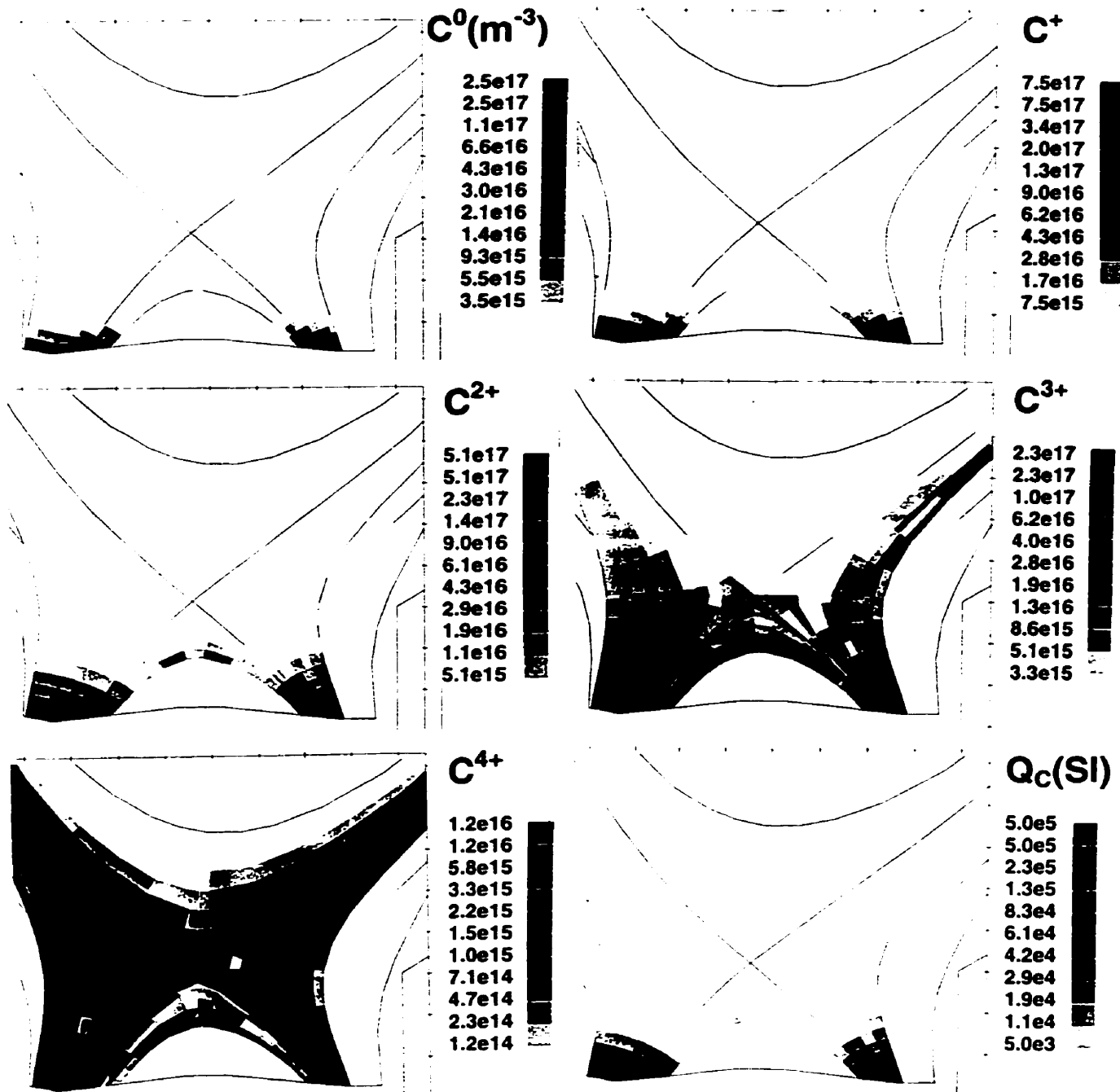


Figure 4.1.5: Poloidal contour plots of the carbon cloud originating at the target for the 32 eV case. Shown are particle densities of the carbon neutrals and the first four ionization states [ $m^{-3}$ ], and the total amount of radiation from all the carbon species [ $Wm^{-3}$ ] (compare  $Q_c$  with  $Q_{qe}$  of the previous plot).

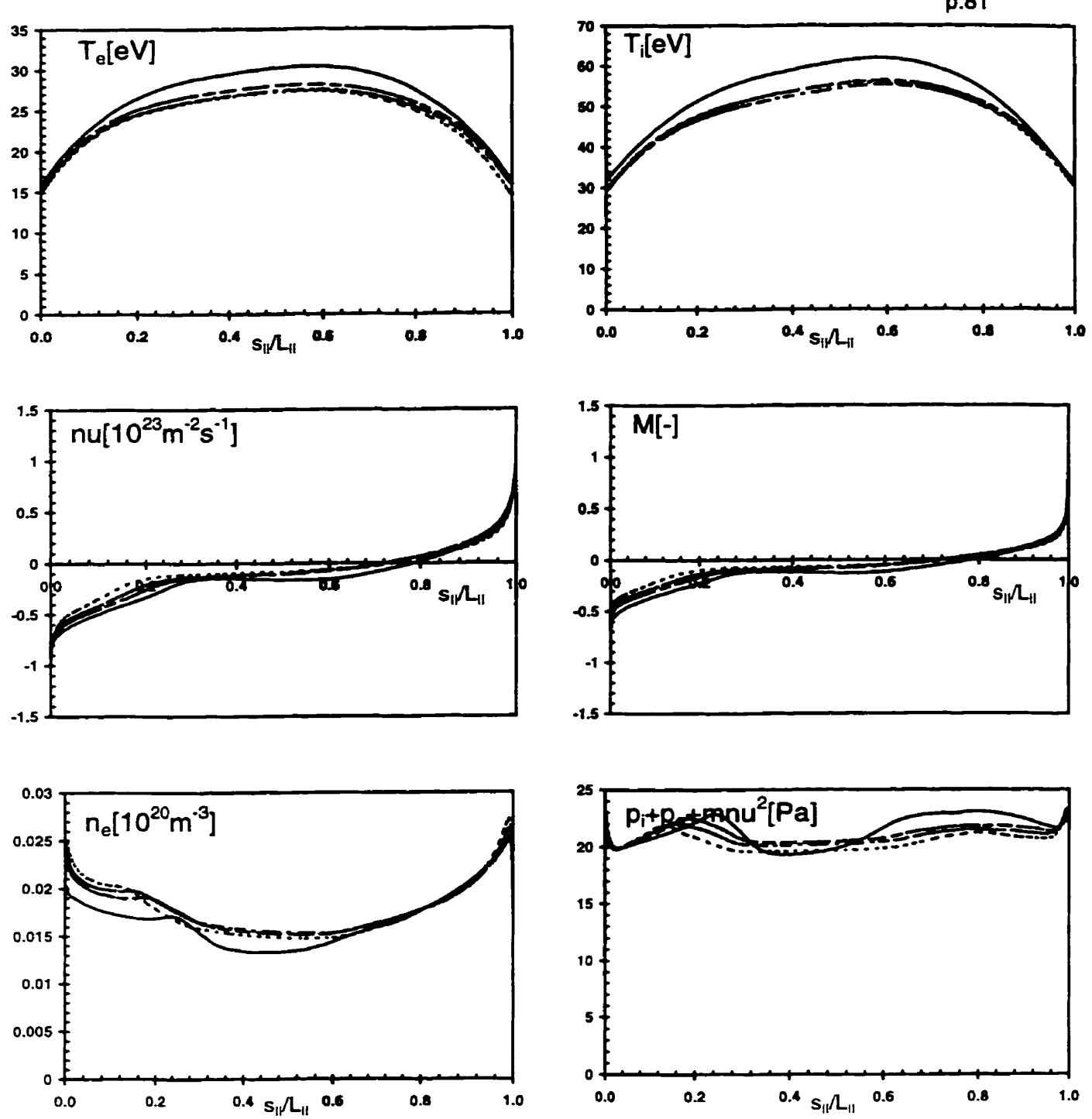


Fig.4.1.6: Along-B plots of plasma variables for the 16 eV,  $10^{23} \text{ m}^{-2} \text{s}^{-1}$  case at four radial locations in the SOL (solid line, separatrix ring,  $ir=8$ ; dashed line,  $ir=10$ ; dot-dashed line,  $ir=12$ ; dotted line,  $ir=14$ ).

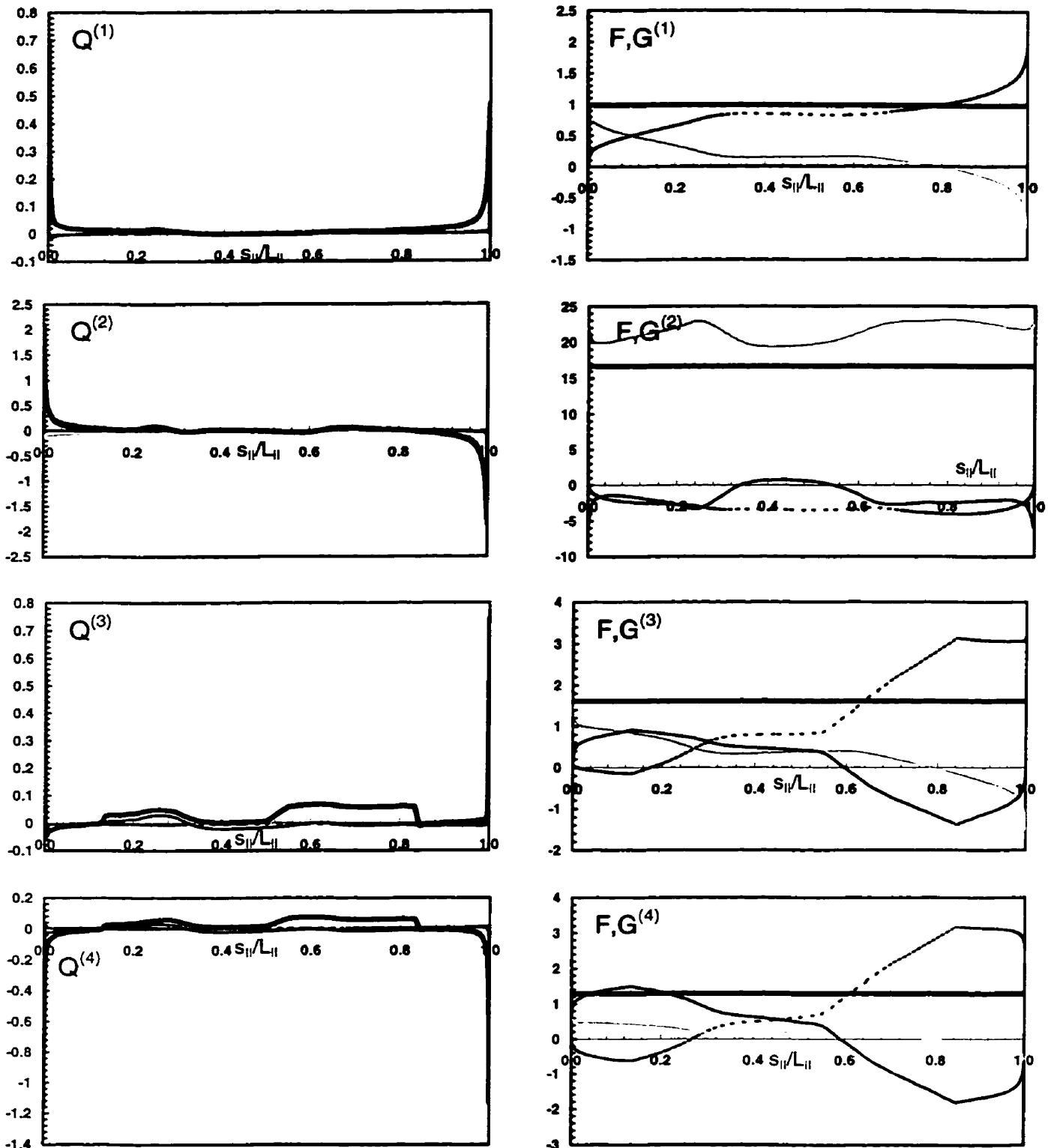


Fig.4.1.7: Along- $\mathbf{B}$  plots of sources and fluxes for the 16 eV,  $10^{23} \text{ m}^{-2}\text{s}^{-1}$  case on the separatrix ring,  $ir=8$ . Sources: light grey line, cross-field; dark grey line, neutral; black line, flux expansion; dotted line, plasma; thick line, total  $\mathbf{Q}$ . Fluxes: grey line,  $\mathbf{F}$ ; black line,  $\mathbf{G}$ ; dotted line,  $\mathbf{Q}$  integrated from 0 to  $s_{\text{II}}$ ; thick line, sum.

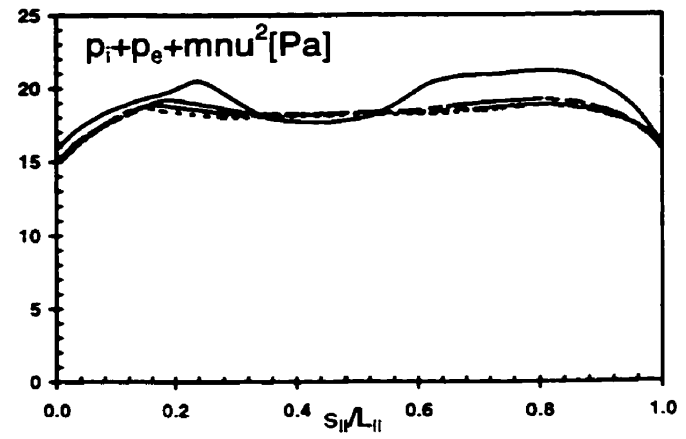
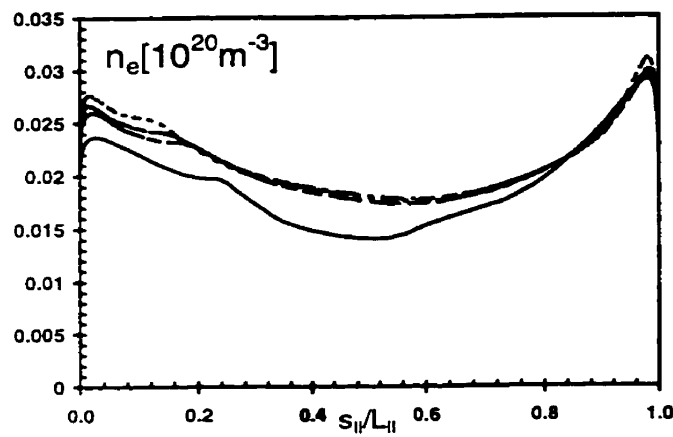
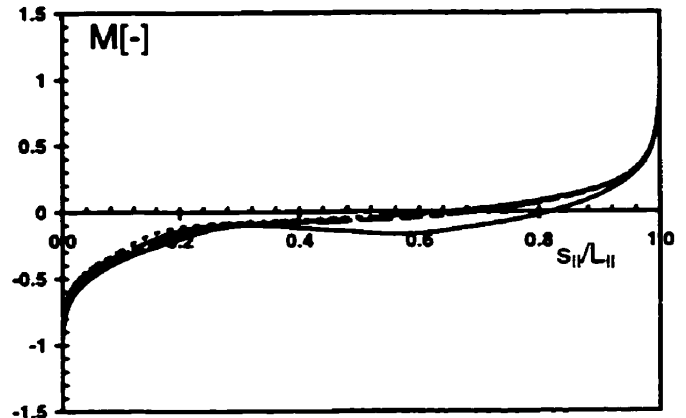
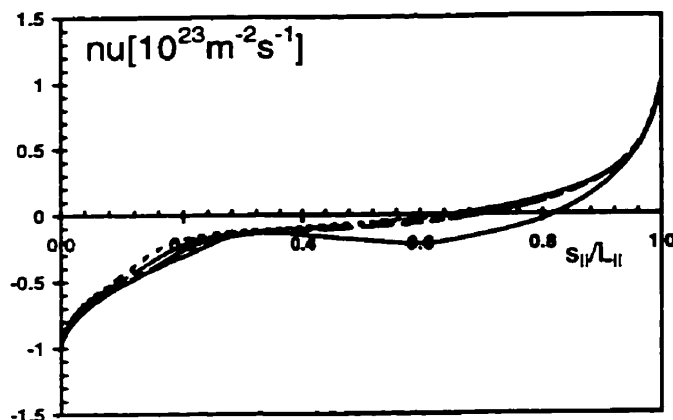
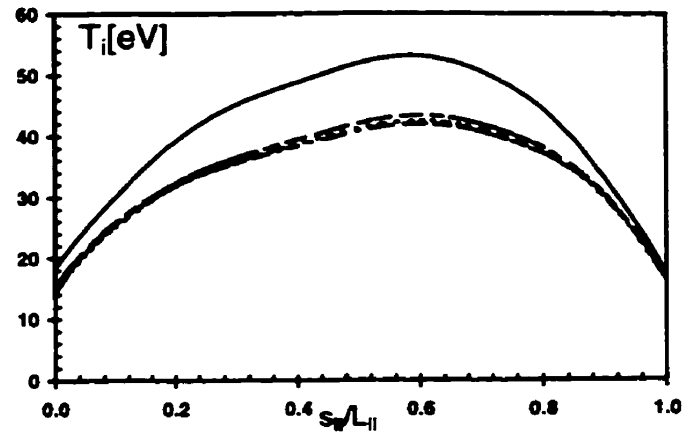
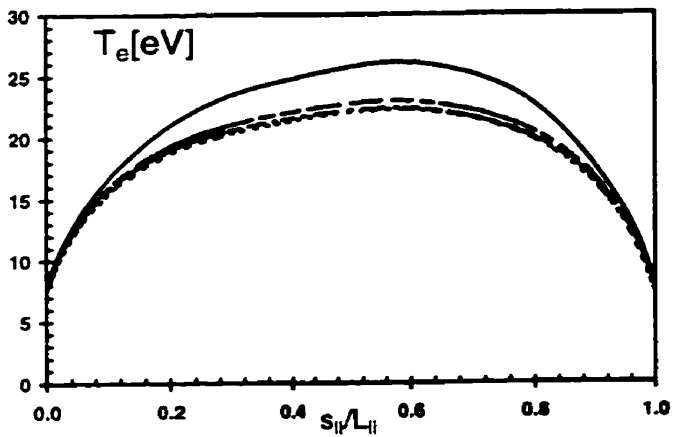


Fig.4.1.8: Along- $\mathbf{B}$  plots of plasma variables for the 8 eV,  $10^{23} \text{m}^{-2} \text{s}^{-1}$  case at four radial locations in the SOL (solid line, separatrix ring, ir=8; dashed line, ir=10; dot-dashed line, ir=12; dotted line, ir=14).

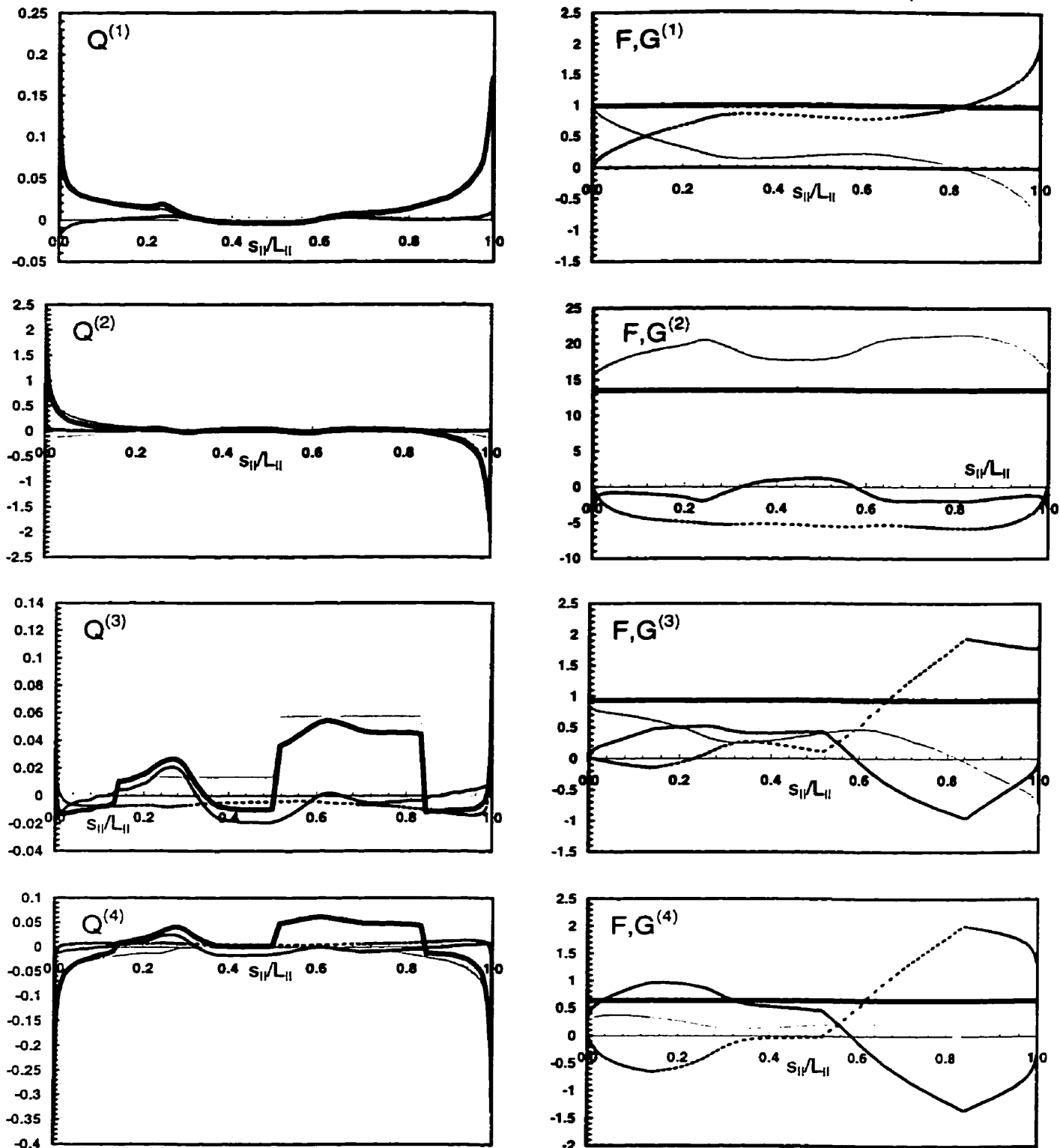


Fig.4.1.9: Along-B plots of sources and fluxes for the 8 eV,  $10^{23} \text{ m}^{-2} \text{s}^{-1}$  case on the separatrix ring, ir=8. Sources: light grey line, cross-field; dark grey line, neutral; black line, flux expansion; dotted line, plasma; thick line, total  $Q$ . Fluxes: grey line,  $F$ ; black line,  $G$ ; dotted line,  $Q$  integrated from 0 to  $s_{II}$ ; thick line, sum.

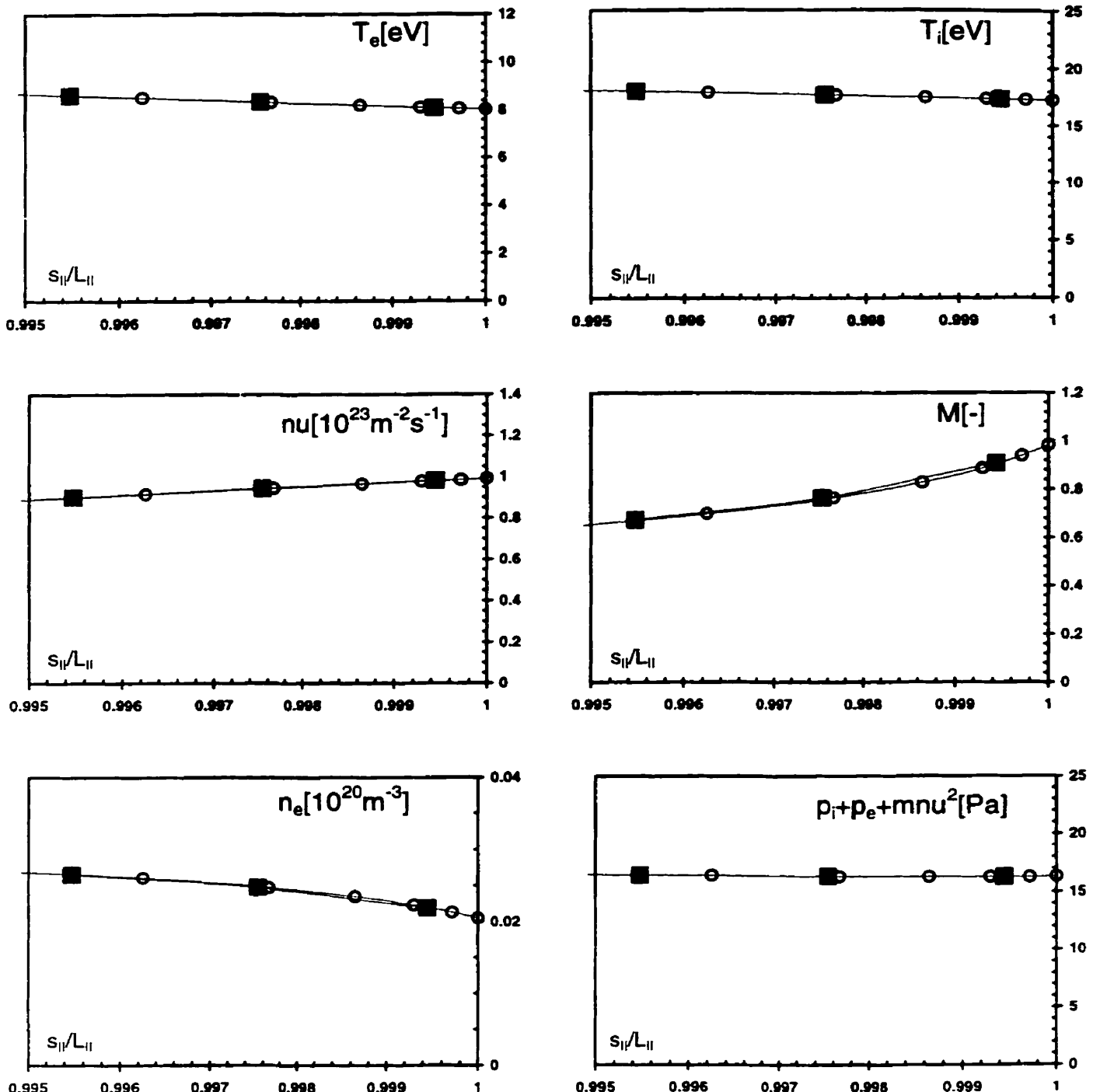


Fig.4.1.10: Along- $\mathbf{B}$  plots of plasma variables for the 8 eV,  $10^{23} \text{ m}^{-2} \text{s}^{-1}$  case in the vicinity of the inner target on the separatrix ring,  $ir=8$ . Circles indicate fine grid point values, while squares indicate coarse grid points.

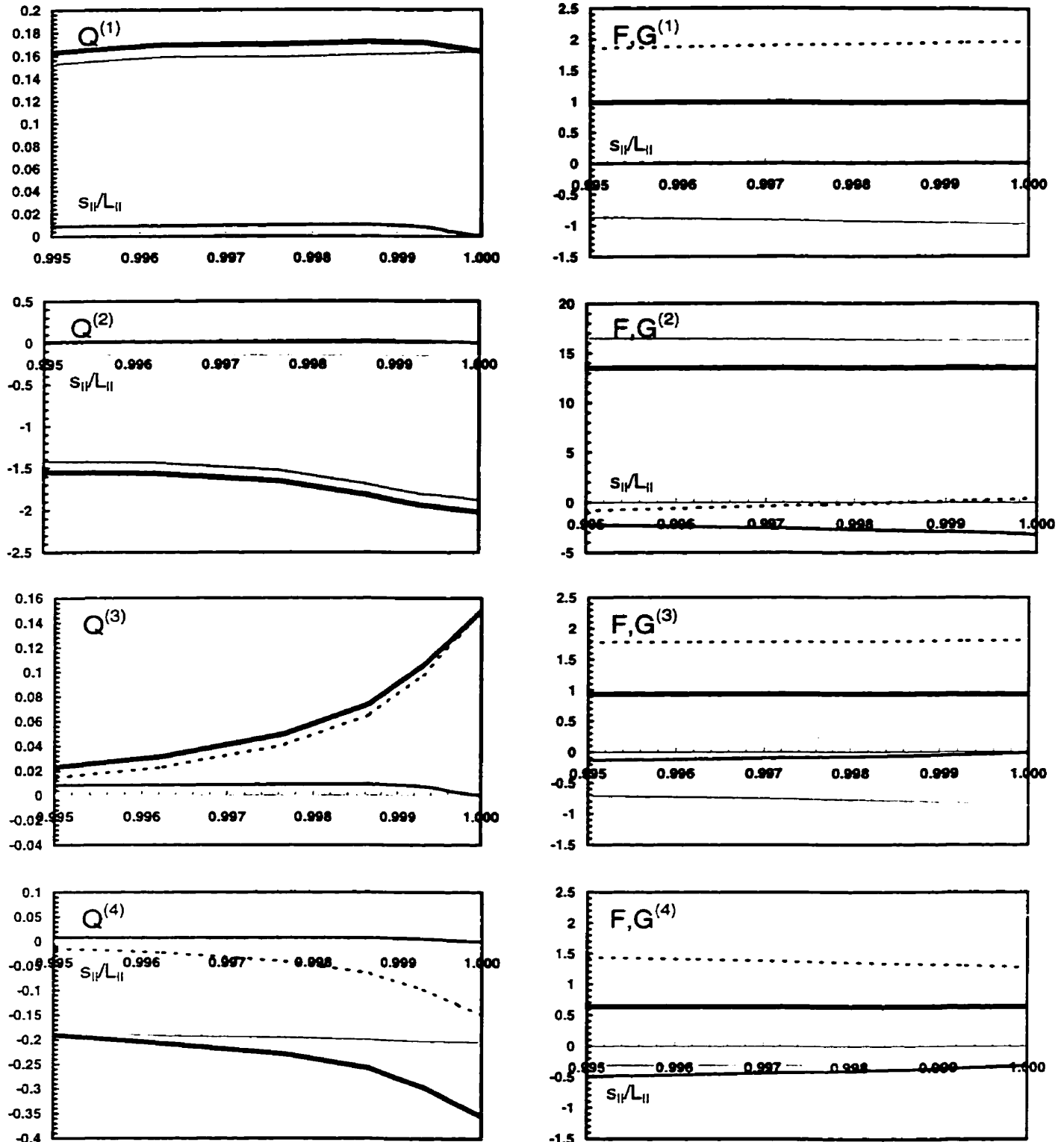


Fig.4.1.11: Along- $\mathbf{B}$  plots of sources and fluxes for the 8 eV,  $10^{23} \text{ m}^{-2} \text{ s}^{-1}$  case in the vicinity of the inner target on the separatrix ring,  $ir=8$ . Sources: light grey line, cross-field; dark grey line, neutral; black line, flux expansion; dotted line, plasma; thick line, total  $Q$ . Fluxes: grey line,  $F$ ; black line,  $G$ ; dotted line,  $Q$  integrated from 0 to  $s_{||}$ ; thick line, sum.

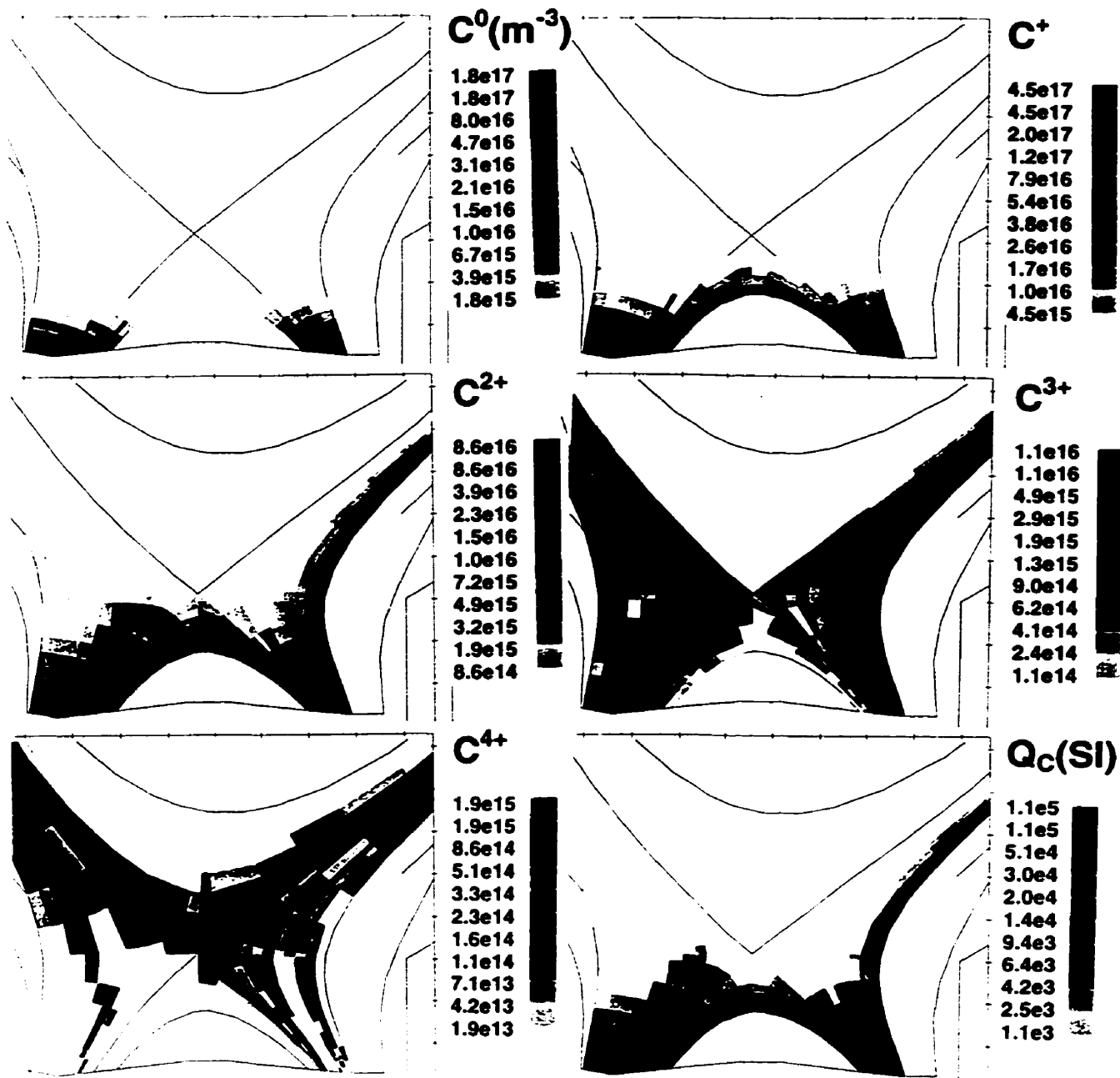


Figure 4.1.12 Poloidal contour plots of the carbon cloud originating at the target for the 8 eV case. Shown are particle densities of the carbon neutrals and the first four ionization states [ $m^{-3}$ ], and the total amount of radiation from all the carbon species [ $Wm^{-3}$ ] (compare  $Q_c$  with  $Q_{qe}$  of the previous plot).

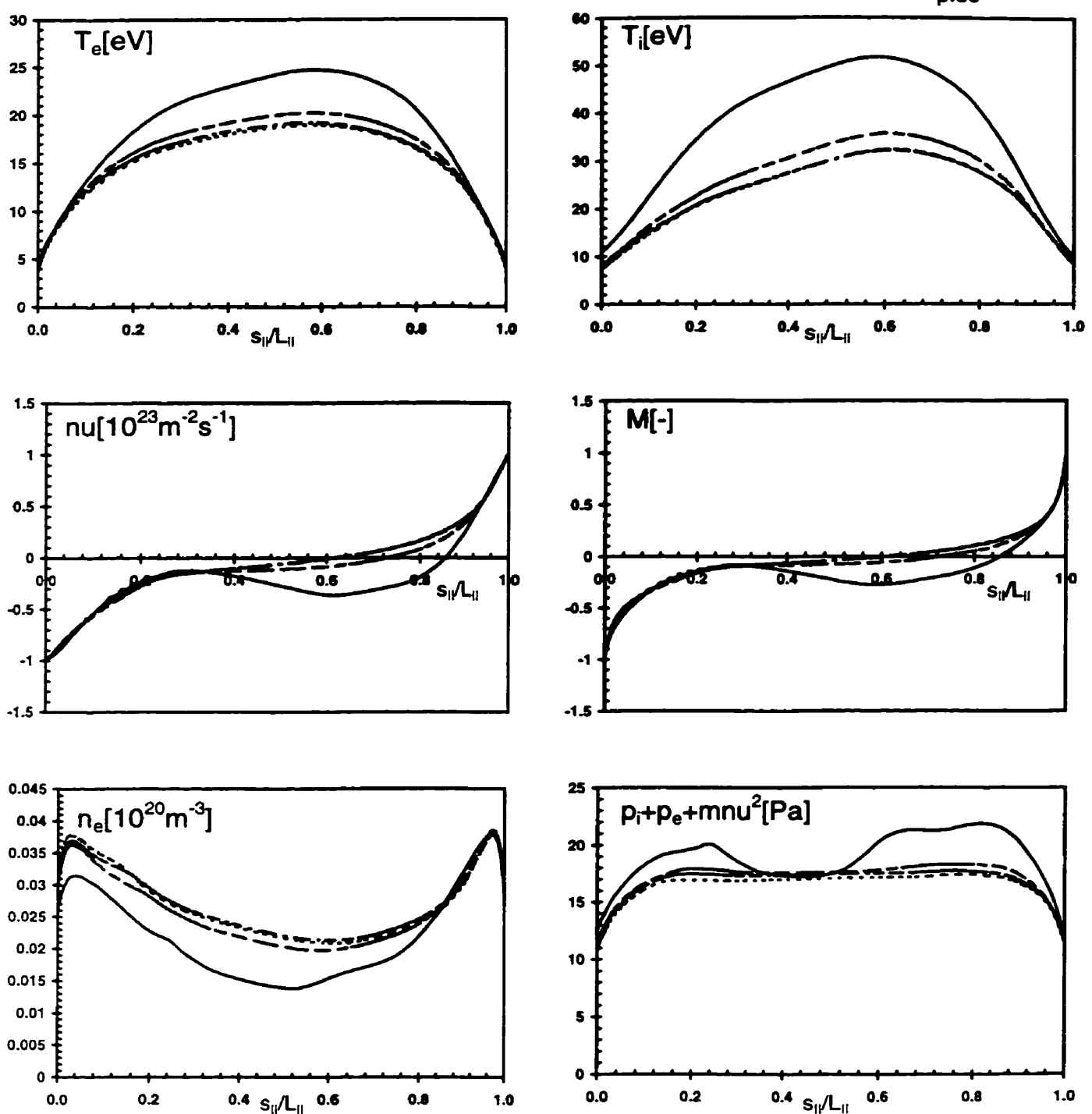


Fig.4.1.13: Along-B plots of plasma variables for the 4 eV,  $10^{23} \text{ m}^{-2} \text{s}^{-1}$  case at four radial locations in the SOL (solid line, separatrix ring,  $ir=8$ ; dashed line,  $ir=10$ ; dot-dashed line,  $ir=12$ ; dotted line,  $ir=14$ ).

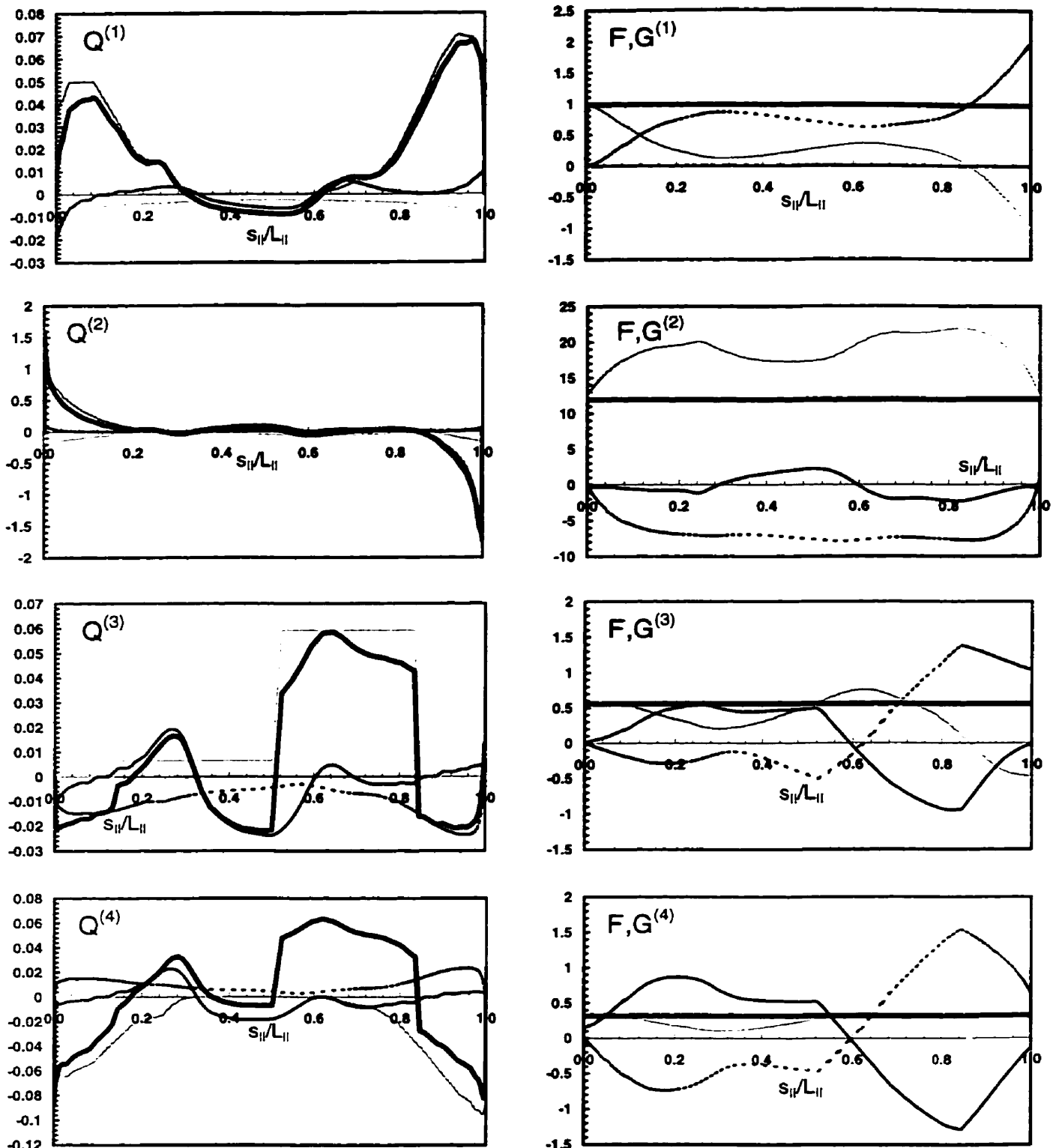


Fig.4.1.14: Along- $\mathbf{B}$  plots of sources and fluxes for the 4 eV,  $10^{23} \text{ m}^{-2}\text{s}^{-1}$  case on the separatrix ring, ir=8. Sources: light grey line, cross-field; dark grey line, neutral; black line, flux expansion; dotted line, plasma; thick line, total  $Q$ . Fluxes: grey line,  $F$ ; black line,  $G$ ; dotted line,  $Q$  integrated from 0 to  $s_{||}$ ; thick line, sum.

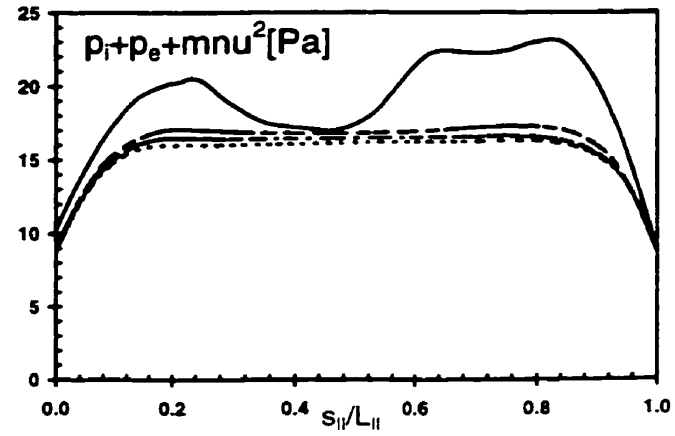
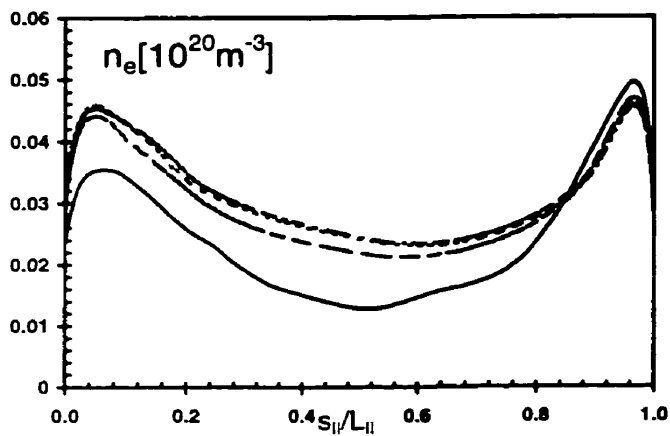
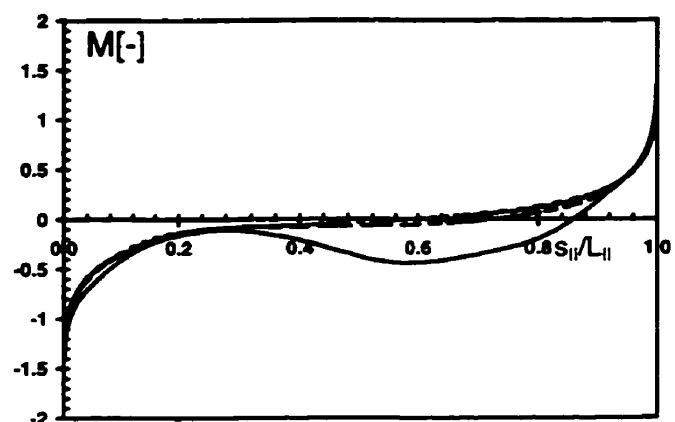
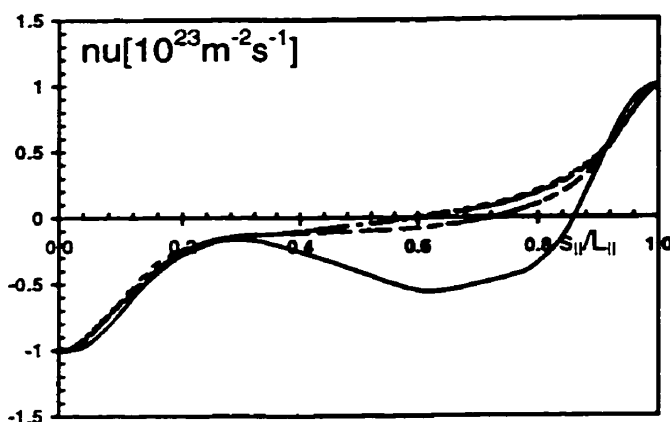
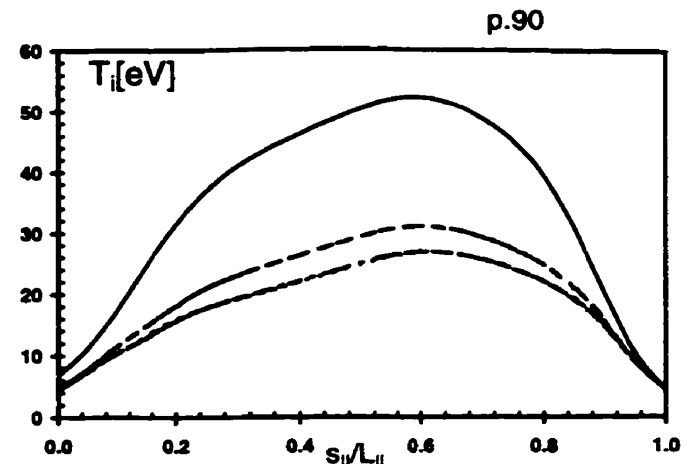
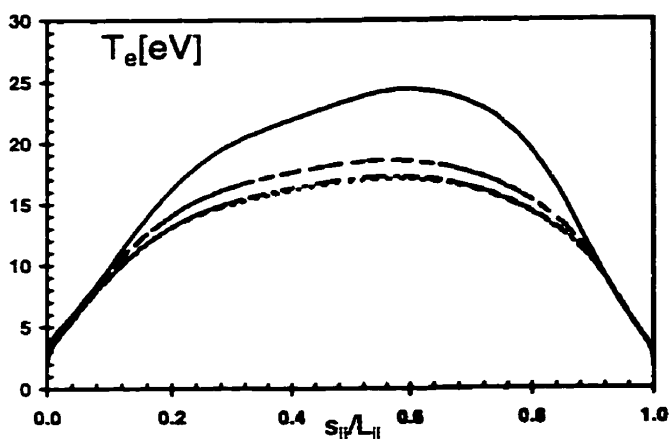


Fig.4.1.15: Along-B plots of plasma variables for the 2 eV,  $10^{23} \text{ m}^{-2} \text{s}^{-1}$  case at four radial locations in the SOL (solid line, separatrix ring, ir=8; dashed line, ir=10; dot-dashed line, ir=12; dotted line, ir=14).

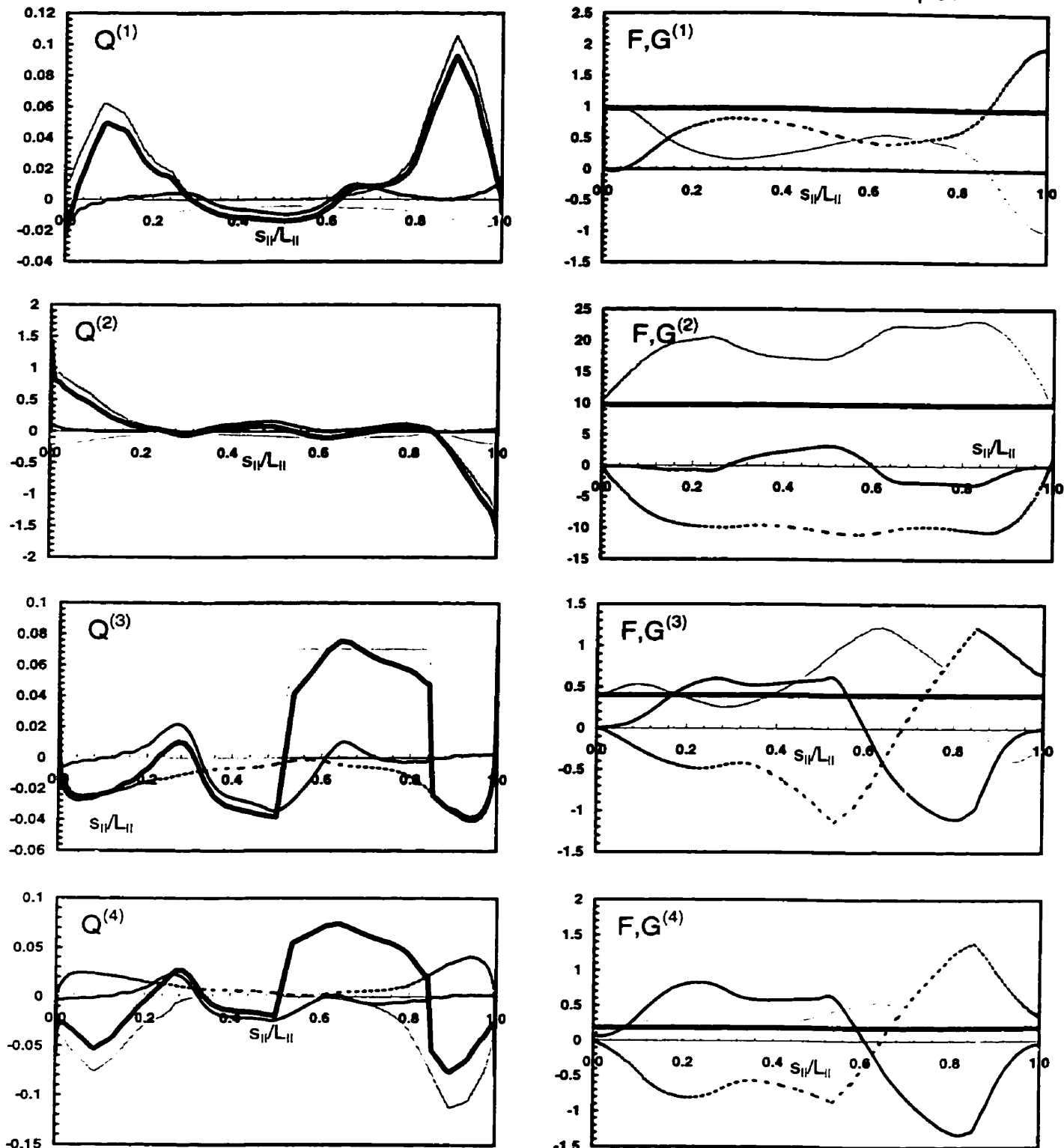


Fig.4.1.16: Along- $\mathbf{B}$  plots of sources and fluxes for the 2 eV,  $10^{23} \text{ m}^{-2} \text{s}^{-1}$  case on the separatrix ring,  $ir=8$ . Sources: light grey line, cross-field; dark grey line, neutral; black line, flux expansion; dotted line, plasma; thick line, total  $Q$ . Fluxes: grey line,  $F$ ; black line,  $G$ ; dotted line,  $\mathbf{Q}$  integrated from 0 to  $s_{II}$ ; thick line, sum.

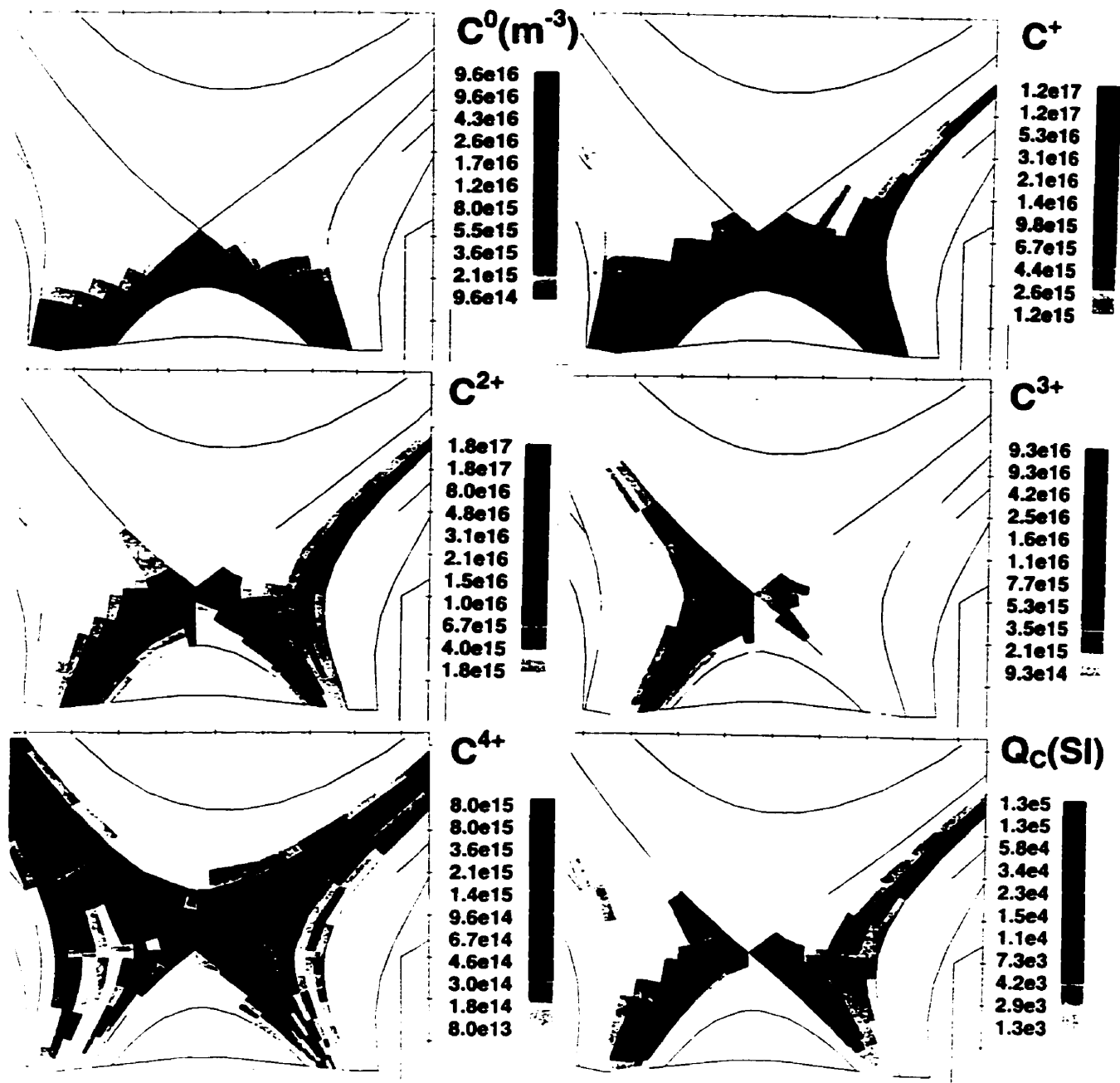


Figure 4.1.17 Poloidal contour plots of the carbon cloud originating at the target for the 2 eV case. Shown are particle densities of the carbon neutrals and the first four ionization states [m<sup>-3</sup>], and the total amount of radiation from all the carbon species [Wm<sup>-3</sup>] (compare Q<sub>c</sub> with Q<sub>qe</sub> of the previous plot).

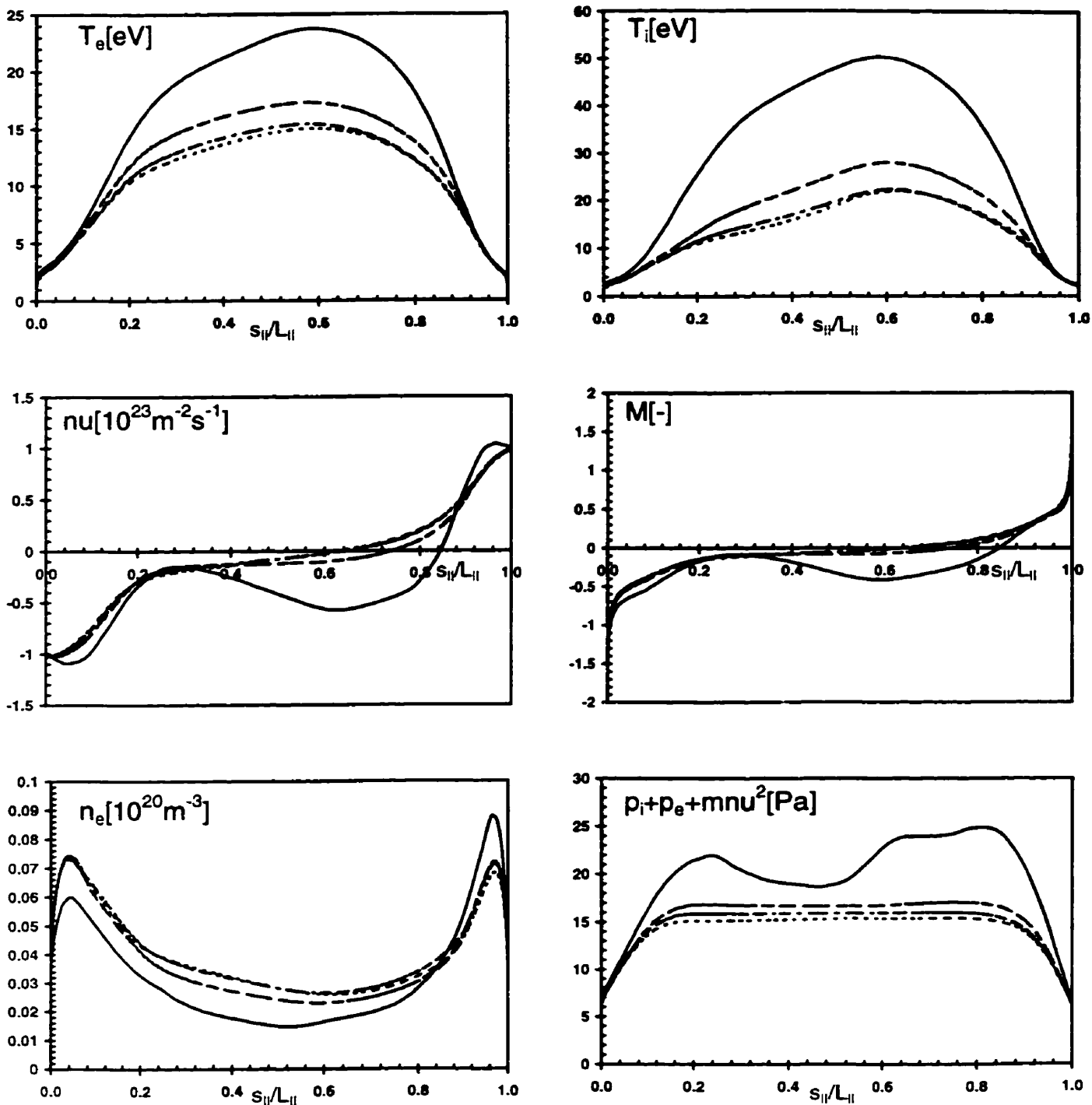


Fig.4.1.18: Along-B plots of plasma variables for the  $1 \text{ eV}, 10^{23} \text{ m}^{-2} \text{s}^{-1}$  case at four radial locations in the SOL (solid line, separatrix ring, ir=8; dashed line, ir=10; dot-dashed line, ir=12; dotted line, ir=14).

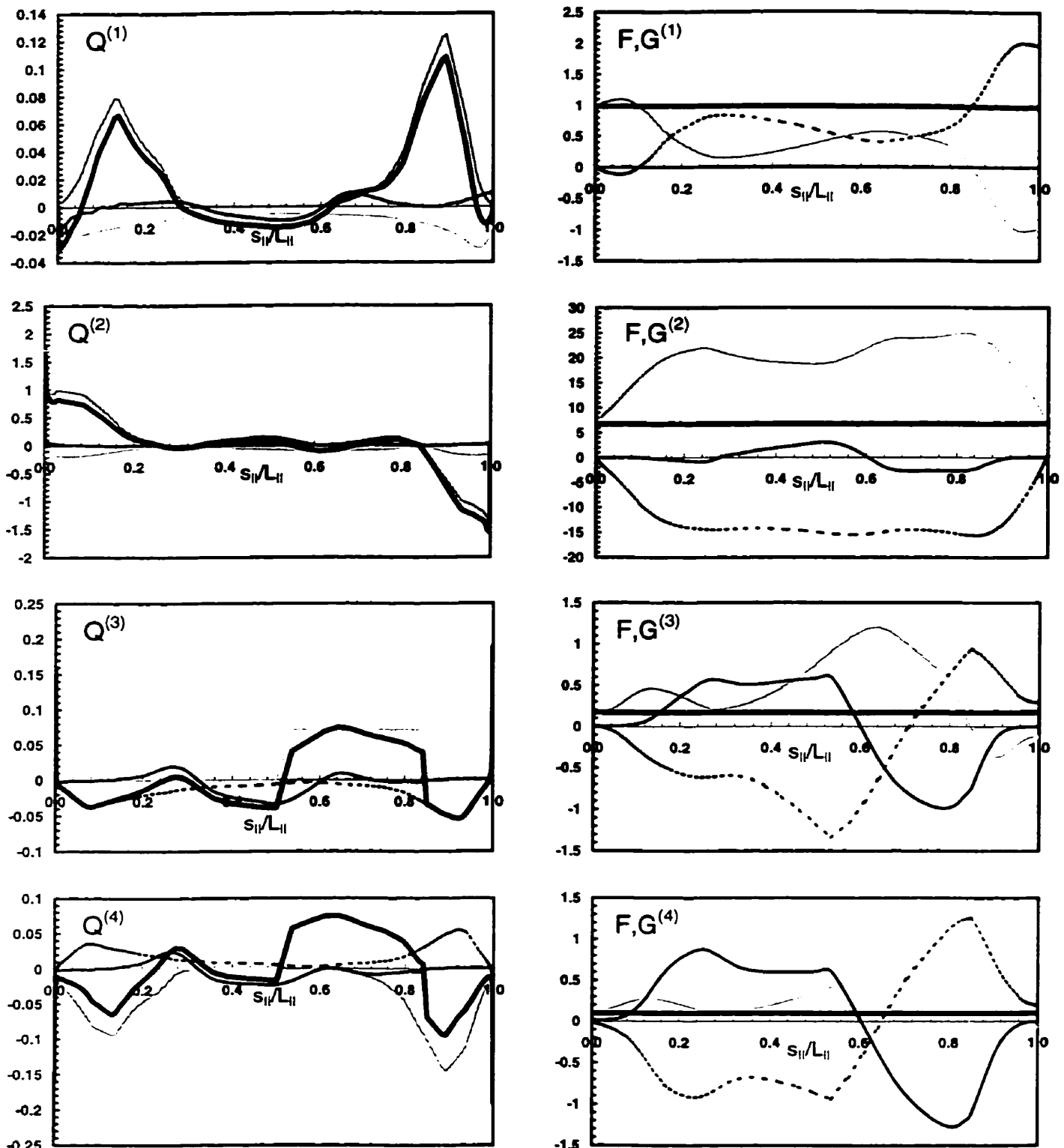


Fig.4.1.19: Along- $\mathbf{B}$  plots of sources and fluxes for the 1 eV,  $10^{23} \text{ m}^{-2} \text{ s}^{-1}$  case on the separatrix ring,  $ir=8$ . Sources: light grey line, cross-field; dark grey line, neutral; black line, flux expansion; dotted line, plasma; thick line, total  $\mathbf{Q}$ . Fluxes: grey line,  $\mathbf{F}$ ; black line,  $\mathbf{G}$ ; dotted line,  $\mathbf{Q}$  integrated from 0 to  $s_{\parallel}$ ; thick line, sum.

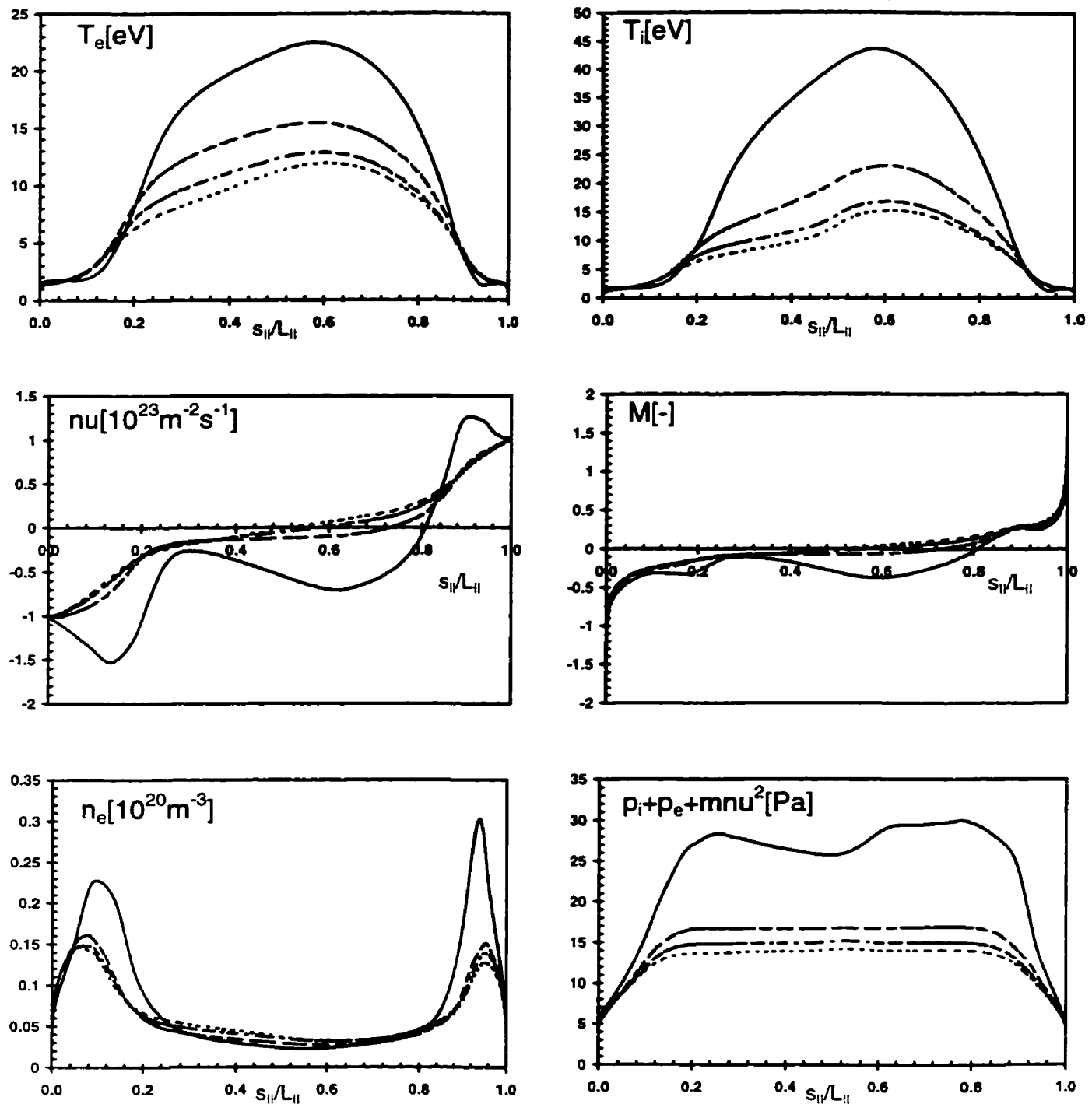


Fig.4.1.20: Along- $\mathbf{B}$  plots of plasma variables for the  $0.5 \text{ eV}, 10^{23} \text{ m}^{-3}$  case at four radial locations in the SOL (solid line, separatrix ring,  $ir=8$ ; dashed line,  $ir=10$ ; dot-dashed line,  $ir=12$ ; dotted line,  $ir=14$ ).

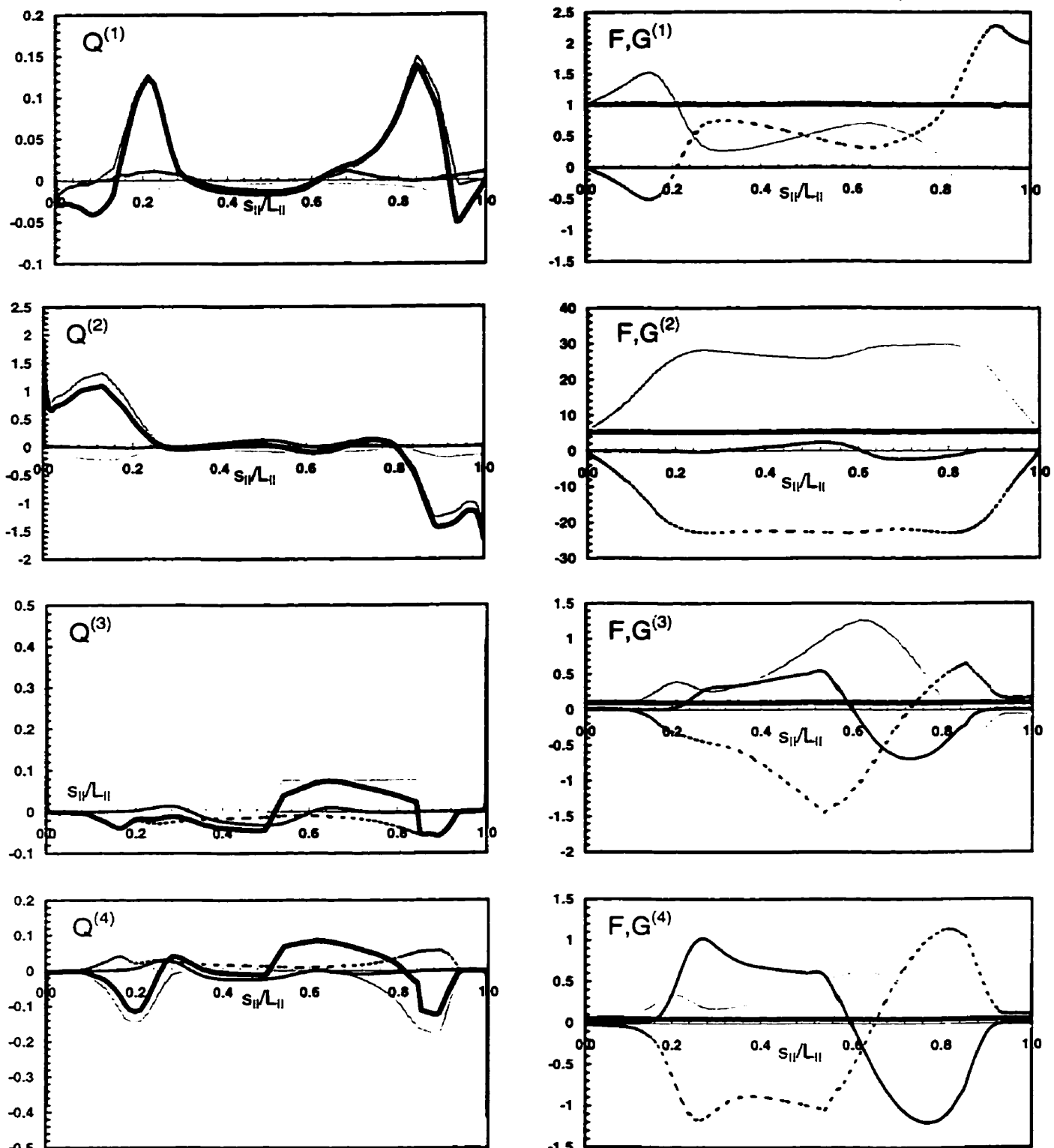


Fig.4.1.21: Along- $\mathbf{B}$  plots of sources and fluxes for the  $0.5 \text{ eV}, 10^{23} \text{ m}^{-2} \text{s}^{-1}$  case on the separatrix ring,  $ir=8$ . Sources: light grey line, cross-field; dark grey line, neutral; black line, flux expansion; dotted line, plasma; thick line, total  $Q$ . Fluxes: grey line,  $F$ ; black line,  $G$ ; dotted line,  $Q$  integrated from 0 to  $s_{||}$ ; thick line, sum.

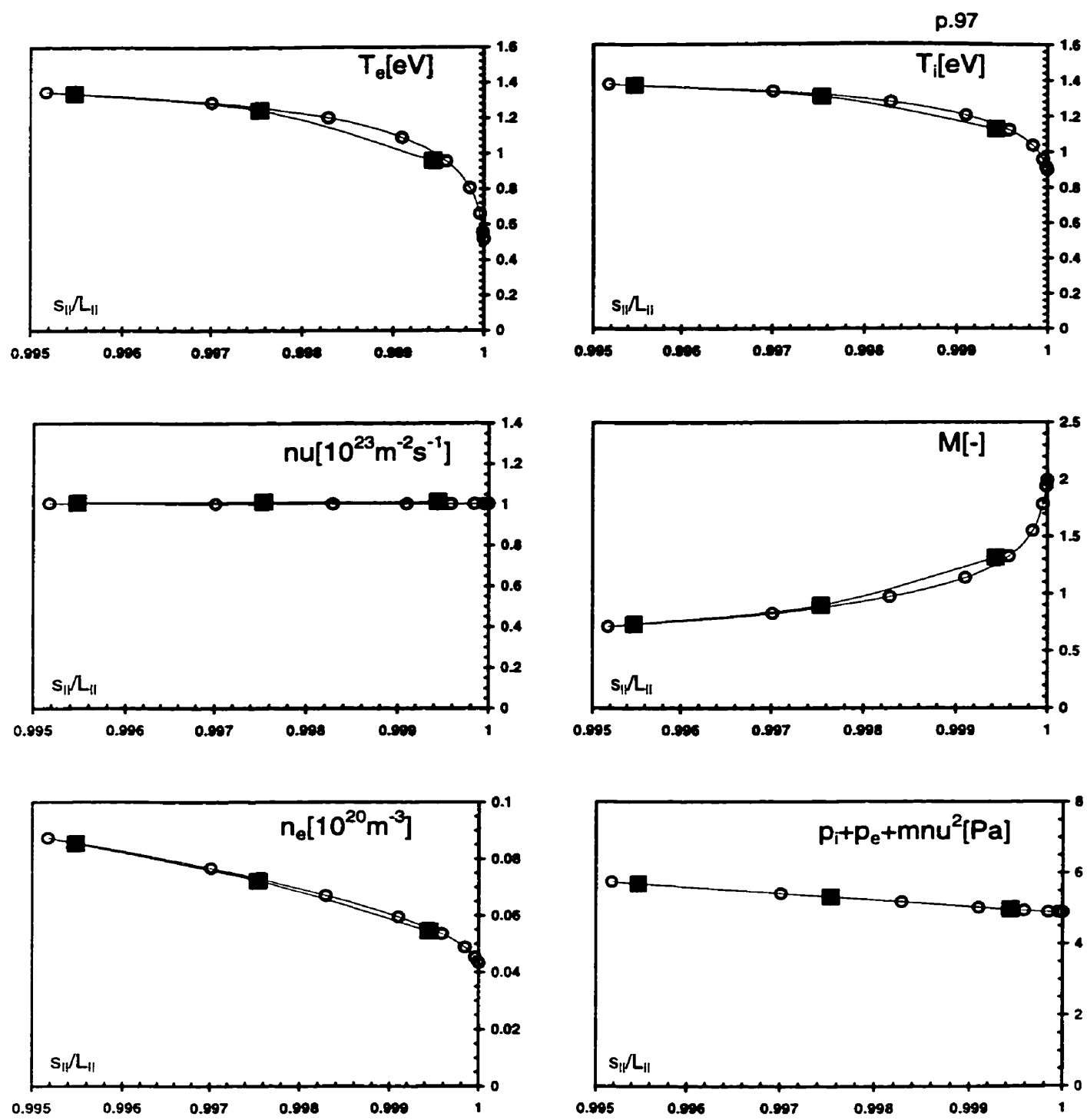


Fig.4.1.22: Along-B plots of plasma variables for the 0.5 eV,  $10^{23} \text{ m}^{-2} \text{s}^{-1}$  case in the vicinity of the inner target on the separatrix ring,  $ir=8$ . Circles indicate fine grid point values, while squares indicate coarse grid points.

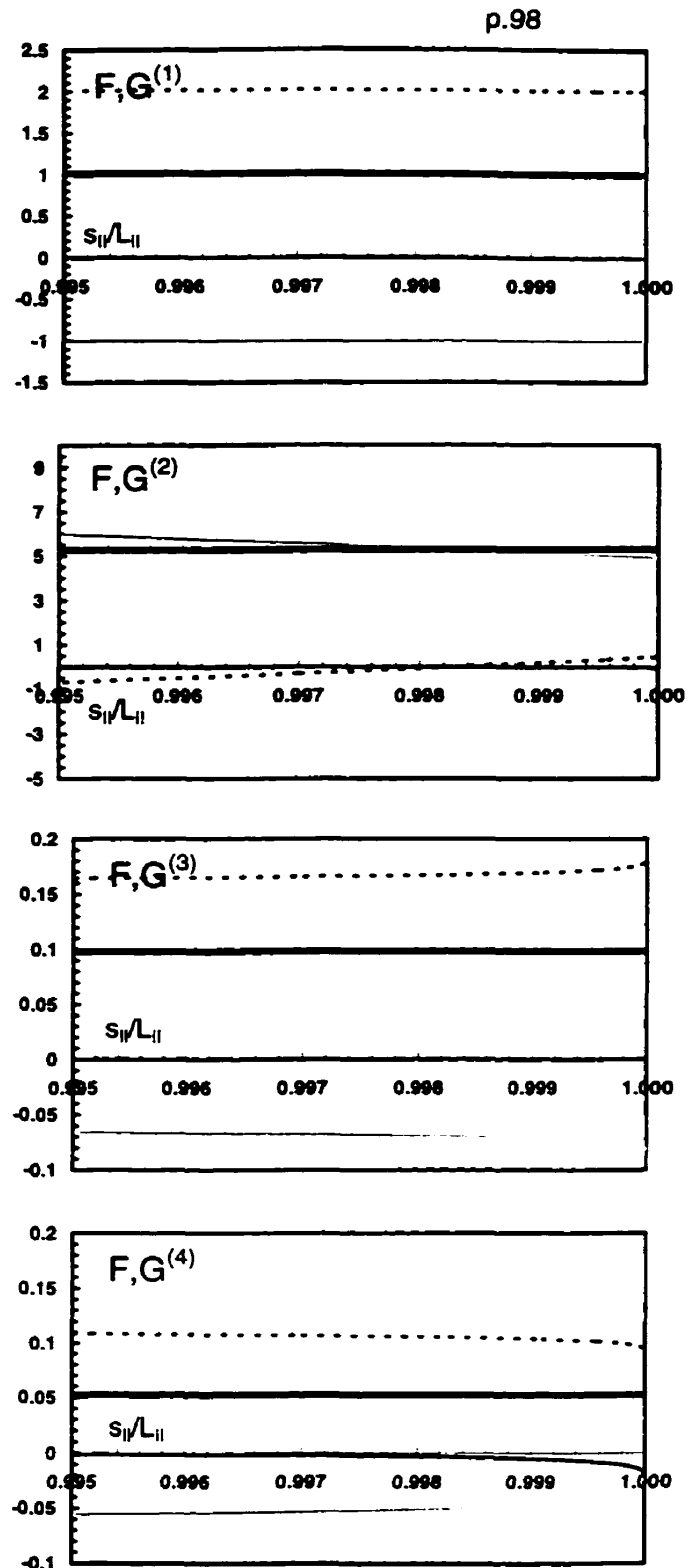
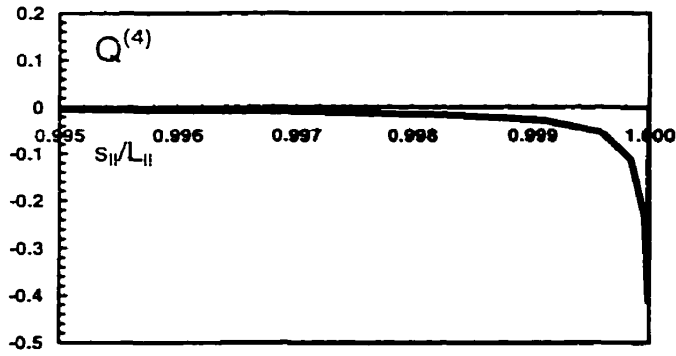
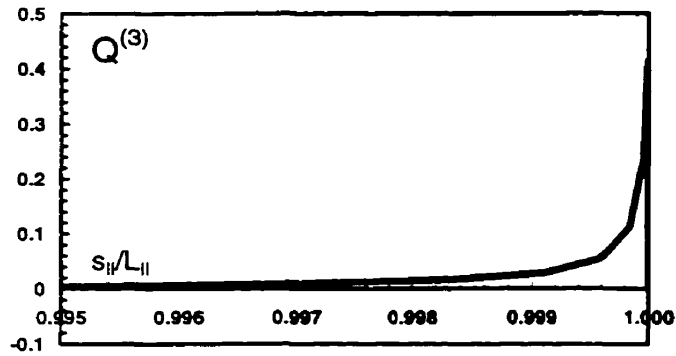
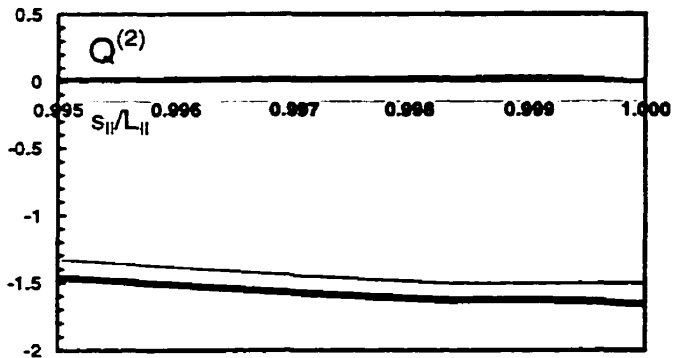
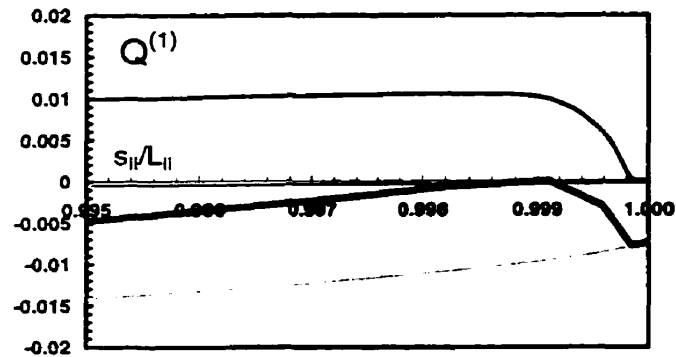


Fig.4.1.23: Along-B plots of sources and fluxes for the 0.5 eV,  $10^{23} \text{ m}^{-2} \text{s}^{-1}$  case in the vicinity of the inner target on the separatrix ring, ir=8. Sources: light grey line, cross-field; dark grey line, neutral; black line, flux expansion; dotted line, plasma; thick line, total  $\mathbf{Q}$ . Fluxes: grey line,  $\mathbf{F}$ ; black line,  $\mathbf{G}$ ; dotted line,  $\mathbf{Q}$  integrated from 0 to  $s_{||}$ ; thick line, sum. The energy sources are dominated by the electric field term of the plasma source.

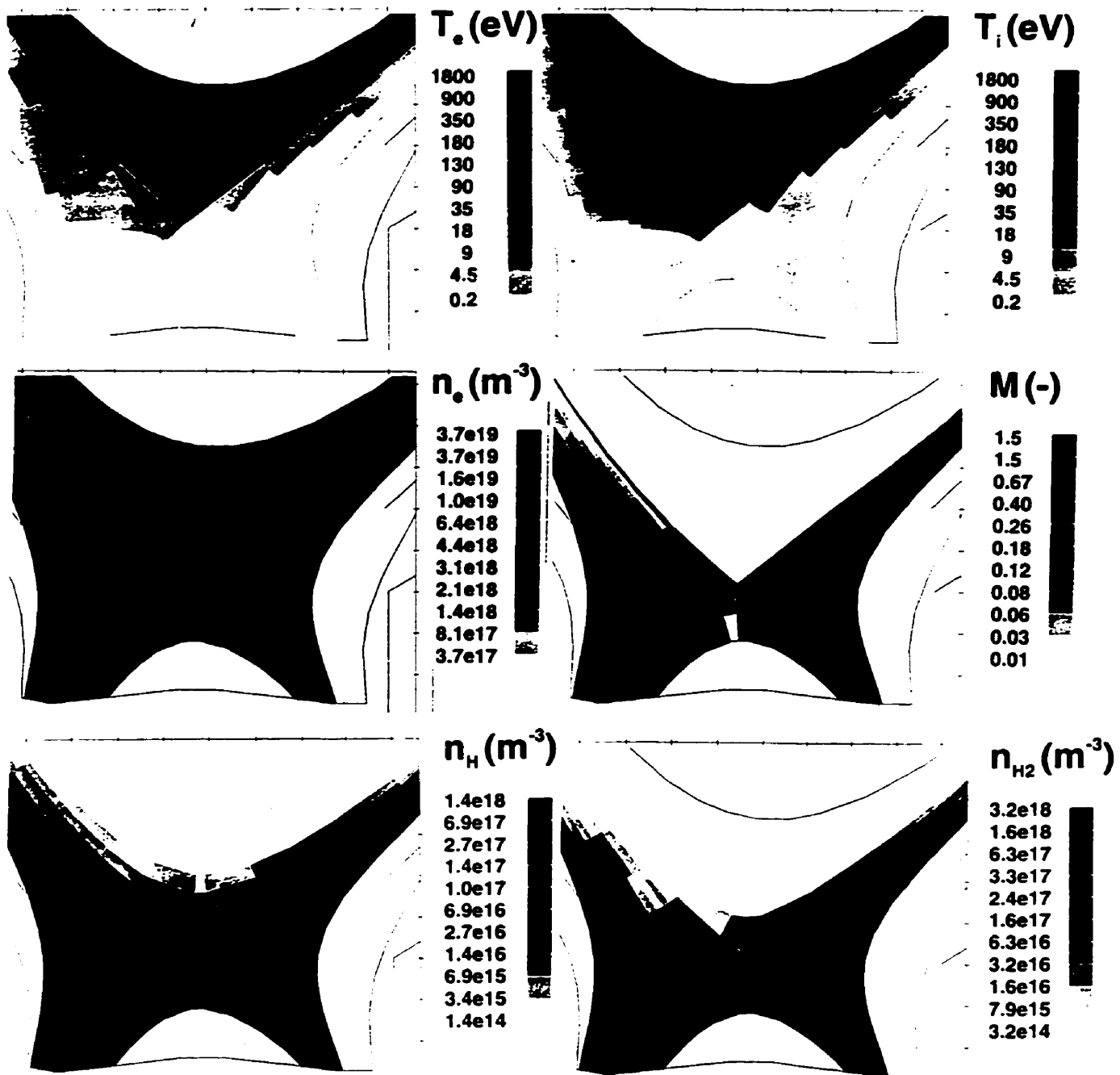


Figure 4.1.24 Poloidal contour plots of plasma variables and neutral densities for the 0.5 eV case (absolute value of the Mach number is shown).

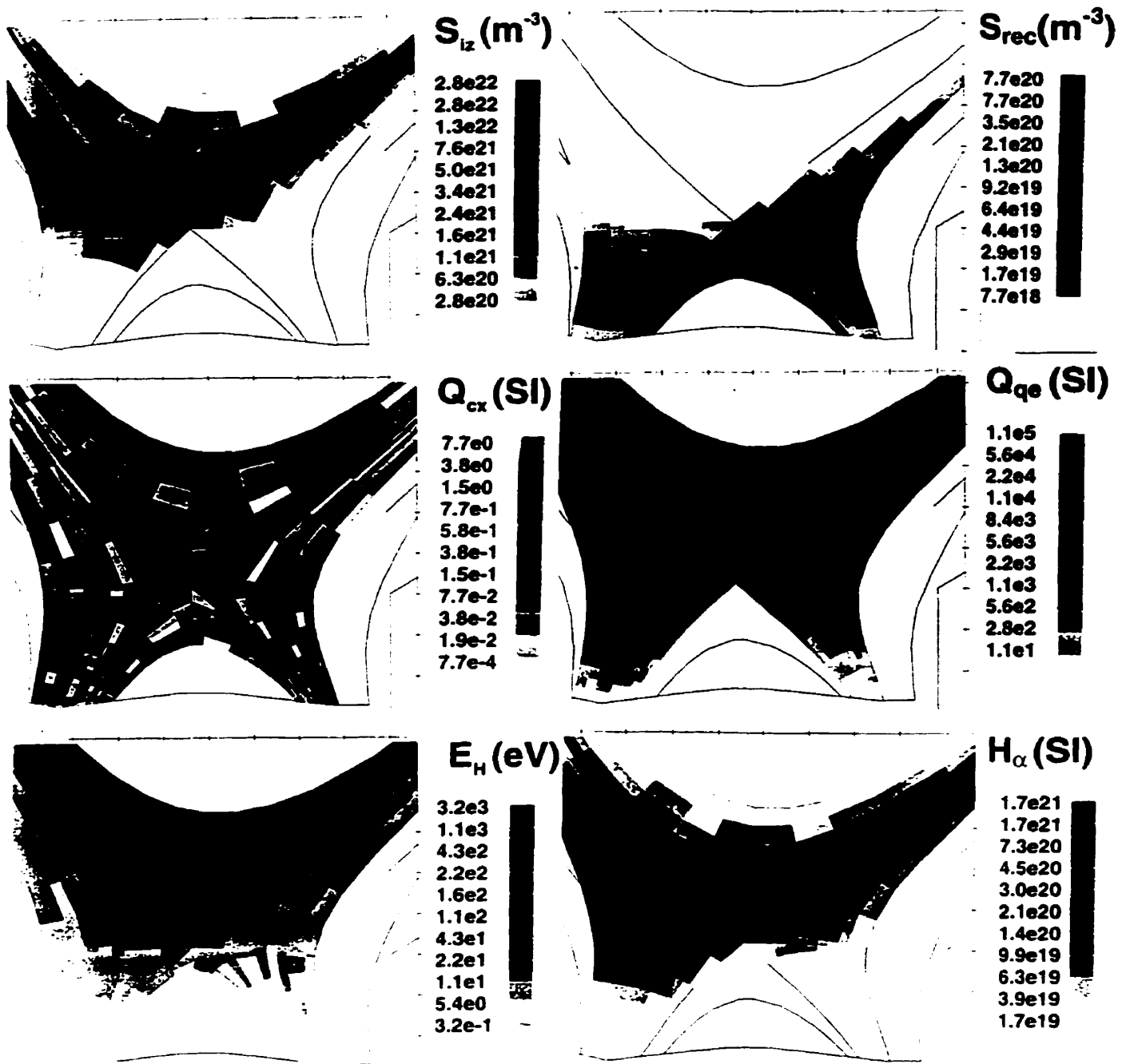


Figure 4.1.25 Poloidal contour plots of neutral sources for the 0.5 eV case: ionization  $S_{iz}$ , recombination  $S_{rec}$ , momentum removal  $Q_{cx} = m(u - v_{LH})S_{cx}$  [Pa/m] and electron cooling  $Q_{qe}$  [ $\text{Wm}^{-3}$ ] (absolute value of  $Q_{qe}$  is shown). Also included is the average atom energy  $E_H$  [eV] and intensity of  $H_\alpha$  line emission [ $\text{m}^3\text{s}^{-1}$ ].

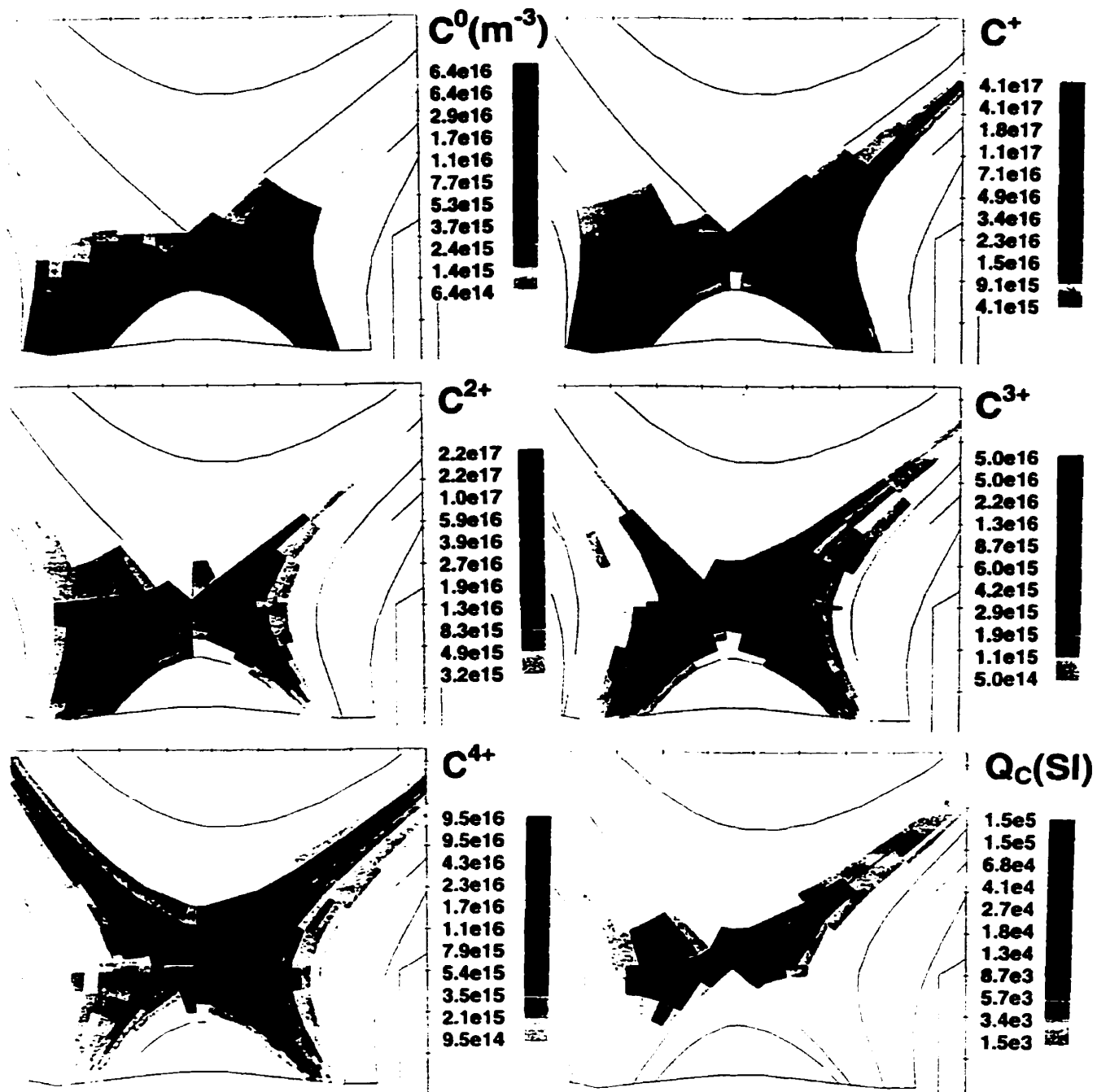


Figure 4.1.26 Poloidal contour plots of the carbon cloud originating at the target for the 0.5 eV case. Shown are particle densities of the carbon neutrals and the first four ionization states [ $m^{-3}$ ], and the total amount of radiation from all the carbon species [ $W m^{-3}$ ] (compare  $Q_c$  with  $Q_{ce}$  of the previous plot).

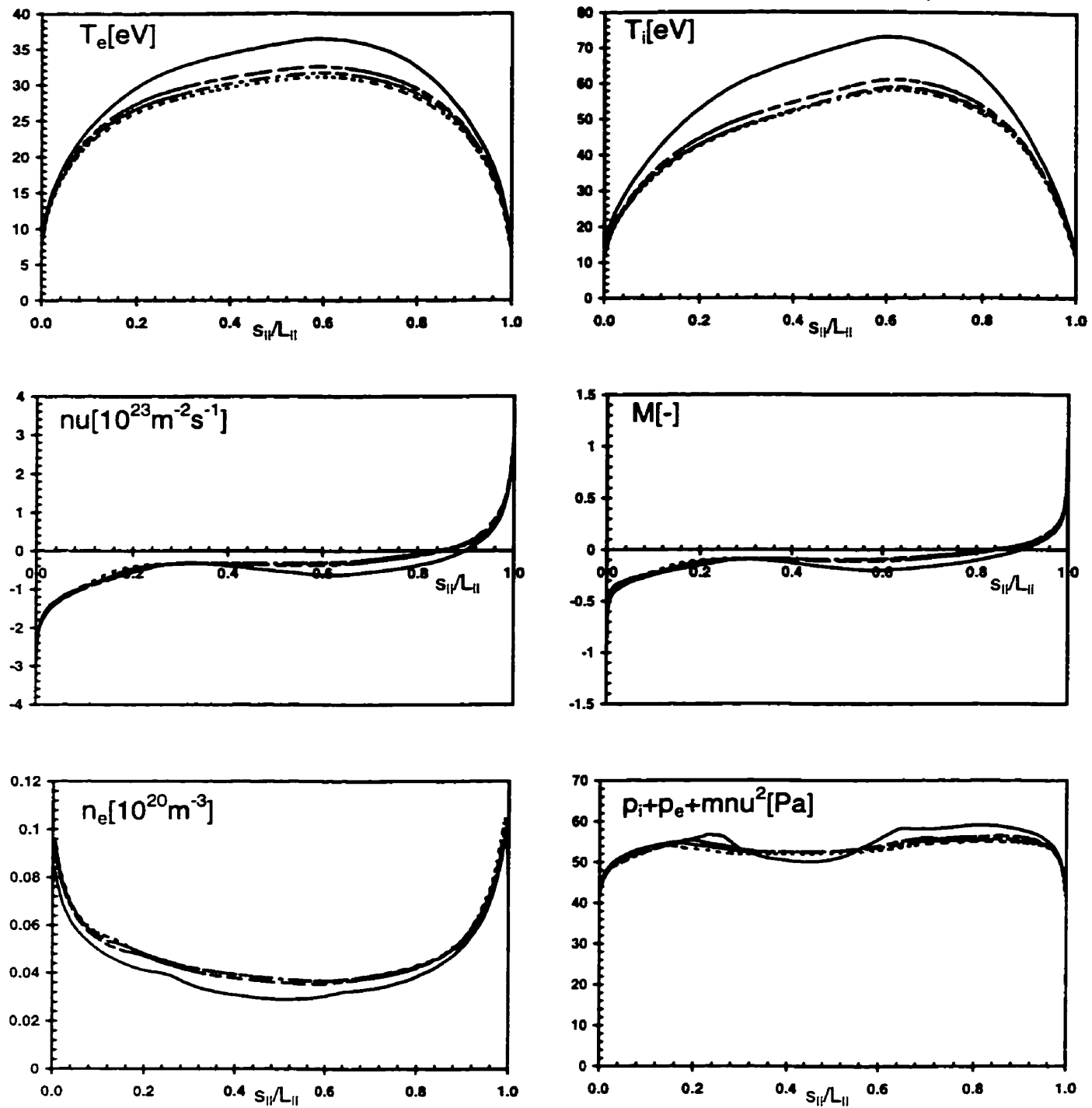


Fig.4.1.27: Along- $\mathbf{B}$  plots of plasma variables for the  $8 \text{ eV}, 3 \times 10^{23} \text{ m}^{-2} \text{s}^{-1}$  case at four radial locations in the SOL (solid line, separatrix ring,  $ir=8$ ; dashed line,  $ir=10$ ; dot-dashed line,  $ir=12$ ; dotted line,  $ir=14$ ).

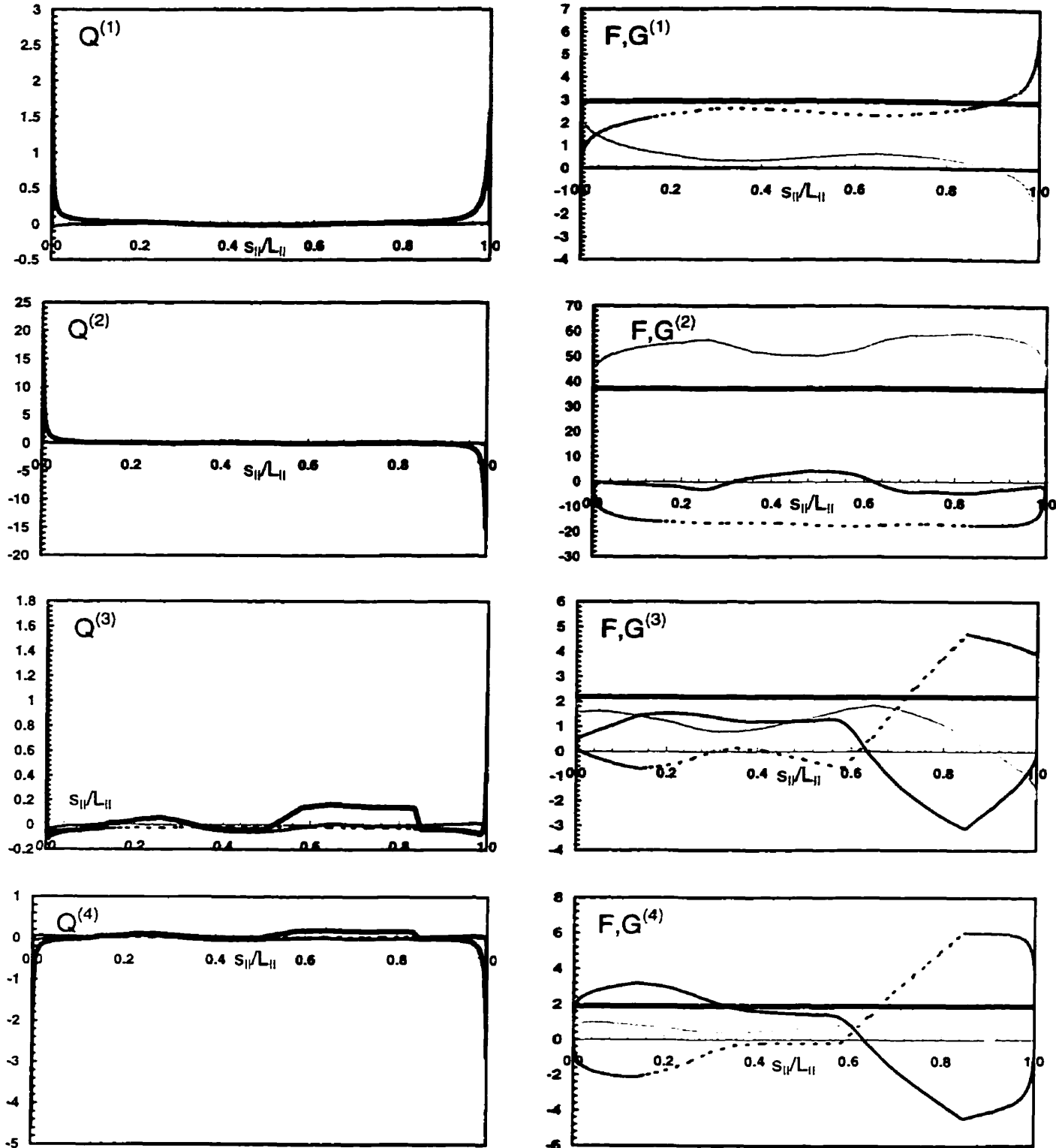


Fig.4.1.28: Along- $\mathbf{B}$  plots of sources and fluxes for the 8 eV,  $3 \times 10^{23} \text{ m}^{-2}\text{s}^{-1}$  case on the separatrix ring,  $ir=8$ . Sources: light grey line, cross-field; dark grey line, neutral; black line, flux expansion; dotted line, plasma; thick line, total  $\mathbf{Q}$ . Fluxes: grey line,  $\mathbf{F}$ ; black line,  $\mathbf{G}$ ; dotted line,  $\mathbf{Q}$  integrated from 0 to  $s_{||}$ ; thick line, sum.

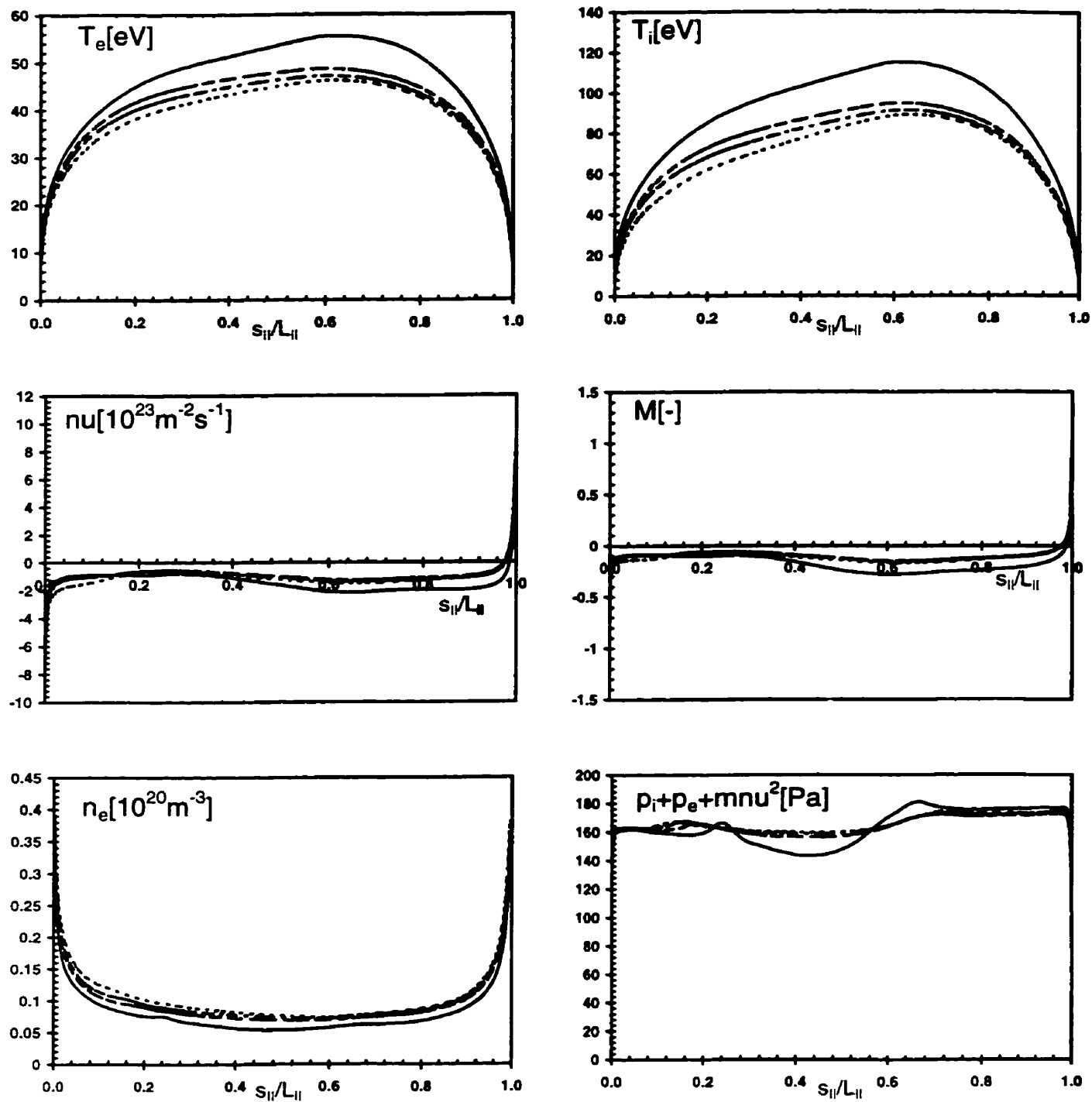


Fig.4.1.29: Along- $\mathbf{B}$  plots of plasma variables for the 8 eV,  $10^{24} \text{ m}^{-2} \text{s}^{-1}$  case at four radial locations in the SOL (solid line, separatrix ring, ir=8; dashed line, ir=10; dot-dashed line, ir=12; dotted line, ir=14).

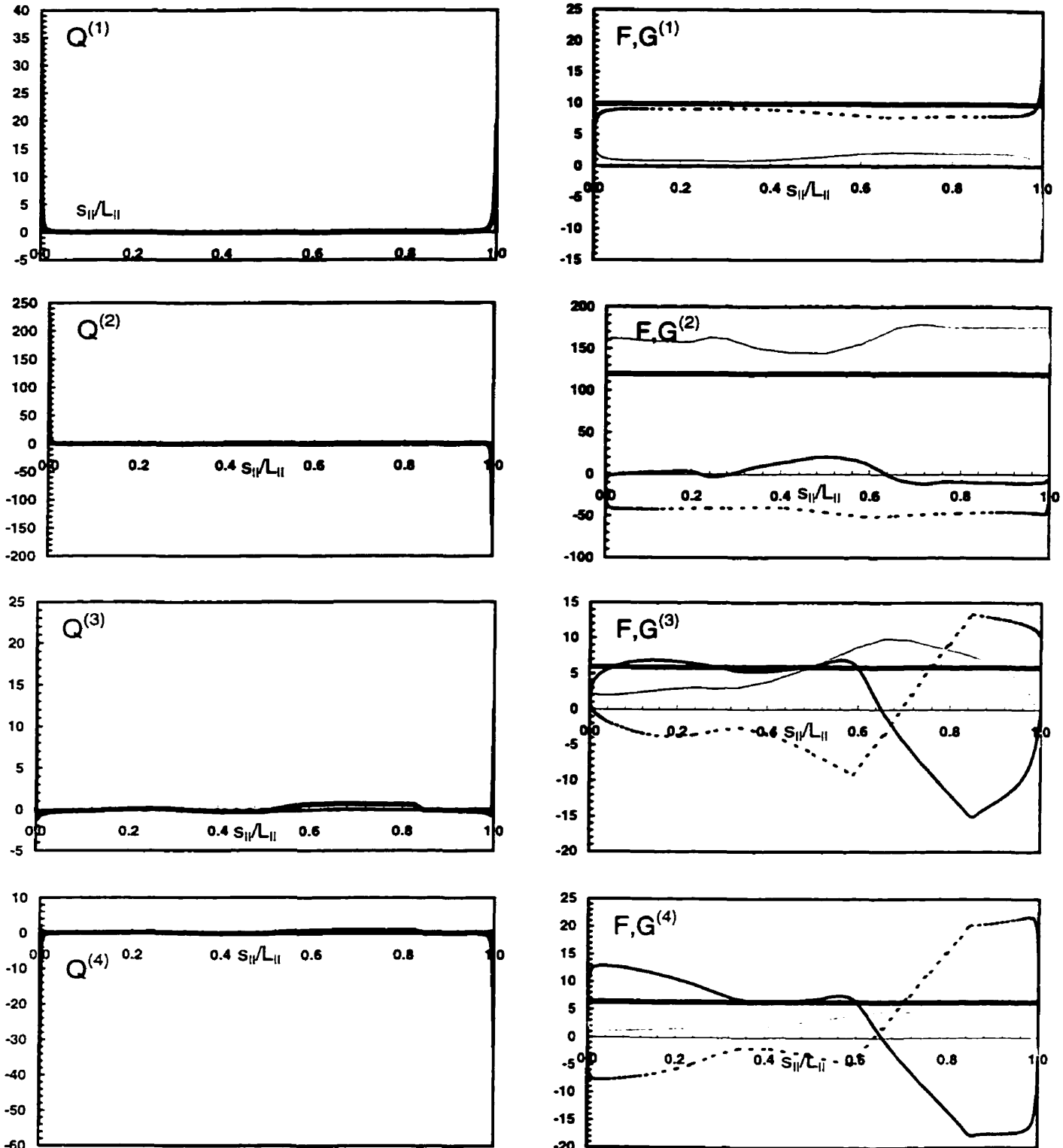


Fig.4.1.30: Along- $\mathbf{B}$  plots of sources and fluxes for the 8 eV,  $10^{24} \text{ m}^{-2} \text{s}^{-1}$  case on the separatrix ring, ir=8. Sources: light grey line, cross-field; dark grey line, neutral; black line, flux expansion; dotted line, plasma; thick line, total  $\mathbf{Q}$ . Fluxes: grey line,  $\mathbf{F}$ ; black line,  $\mathbf{G}$ ; dotted line,  $\mathbf{Q}$  integrated from 0 to  $s_{||}$ ; thick line, sum.

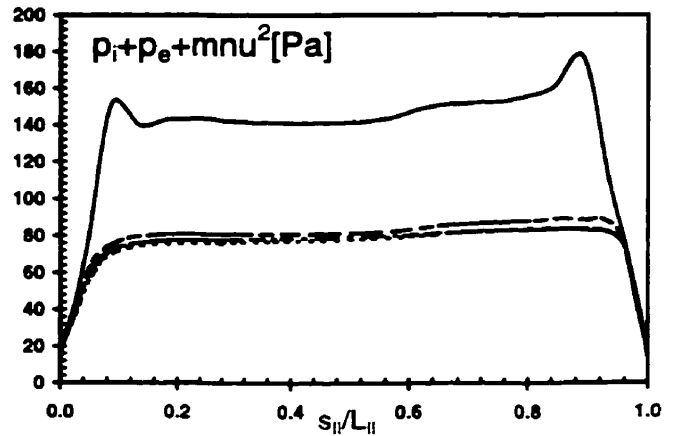
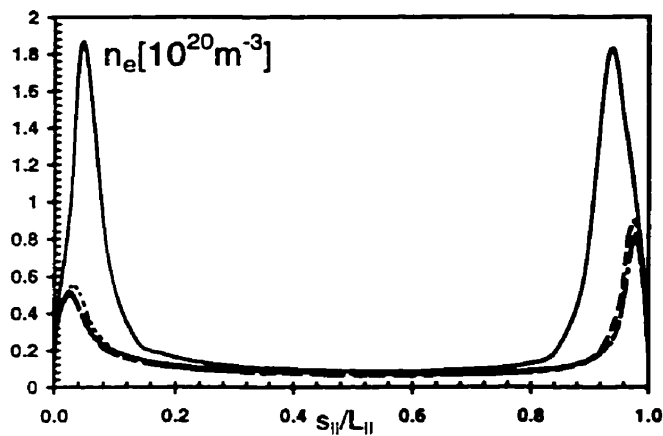
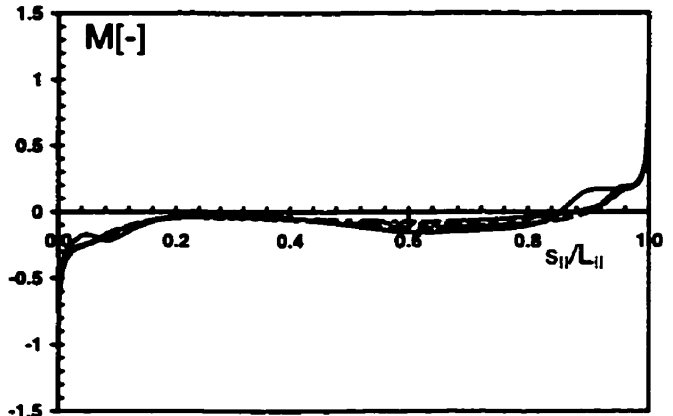
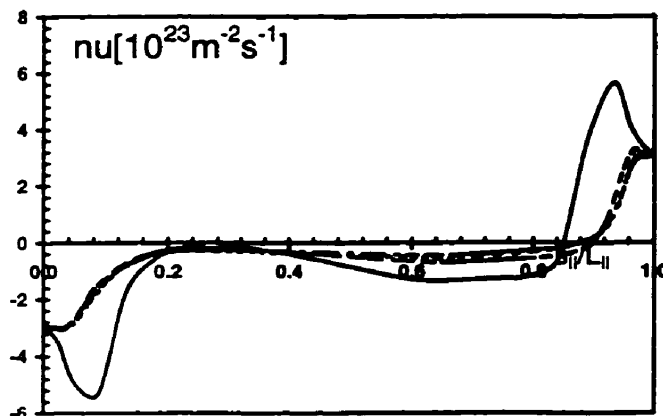
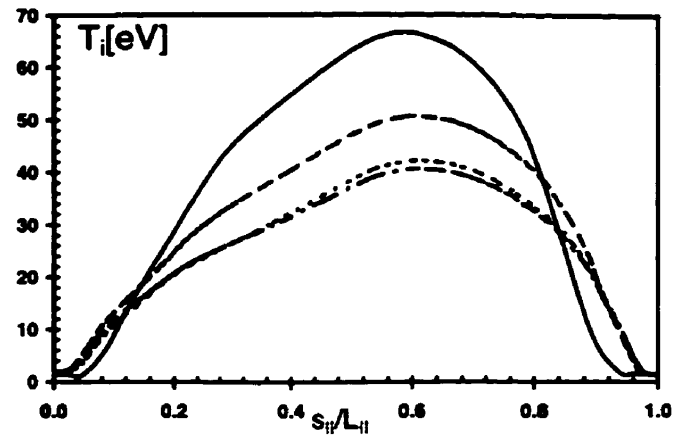
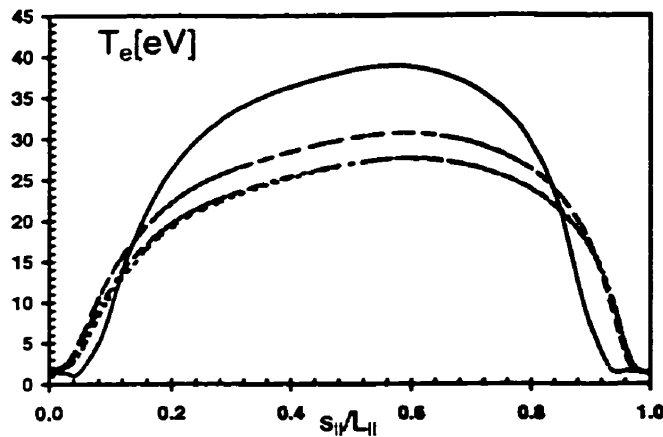


Fig.4.1.31: Along-B plots of plasma variables for the  $0.5 \text{ eV}, 3 \cdot 10^{23} \text{ m}^{-2} \text{s}^{-1}$  case at four radial locations in the SOL (solid line, separatrix ring, ir=8; dashed line, ir=10; dot-dashed line, ir=12; dotted line, ir=14).

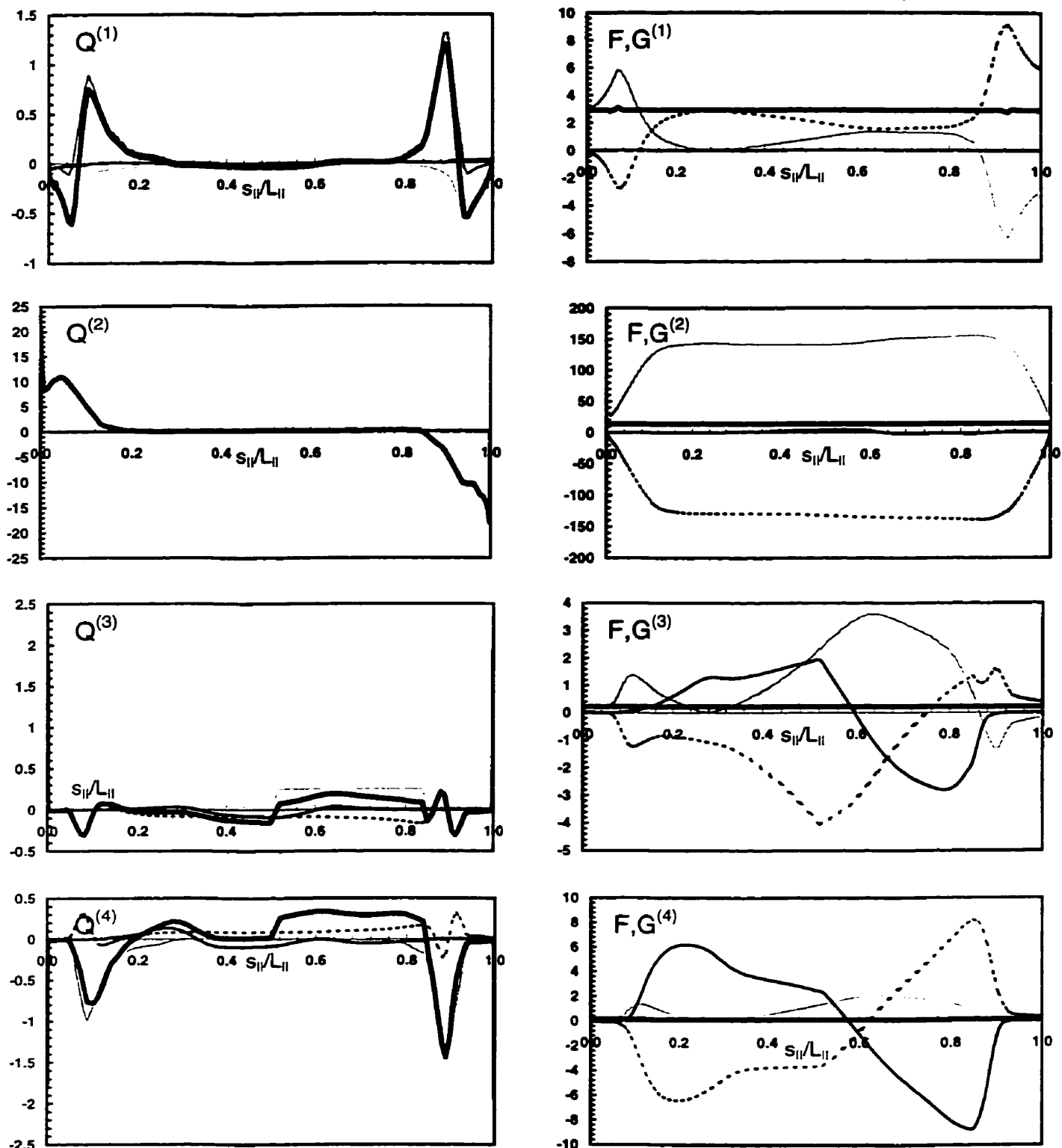


Fig.4.1.32: Along- $\mathbf{B}$  plots of sources and fluxes for the  $0.5 \text{ eV}, 3 \cdot 10^{23} \text{ m}^{-2} \text{s}^{-1}$  case on the separatrix ring,  $ir=8$ . Sources: light grey line, cross-field; dark grey line, neutral; black line, flux expansion; dotted line, plasma; thick line, total  $\mathbf{Q}$ . Fluxes: grey line,  $\mathbf{F}$ ; black line,  $\mathbf{G}$ ; dotted line,  $\mathbf{Q}$  integrated from 0 to  $s_{||}$ ; thick line, sum.

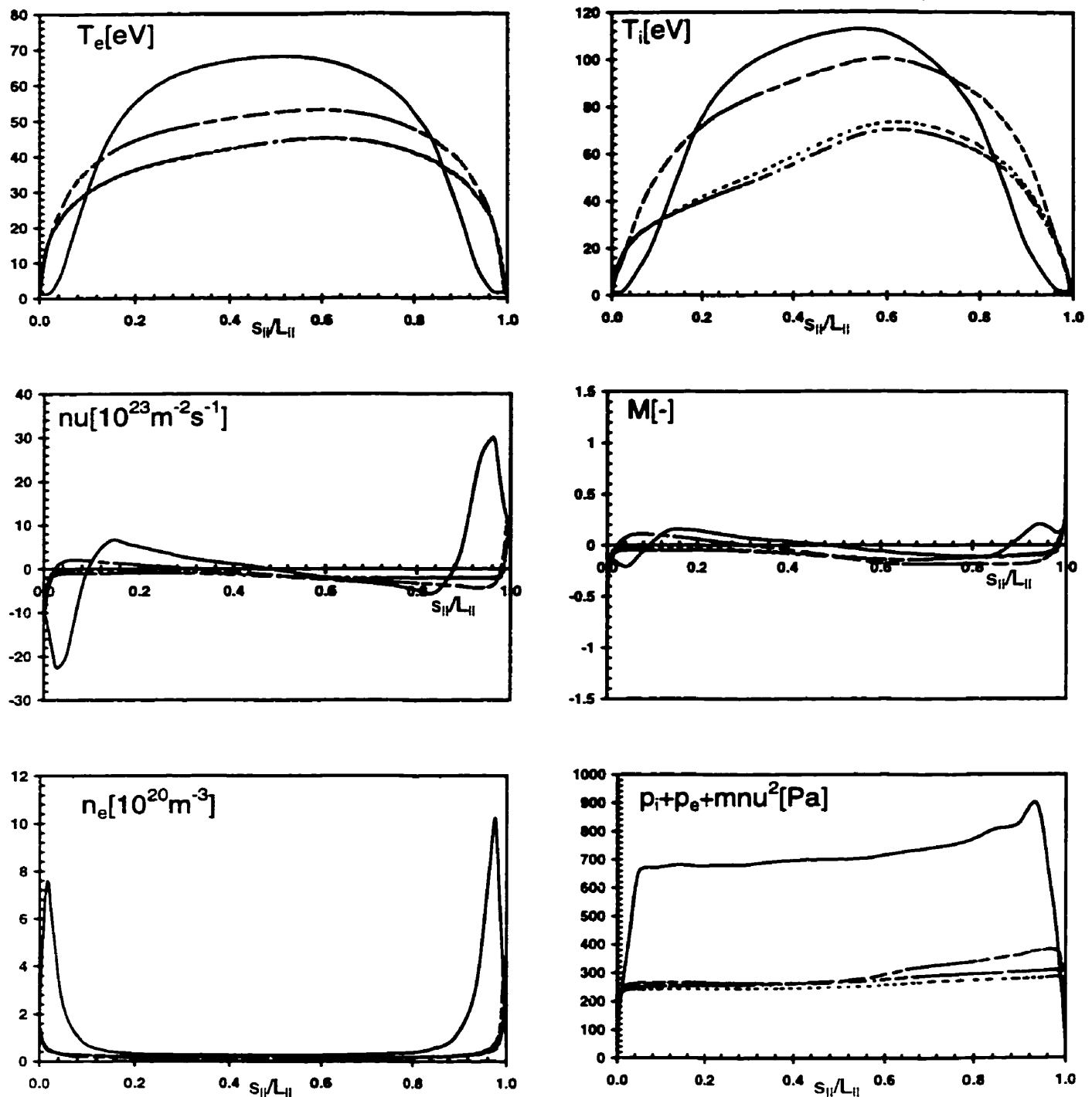


Fig.4.1.33: Along- $\mathbf{B}$  plots of plasma variables for the  $0.5 \text{ eV}, 10^{24} \text{ m}^{-2} \text{s}^{-1}$  case at four radial locations in the SOL (solid line, separatrix ring, ir=8; dashed line, ir=10; dot-dashed line, ir=12; dotted line, ir=14). The evolution was constrained by the additional upstream constraint,  $n_u^{sep} \sim 3 \cdot 10^{19} \text{ m}^{-3}$ .

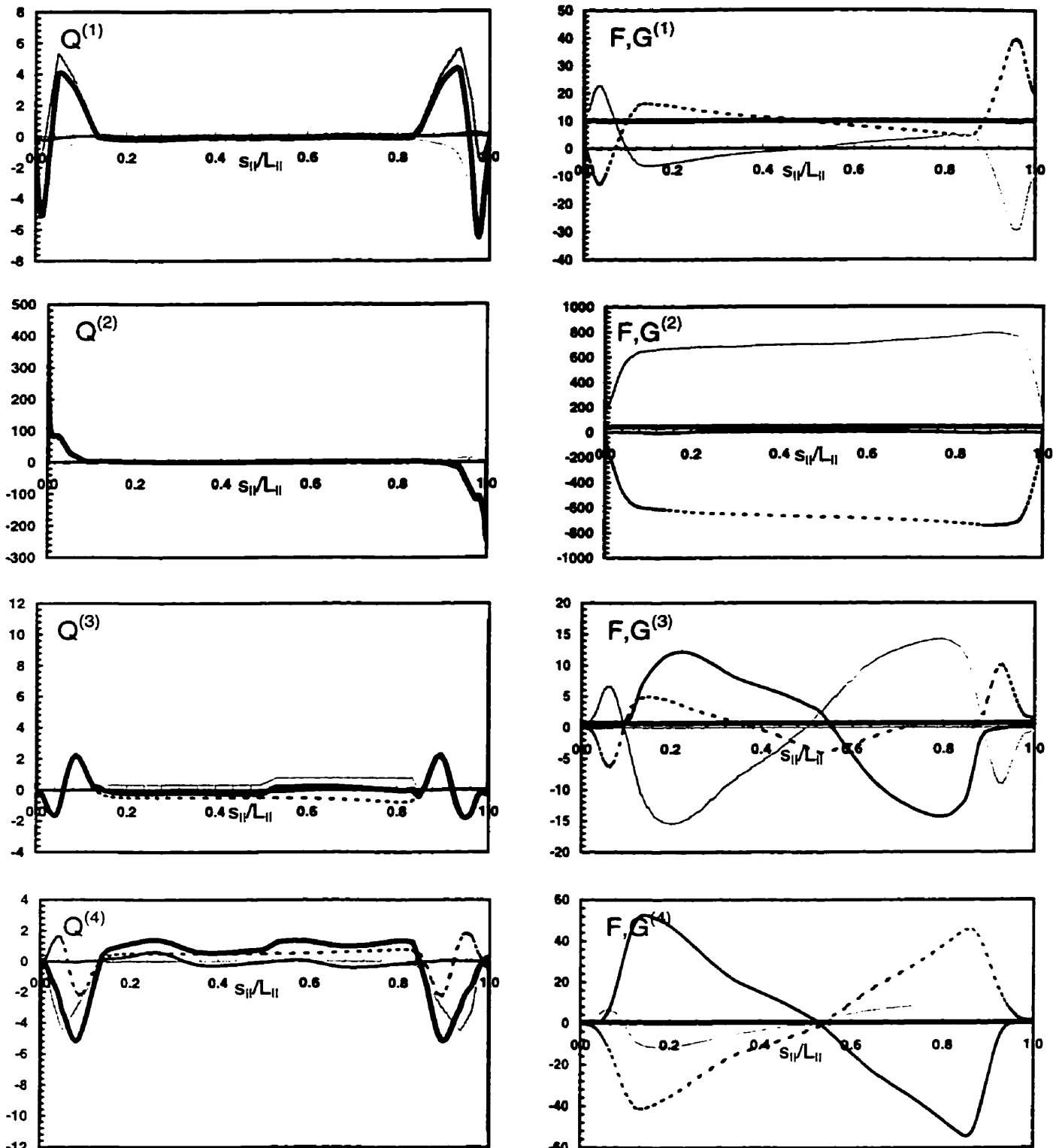


Fig.4.1.34: Along- $\mathbf{B}$  plots of sources and fluxes for the  $0.5 \text{ eV}, 10^{24} \text{ m}^{-2} \text{s}^{-1}$  case on the separatrix ring,  $ir=8$ . Sources: light grey line, cross-field; dark grey line, neutral; black line, flux expansion; dotted line, plasma; thick line, total  $\mathbf{Q}$ . Fluxes: grey line,  $\mathbf{F}$ ; black line,  $\mathbf{G}$ ; dotted line,  $\mathbf{Q}$  integrated from 0 to  $s_{\parallel}$ ; thick line, sum.

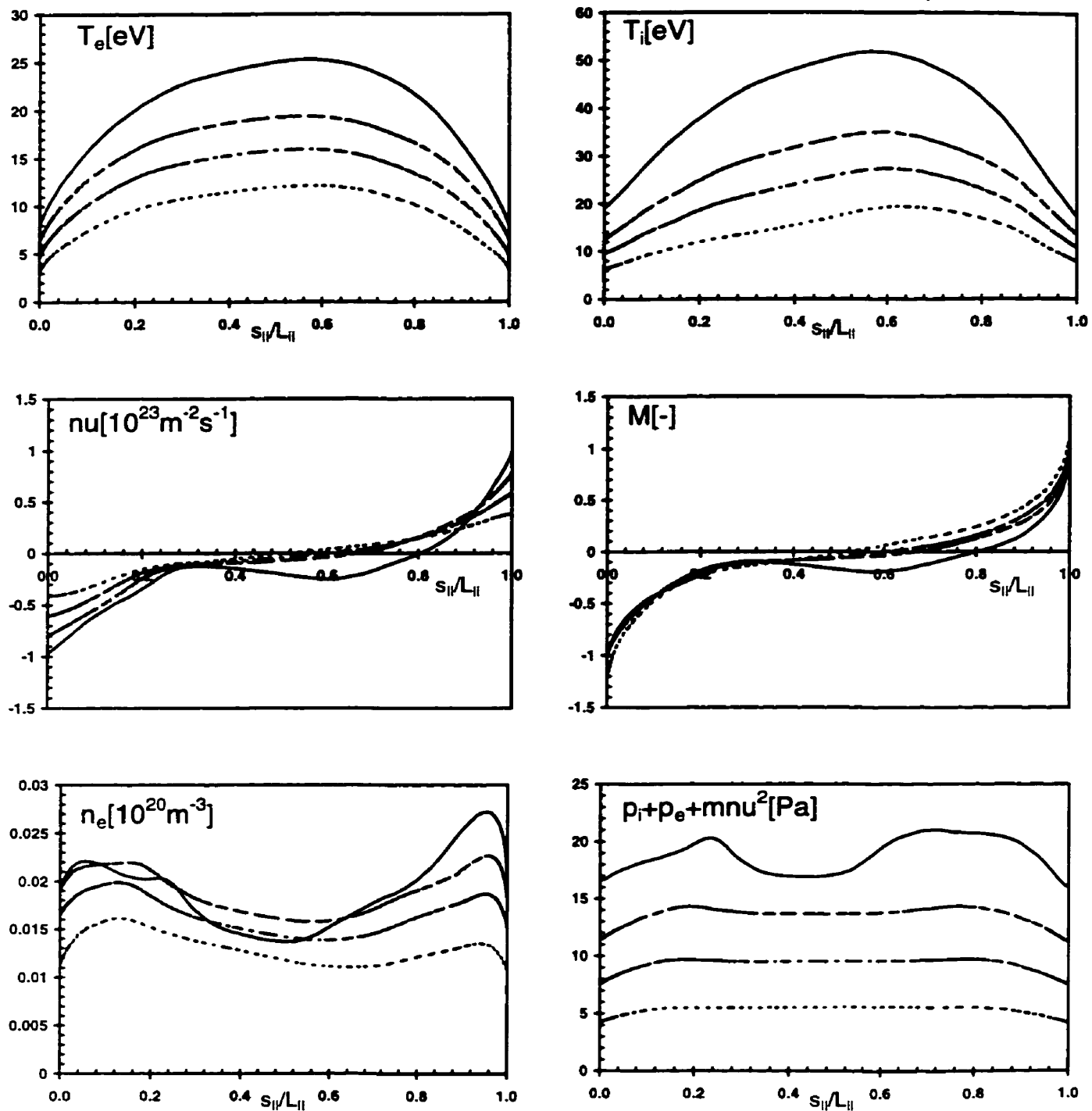


Fig.4.1.35: Along-B plots of plasma variables for the radially decaying target profile case at four radial locations in the SOL (solid line, separatrix ring,  $ir=8$ ; dashed line,  $ir=10$ ; dot-dashed line,  $ir=12$ ; dotted line,  $ir=14$ ).

$n_{u,t}$ $10^{23} \text{ m}^{-2}\text{s}^{-1}$	$T_{e,t}$ eV	$T_{i,t}$ eV	$n_{e,t}$ $10^{19} \text{ m}^{-3}$	$M_{t,u}$	$T_{e,u}$ eV	$T_{i,u}$ eV	$n_{e,u}$ $10^{19} \text{ m}^{-3}$	$M_{u}$	p.111
1.0	32.0	63.1	0.10	0.99	41.6	86.2	0.13	0.2	
1.0	31.8	62.3	0.11	0.99	39.3	80.5	0.15	0.1	
1.0	31.3	61.4	0.11	0.99	38.6	78.9	0.15	0.1	
1.0	30.9	60.6	0.11	0.99	38.3	79.1	0.15	0.1	
1.0	16.0	29.1	0.16	0.99	29.9	61.1	0.15	0.2	
1.0	15.9	29.5	0.16	0.99	27.4	54.6	0.17	0.1	
1.0	15.9	30.5	0.15	0.99	27.1	54.1	0.17	0.1	
1.0	15.9	32.5	0.15	0.99	27.5	56.7	0.16	0.1	
1.0	8.0	17.3	0.21	0.99	25.6	52.8	0.14	0.2	
1.0	8.0	16.3	0.21	0.99	22.8	43.2	0.18	0.1	
1.0	7.9	16.6	0.21	0.99	22.3	41.5	0.18	0.1	
1.0	7.2	16.3	0.21	0.99	22.4	42.1	0.18	0.1	
1.0	4.00	9.76	0.28	0.99	24.4	50.9	0.14	0.2	
1.0	3.97	8.75	0.29	0.99	20.1	34.7	0.20	0.1	
1.0	3.97	8.64	0.29	0.99	19.1	31.3	0.22	0.1	
1.0	3.65	8.47	0.29	0.99	18.9	31.4	0.21	0.1	
1.0	2.00	4.60	0.30	1.33	21.8	45.1	0.16	0.3	
1.0	1.93	4.25	0.30	1.36	18.1	28.5	0.24	0.1	
1.0	1.97	4.40	0.30	1.35	16.9	24.9	0.26	0.1	
1.0	1.74	3.90	0.30	1.40	16.5	24.4	0.26	0.1	
1.0	1.00	1.72	0.35	1.78	23.3	49.2	0.15	0.3	
1.0	0.99	1.73	0.34	1.79	17.2	26.8	0.24	0.1	
1.0	0.97	1.69	0.35	1.79	15.2	21.1	0.27	0.1	
1.0	0.99	1.73	0.33	1.81	14.8	20.8	0.27	0.1	
1.0	0.50	0.82	0.45	2.01	22.0	43.0	0.25	0.3	
1.0	0.50	0.86	0.43	2.03	15.4	21.5	0.30	0.1	
1.0	0.52	0.89	0.43	2.02	12.9	15.8	0.35	0.1	
1.0	0.53	0.90	0.42	2.01	12.1	15.0	0.36	0.1	
3.0	0.61	1.05	1.31	1.88	37.8	61.0	0.95	0.1	
3.0	0.56	0.96	1.32	1.91	29.6	43.5	0.79	0.1	
3.0	0.56	0.96	1.36	1.89	26.4	34.3	0.92	0.1	
3.0	0.56	0.96	1.30	1.91	25.4	34.0	0.87	0.1	
10.0	0.55	0.93	4.28	1.88	55.2	70.0	3.00	0.0	
10.0	0.63	1.07	4.30	1.72	48.5	64.2	2.28	0.1	
10.0	0.53	0.88	4.80	1.76	37.5	41.8	3.37	0.1	
10.0	0.54	0.85	5.10	1.74	41.5	50.0	2.90	0.1	

Table 4.1.1: A listing of inner target and upstream (mid-point) conditions at four radial locations in the SOL (the top row is the separatrix ring,  $ir=8$ , followed by  $ir=10, 12$  and  $14$ ) for the attached-detached transition discussed in section 4.1.

P_in MW/m <sup>2</sup>	q,t(i+e) MW/m <sup>2</sup>	I/dq_OSM	I/dq_2PM	I/dp_OSM	I/dp_2PM	I/dc_OSM	I/dc_2PM
13.6	5.77	1.18	1.14	1.06	0.88	1.18	1.27
13.4	5.75	1.17	1.12	1.07	0.92	1.18	1.45
13.3	5.63	1.18	1.14	1.06	0.91	1.18	1.44
13.3	5.46	1.22	1.16	1.06	0.93	1.16	1.40
7.8	2.90	1.34	1.28	1.14	0.99	1.33	1.56
7.5	2.86	1.30	1.25	1.13	0.97	1.33	1.75
7.4	2.82	1.31	1.23	1.13	0.99	1.32	1.70
7.2	2.62	1.37	1.15	1.14	0.95	1.32	1.49
5.5	1.50	1.84	1.73	1.30	1.11	1.49	1.72
4.8	1.45	1.66	1.55	1.31	1.16	1.49	1.87
4.7	1.41	1.66	1.50	1.30	1.13	1.49	1.85
4.6	1.29	1.78	1.57	1.33	1.17	1.49	1.70
5.2	0.81	3.20	2.96	1.54	1.41	1.59	1.88
3.6	0.75	2.41	2.25	1.58	1.53	1.59	2.14
3.4	0.75	2.25	2.14	1.57	1.53	1.61	2.24
3.3	0.72	2.32	2.24	1.58	1.55	1.64	2.21
5.0	0.41	6.15	5.39	1.93	2.06	1.67	2.71
3.1	0.42	3.69	3.47	1.94	2.14	1.64	2.64
2.8	0.41	3.41	3.03	1.90	2.04	1.75	2.84
2.7	0.41	3.29	3.31	1.92	2.14	1.79	2.86
5.6	0.22	12.98	11.86	2.90	2.88	1.79	2.38
2.7	0.21	6.40	5.83	2.60	2.71	1.72	2.74
2.2	0.21	5.31	4.88	2.54	2.58	1.89	3.28
2.1	0.21	4.95	4.60	2.47	2.53	1.96	3.28
5.6	0.12	24.35	21.88	4.83	5.92	1.96	2.92
2.3	0.12	9.38	8.61	3.40	3.73	1.79	3.38
1.7	0.12	6.88	6.04	3.20	3.29	2.04	4.31
1.4	0.13	5.60	5.19	3.00	3.26	2.17	4.39
21.3	0.42	25.36	22.83	9.80	9.61	1.59	1.67
11.3	0.39	14.49	13.34	6.40	6.25	1.59	1.72
9.1	0.39	11.67	10.62	6.40	5.97	1.61	1.94
8.8	0.39	11.28	10.55	5.90	5.68	1.64	2.06
58.4	1.18	24.75	22.78	14.50	13.08	1.18	1.22
36.4	1.28	14.22	13.40	9.90	8.97	1.18	0.99
25.1	1.08	11.62	10.54	10.40	9.73	1.18	1.56
29.9	1.20	12.46	12.33	10.30	9.39	1.16	1.25

Table 4.1.2: A comparison of the OSM2 results and 2PM predictions in terms of the correction factors defined in the text by equation (4.1.1); the rows correspond exactly to Table 4.1.1. The first two columns give the power deposited in the ring and the power reaching the inner target (same flux units).

Te_u dc = 1	Te_u dc_OSM	Te_u eV	n_u dp = 1	n_u dp_OSM	ne_u 10^19 m3	Tave_u dc = 1	Tave_u dc_OSM	Tave_u eV
44.81	43.41	41.6	0.15	0.16	0.13	54.01	53.16	63.90
42.90	41.73	39.3	0.16	0.17	0.15	52.52	51.83	59.90
42.19	40.94	38.6	0.16	0.17	0.15	51.71	50.97	58.75
41.92	40.45	38.3	0.16	0.17	0.15	51.20	50.33	58.70
36.34	33.57	29.9	0.15	0.17	0.15	37.64	35.14	45.50
33.81	31.54	27.4	0.17	0.19	0.17	35.42	33.43	41.00
33.23	30.95	27.1	0.17	0.19	0.17	35.07	33.12	40.60
33.03	30.41	27.5	0.17	0.19	0.16	35.28	33.11	42.10
35.50	29.85	25.6	0.13	0.16	0.14	35.72	30.18	39.20
31.34	27.18	22.8	0.15	0.20	0.18	31.58	27.53	33.00
30.55	26.48	22.3	0.16	0.21	0.18	30.83	26.87	31.90
30.65	26.02	22.4	0.15	0.20	0.18	30.90	26.39	32.25
40.75	29.24	24.4	0.10	0.15	0.14	40.77	29.28	37.65
32.08	24.97	20.1	0.13	0.21	0.20	32.10	25.01	27.40
30.32	24.04	19.1	0.14	0.22	0.22	30.34	24.09	25.20
30.11	23.68	18.9	0.14	0.22	0.21	30.13	23.73	25.15
48.69	28.98	21.8	0.08	0.15	0.16	48.70	28.99	33.45
34.70	23.89	18.1	0.11	0.22	0.24	34.70	23.90	23.30
32.34	22.77	16.9	0.13	0.24	0.26	32.35	22.78	20.90
31.31	22.27	16.5	0.12	0.23	0.26	31.31	22.28	20.45
62.06	29.84	23.3	0.05	0.15	0.15	62.06	29.84	36.25
39.00	22.94	17.2	0.09	0.23	0.24	39.00	22.94	22.00
34.38	21.34	15.2	0.11	0.27	0.27	34.38	21.34	18.15
32.83	20.79	14.8	0.11	0.26	0.27	32.83	20.79	17.80
74.36	29.87	22.0	0.04	0.20	0.25	74.36	29.87	32.50
41.32	21.80	15.4	0.08	0.27	0.30	41.32	21.80	18.45
33.96	19.58	12.9	0.11	0.34	0.35	33.96	19.58	14.35
30.20	18.46	12.1	0.11	0.33	0.36	30.20	18.46	13.55
110.20	43.75	37.8	0.10	0.97	0.95	110.20	43.75	49.40
74.21	34.57	29.6	0.13	0.81	0.79	74.21	34.57	36.55
64.34	31.89	26.4	0.15	0.99	0.92	64.34	31.89	30.35
62.38	31.22	25.4	0.15	0.90	0.87	62.38	31.22	29.70
145.98	58.37	55.2	0.23	3.33	3.00	145.98	58.37	62.60
103.10	48.29	48.5	0.25	2.52	2.28	103.10	48.29	56.35
85.88	42.61	37.5	0.35	3.60	3.37	85.88	42.61	39.65
91.02	44.28	41.5	0.31	3.18	2.90	91.02	44.28	45.75

Table 4.1.3: A similar comparison as in Table 4.1.2, but in terms of the upstream density, electron temperature and average temperature predicted by the simple 2PM, modified 2PM and OSM2.

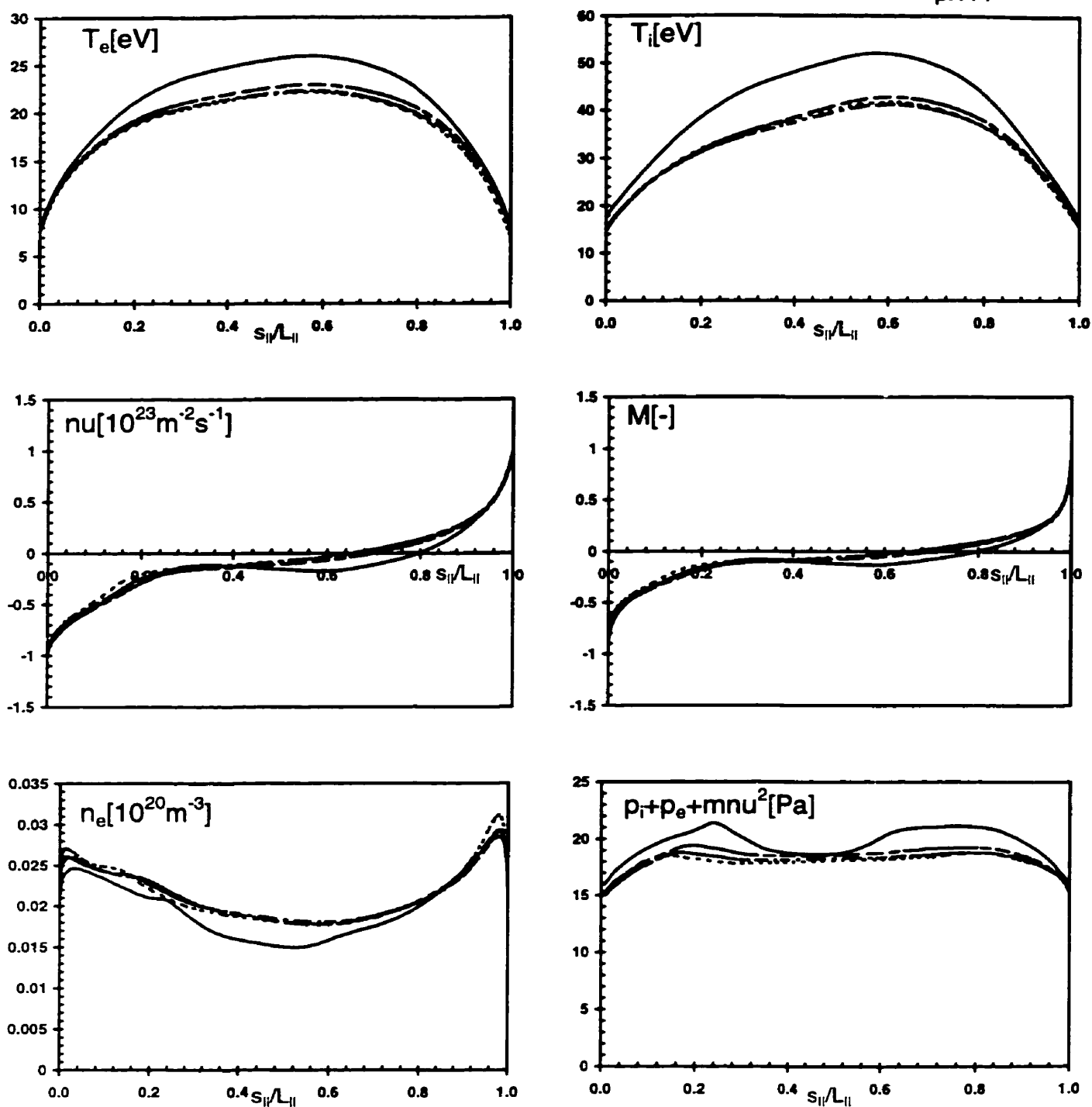


Fig.4.2.1: Along-B plots of plasma variables for case A with uniform cross-field particle source at four radial locations in the SOL (solid line, separatrix ring,  $ir=8$ ; dashed line,  $ir=10$ ; dot-dashed line,  $ir=12$ ; dotted line,  $ir=14$ ). Compare with Fig.4.1.8.

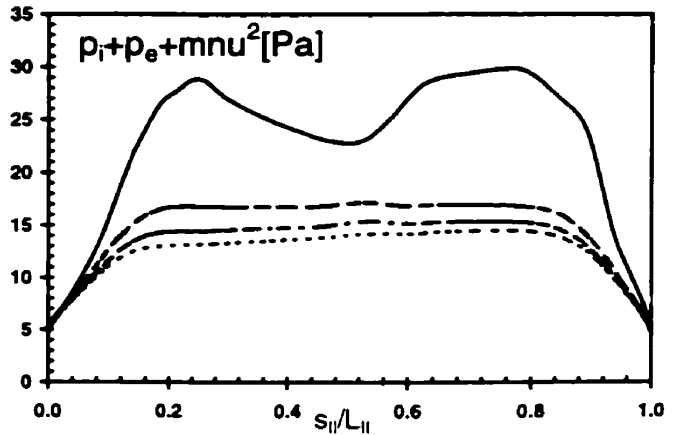
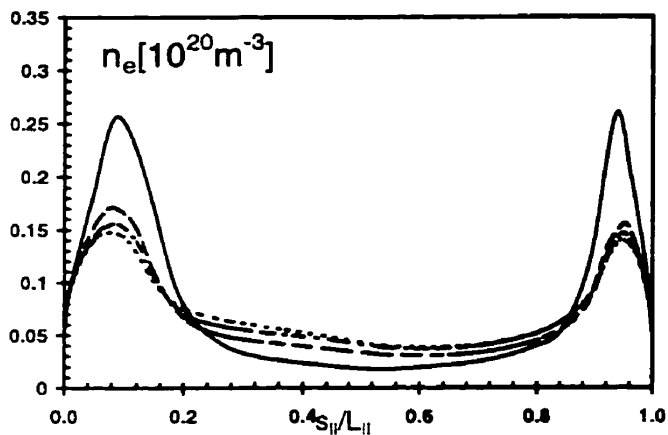
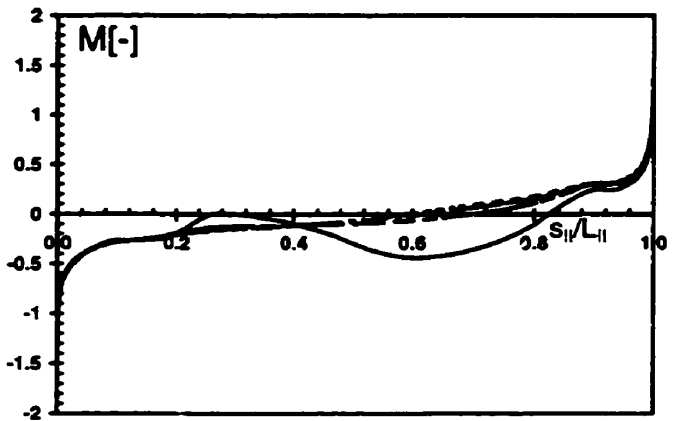
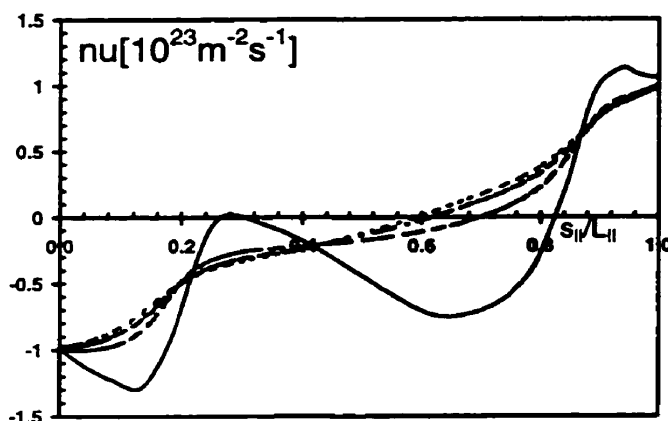
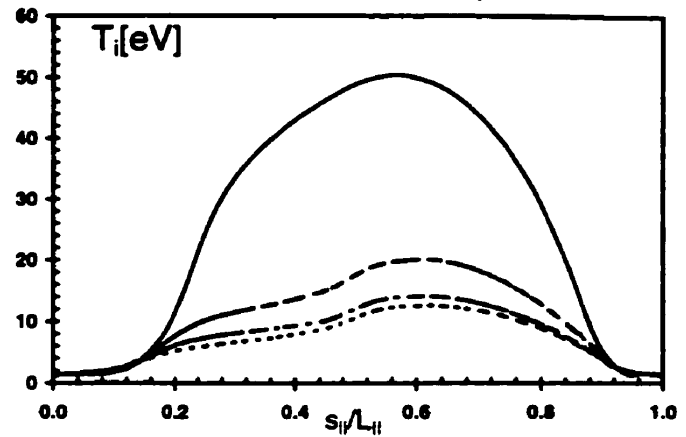
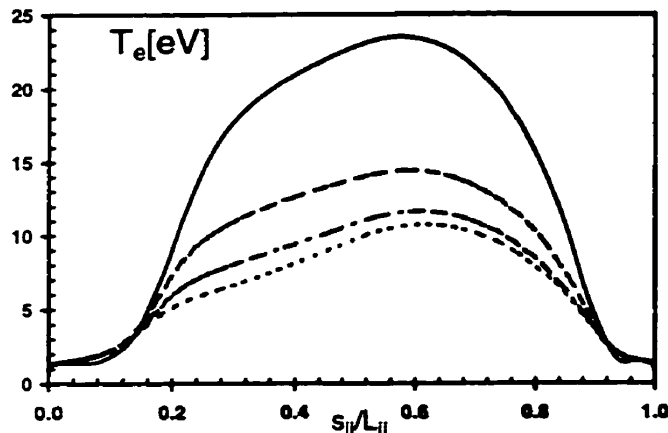


Fig.4.2.2: Along-B plots of plasma variables for case B with uniform cross-field particle source at four radial locations in the SOL (solid line, separatrix ring,  $ir=8$ ; dashed line,  $ir=10$ ; dot-dashed line,  $ir=12$ ; dotted line,  $ir=14$ ). Compare with Fig.4.1.20.

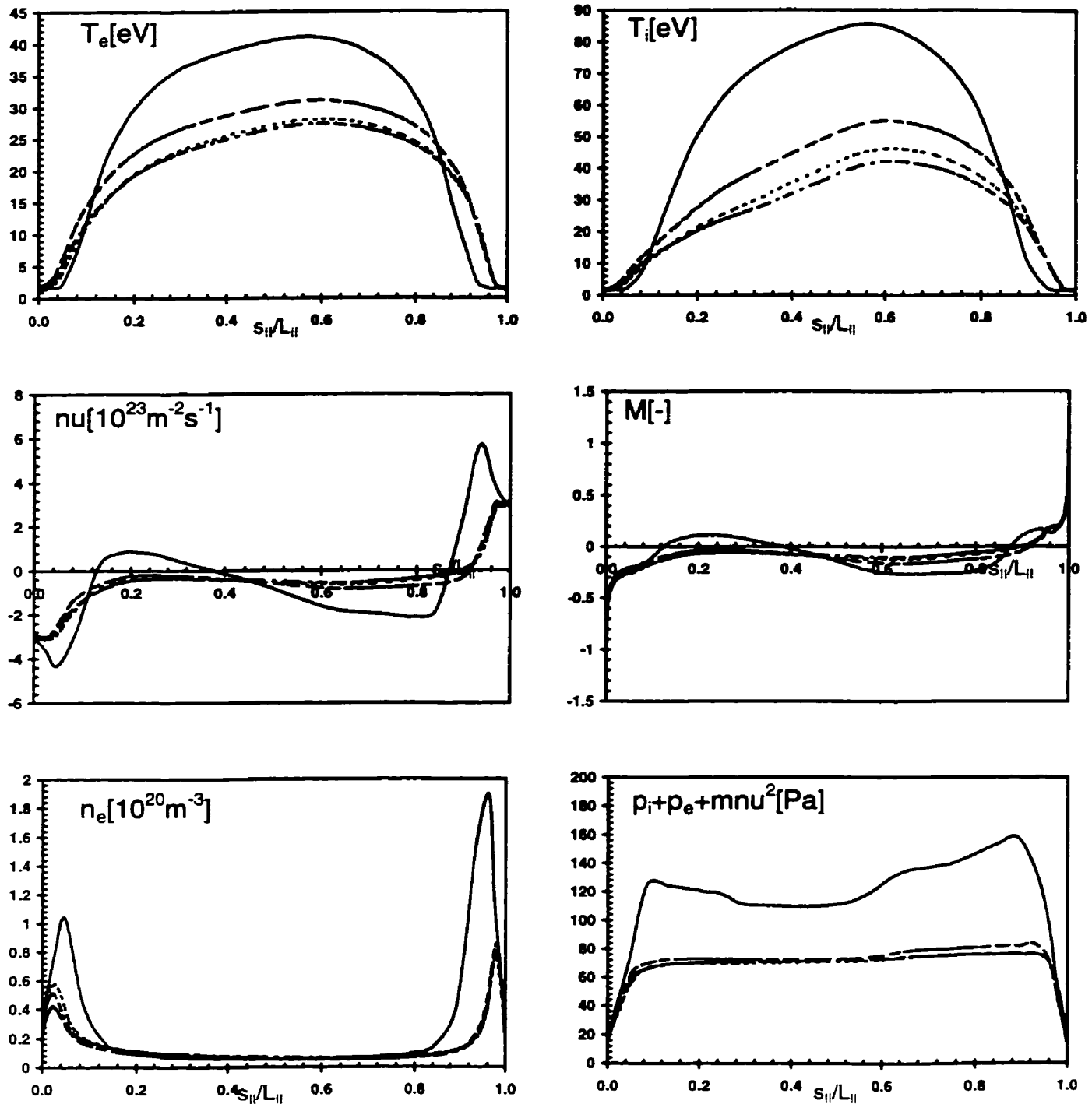


Fig.4.2.3: Along-B plots of plasma variables for case C with a square root density dependent cross-field particle source at four radial locations in the SOL (solid line, separatrix ring, ir=8; dashed line, ir=10; dot-dashed line, ir=12; dotted line, ir=14). Compare with Fig.4.1.31.

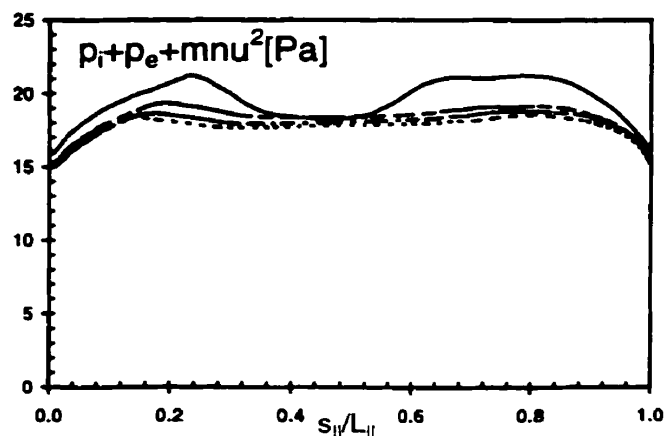
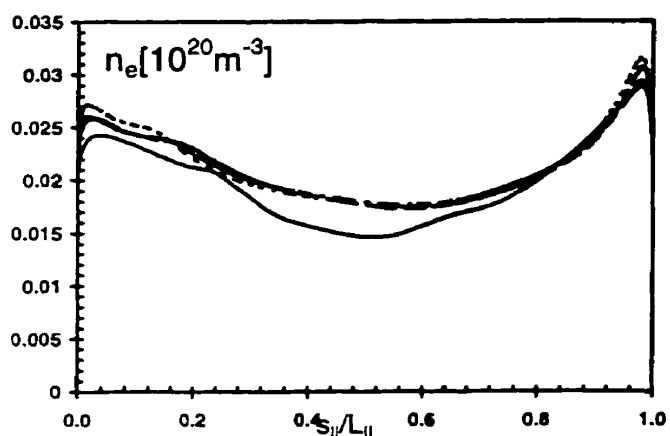
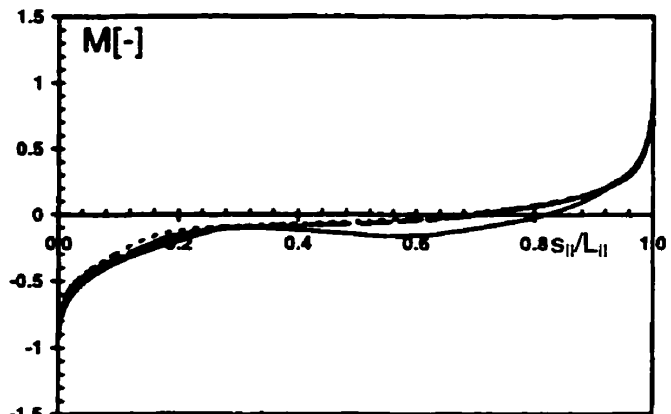
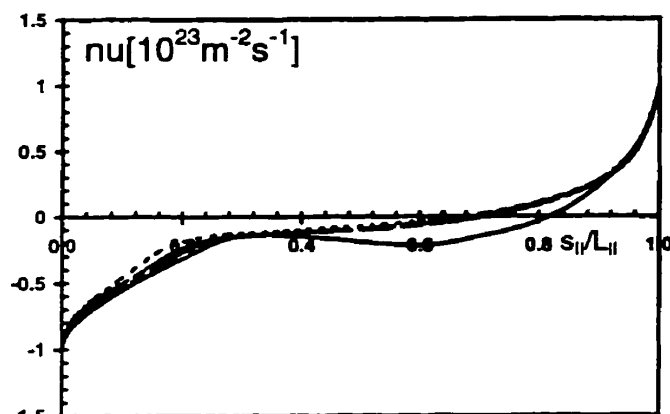
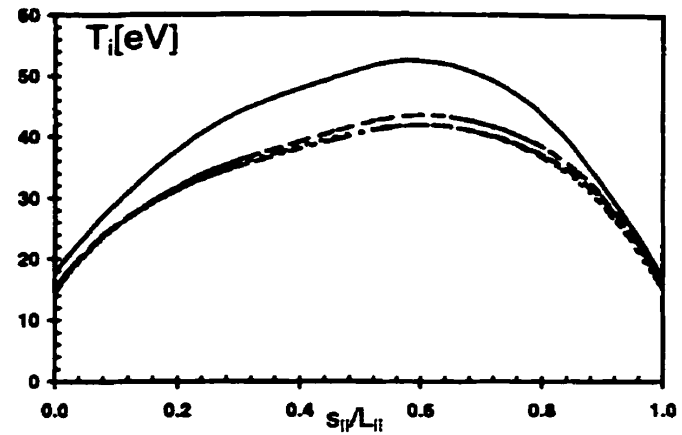
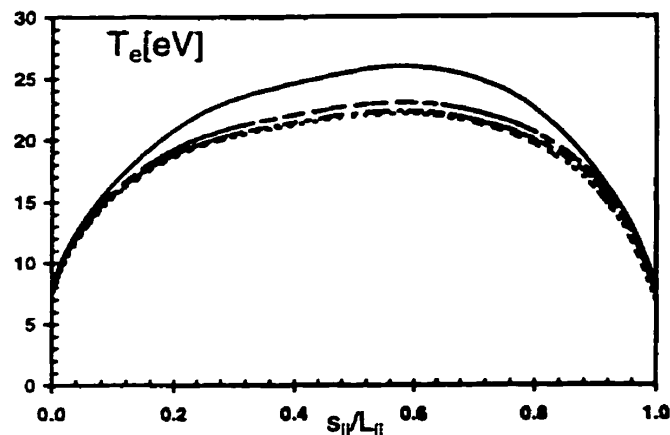


Fig.4.2.4: Along-B plots of plasma variables for case A with uniform cross-field momentum source at four radial locations in the SOL (solid line, separatrix ring, ir=8; dashed line, ir=10; dot-dashed line, ir=12; dotted line, ir=14). Compare with Fig.4.1.8.

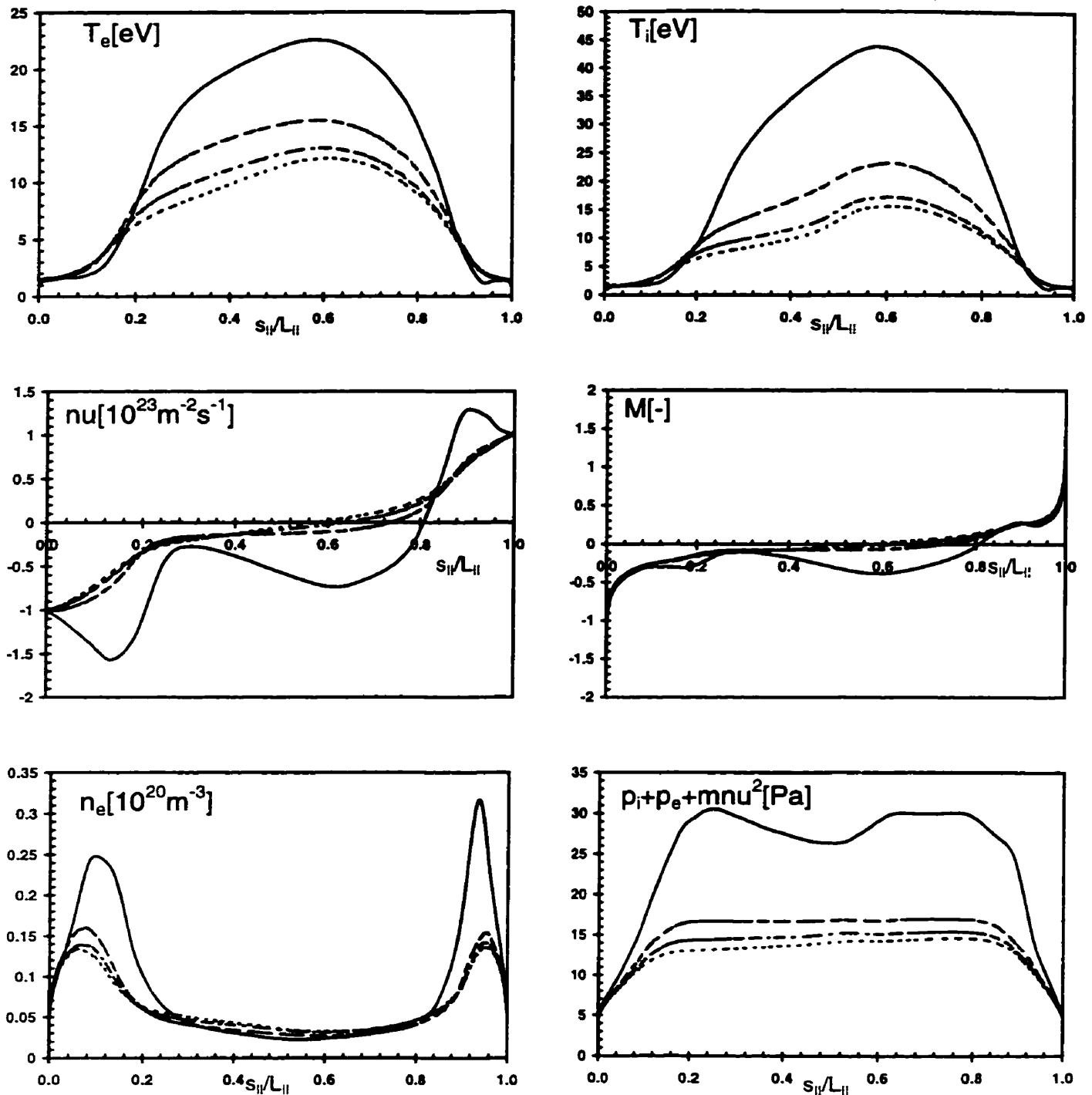


Fig.4.2.5: Along-B plots of plasma variables for case B with uniform cross-field momentum source at four radial locations in the SOL (solid line, separatrix ring,  $ir=8$ ; dashed line,  $ir=10$ ; dot-dashed line,  $ir=12$ ; dotted line,  $ir=14$ ). Compare with Fig.4.1.20.

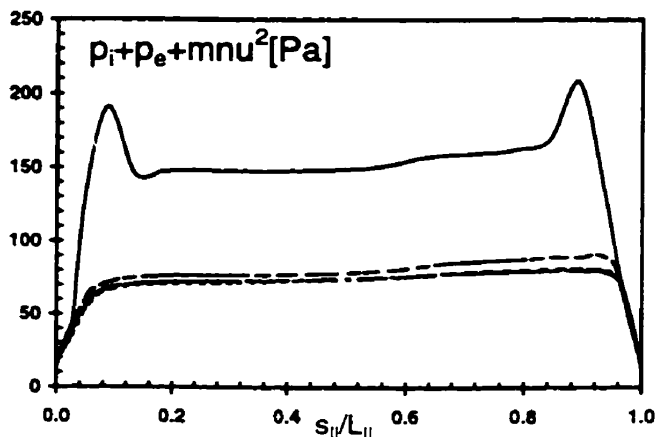
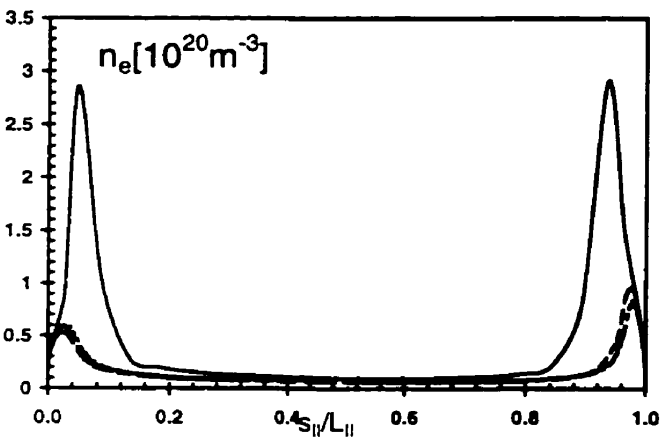
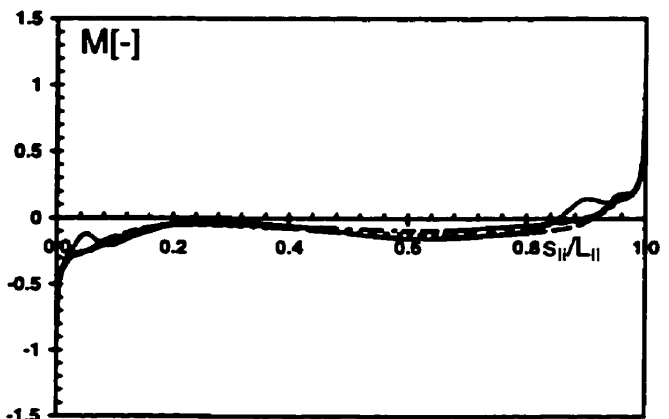
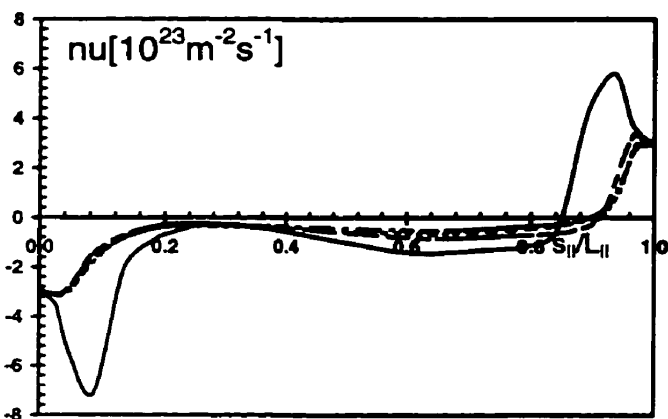
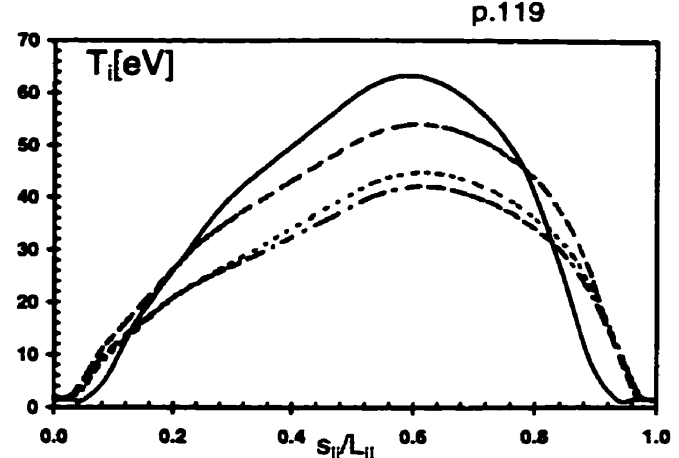
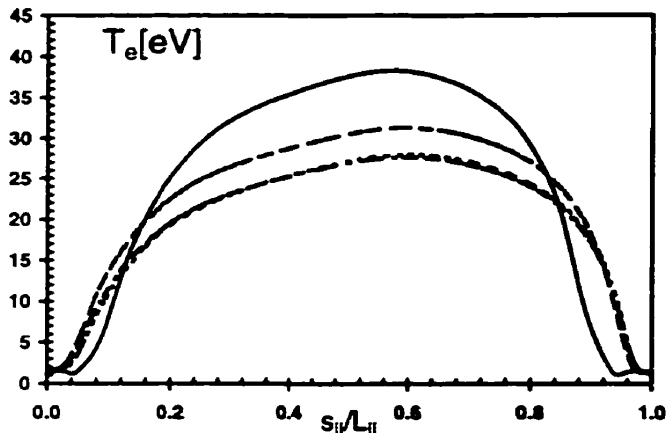


Fig.4.2.6: Along- $\mathbf{B}$  plots of plasma variables for case C with a square root density dependent cross-field momentum source at four radial locations in the SOL (solid line, separatrix ring,  $ir=8$ ; dashed line,  $ir=10$ ; dot-dashed line,  $ir=12$ ; dotted line,  $ir=14$ ). Compare with Fig.4.1.31.

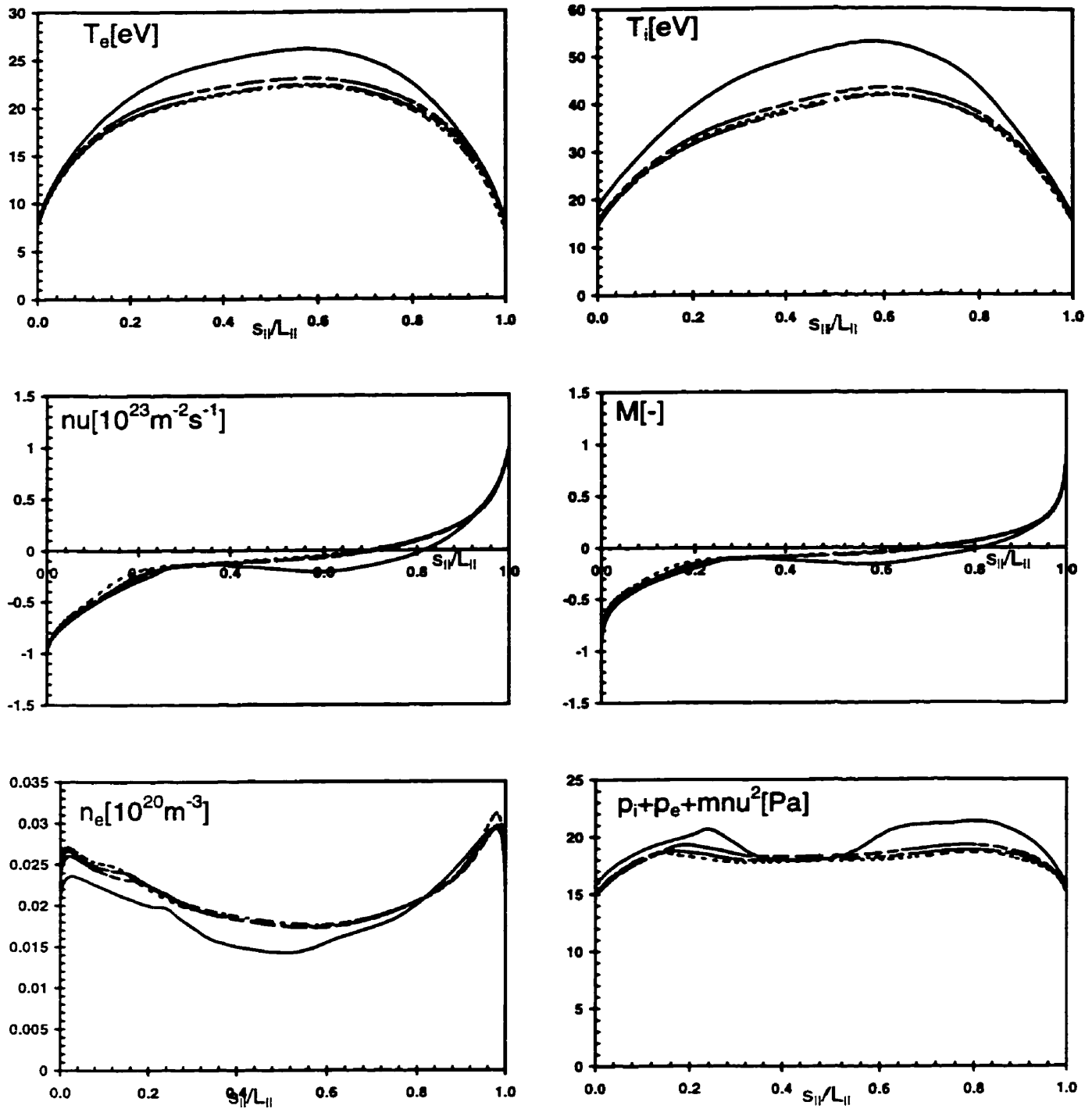


Fig.4.2.7: Along-B plots of plasma variables for case A with pressure depedent cross-field energy sources at four radial locations in the SOL (solid line, separatrix ring,  $ir=8$ ; dashed line,  $ir=10$ ; dot-dashed line,  $ir=12$ ; dotted line,  $ir=14$ ). Compare with Fig.4.1.8.

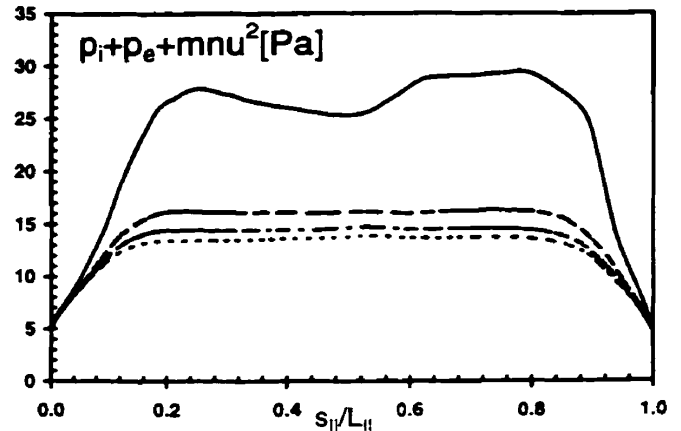
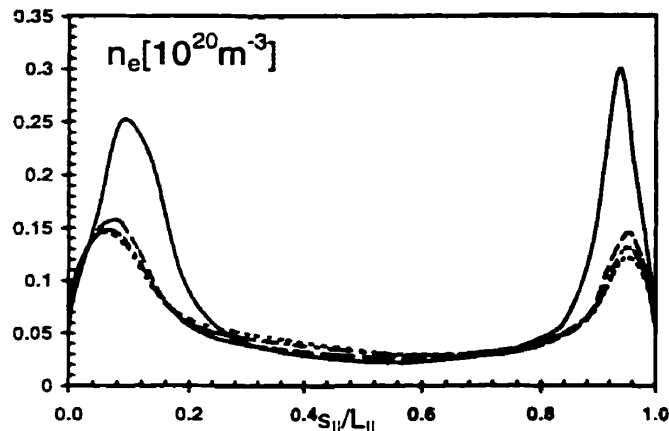
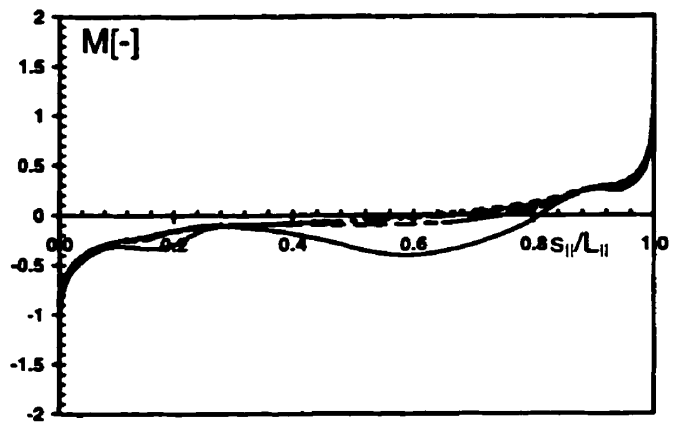
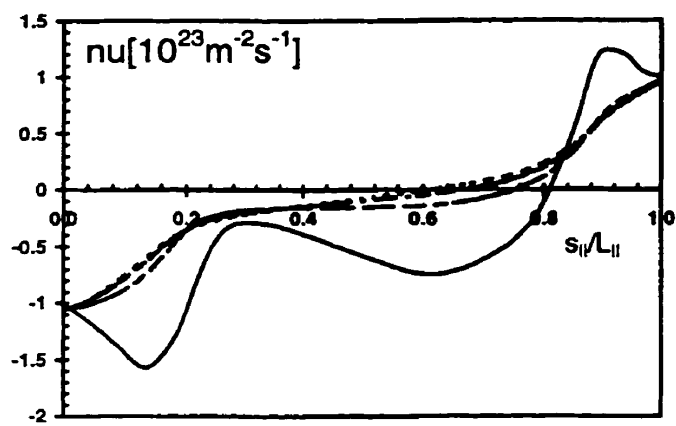
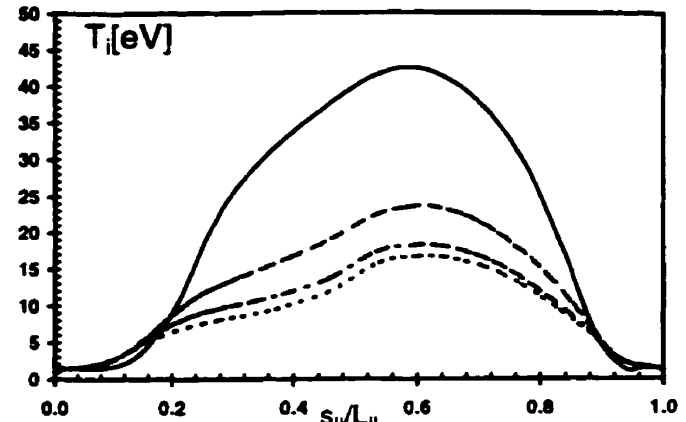
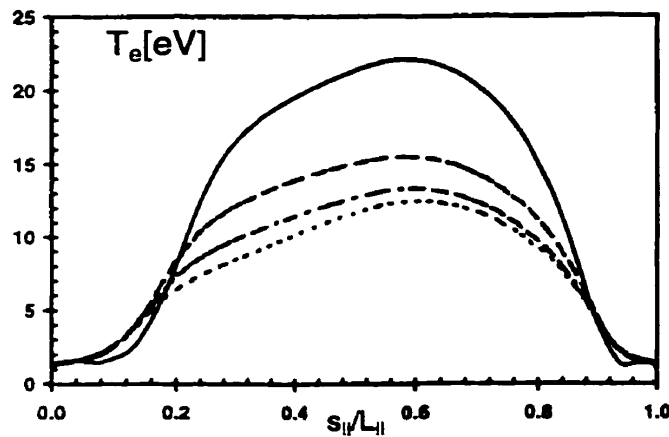


Fig.4.2.8: Along- $\mathbf{B}$  plots of plasma variables for case B with pressure dependent cross-field energy source at four radial locations in the SOL (solid line, separatrix ring,  $ir=8$ ; dashed line,  $ir=10$ ; dot-dashed line,  $ir=12$ ; dotted line,  $ir=14$ ). Compare with Fig.4.1.20.

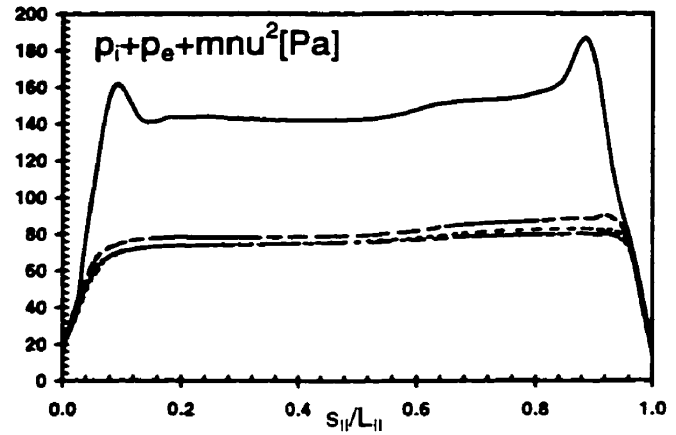
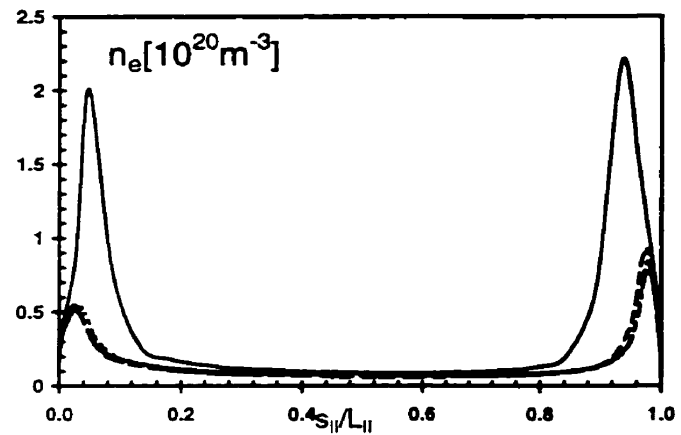
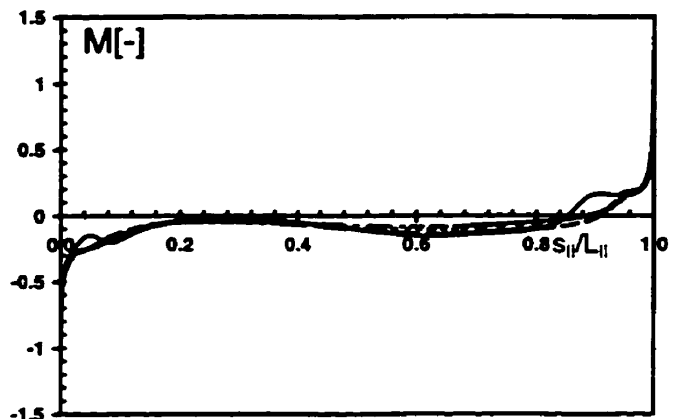
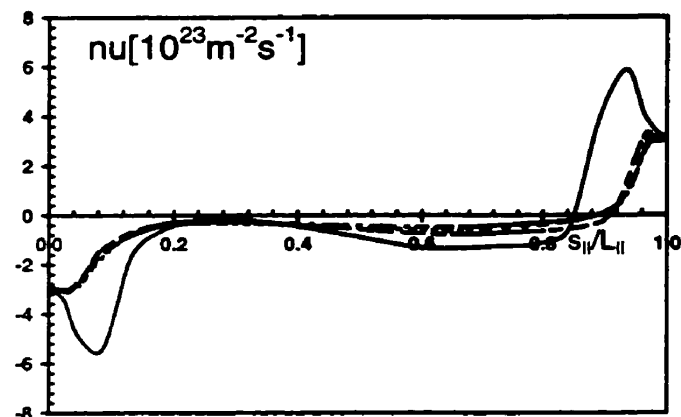
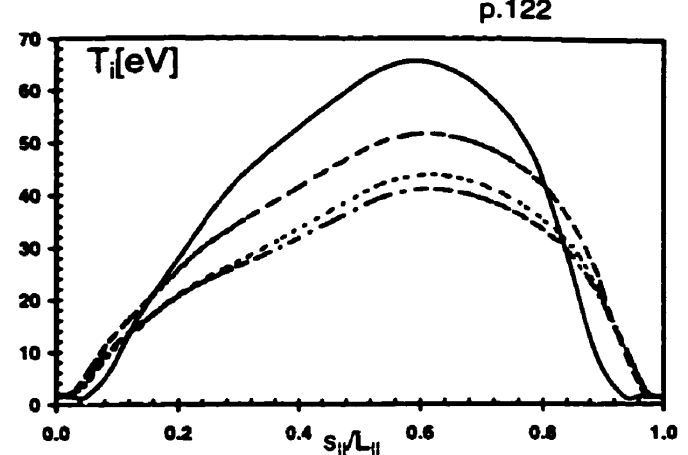
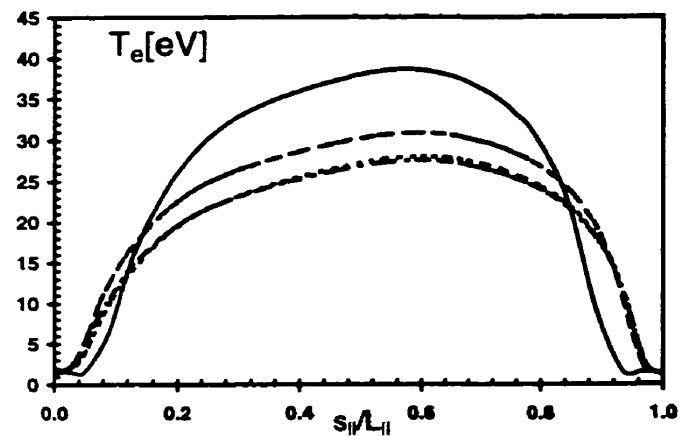


Fig.4.2.9: Along-B plots of plasma variables for case C with pressure dependent cross-field energy source at four radial locations in the SOL (solid line, separatrix ring,  $ir=8$ ; dashed line,  $ir=10$ ; dot-dashed line,  $ir=12$ ; dotted line,  $ir=14$ ). Compare with Fig.4.1.31.

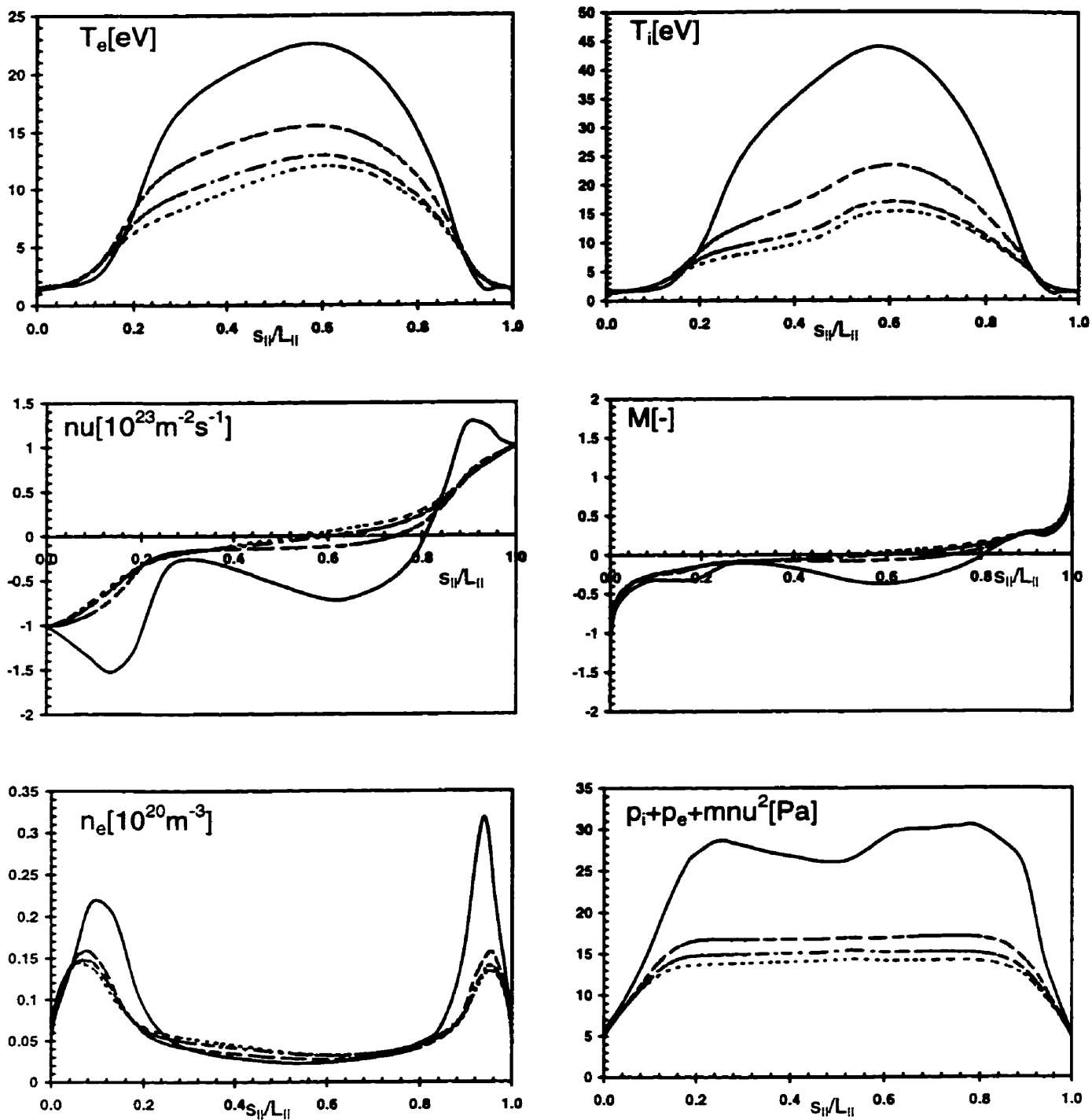


Fig.4.2.10: Along- $\mathbf{B}$  plots of plasma variables for case B without volumetric recombination, at four radial locations in the SOL (solid line, separatrix ring,  $ir=8$ ; dashed line,  $ir=10$ ; dot-dashed line,  $ir=12$ ; dotted line,  $ir=14$ ). Compare with Fig.4.1.20.

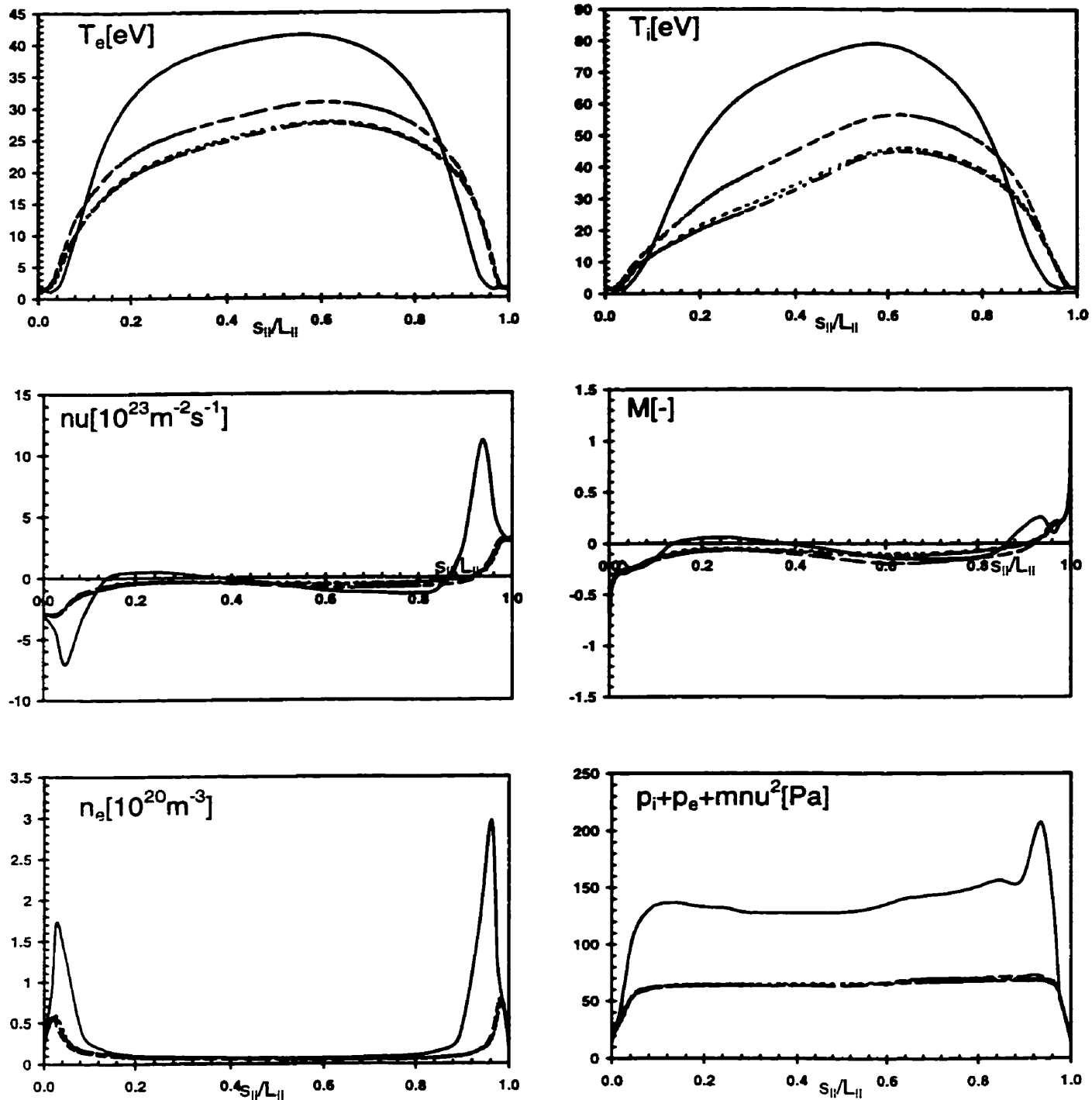


Fig.4.2.11: Along-B plots of plasma variables for case C without volumetric recombination, at four radial locations in the SOL (solid line, separatrix ring, ir=8; dashed line, ir=10; dot-dashed line, ir=12; dotted line, ir=14). Compare with Fig.4.1.31.

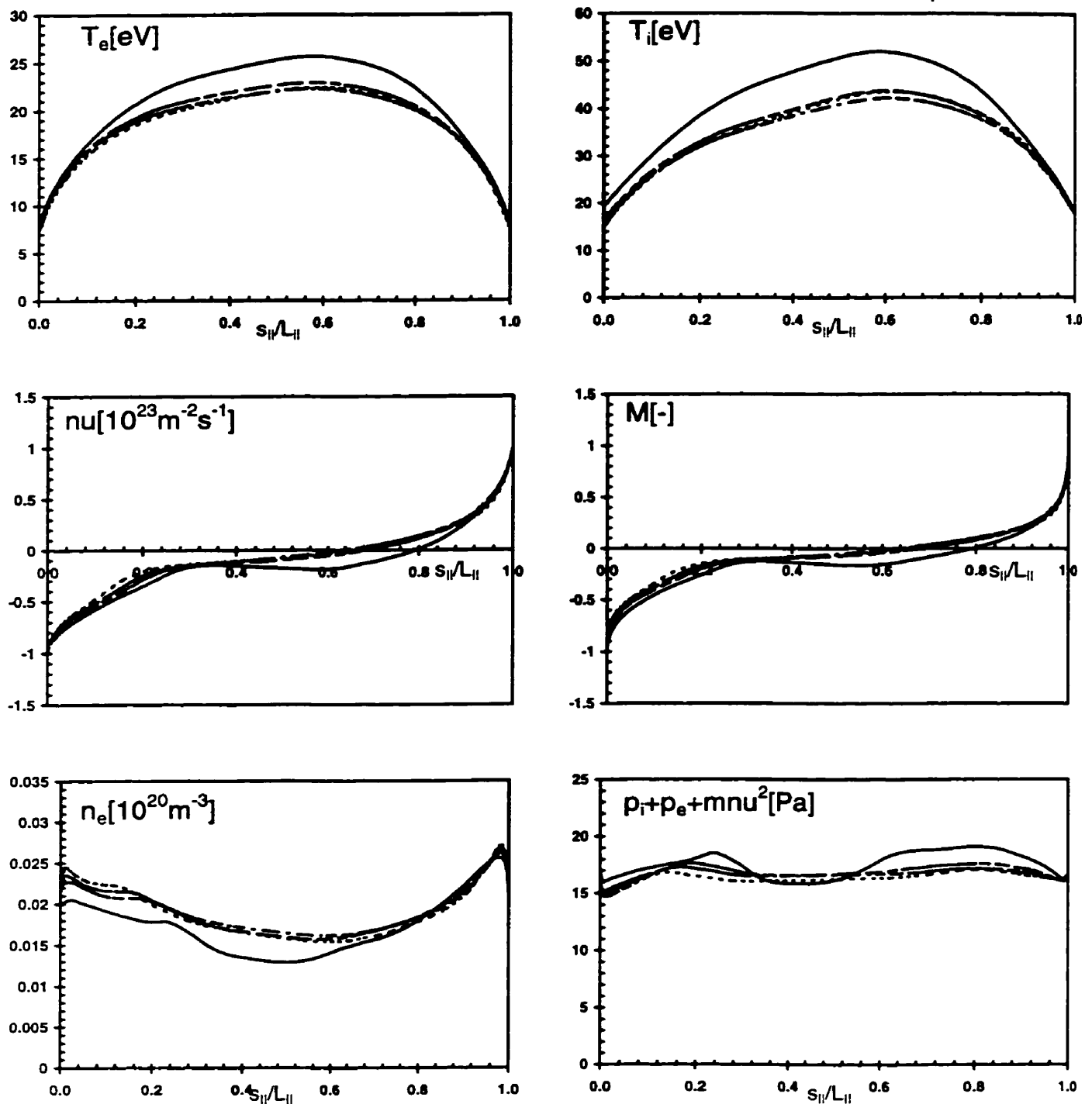


Fig.4.2.12: Along-B plots of plasma variables for case A with neutral velocity equal to half the plasma velocity, at four radial locations in the SOL (solid line, separatrix ring,  $ir=8$ ; dashed line,  $ir=10$ ; dot-dashed line,  $ir=12$ ; dotted line,  $ir=14$ ). Compare with Fig.4.1.8.

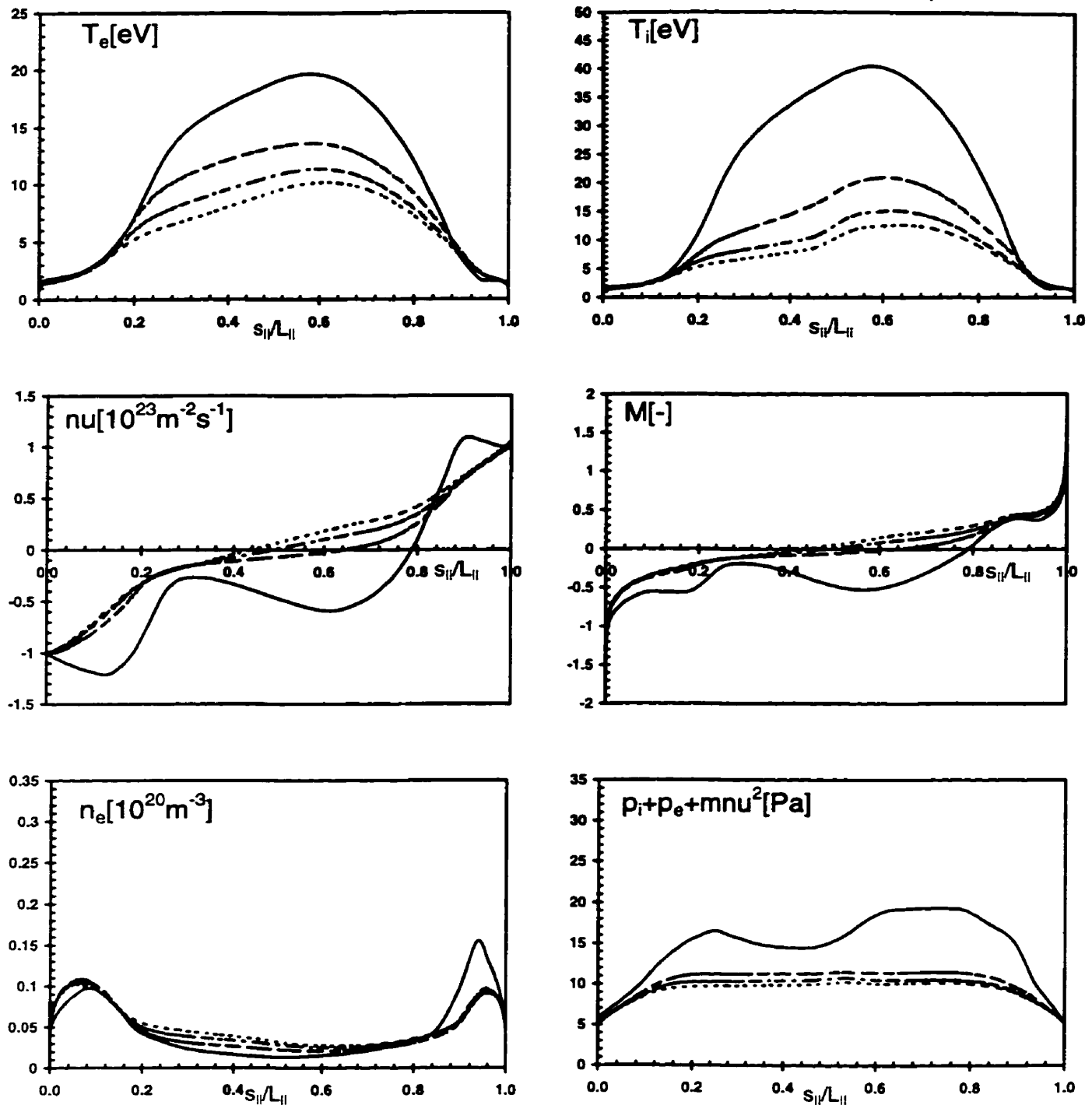


Fig.4.2.13: Along- $\mathbf{B}$  plots of plasma variables for case B with neutral velocity equal to half the plasma velocity, at four radial locations in the SOL (solid line, separatrix ring,  $ir=8$ ; dashed line,  $ir=10$ ; dot-dashed line,  $ir=12$ ; dotted line,  $ir=14$ ). Compare with Fig.4.1.20.

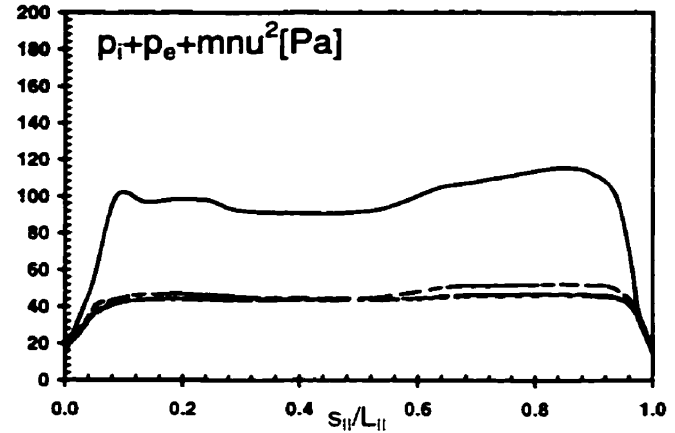
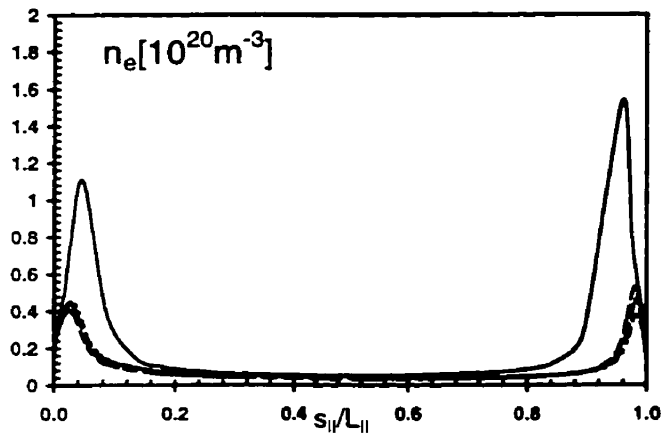
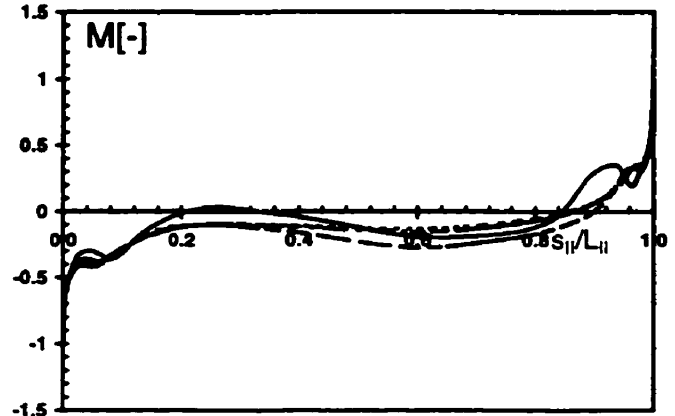
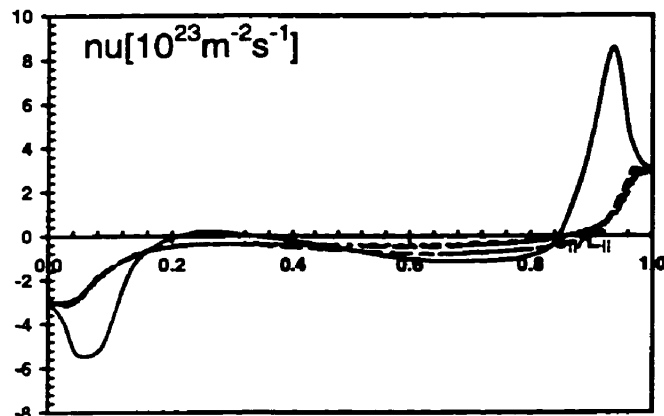
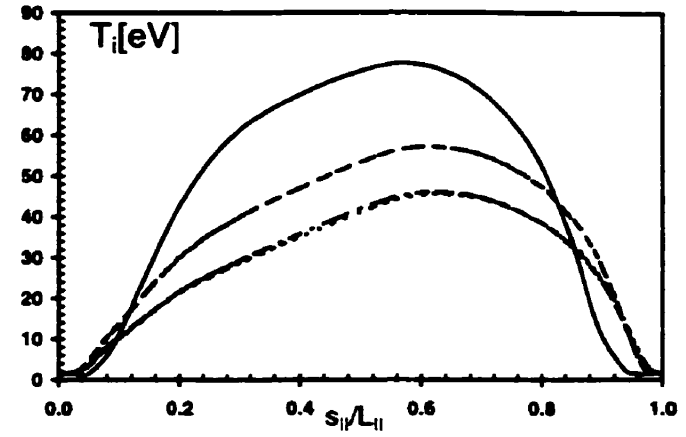
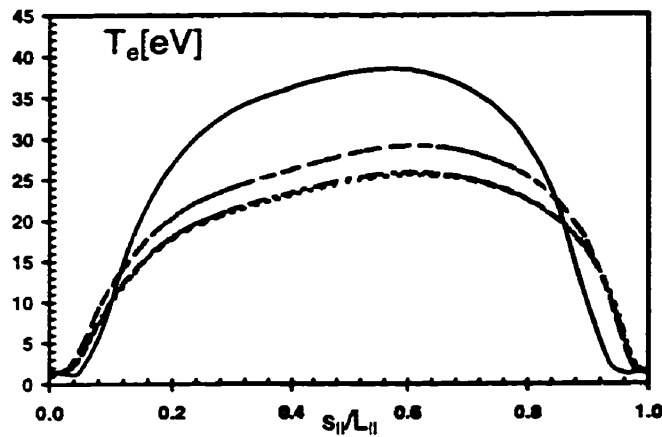


Fig.4.2.14: Along- $\mathbf{B}$  plots of plasma variables for case C with neutral velocity equal to half the plasma velocity, at four radial locations in the SOL (solid line, separatrix ring, ir=8; dashed line, ir=10; dot-dashed line, ir=12; dotted line, ir=14). Compare with Fig.4.1.31.

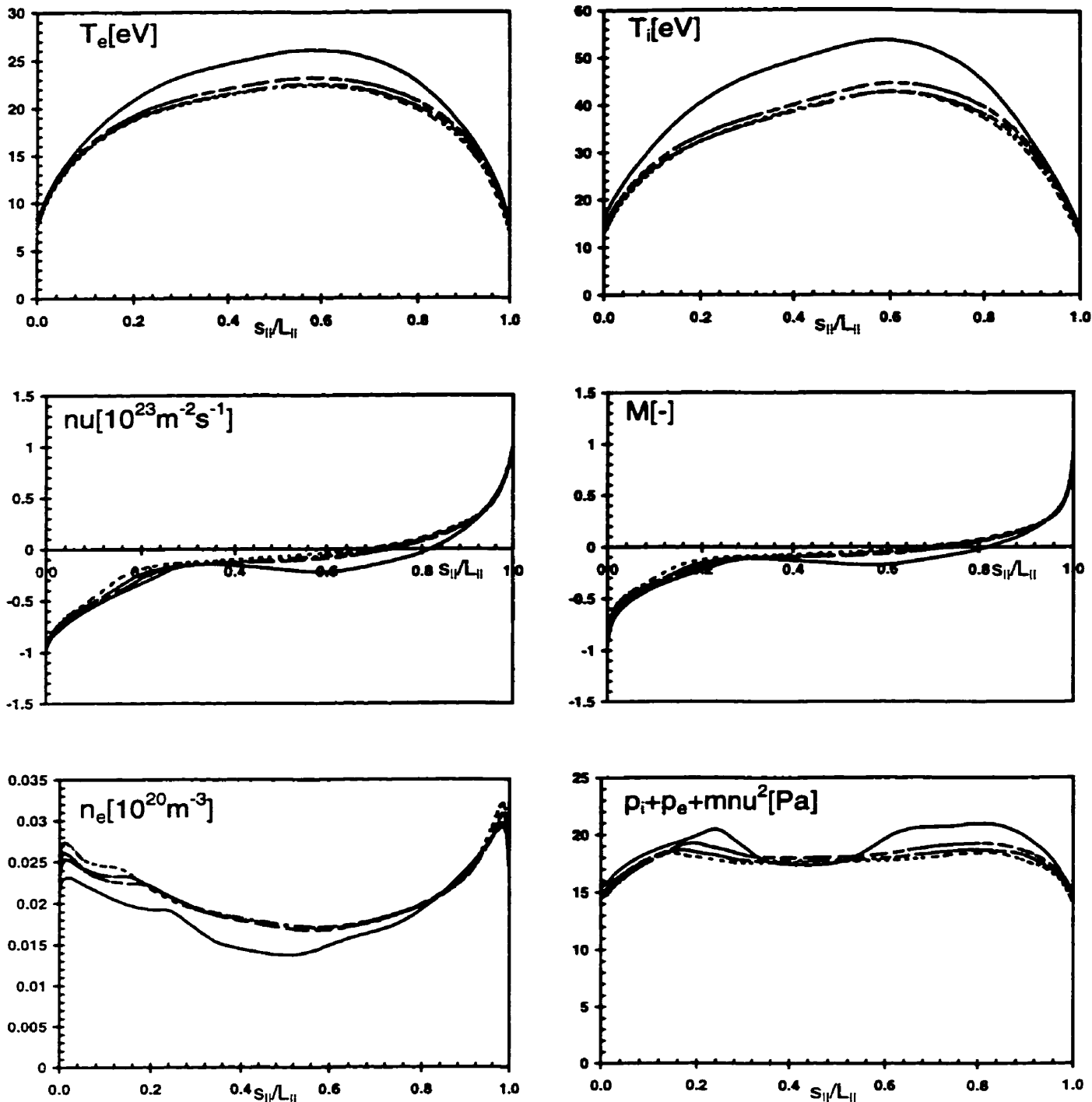


Fig.4.2.15: Along-B plots of plasma variables for case A including the ion energy term  $Q_{qi}$  at four radial locations in the SOL (solid line, separatrix ring,  $ir=8$ ; dashed line,  $ir=10$ ; dot-dashed line,  $ir=12$ ; dotted line,  $ir=14$ ). Compare with Fig.4.1.8.

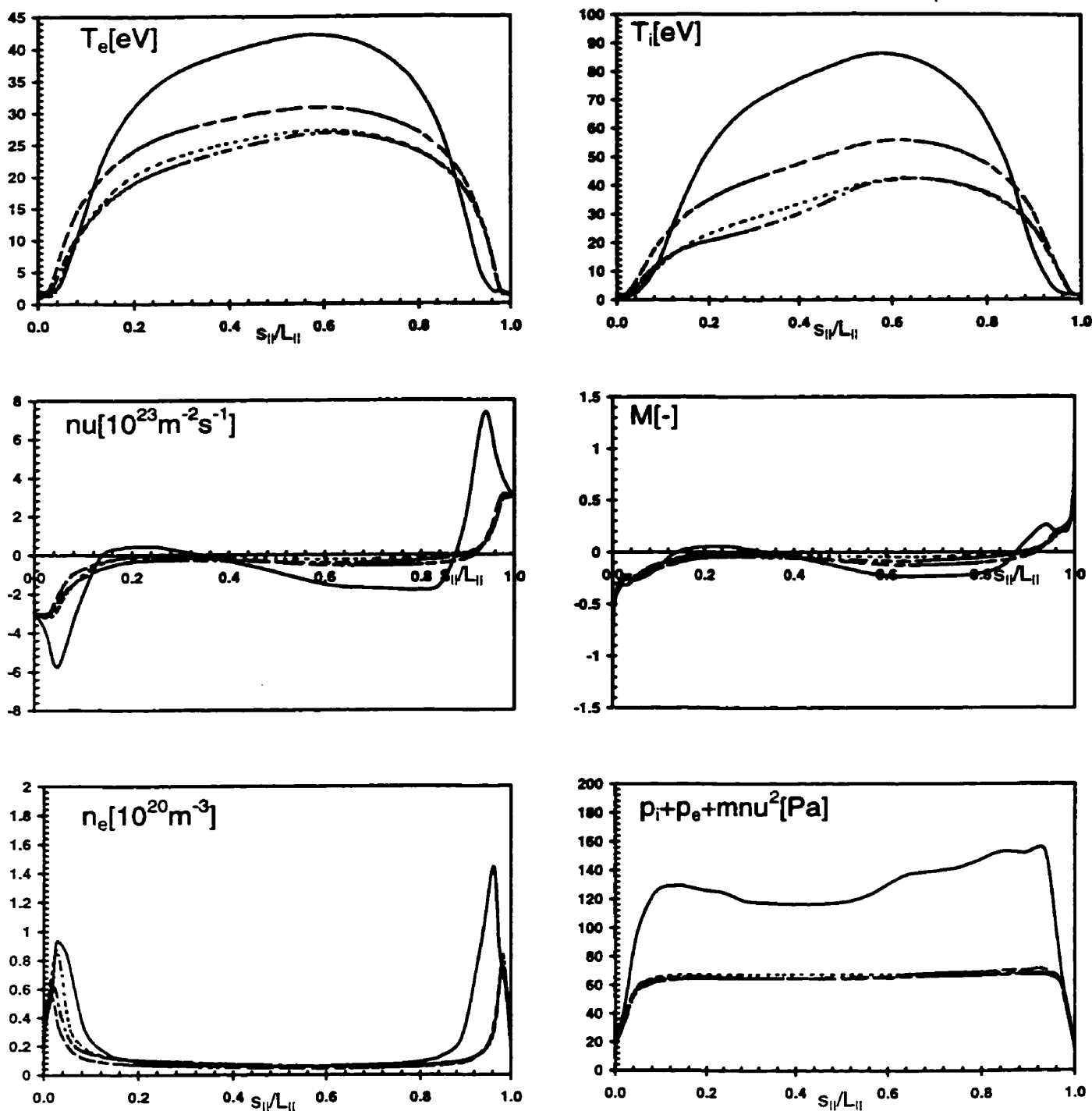


Fig.4.2.16: Along- $\mathbf{B}$  plots of plasma variables for case C including the ion energy term  $Q_{\phi i}$  at four radial locations in the SOL (solid line, separatrix ring, ir=8; dashed line, ir=10; dot-dashed line, ir=12; dotted line, ir=14). Compare with Fig.4.1.31.

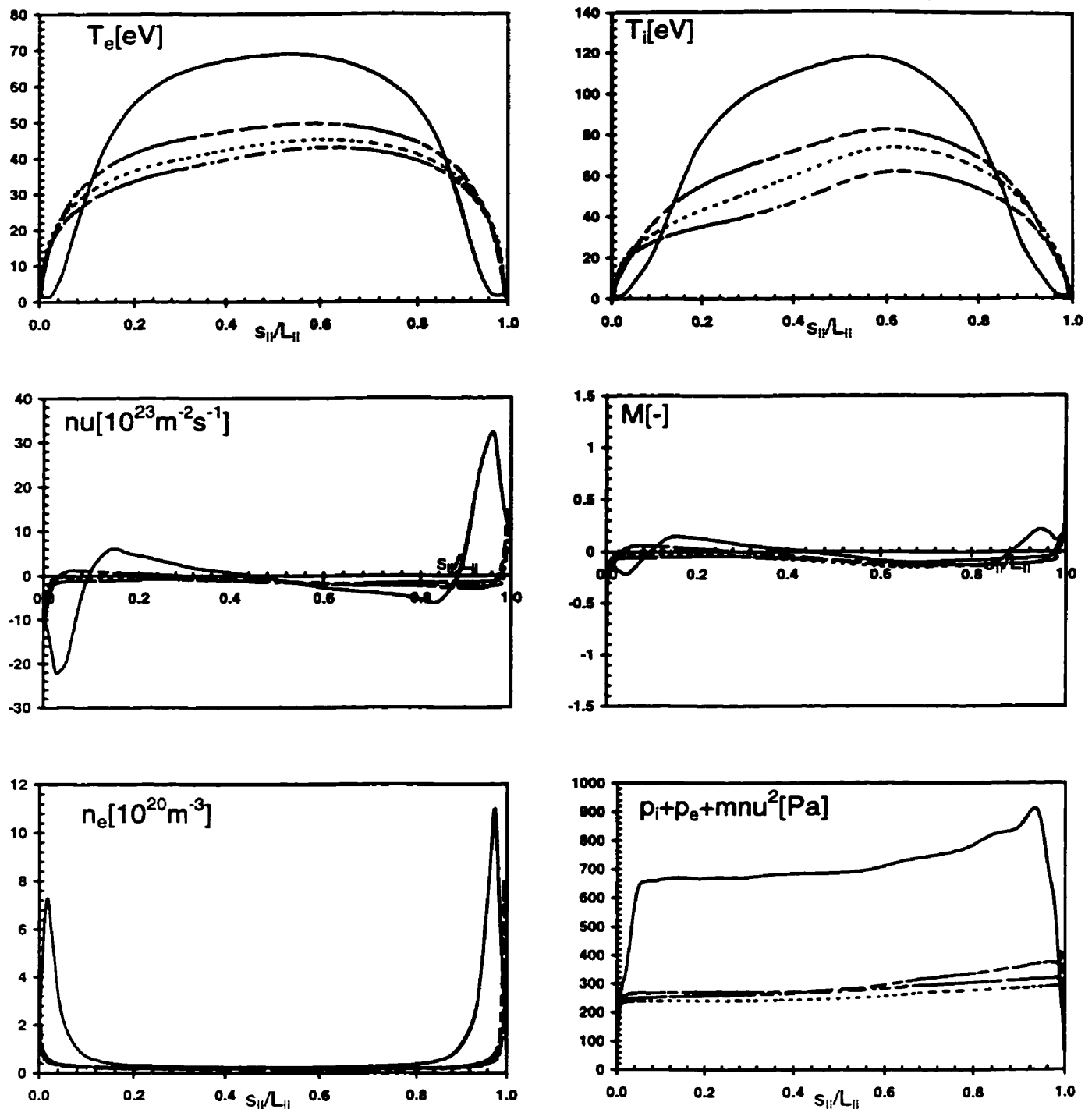


Fig.4.2.17: Along- $\mathbf{B}$  plots of plasma variables for the  $0.5 \text{ eV}, 10^{24} \text{ m}^{-2} \text{s}^{-1}$  case including the ion energy term  $Q_{qi}$ , at four radial locations in the SOL (solid line, separatrix ring, ir=8; dashed line, ir=10; dot-dashed line, ir=12; dotted line, ir=14). The evolution was stable, even without the  $n_e^{exp}$  constraint. Compare with Fig. 4.1.33.

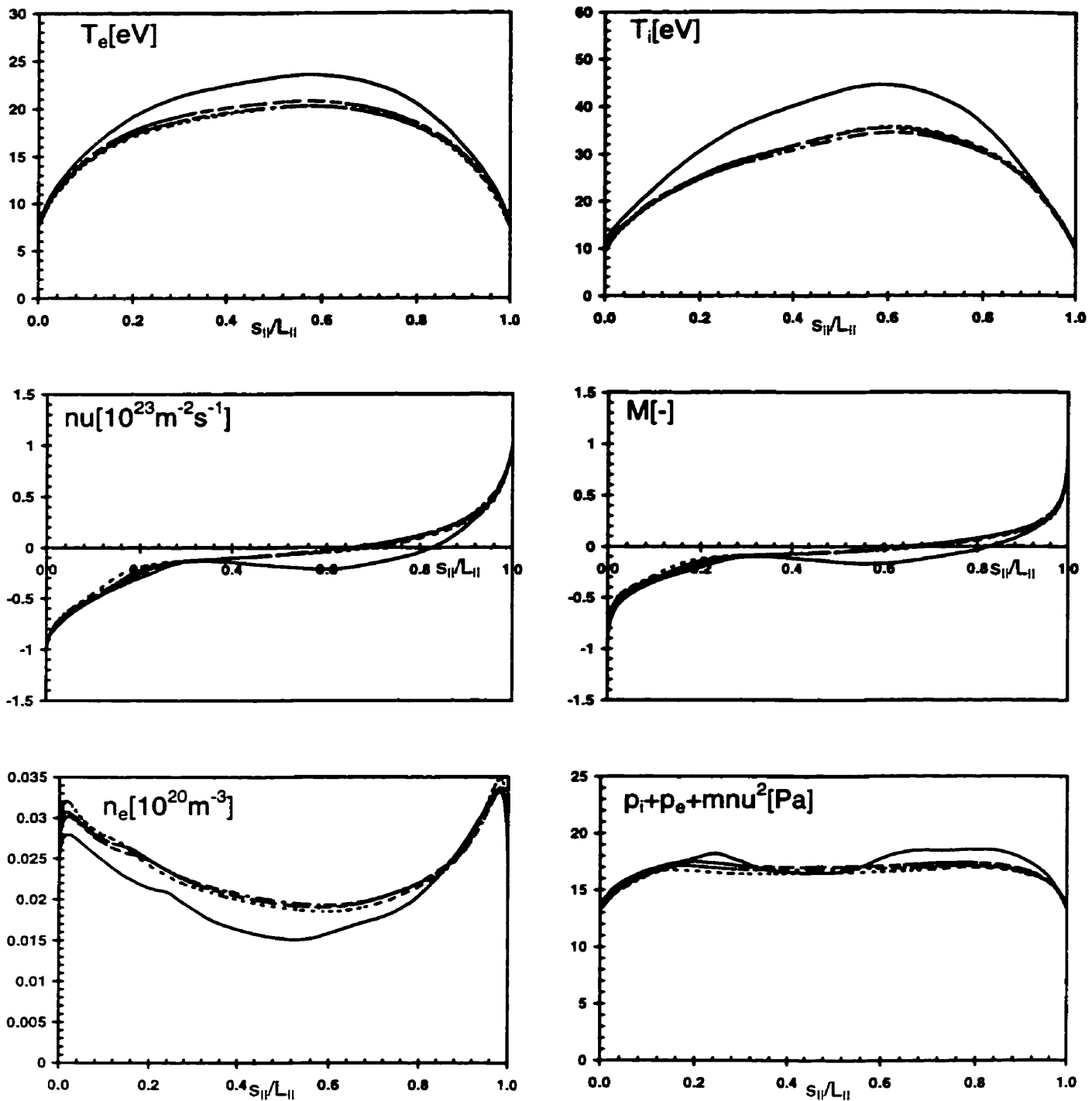


Fig.4.2.18: Along-B plots of plasma variables for case A without impurity cooling ( $Q_z = 0$ ) at four radial locations in the SOL (solid line, separatrix ring,  $ir=8$ ; dashed line,  $ir=10$ ; dot-dashed line,  $ir=12$ ; dotted line,  $ir=14$ ). Compare with Fig.4.1.8.

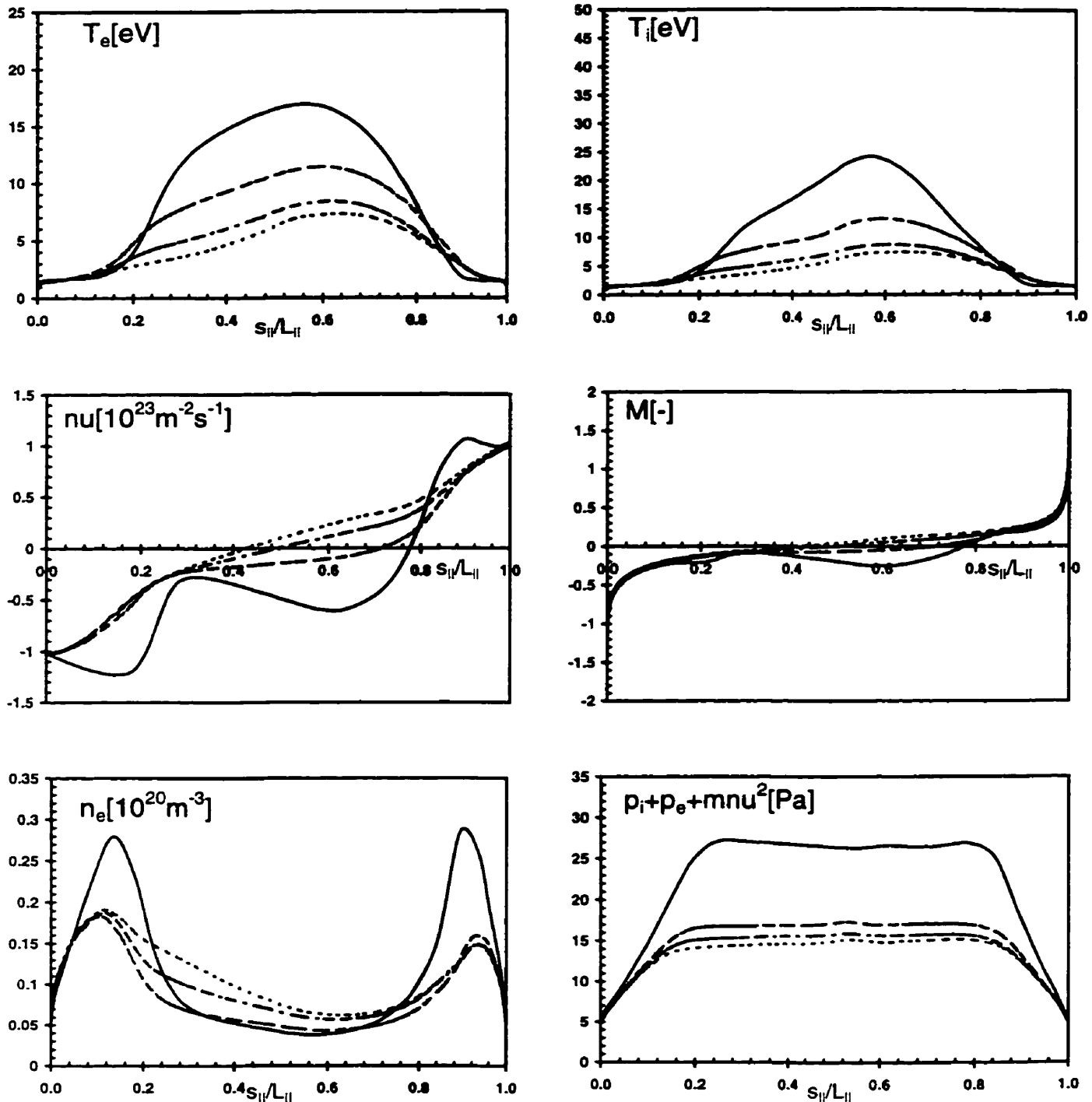


Fig.4.2.19: Along- $\mathbf{B}$  plots of plasma variables for case B without impurity cooling ( $Q_Z = 0$ ) at four radial locations in the SOL (solid line, separatrix ring,  $ir=8$ ; dashed line,  $ir=10$ ; dot-dashed line,  $ir=12$ ; dotted line,  $ir=14$ ). Compare with Fig.4.1.20.

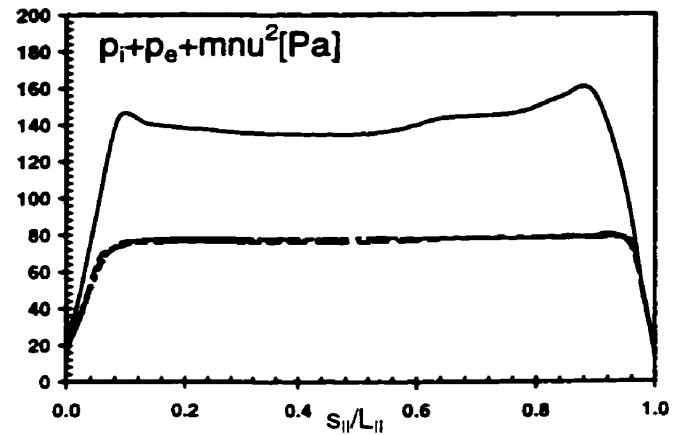
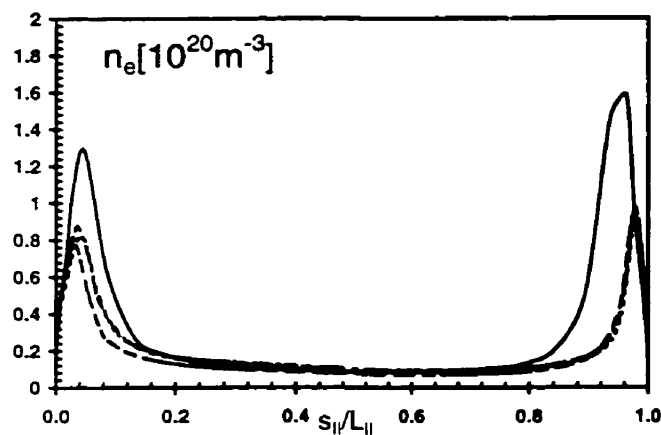
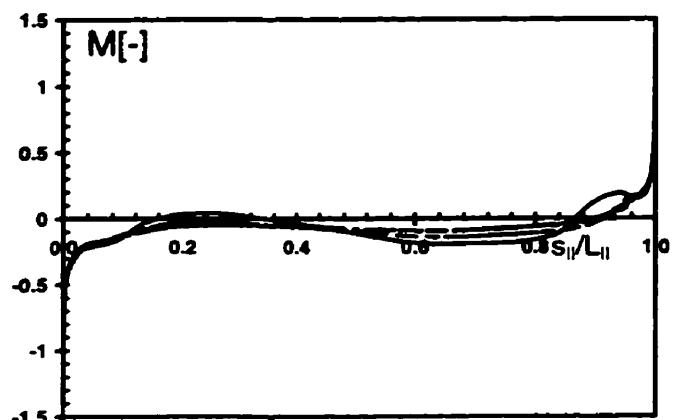
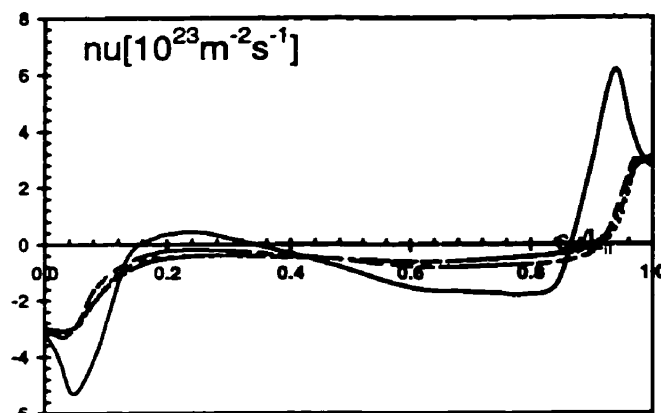
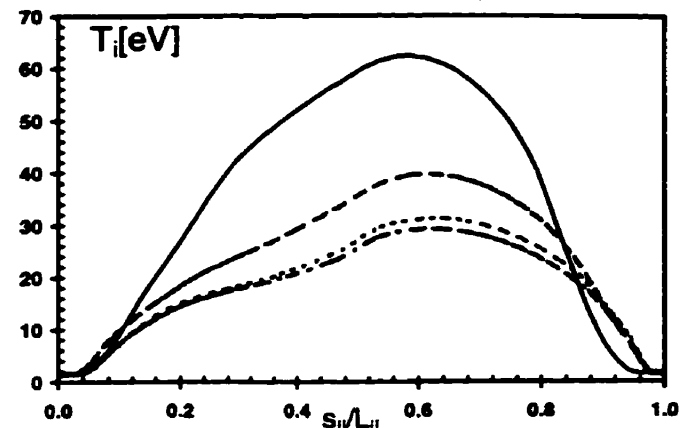
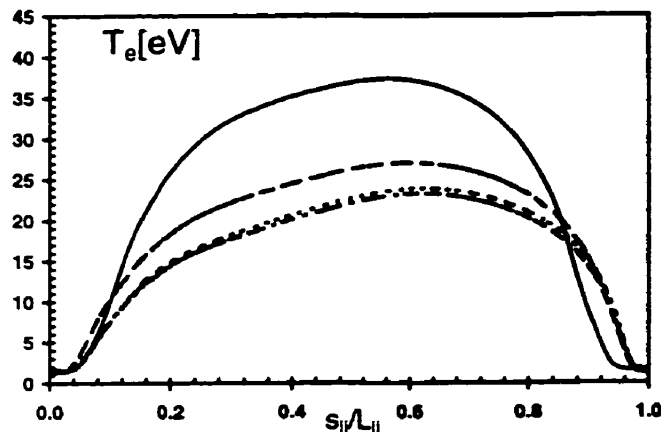


Fig.4.2.20: Along- $\mathbf{B}$  plots of plasma variables for case C without impurity cooling ( $Q_z = 0$ ) at four radial locations in the SOL (solid line, separatrix ring,  $ir=8$ ; dashed line,  $ir=10$ ; dot-dashed line,  $ir=12$ ; dotted line,  $ir=14$ ). Compare with Fig.4.1.31.

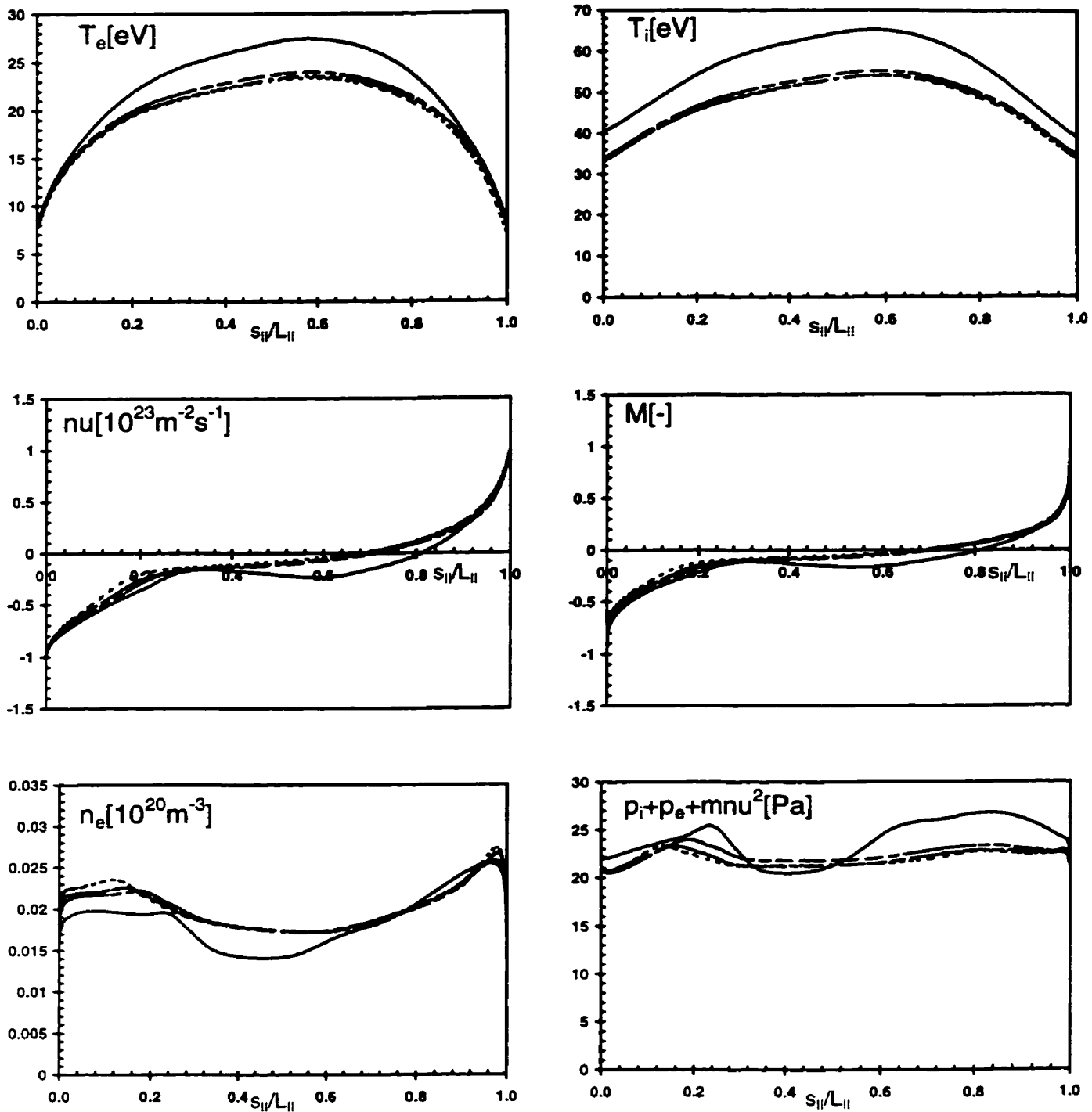


Fig.4.2.21: Along- $\mathbf{B}$  plots of plasma variables for case A without electron-ion energy equipartition ( $Q_{ci} = 0$ ) at four radial locations in the SOL (solid line, separatrix ring,  $ir=8$ ; dashed line,  $ir=10$ ; dot-dashed line,  $ir=12$ ; dotted line,  $ir=14$ ). Compare with Fig.4.1.8.

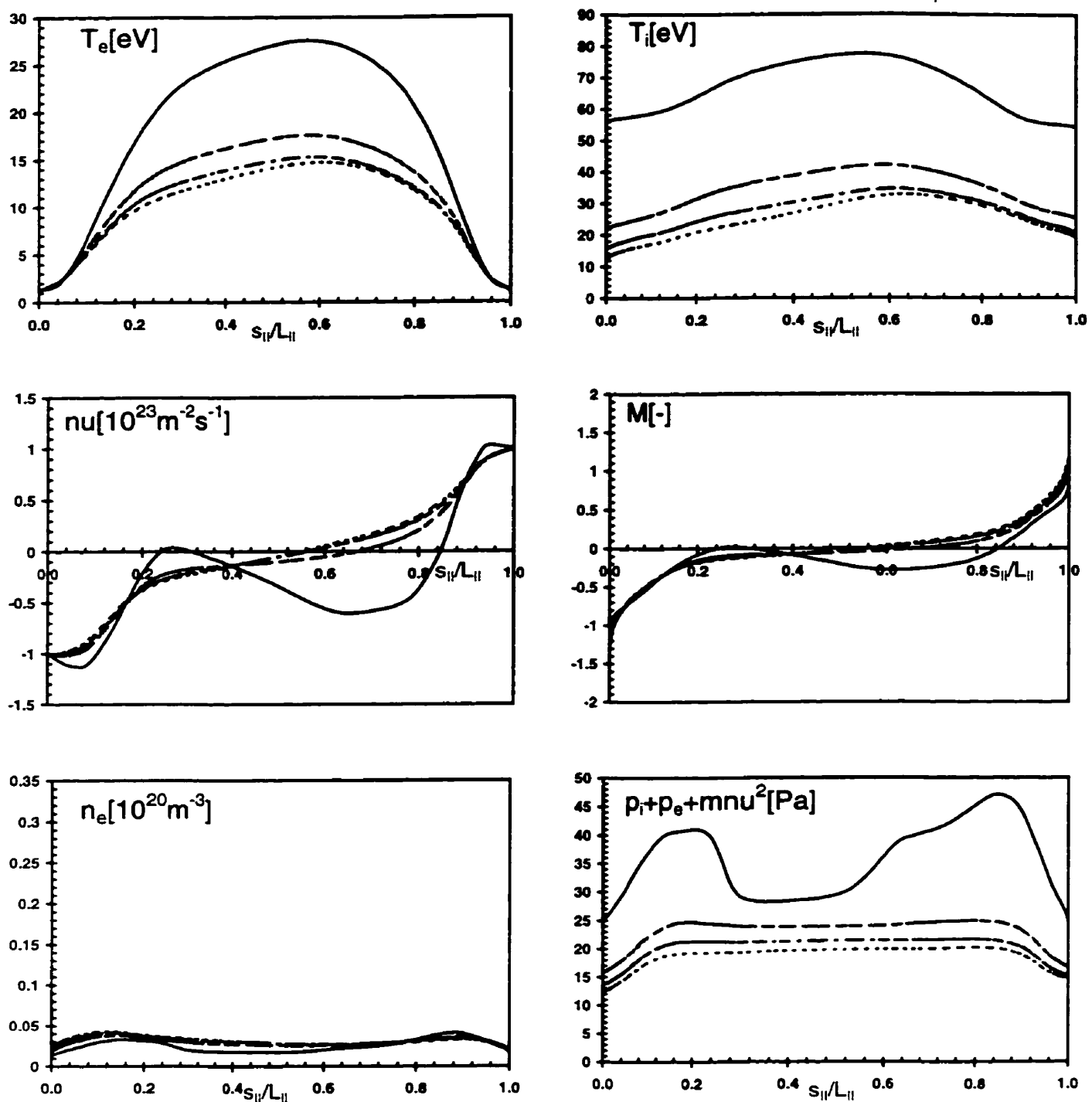


Fig.4.2.22: Along- $B$  plots of plasma variables for case B without electron-ion energy equipartition ( $Q_{ci} = 0$ ) at four radial locations in the SOL (solid line, separatrix ring, ir=8; dashed line, ir=10; dot-dashed line, ir=12; dotted line, ir=14). Compare with Fig.4.1.20.

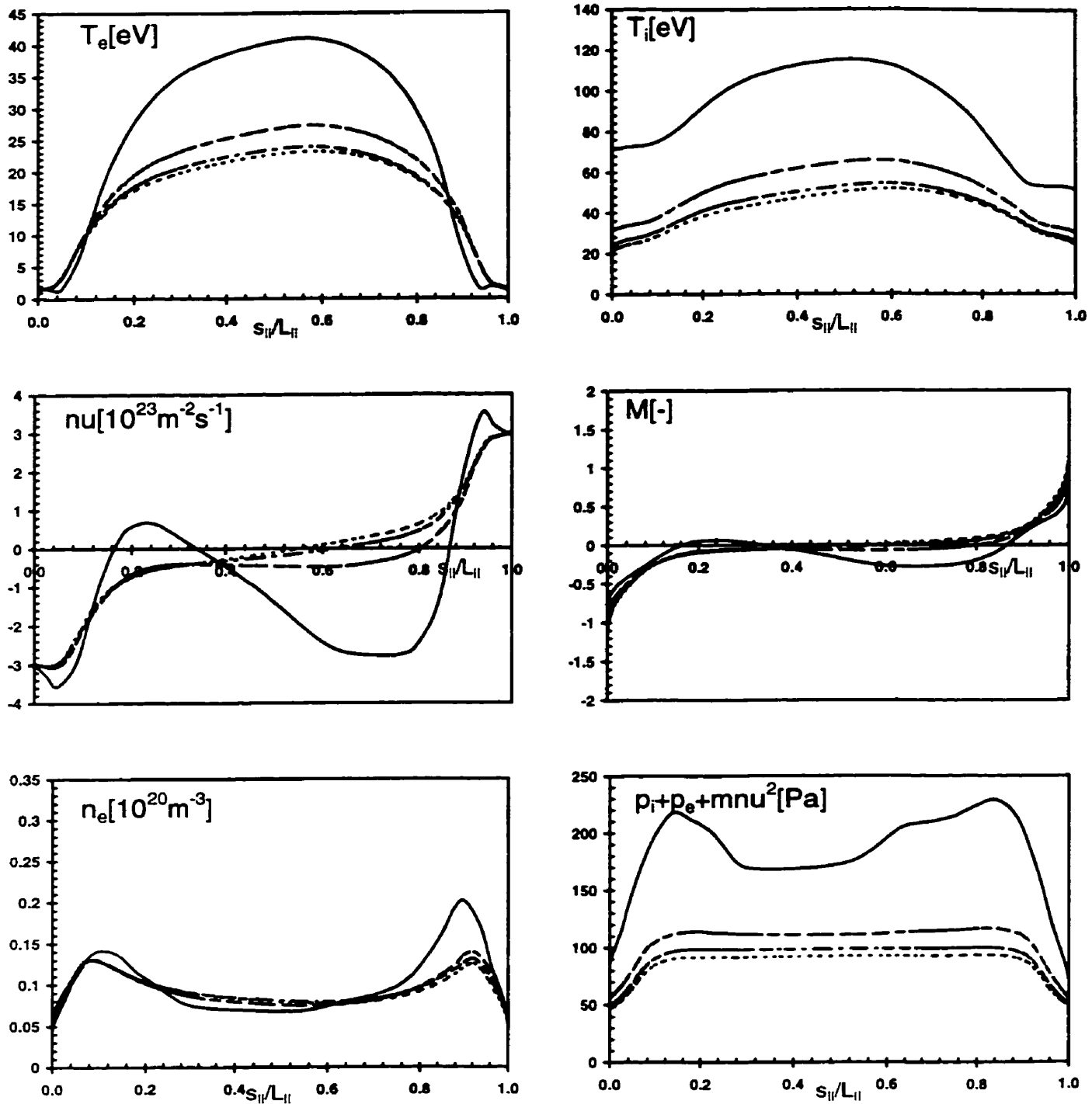


Fig.4.2.23: Along-B plots of plasma variables for case C without electron-ion energy equipartition ( $Q_{ei} = 0$ ) at four radial locations in the SOL (solid line, separatrix ring,  $ir=8$ ; dashed line,  $ir=10$ ; dot-dashed line,  $ir=12$ ; dotted line,  $ir=14$ ). Compare with Fig.4.1.31.

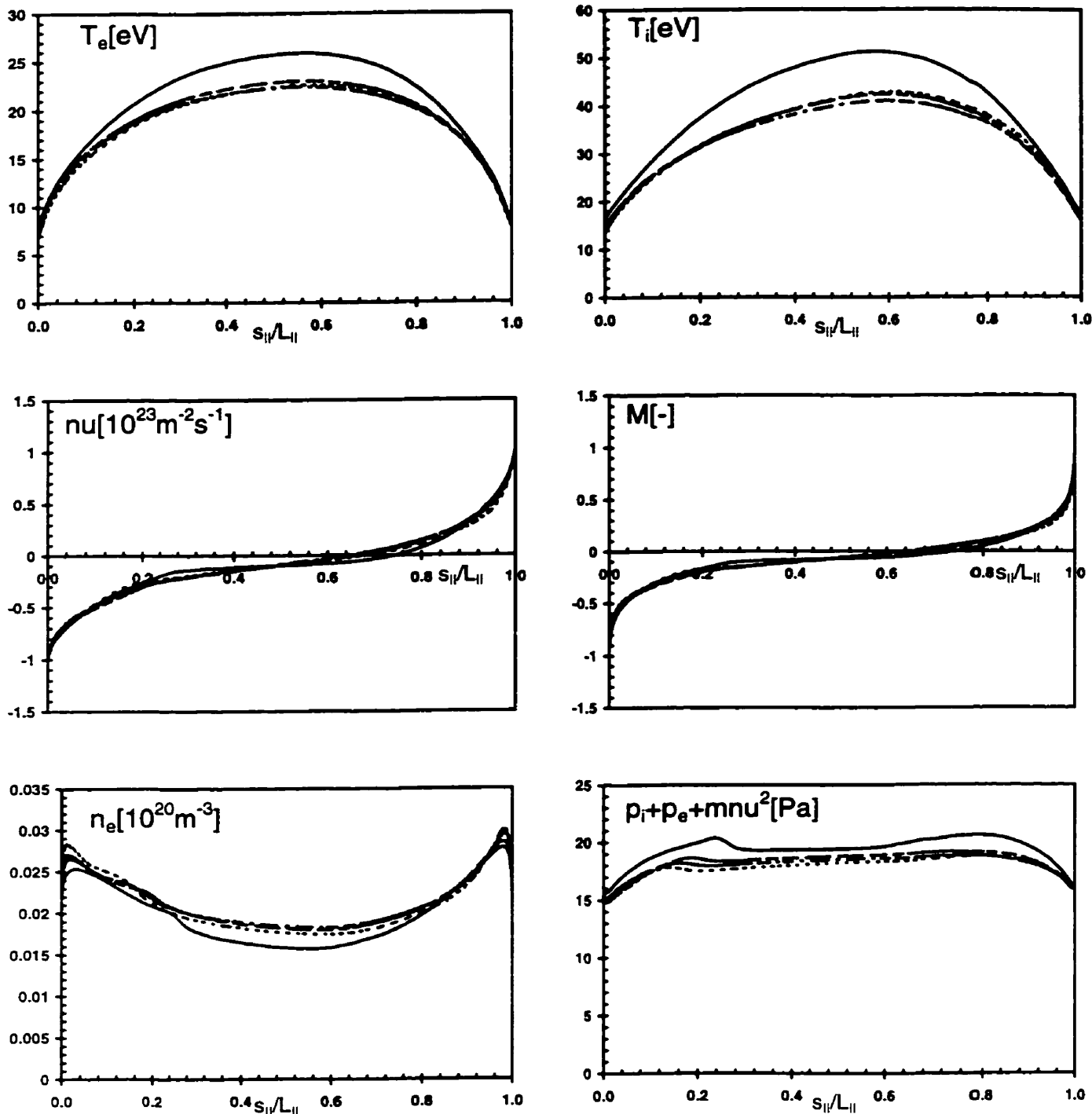


Fig.4.2.24: Along-B plots of plasma variables for case A without flux expansion terms ( $Q_B = 0$ ) at four radial locations in the SOL (solid line, separatrix ring,  $ir=8$ ; dashed line,  $ir=10$ ; dot-dashed line,  $ir=12$ ; dotted line,  $ir=14$ ). Compare with Fig.4.1.8.

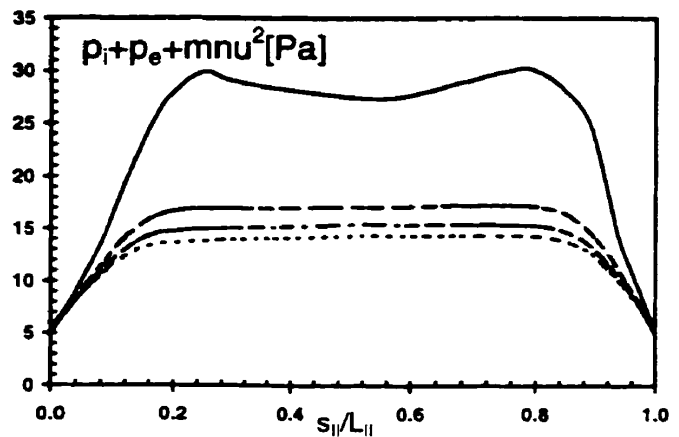
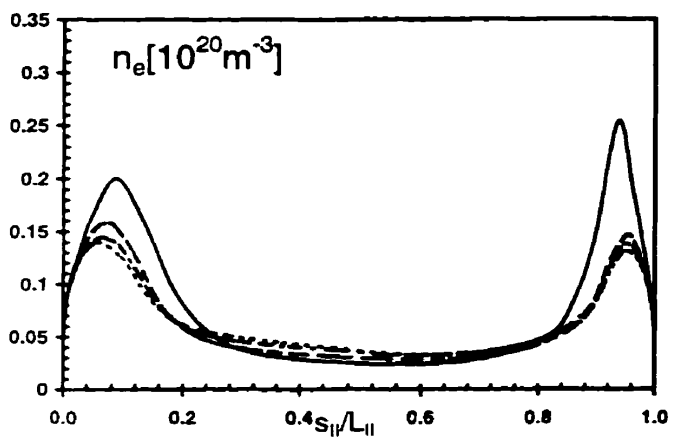
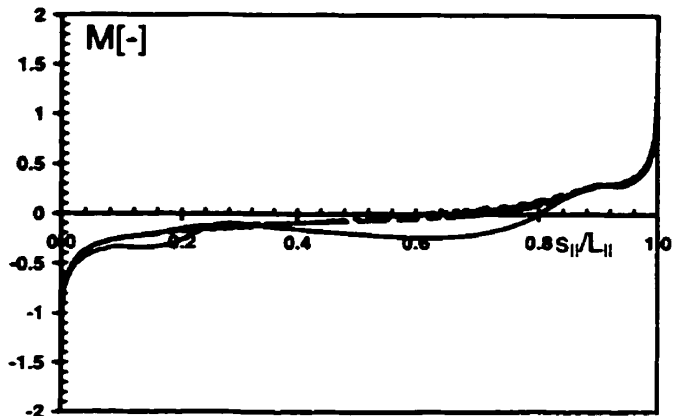
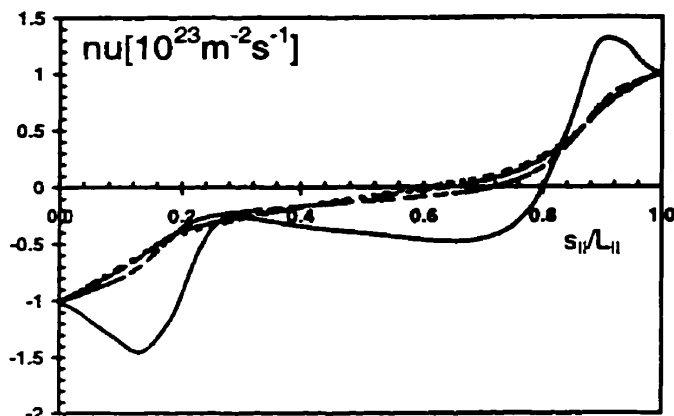
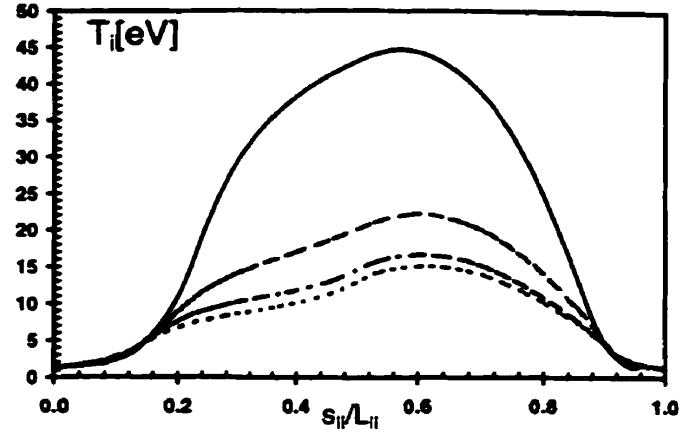
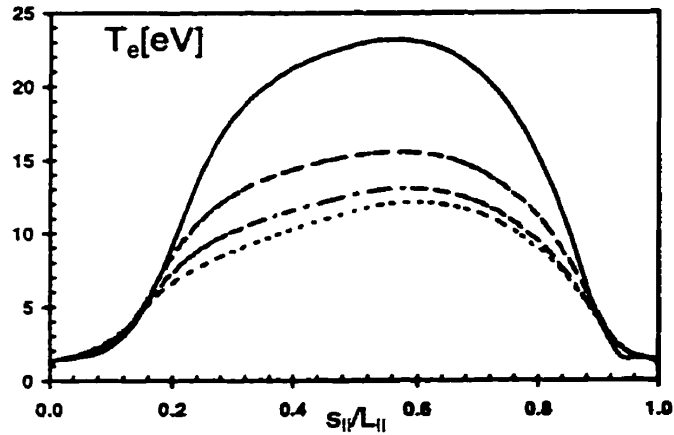


Fig.4.2.25: Along-B plots of plasma variables for case B without flux expansion terms ( $Q_B = 0$ ) at four radial locations in the SOL (solid line, separatrix ring,  $ir=8$ ; dashed line,  $ir=10$ ; dot-dashed line,  $ir=12$ ; dotted line,  $ir=14$ ). Compare with Fig.4.1.20.

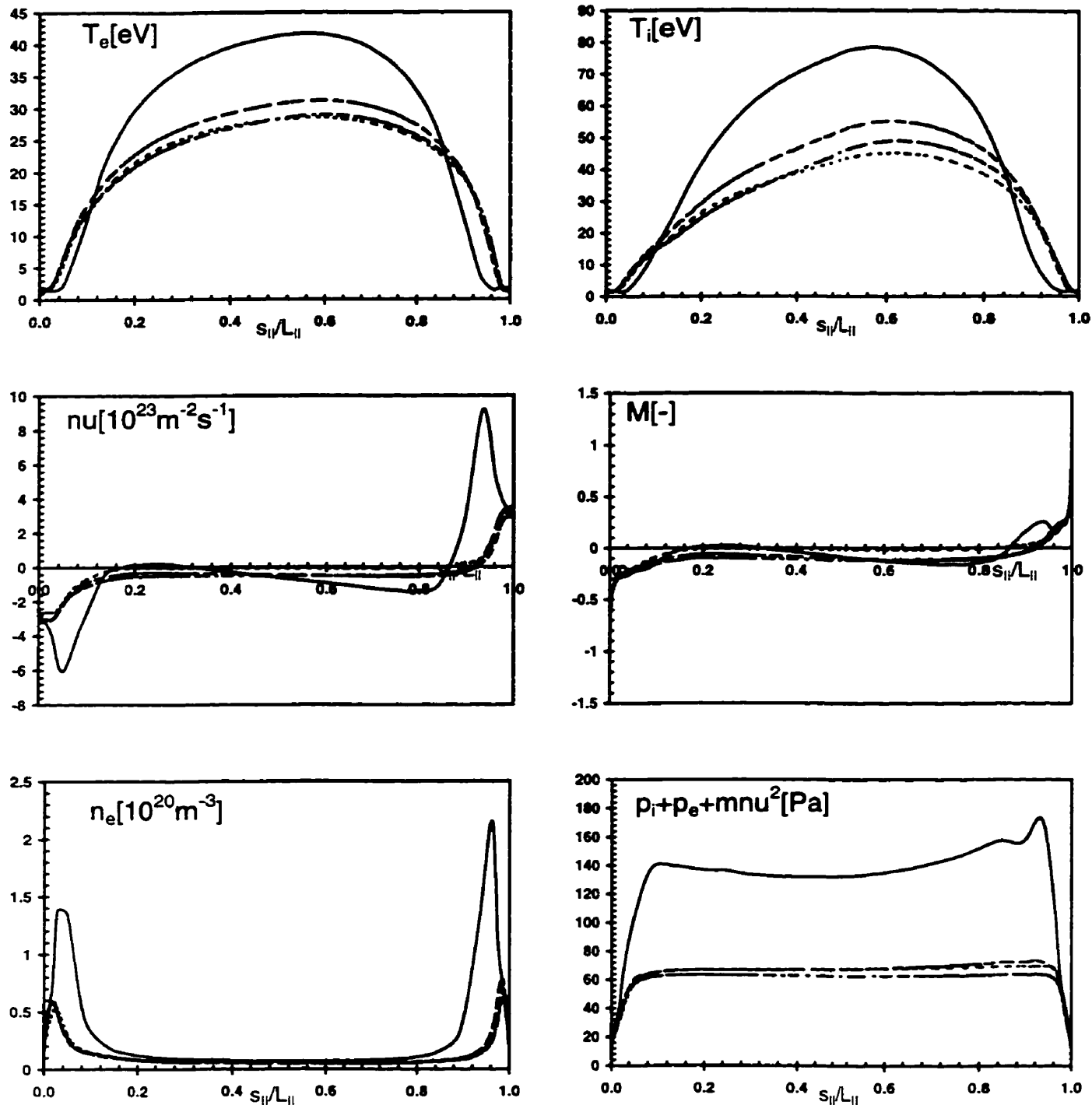


Fig.4.2.26: Along- $\mathbf{B}$  plots of plasma variables for case C without flux expansion terms ( $Q_B = 0$ ) at four radial locations in the SOL (solid line, separatrix ring,  $r=8$ ; dashed line,  $r=10$ ; dot-dashed line,  $r=12$ ; dotted line,  $r=14$ ). Compare with Fig.4.1.31.

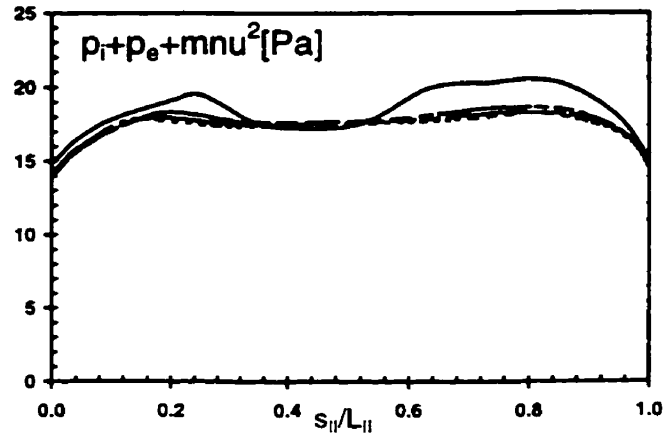
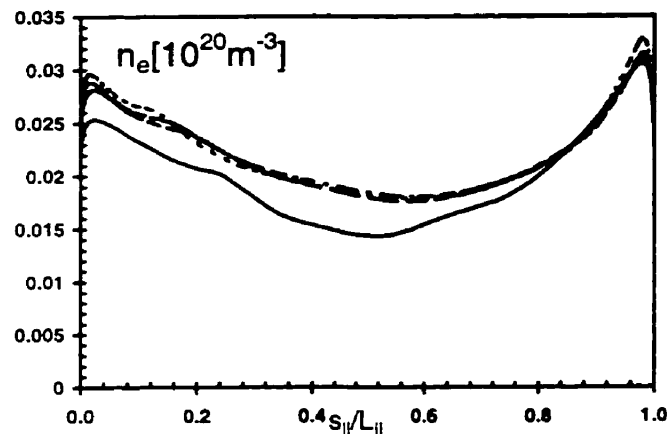
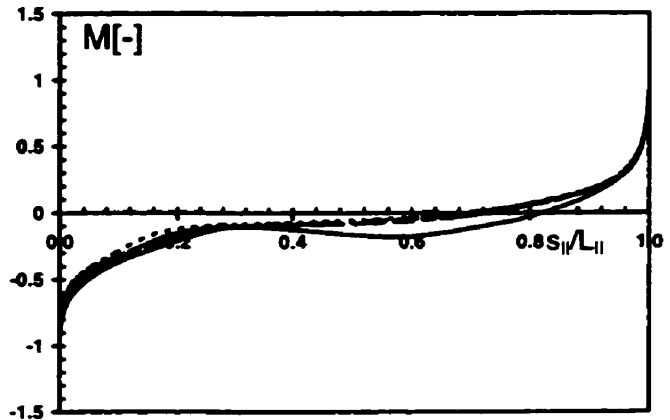
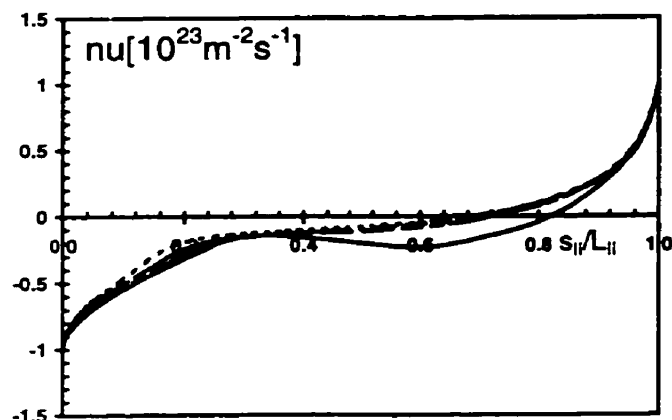
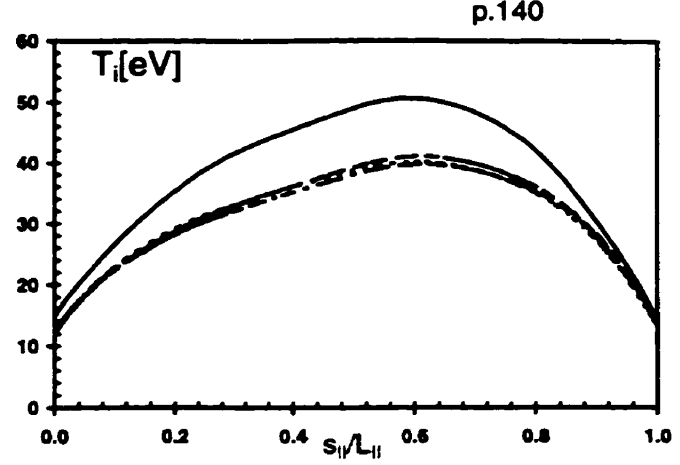
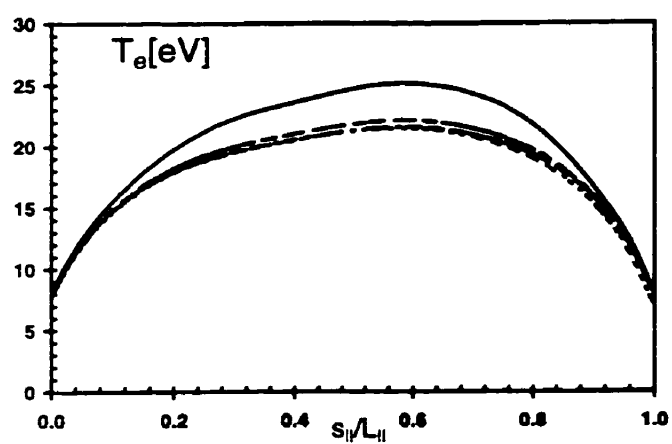


Fig.4.2.27: Along-B plots of plasma variables for case A with the electron heat transmission coefficient reduced by unity, at four radial locations in the SOL (solid line, separatrix ring, ir=8; dashed line, ir=10; dot-dashed line, ir=12; dotted line, ir=14). Compare with Fig.4.1.8.

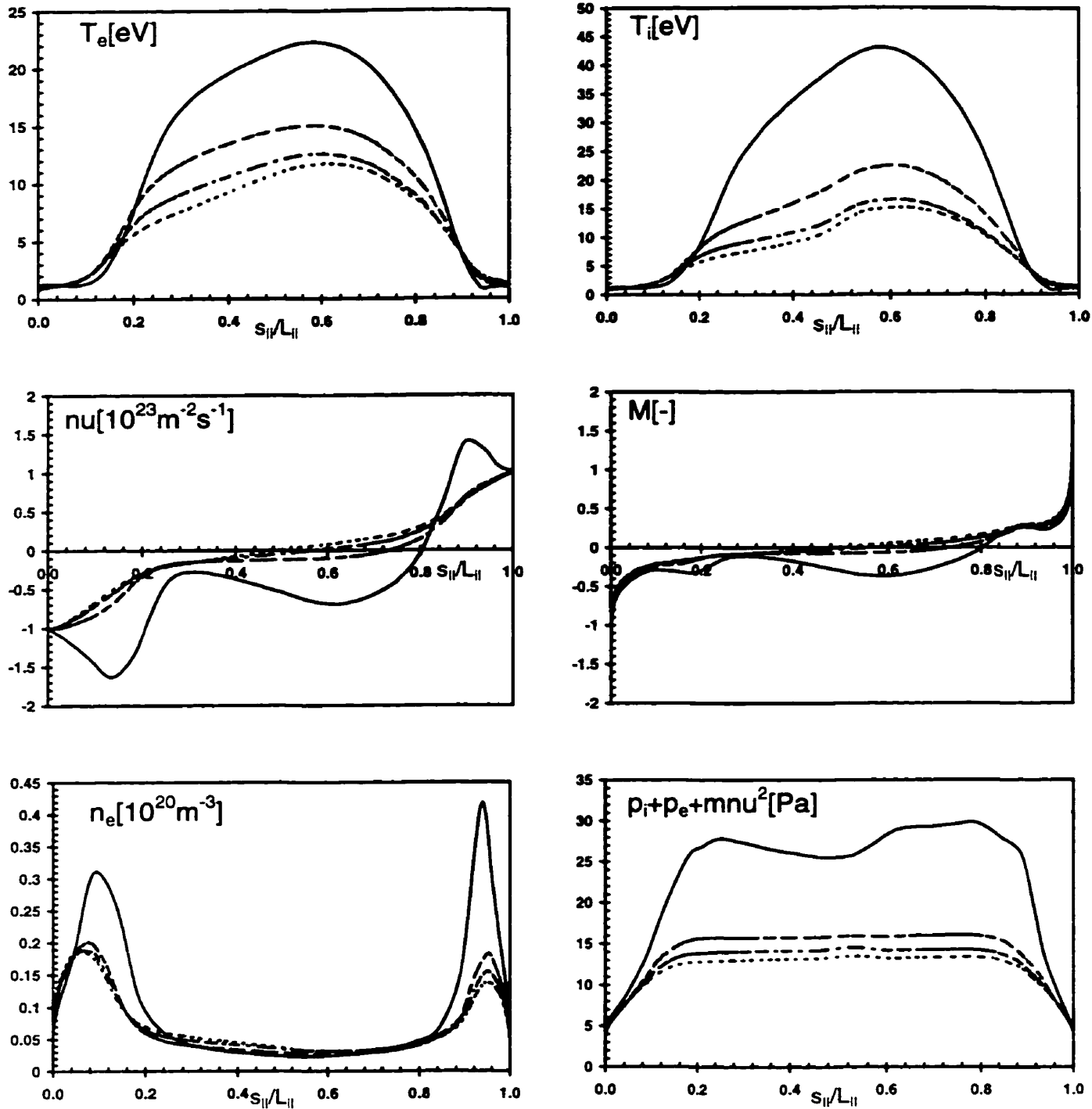


Fig.4.2.28: Along- $\mathbf{B}$  plots of plasma variables for case B with the electron heat transmission coefficient reduced by unity, at four radial locations in the SOL (solid line, separatrix ring,  $ir=8$ ; dashed line,  $ir=10$ ; dot-dashed line,  $ir=12$ ; dotted line,  $ir=14$ ). Compare with Fig.4.1.20.

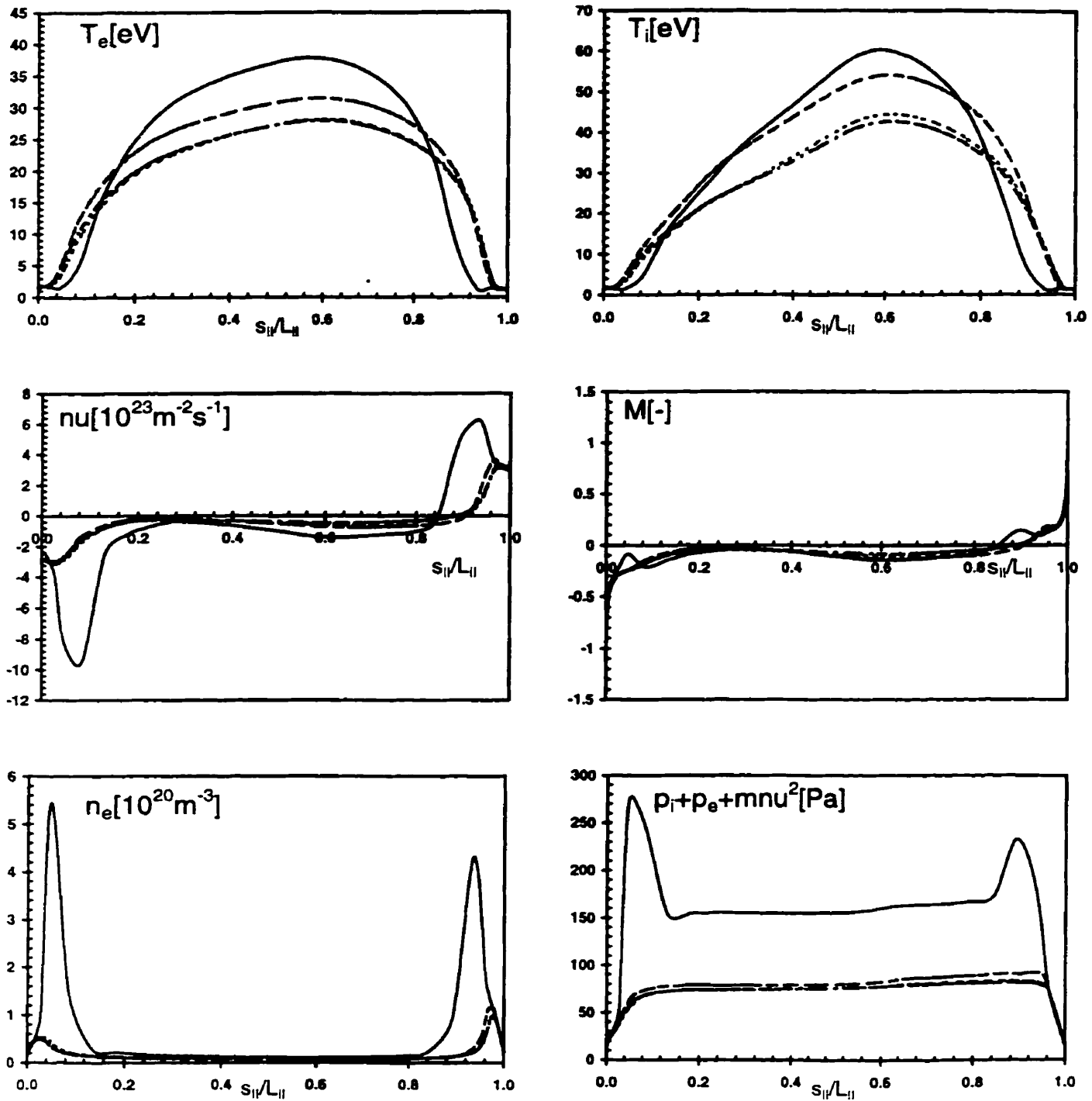


Fig.4.2.29: Along-B plots of plasma variables for case C with the electron heat transmission coefficient reduced by unity, at four radial locations in the SOL (solid line, separatrix ring,  $ir=8$ ; dashed line,  $ir=10$ ; dot-dashed line,  $ir=12$ ; dotted line,  $ir=14$ ). The evolution was constrained by the additional requirement that  $n_u^{sep} \sim 10^{19} \text{ m}^{-3}$ . Compare with Fig.4.1.31.

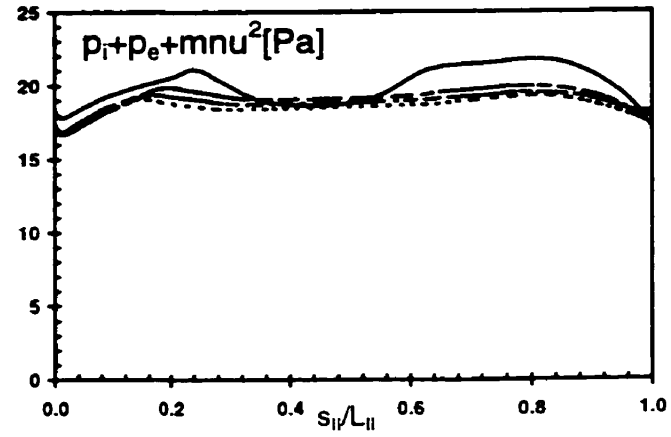
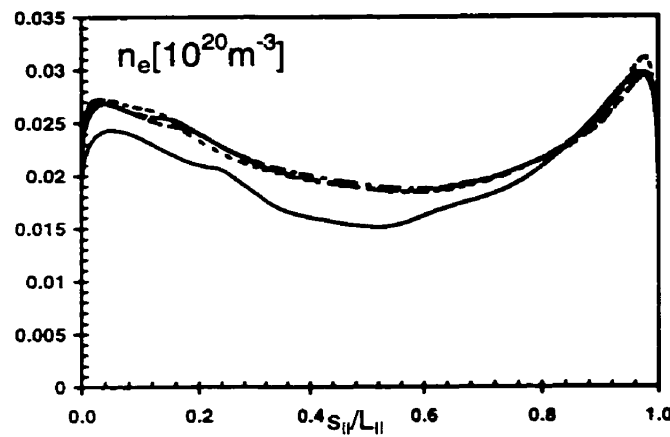
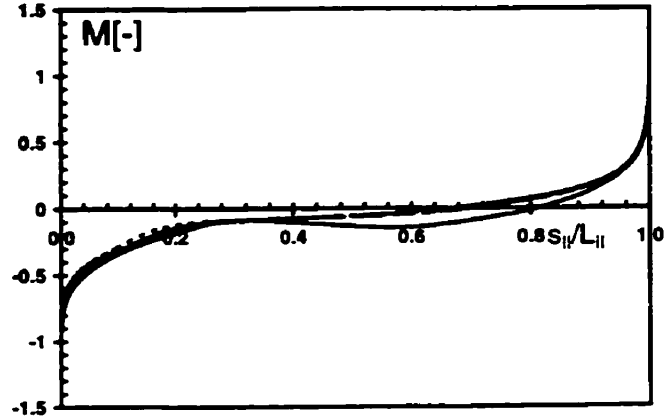
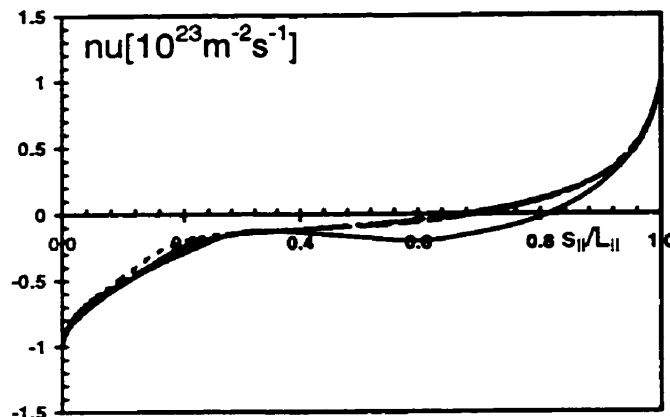
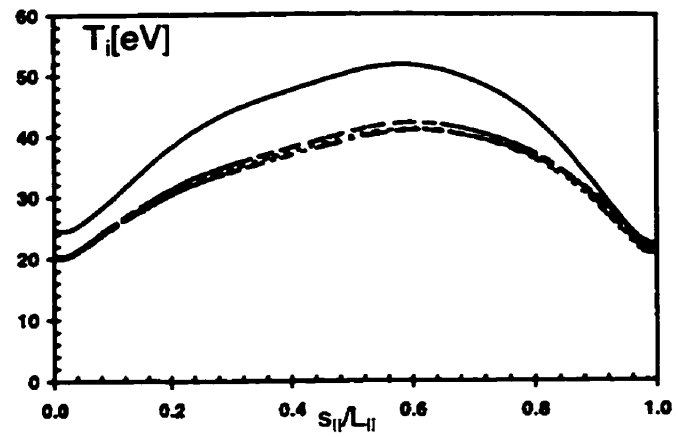
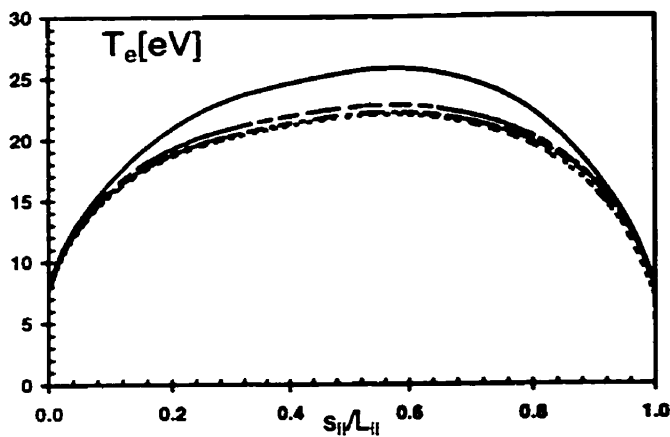


Fig.4.2.30: Along-B plots of plasma variables for case A with the ion heat transmission coefficient reduced by unity, at four radial locations in the SOL (solid line, separatrix ring, ir=8; dashed line, ir=10; dot-dashed line, ir=12; dotted line, ir=14). Compare with Fig.4.1.8.

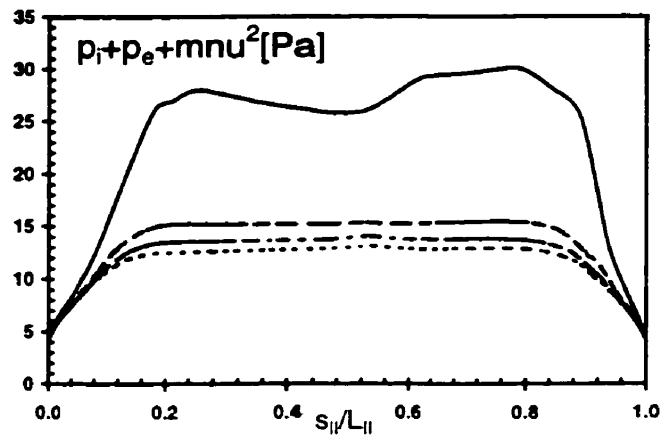
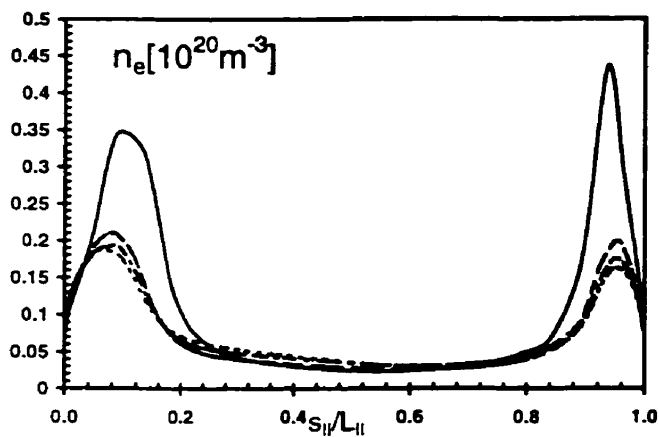
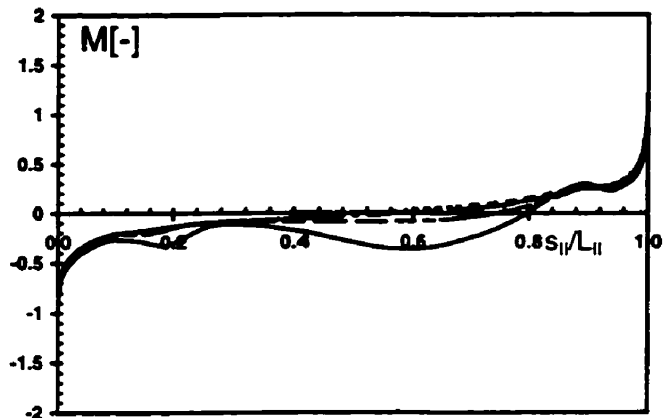
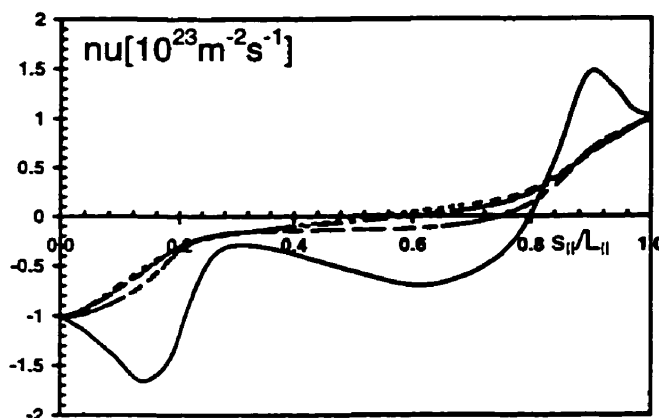
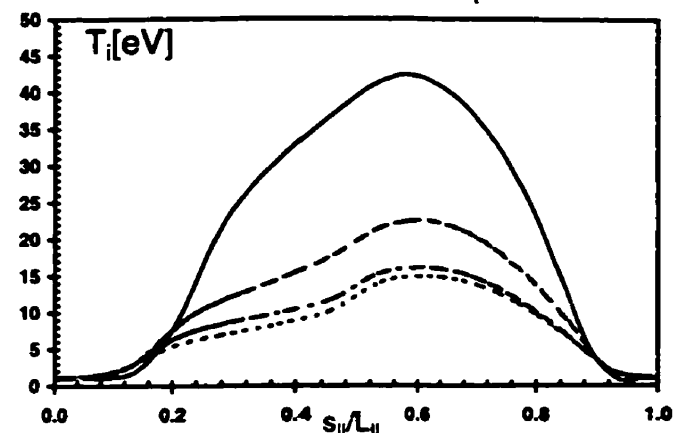
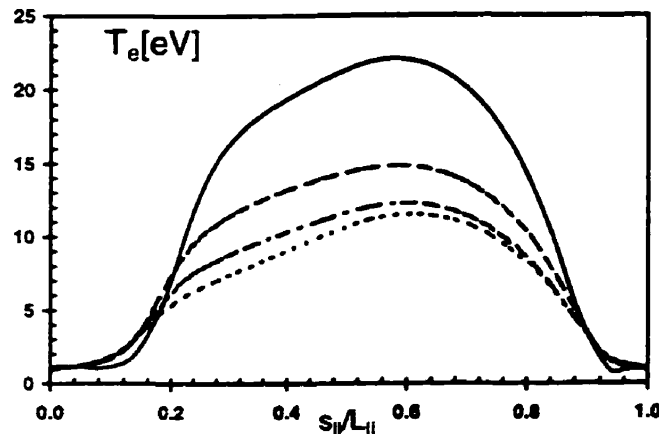


Fig.4.2.31: Along-B plots of plasma variables for case B with the ion heat transmission coefficient reduced by unity, at four radial locations in the SOL (solid line, separatrix ring,  $ir=8$ ; dashed line,  $ir=10$ ; dot-dashed line,  $ir=12$ ; dotted line,  $ir=14$ ). Compare with Fig.4.1.20.

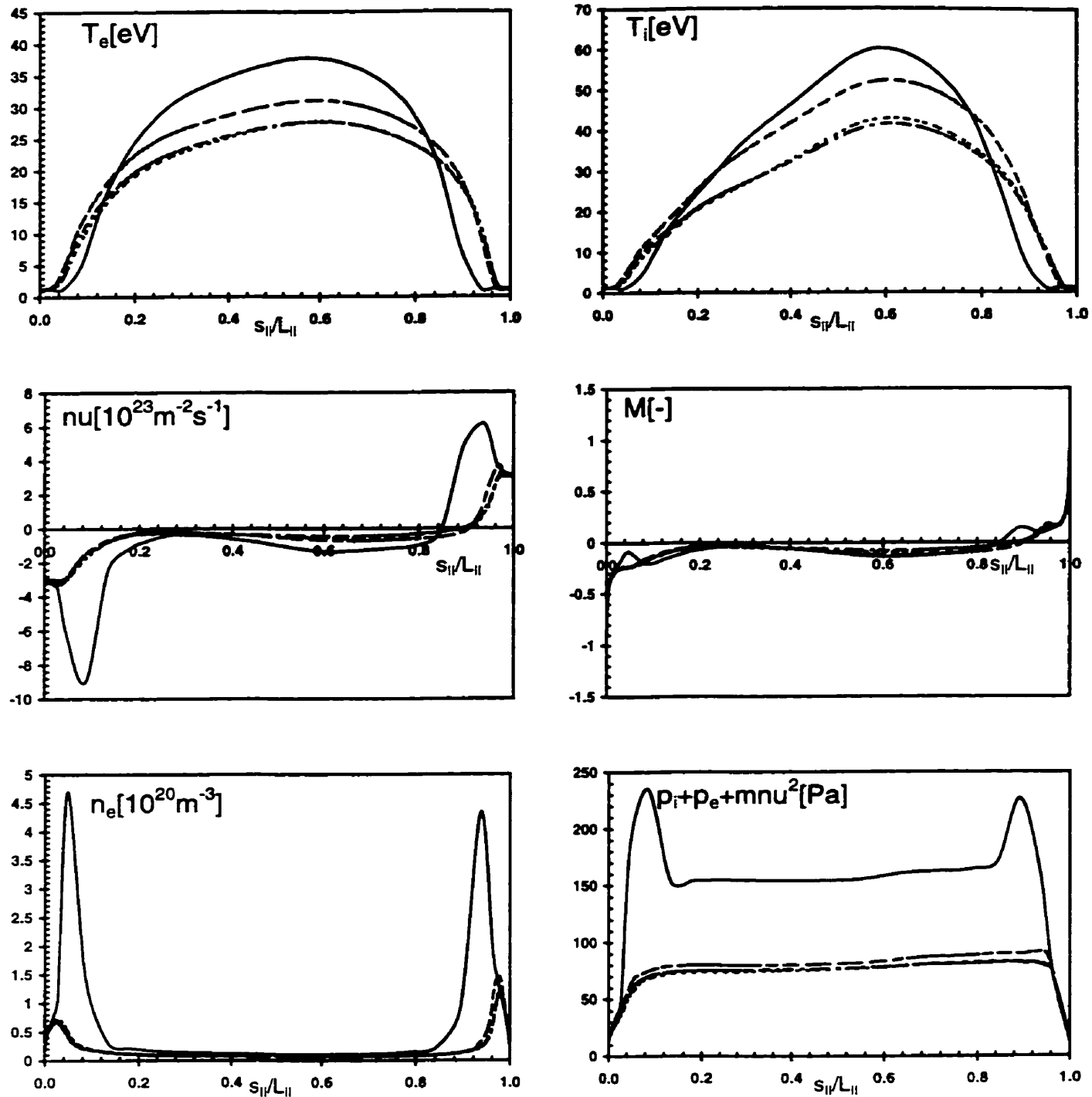


Fig.4.2.32: Along- $\mathbf{B}$  plots of plasma variables for case C with the ion heat transmission coefficient reduced by unity, at four radial locations in the SOL (solid line, separatrix ring,  $ir=8$ ; dashed line,  $ir=10$ ; dot-dashed line,  $ir=12$ ; dotted line,  $ir=14$ ). The evolution was constrained by the additional requirement that  $n_u^{\text{sep}} \sim 10^{19} m^{-3}$ . Compare with Fig.4.1.31.

Case list		$P_{in}$	$T_{e,u}$	$T_{i,u}$	$n_u$	$M_u$	$f^{(1)}$	$f^{(2)}$	$n_e^{\text{peak}}$	$n_u^{\text{peak}}$
		[MWm $^{-2}$ ]	[eV]	[10 $^{19}$ m $^{-3}$ ]					[10 $^{19}$ m $^{-3}$ ]	[10 $^{23}$ m $^{-2}$ s $^{-1}$ ]
default	A	5.7	25.9	52.4	0.14	0.2	0.94	0.30	0.29	1.0
	B	6.0	22.0	42.0	0.23	0.3	1.83	3.93	3.25	1.28
	C	21.7	38.6	65.0	0.84	0.1	2.66	10.1	17.8	5.7
$Q_{\perp}^{(1)}$	A	5.6	25.8	51.5	0.15	0.15	0.94	0.33	0.29	1.0
	B	6.0	23.1	49.6	0.175	0.3	1.86	3.50	2.67	1.13
	C	22.0	40.8	85.0	0.54	0.2	2.71	9.1	19.5	5.7
$Q_{\perp}^{(2)}$	A	5.65	25.8	51.7	0.14	0.2	0.93	0.31	0.29	1.0
	B	6.0	22.2	42.3	0.22	0.3	1.84	3.98	3.14	1.25
	C	21.5	37.9	60.9	0.93	0.1	2.54	10.3	28.8	5.8
$Q_{\perp}^{(3,4)}$	A	5.60	26.0	52.5	0.14	0.2	0.94	0.32	0.29	1.0
	B	5.79	21.6	41.1	0.22	0.3	1.79	3.81	3.0	1.21
	C	21.6	38.3	63.3	0.86	0.1	2.65	10.4	21.5	5.8
$S_{\text{rec}}$	A	5.7	25.9	52.4	0.14	0.2	0.94	0.30	0.29	1.0
	B	6.04	22.2	42.6	0.23	0.3	1.88	3.96	3.14	1.23
	C	25.0	41.4	78.5	0.66	0.1	3.67	10.0	29.1	11.0
$v_H$	A	5.54	25.5	51.3	0.13	0.2	0.84	0.16	0.26	1.0
	B	4.65	19.3	39.6	0.13	0.5	1.34	1.94	1.53	1.05
	C	23.5	37.8	75.7	0.5	0.2	3.01	6.21	12.3	7.0
$Q_{qi}$	A	5.67	25.8	53.0	0.137	0.2	0.91	0.31	0.29	1.0
	B	—	—	—	—	—	—	—	—	—
	C	28.6	43.6	94.3	0.50	0.2	3.63	9.56	8.7	6.0
$f_z$	A	3.82	23.3	43.8	0.15	0.2	0.94	0.32	0.33	1.0
	B	2.62	16.7	23.1	0.39	0.2	1.30	3.91	2.9	1.05
	C	14.5	37.1	60.8	0.84	0.2	3.47	8.8	15.6	6.1
$Q_{ci}$	A	7.7	27.1	64.7	0.144	0.2	0.89	0.27	0.254	1.0
	B	10.7	27.3	77.3	0.17	0.25	1.98	0.58	0.41	1.0
	C	38.8	40.8	115.0	0.675	0.1	2.71	1.91	2.0	3.5
$Q_B$	A	4.96	25.8	50.9	0.157	0.1	0.88	0.33	0.28	1.0
	B	5.3	23.0	43.9	0.24	0.2	1.94	3.86	2.5	1.27
	C	21.7	41.5	77.3	0.69	0.1	3.2	9.7	22.0	9.4
$\gamma_e$	A	5.16	24.9	49.7	0.14	0.2	0.93	0.32	0.3	1.0
	B	5.9	21.8	41.6	0.23	0.3	1.80	4.57	4.1	1.3
	C	21.5	37.5	57.9	1.0	0.1	2.46	11.7	43.1	6.3
$\gamma_i$	A	5.43	25.6	51.1	0.15	0.2	0.94	0.29	0.29	1.0
	B	5.89	21.7	40.9	0.23	0.3	1.77	4.47	4.3	1.4
	C	21.2	37.4	57.9	1.0	0.1	2.47	11.2	41.5	6.1

Table 4.2.1: A summary of some key results of the parametric sensitivity study for the separatrix flux tube,  $i_r=8$ . Target conditions: Case A: 8 eV, 10 $^{23}$  m $^{-2}$ s $^{-1}$ ; Case B: 0.5 eV, 10 $^{23}$  m $^{-2}$ s $^{-1}$ ; Case C: 0.5 eV, 3×10 $^{23}$  m $^{-2}$ s $^{-1}$ . The variations are defined in the text.

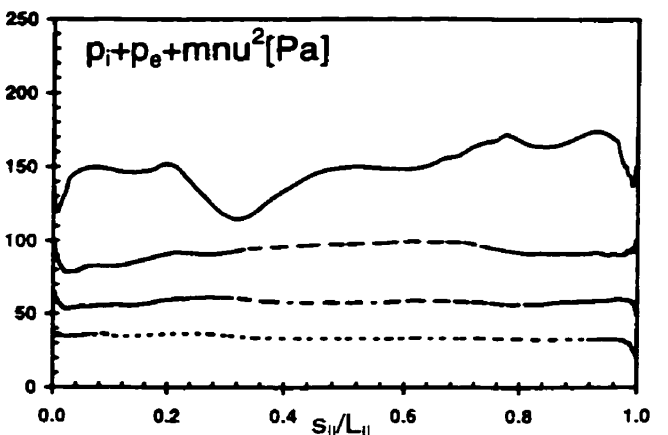
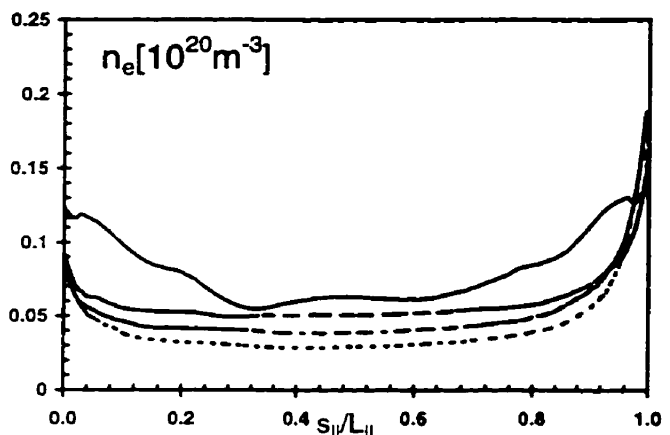
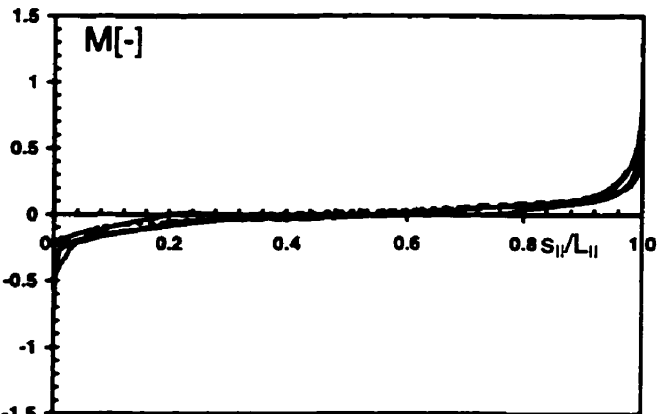
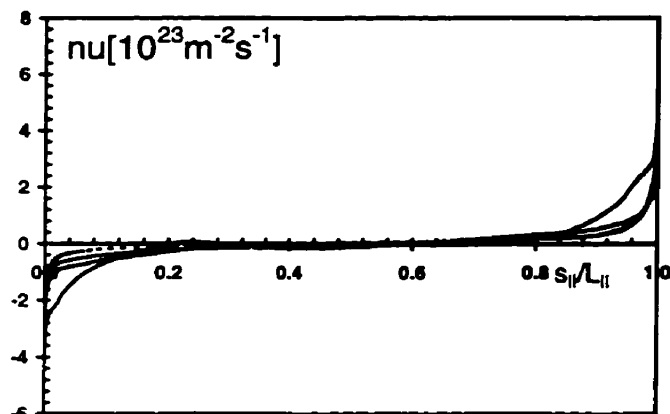
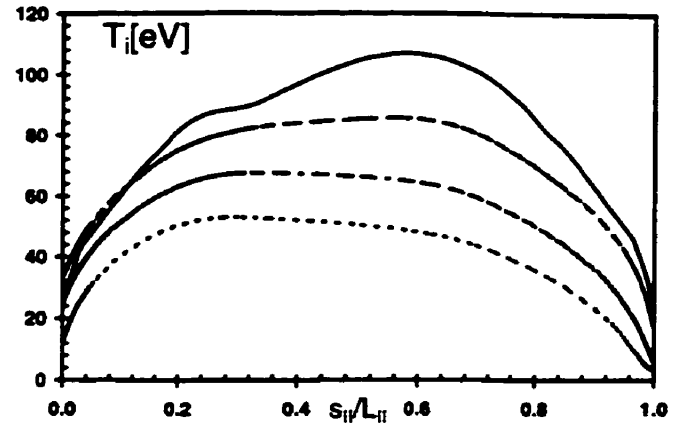
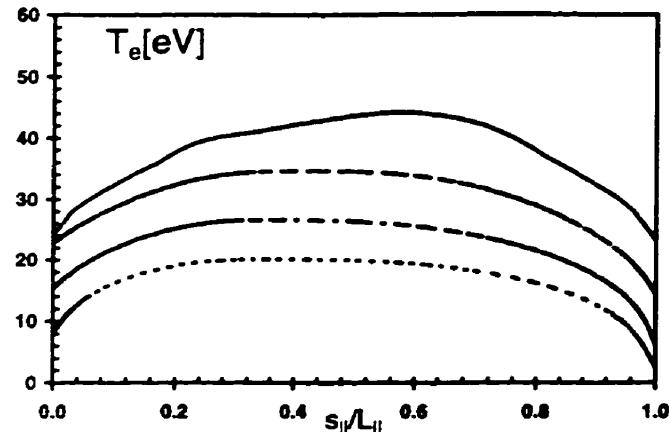


Fig.4.3.1: Along-B plots of plasma variables as calculated by EDGE2D/NIMBUS at four radial locations in the SOL (solid line, separatrix ring, ir=8; dashed line, ir=11; dot-dashed line, ir=14; dotted line, ir=17).

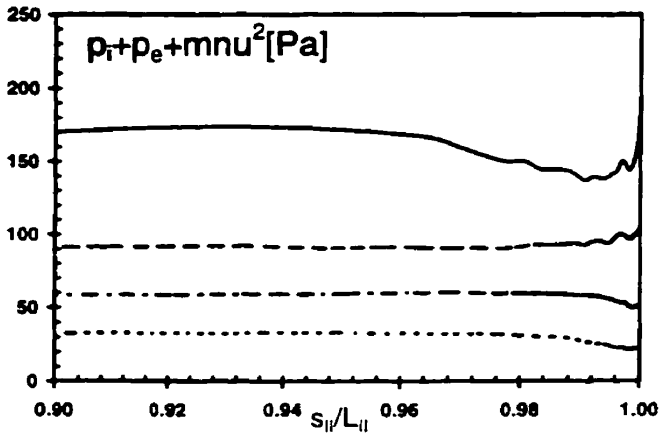
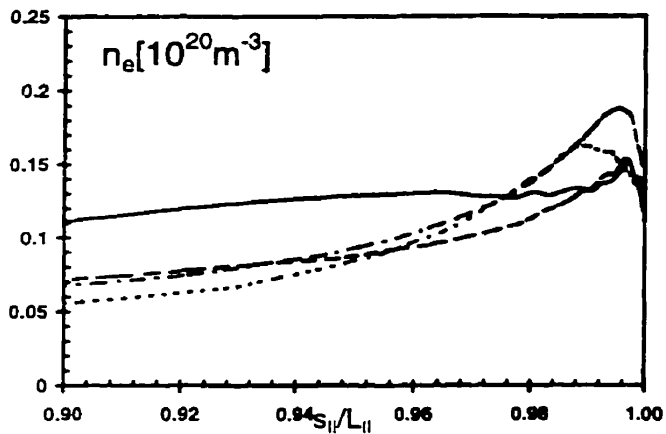
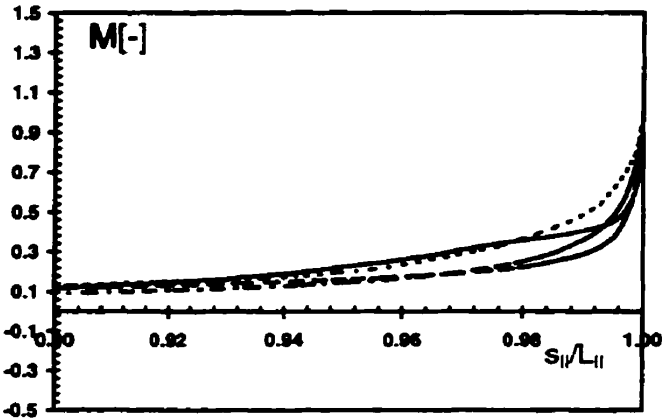
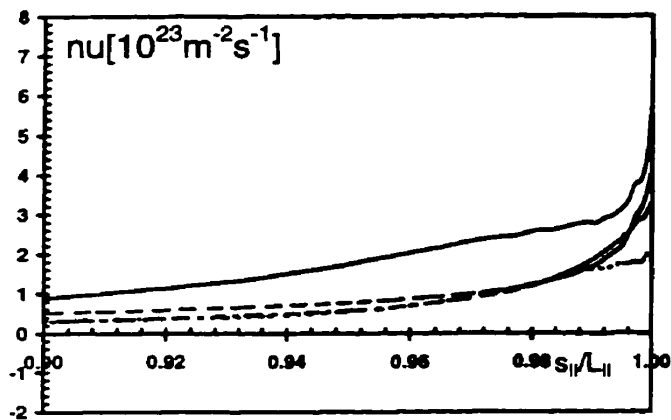
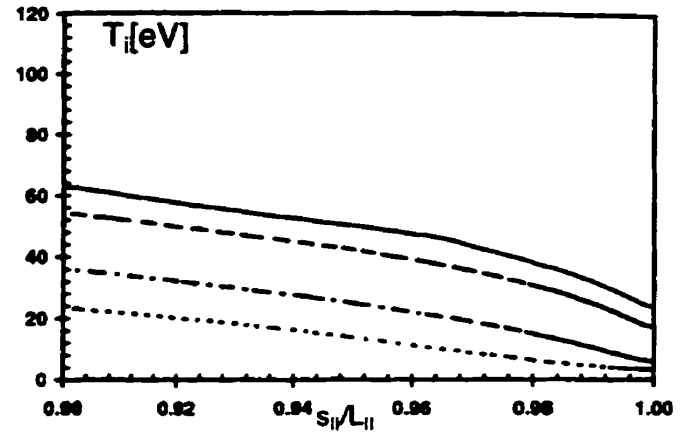
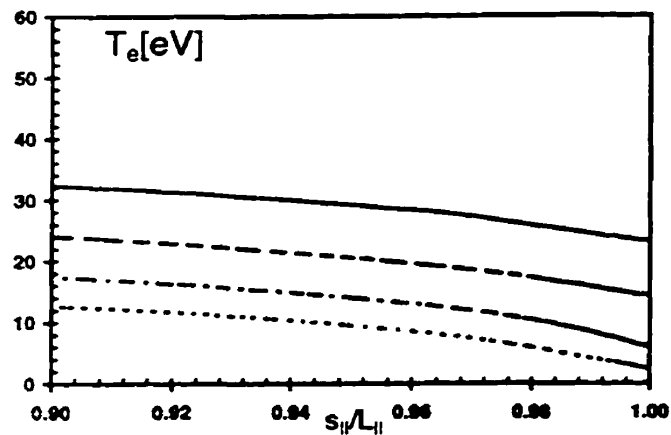


Fig.4.3.2: Along-B plots of plasma variables in the inner divertor volume as calculated by EDGE2D/NIMBUS, at four radial locations in the SOL (solid line, ir=8; dashed line, ir=11; dot-dashed line, ir=14; dotted line, ir=17).

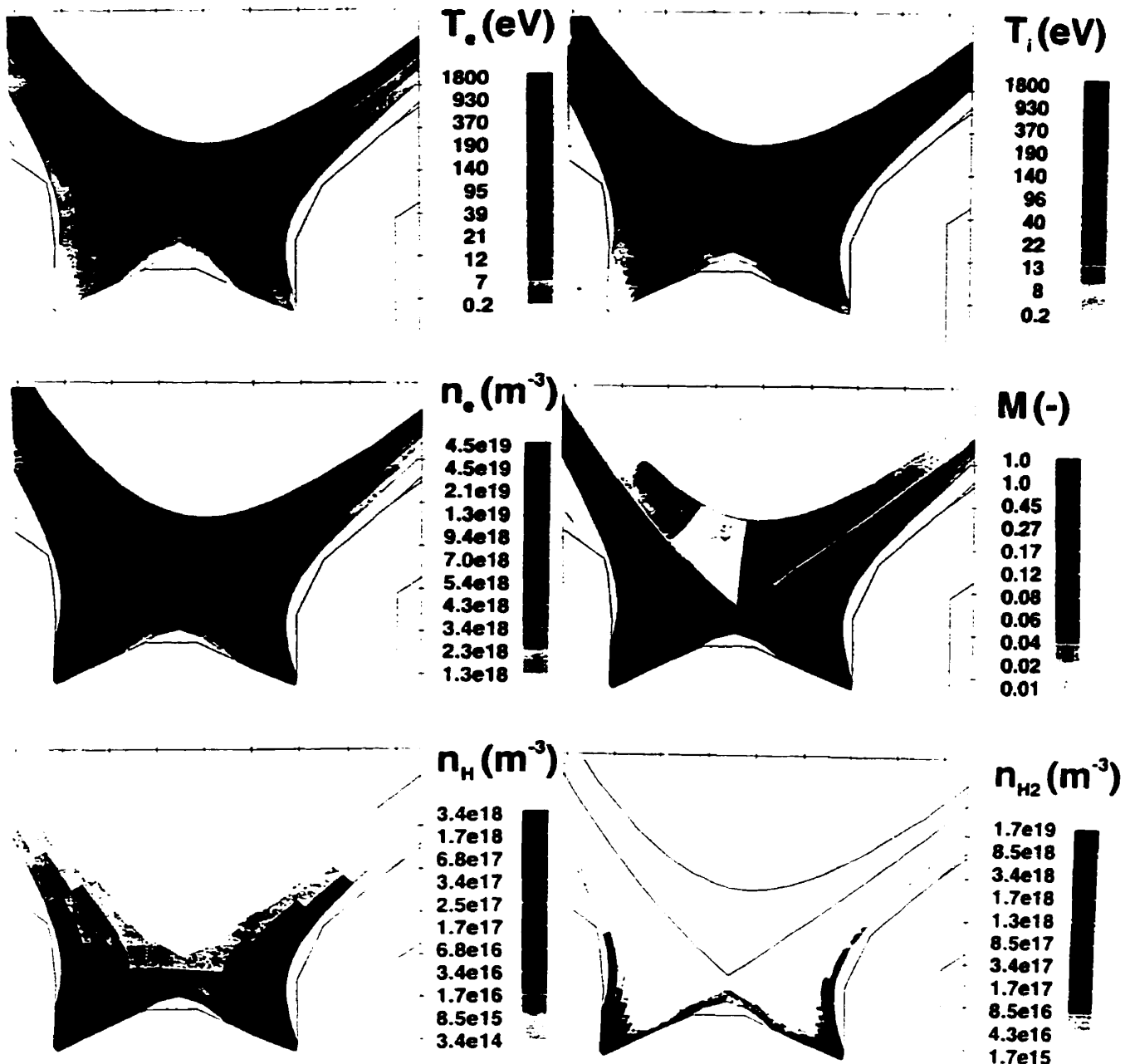


Figure 4.3.3: Poloidal contour plots of plasma variables and neutral densities as calculated by EDGE2D/NIMBUS (absolute value of the Mach number is shown).

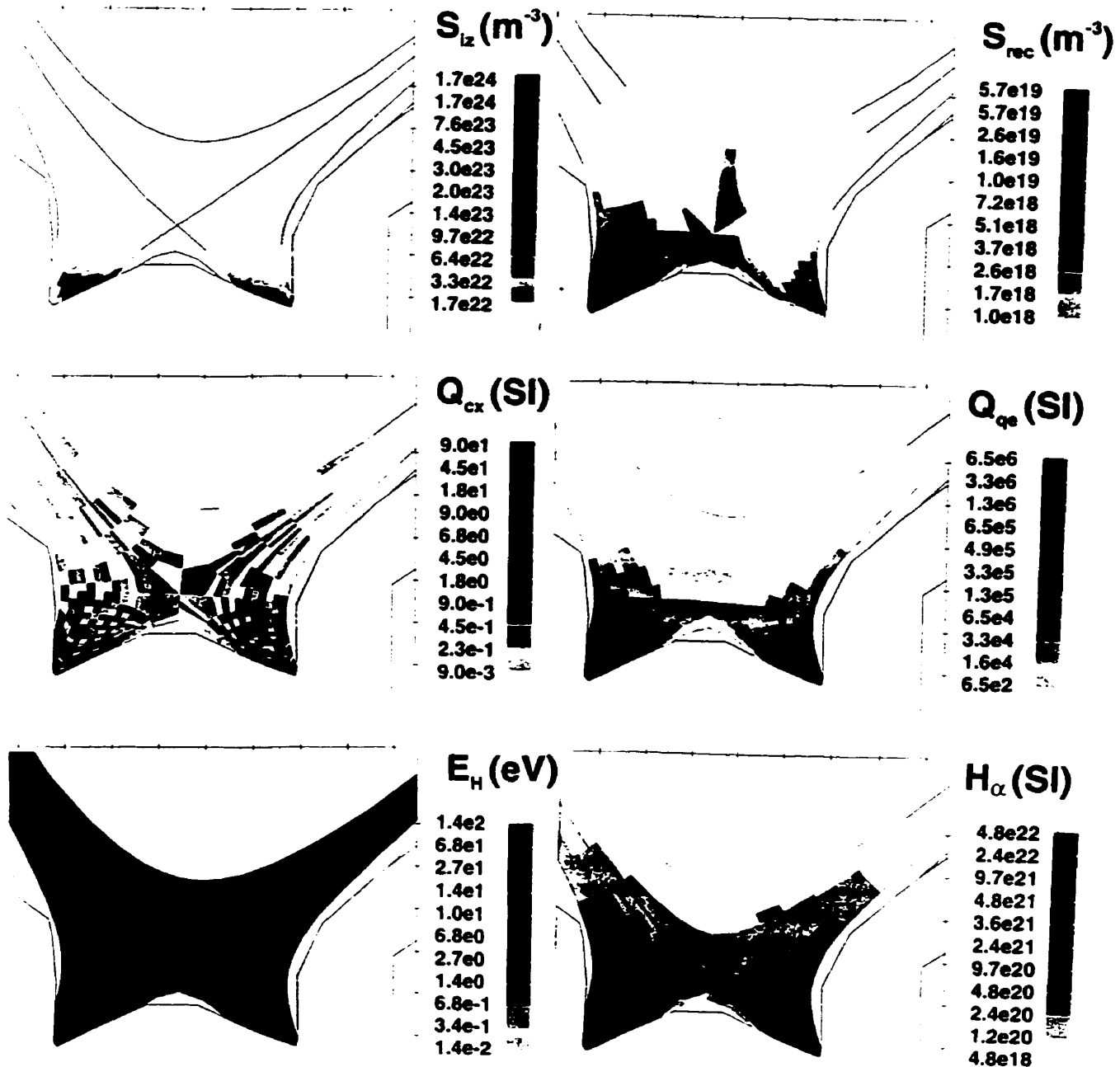


Figure 4.3.4: Poloidal contour plots of neutral sources from EDGE2D/NIMBUS: ionization  $S_{iz}$ , recombination  $S_{rec}$ , momentum removal  $Q_{cx} = m(u - v_{LH})S_{CX}$  [Pa/m] and electron cooling  $Q_{qe}$  [ $\text{Wm}^{-3}$ ] (absolute value of  $Q_{qe}$ ); also the average atom energy  $E_H$  [eV] and intensity of  $H_\alpha$  line emission [ $\text{m}^{-3}\text{s}^{-1}$ ].

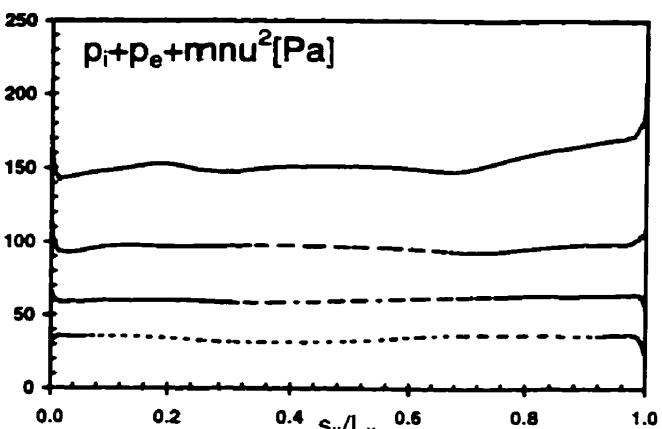
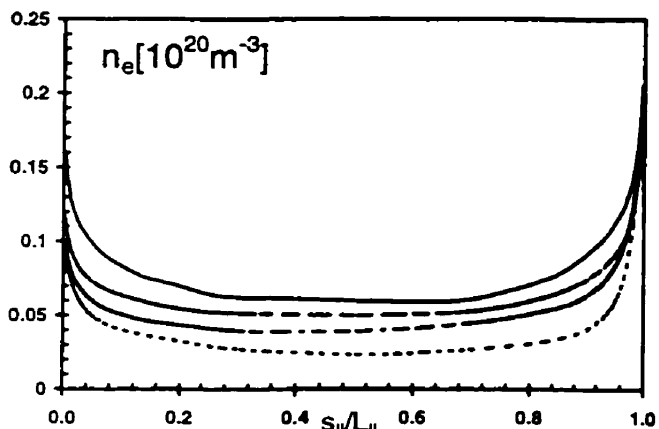
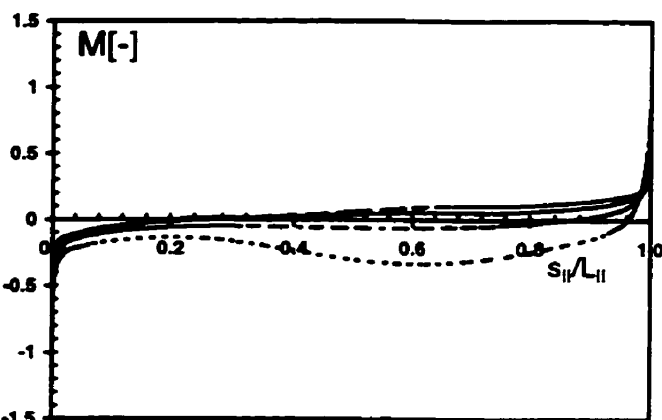
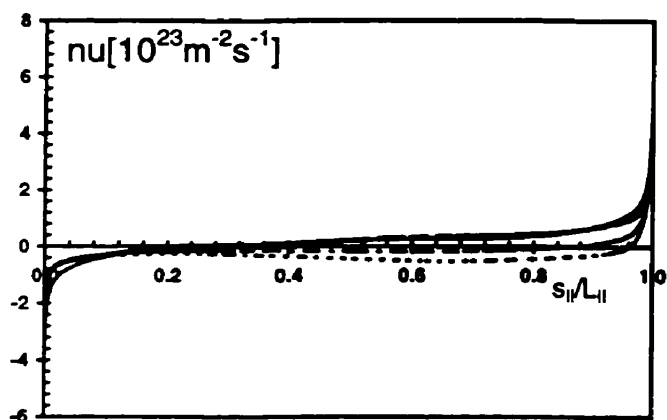
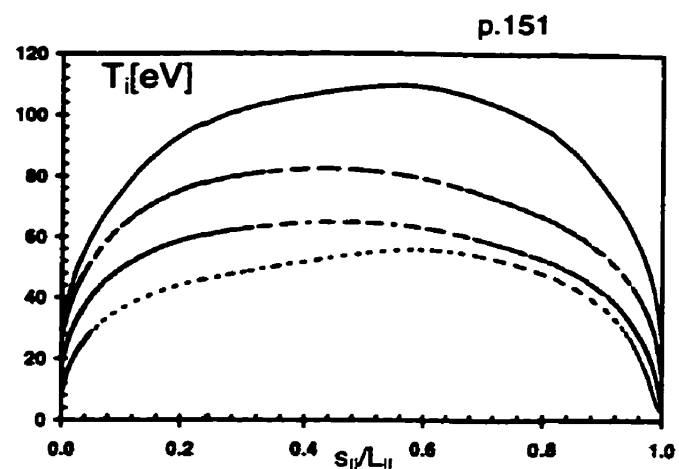
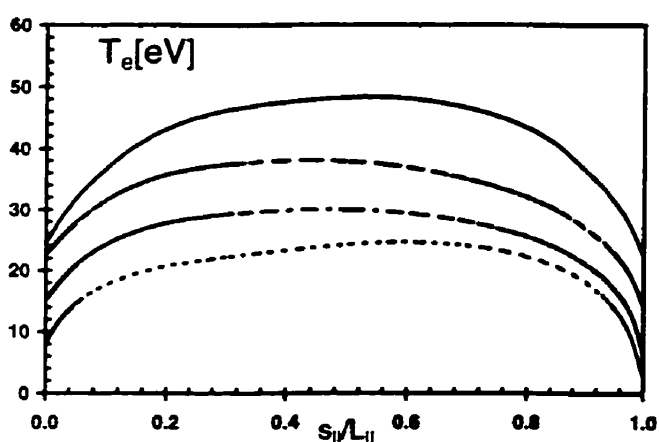


Fig.4.3.5: Along-B plots of plasma variables as calculated by OSM2/NIMBUS at four radial locations in the SOL (solid line, separatrix ring, ir=8; dashed line, ir=11; dot-dashed line, ir=14; dotted line, ir=17).

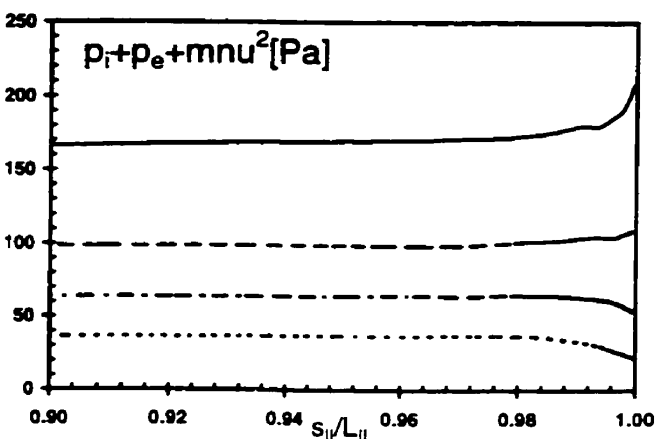
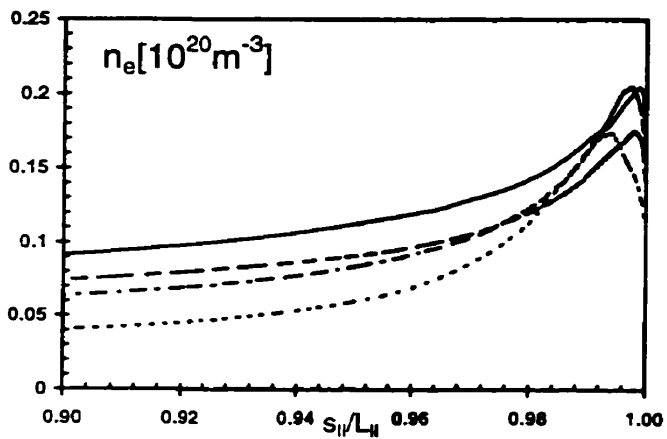
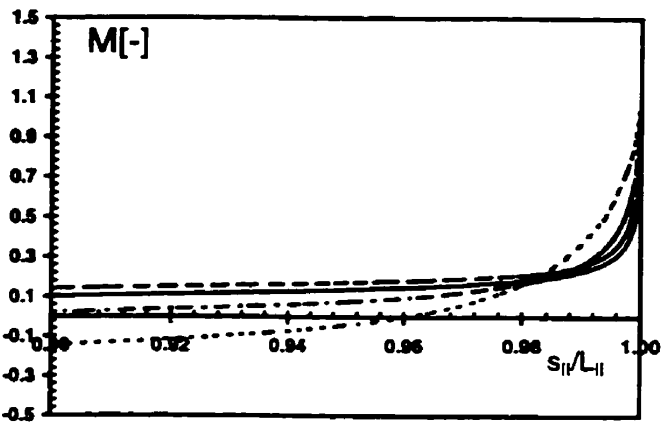
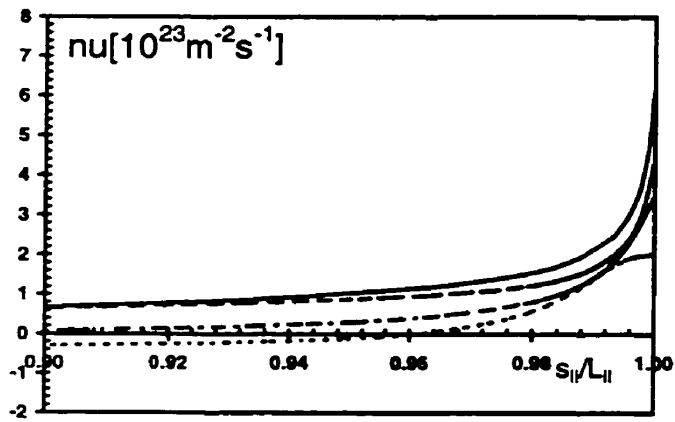
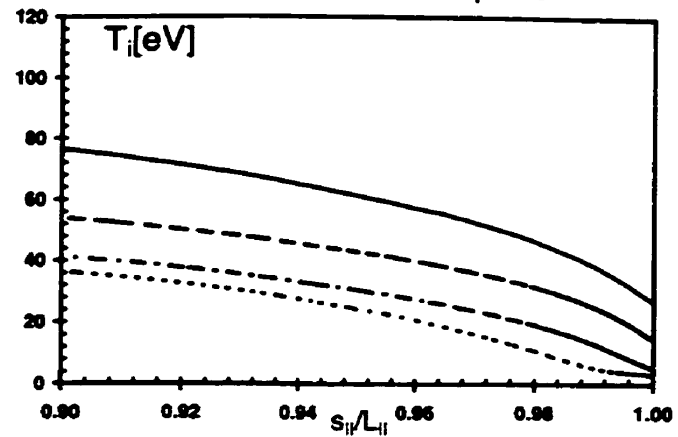
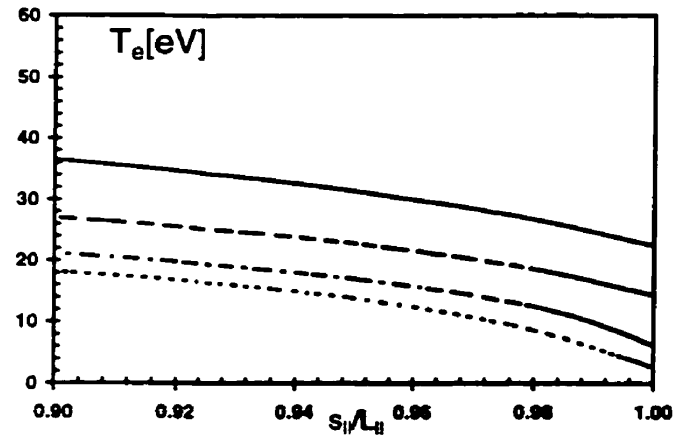


Fig.4.3.6: Along- $\mathbf{B}$  plots of plasma variables in the inner divertor volume as calculated by OSM2/NIMBUS, at four radial locations in the SOL (solid line,  $ir=8$ ; dashed line,  $ir=11$ ; dot-dashed line,  $ir=14$ ; dotted line,  $ir=17$ ).

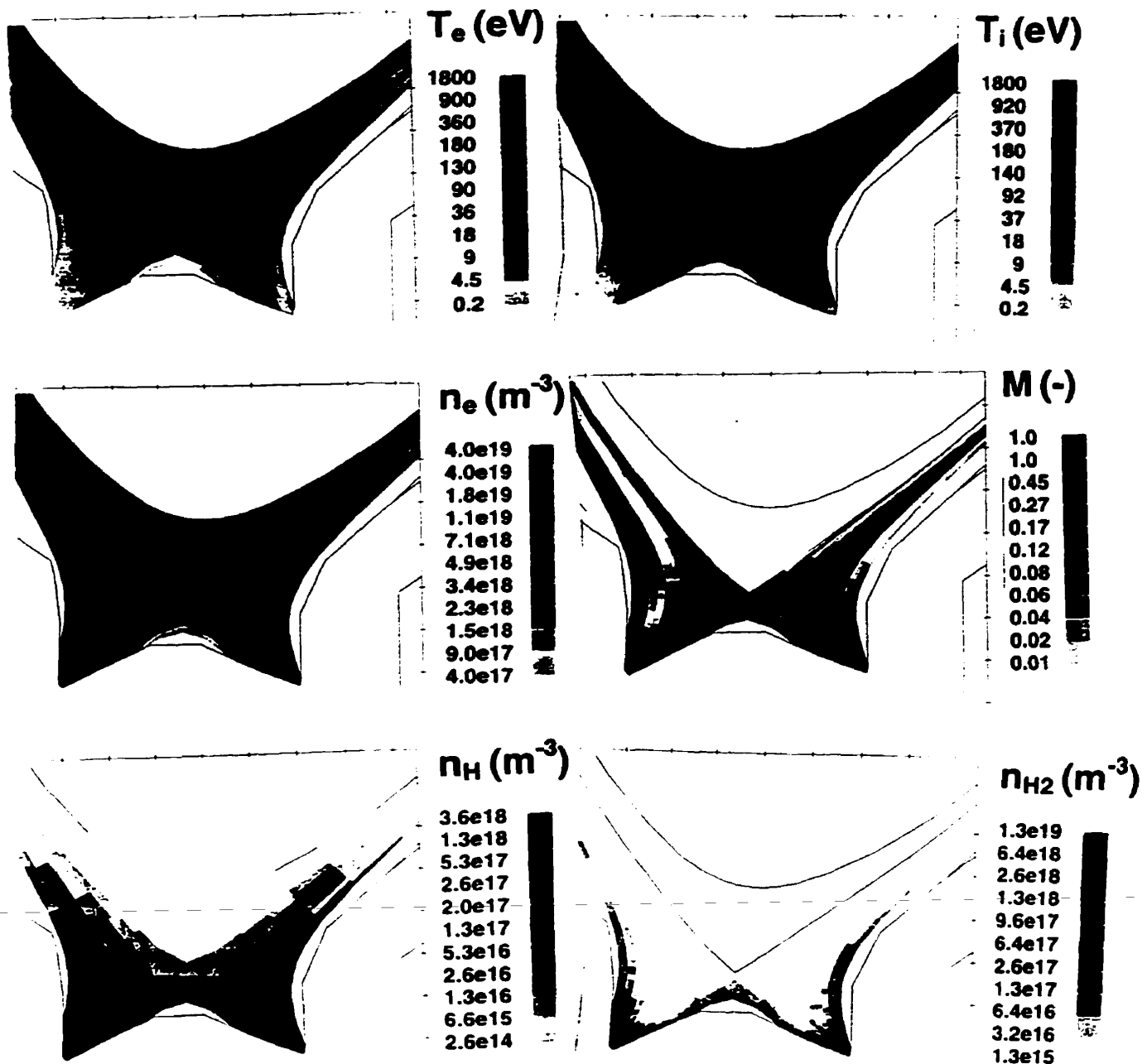


Figure 4.3.7: Poloidal contour plots of plasma variables and neutral densities as calculated by OSM2/NIMBUS using the target  $T_{e,0}$  and  $\Gamma_0$  of the EDGE2D/NIMBUS result as Langmuir probe data.

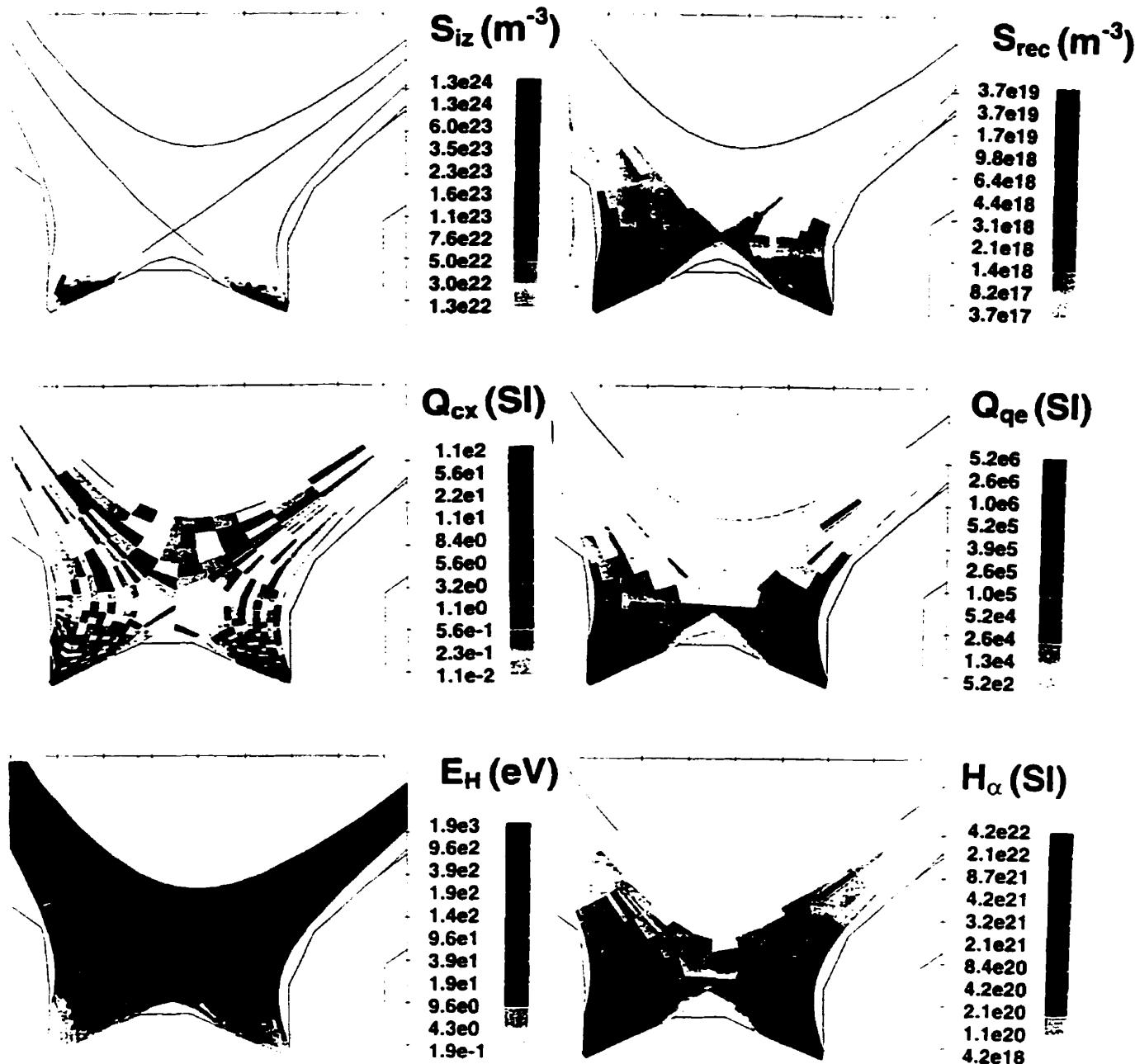


Figure 4.3.8: Poloidal contour plots of neutral sources from OSM2/NIMBUS: ionization  $S_{iz}$ , recombination  $S_{rec}$ , momentum removal  $Q_{cx} = m(u - v_{LH})S_{cx}$  [Pa/m] and electron cooling  $Q_{qe}$  [ $\text{Wm}^{-3}$ ] (absolute value of  $Q_{qe}$ ); also the average atom energy  $E_H$  [eV] and intensity of  $H_\alpha$  line emission [ $\text{m}^{-3}\text{s}^{-1}$ ].

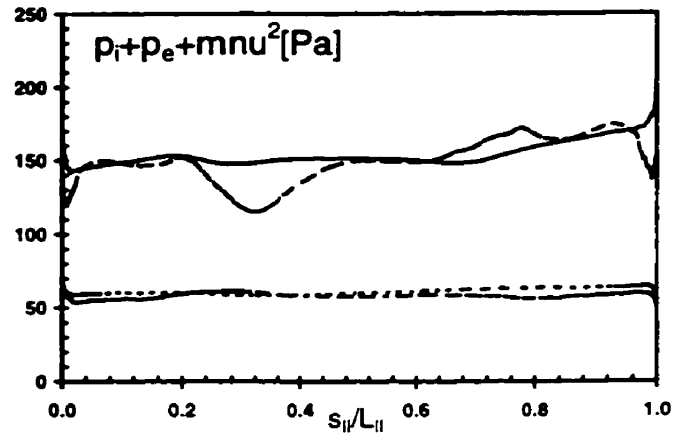
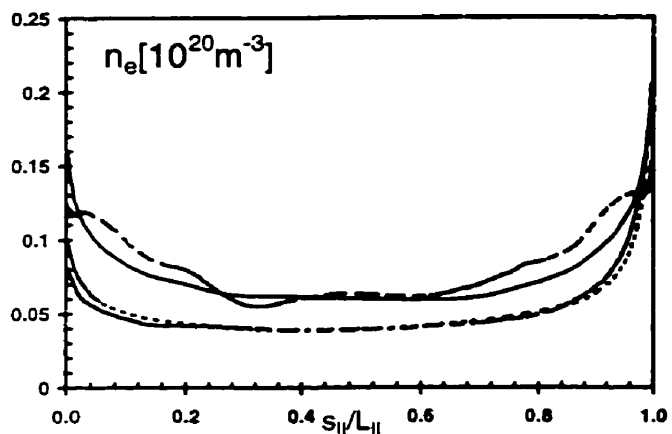
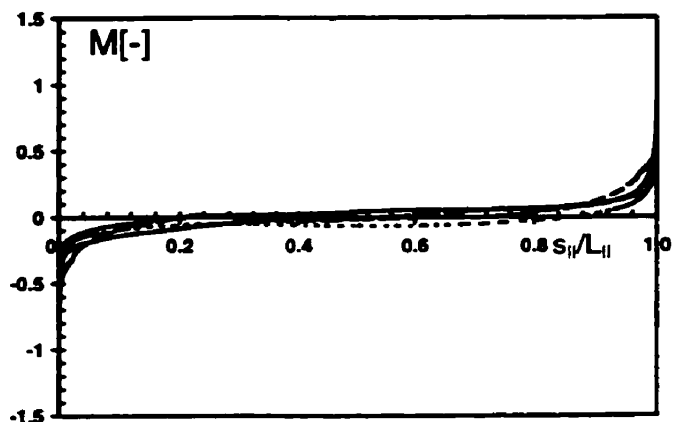
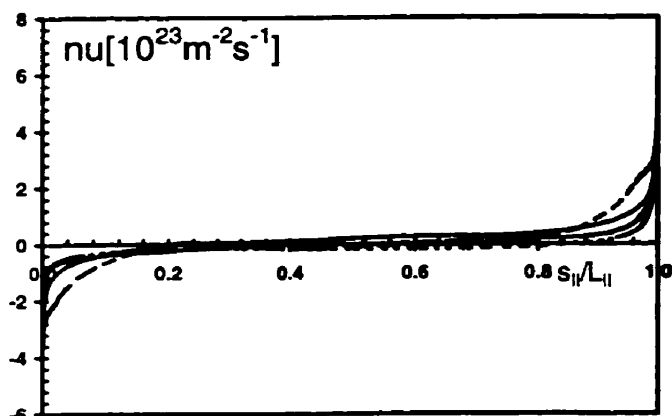
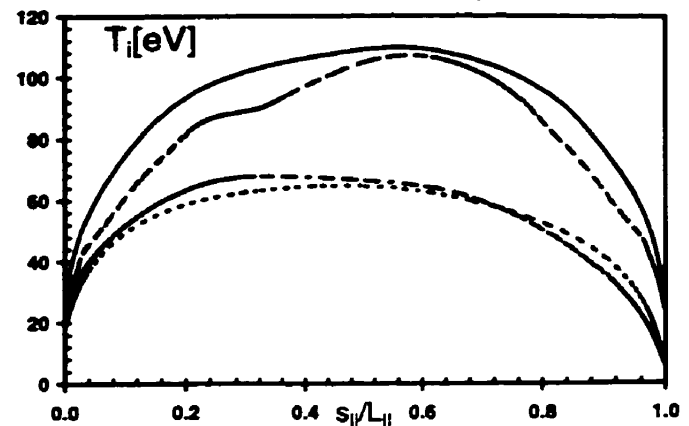
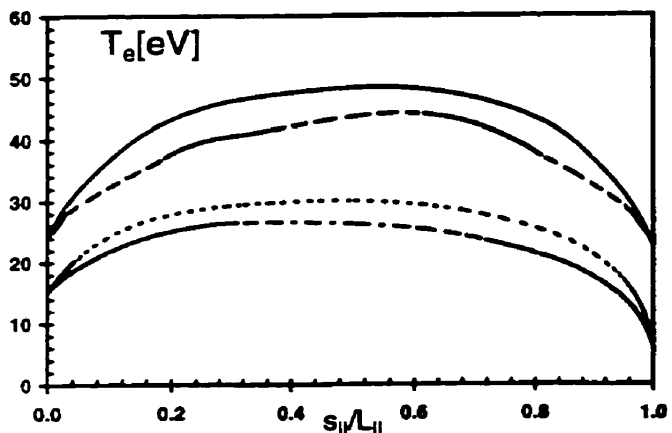


Fig.4.3.9: Along-B plots of a comparison between EDGE2D and OSM2 solutions, Fig.4.3.1 and Fig.4.3.5 at two radial locations in the SOL (solid line, OSM2 at ir=8; dashed line, EDGE2D at ir=8; dotted line, OSM2 at ir=14; dot-dashed line, EDGE2D at ir=14).

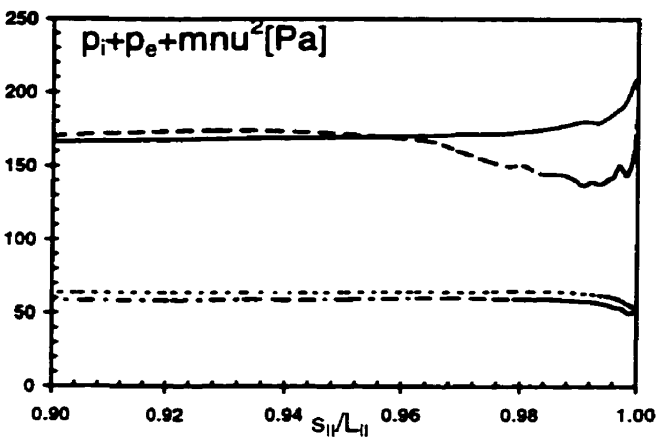
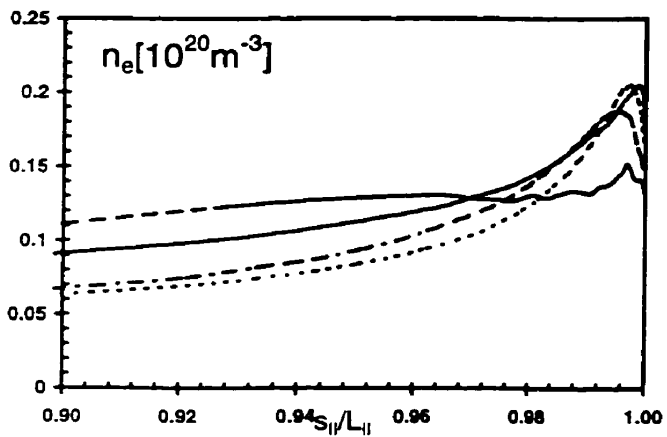
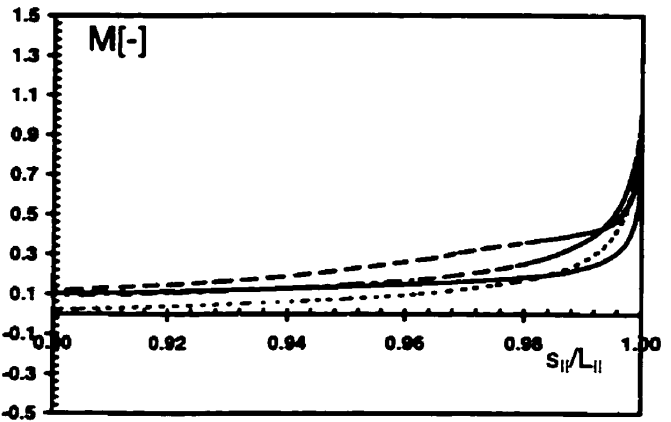
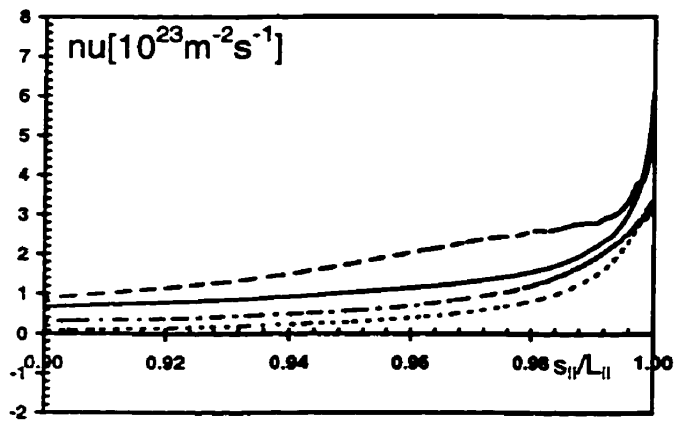
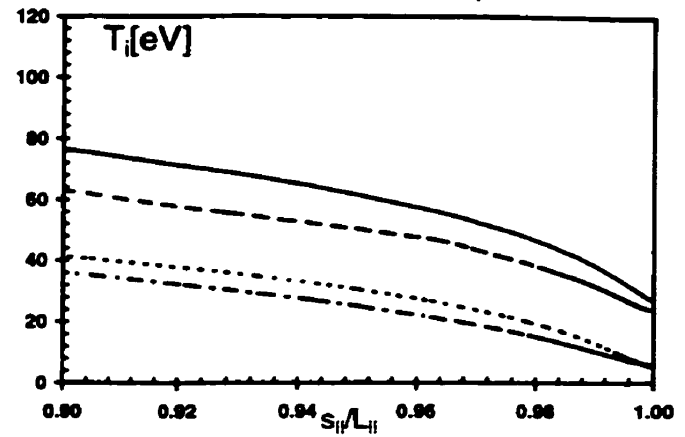
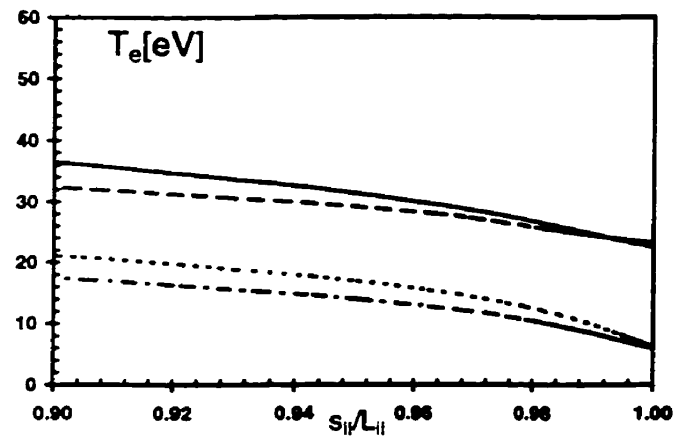


Fig.4.3.10: Along-B plots of a comparison between EDGE2D and OSM2 solutions, Fig.4.3.2 and Fig.4.3.6, in the inner divertor volume and two radial locations in the SOL (solid line, OSM2 at ir=8; dashed line, EDGE2D at ir=8; dotted line, OSM2 at ir=14; dot-dashed line, EDGE2D at ir=14).

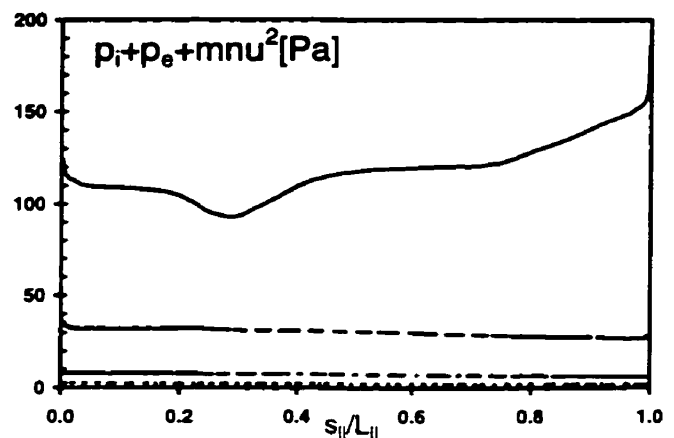
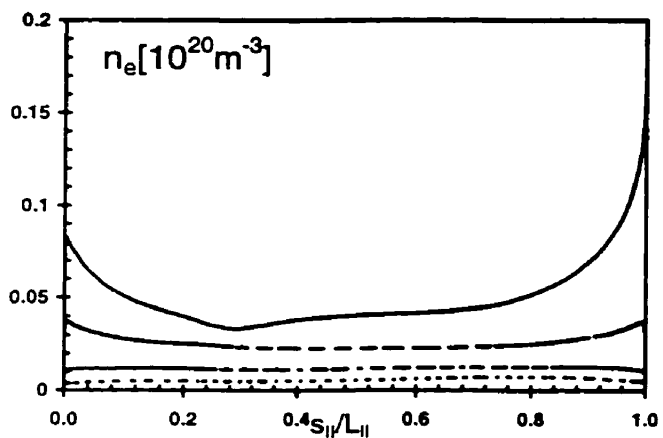
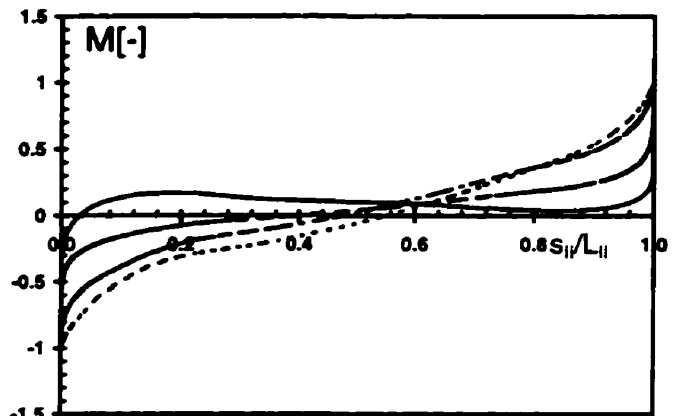
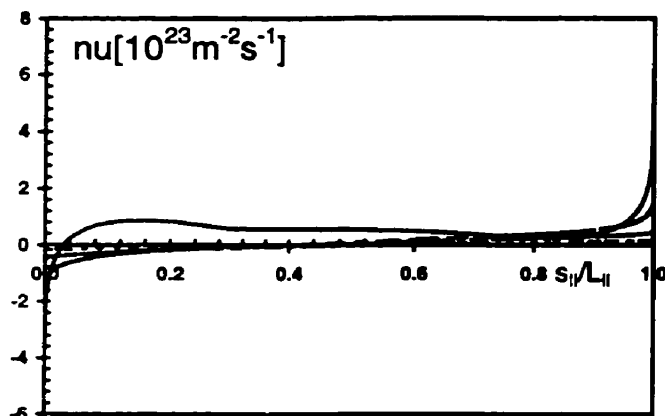
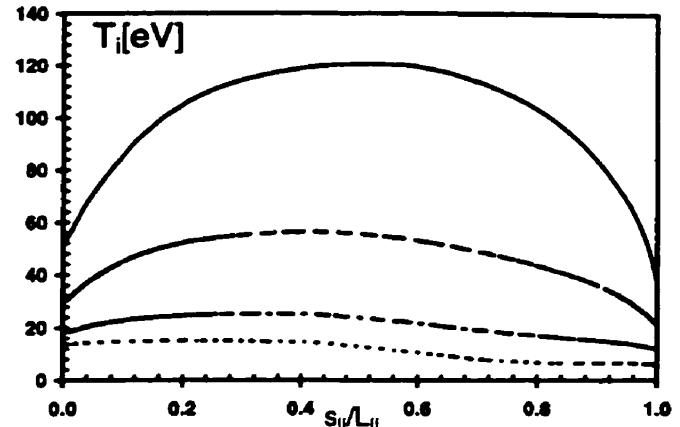
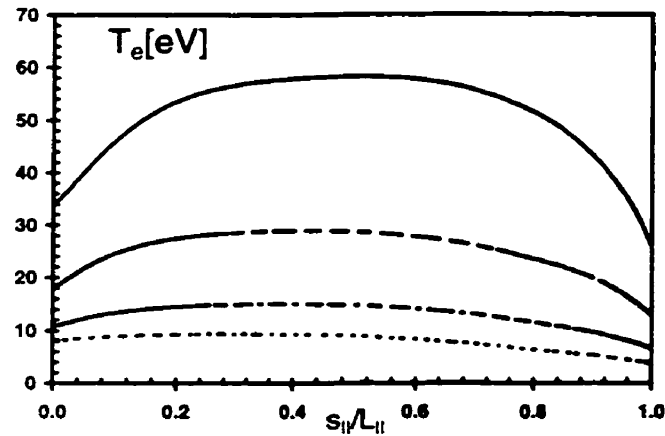


Fig.4.4.1: Along- $\mathbf{B}$  plots of plasma variables obtained with OSM2/NIMBUS for the ohmic JET shot 48310,  $t = 54.4$  sec at four radial locations in the SOL (solid line, separatrix ring, ir=6; dashed line, ir=9; dot-dashed line, ir=12; dotted line, ir=15).

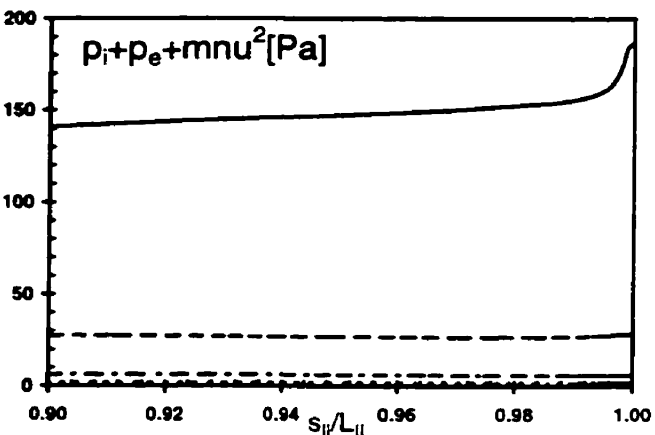
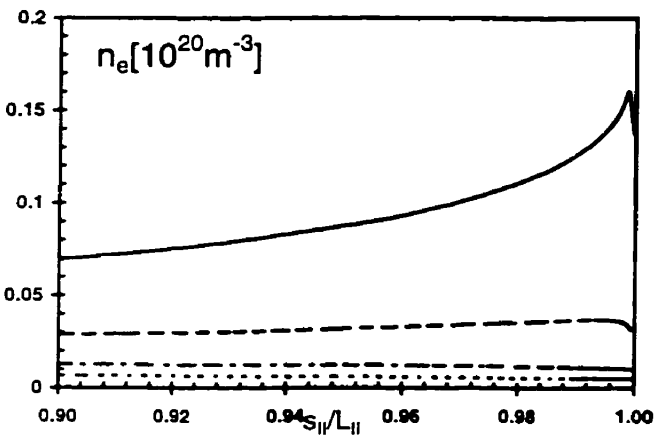
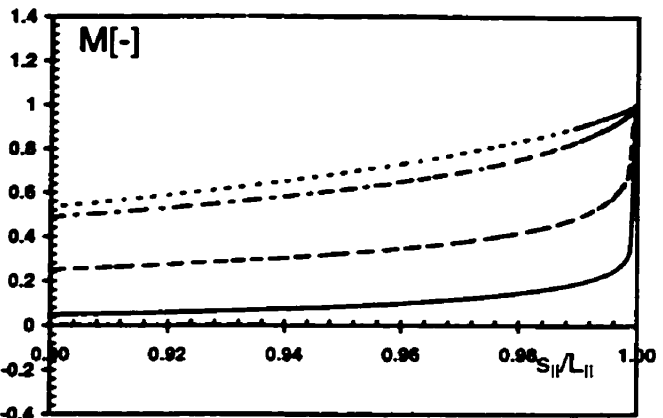
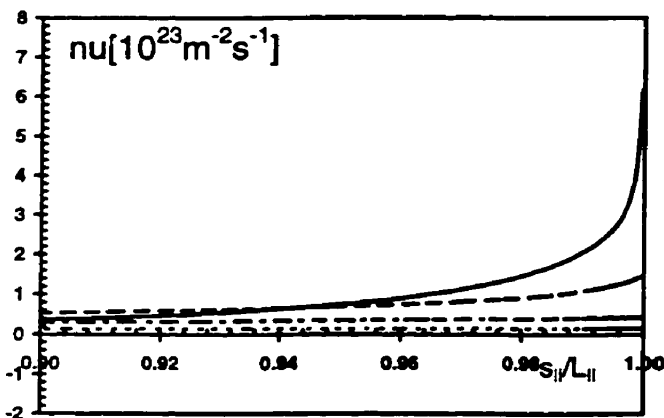
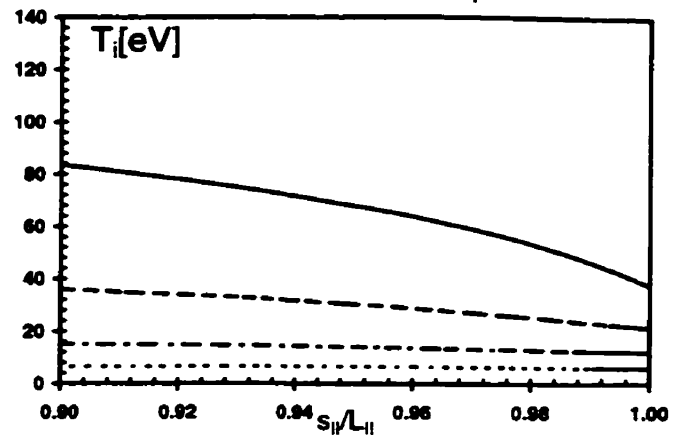
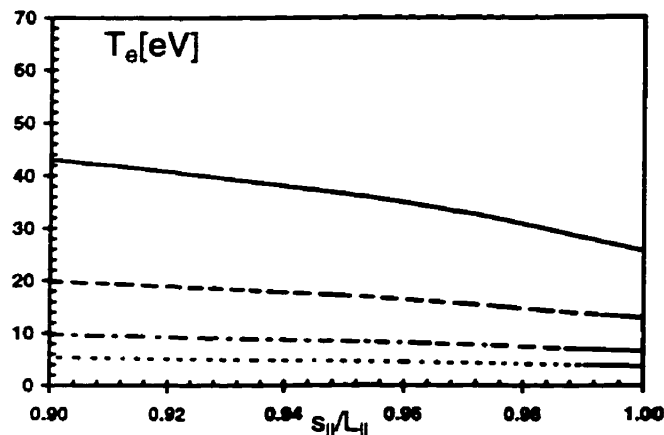


Fig.4.4.2: Along-B plots of plasma variables obtained with OSM2/NIMBUS for the ohmic JET shot 48310,  $t = 54.4$  sec in the vicinity of the inner target and at four radial locations in the SOL (solid line, separatrix ring,  $ir=6$ ; dashed line,  $ir=9$ ; dot-dashed line,  $ir=12$ ; dotted line,  $ir=15$ ).

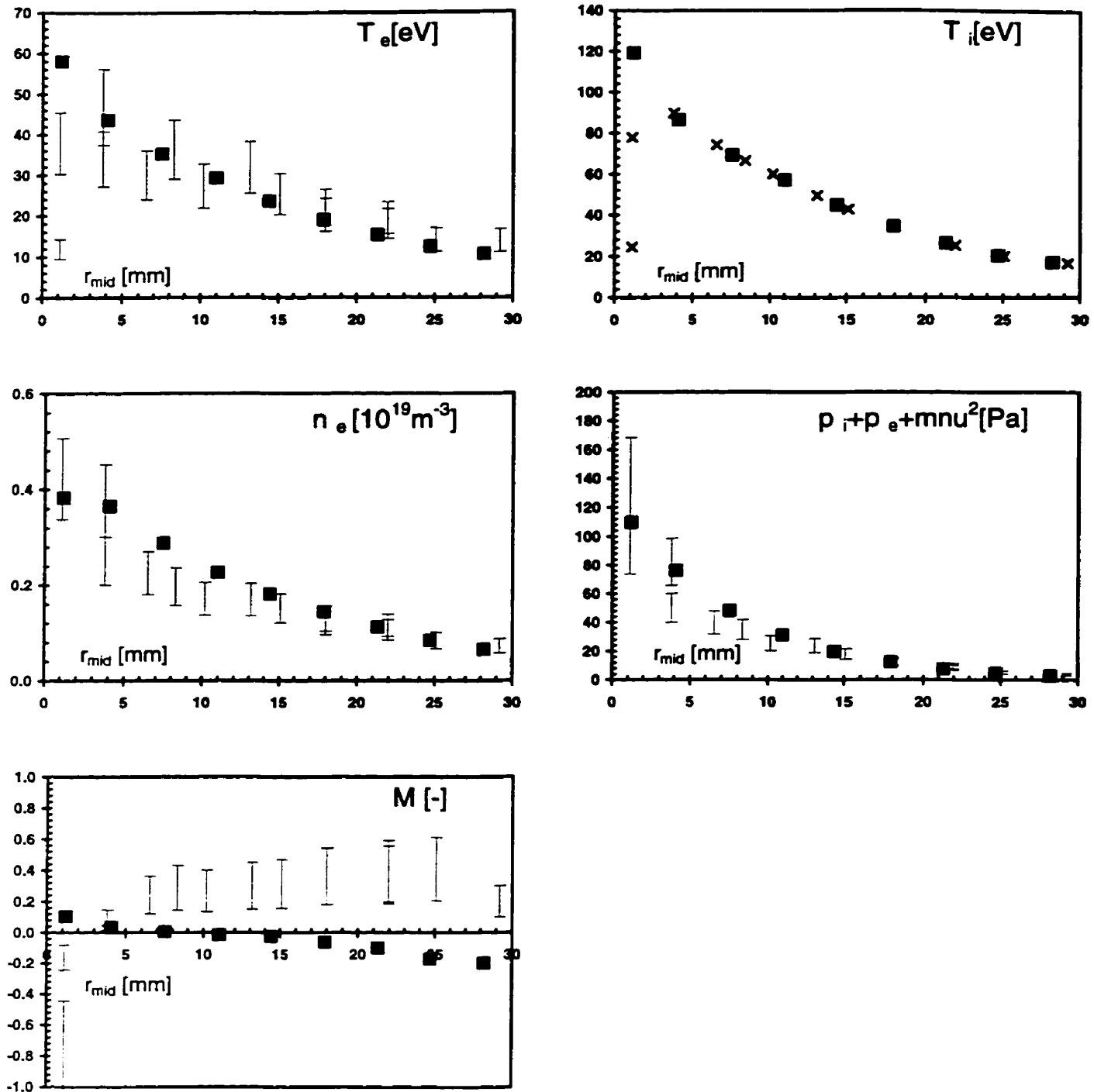


Fig.4.4.3: JET shot 48310,  $t = 54.4$  sec (Ohmic). Radial profiles of plasma variables measured by the upstream reciprocating probe (RCP) and calculated using OSM2/NIMBUS (squares) plotted as a function of the radial distance away from the separatrix at the outer midplane; error bars of 20% reflect only the RCP data scatter. The RCP data was radially shifted in order to satisfy flux-tube pressure balance,  $r_{\text{shift}} = 18$  mm (results are shown only over the extent of the computational region). Since  $T_i^{\text{RCP}}$  was not available,  $T_i^{\text{RCP}} = T_i^{\text{OSM}}$  was assumed.

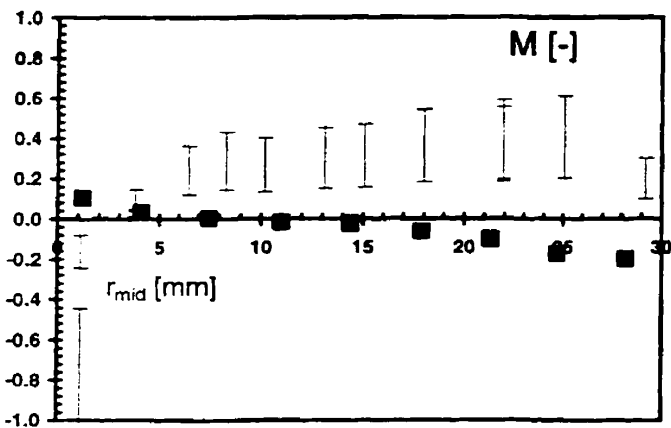
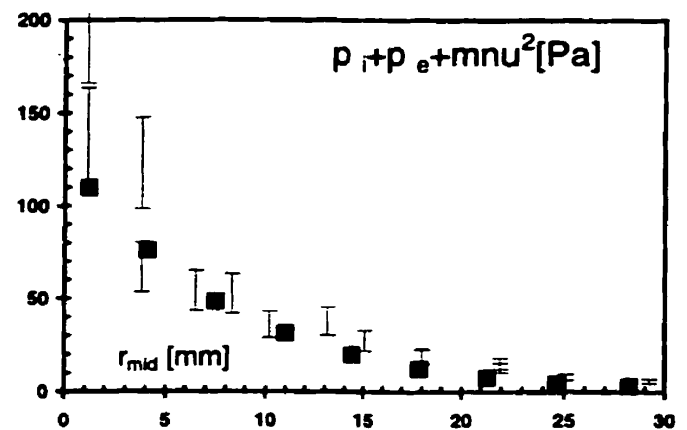
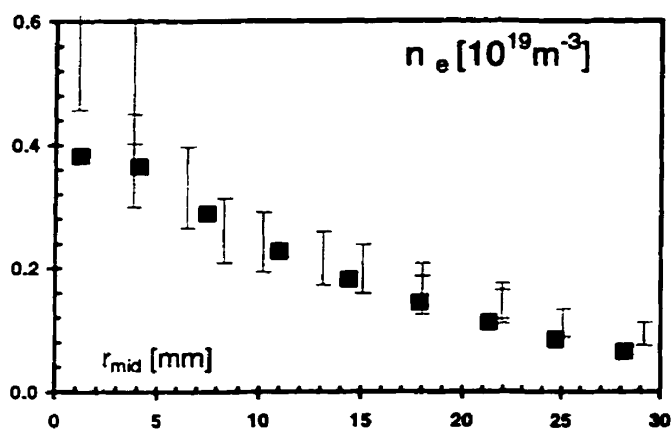
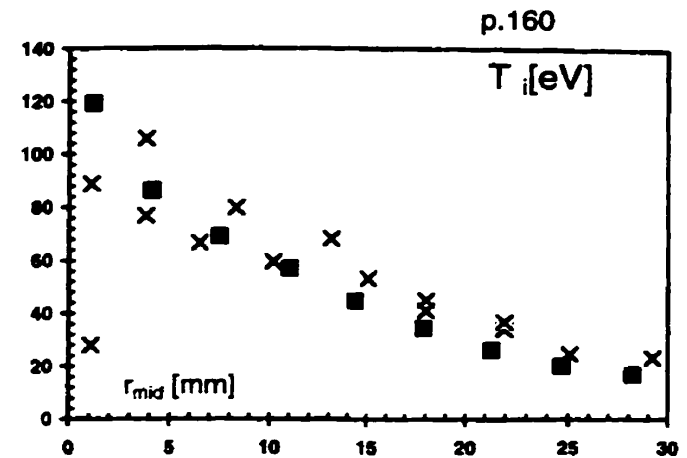
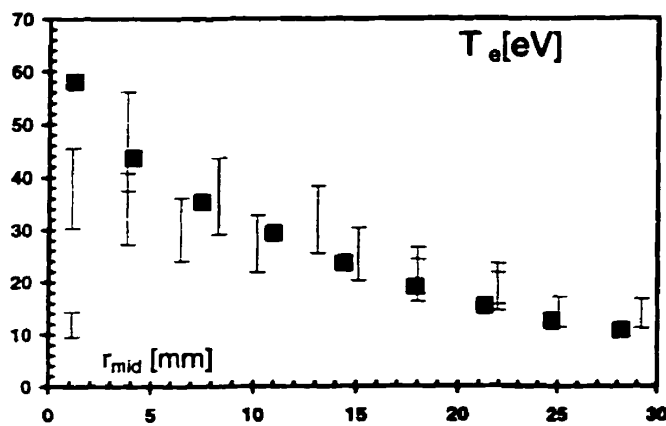


Fig.4.4.4: JET shot 48310,  $t = 54.4$  sec (Ohmic). Same comparison as in Fig.4.4.3, except with  $T_i^{RCP}$  estimated based on the ion-to-electron temperatutre ratio predicted by the OSM2 code,  $T_i^{RCP} = T_e^{RCP} (T_i^{\text{OSM2}} / T_e^{\text{OSM2}})$ .

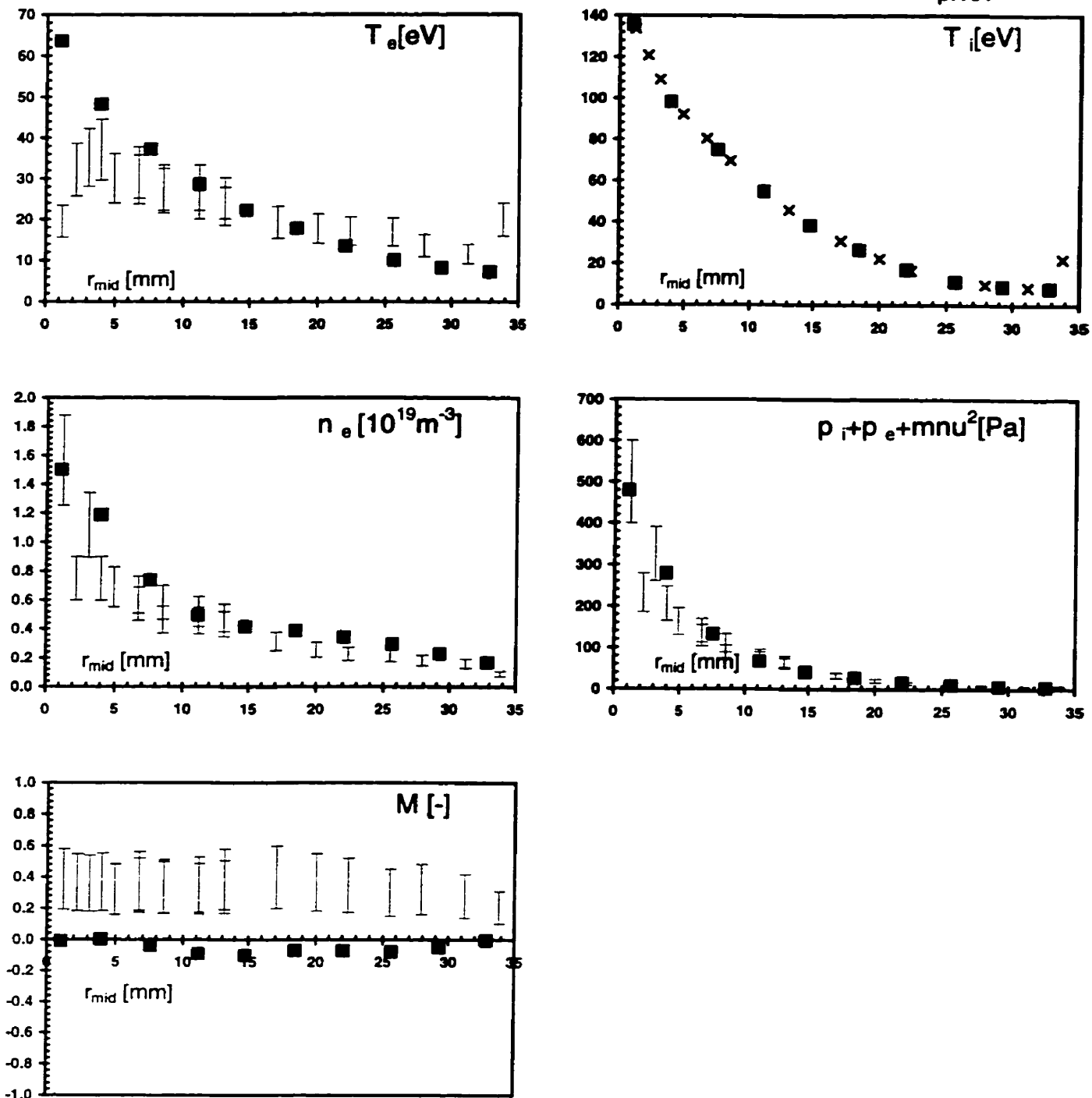


Fig.4.4.5: JET shot 45702,  $t = 61$  sec (L-mode). Radial profiles of plasma variables measured by the upstream reciprocating probe (RCP) and calculated using OSM2/NIMBUS (squares) plotted as a function of the radial distance away from the separatrix at the outer midplane. Radial shift, 20 mm.  $T_i^{\text{RCP}} = T_i^{\text{OSM}}$  assumed.

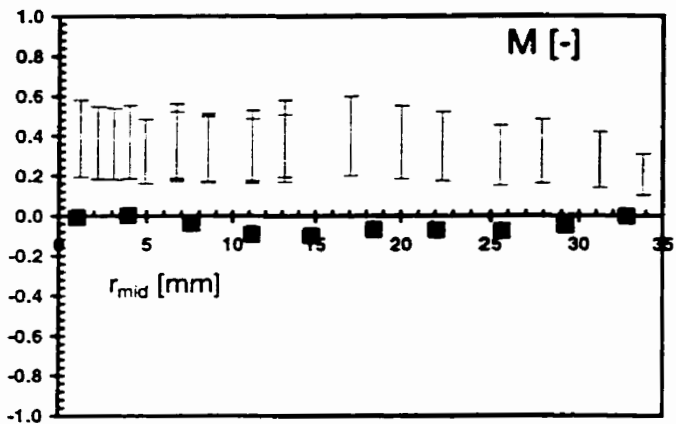
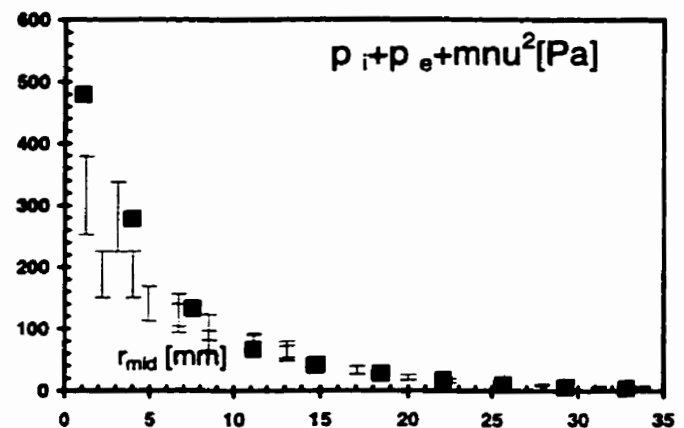
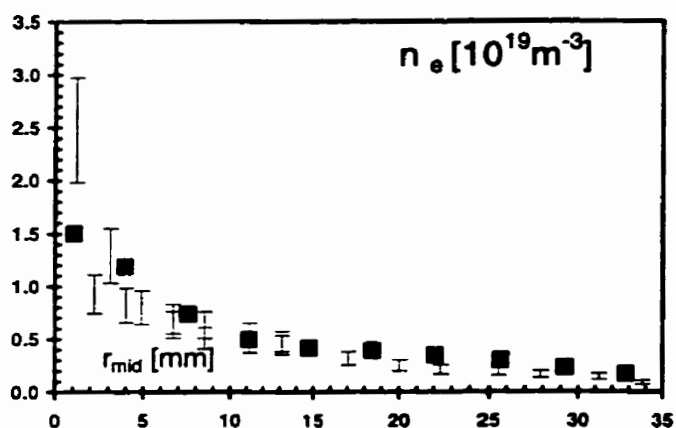
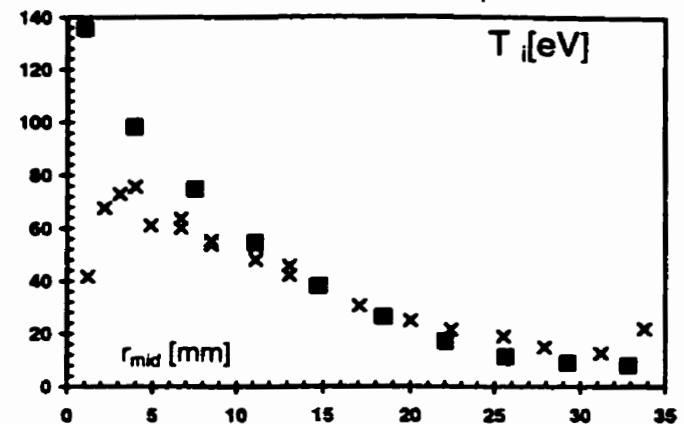
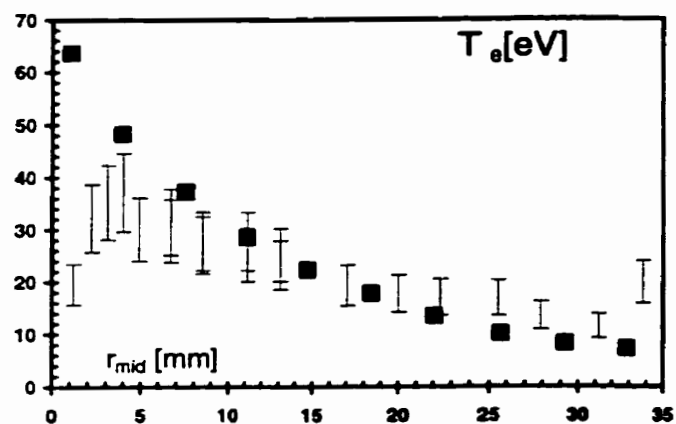


Fig.4.4.6: JET shot 45702,  $t = 61$  sec (L-mode). Same comparison as in Fig.4.4.5, except  $T_i^{RCP} = T_i^{OSM} \bullet$  ( $T_i^{OSM}/T_e^{OSM}$ ).

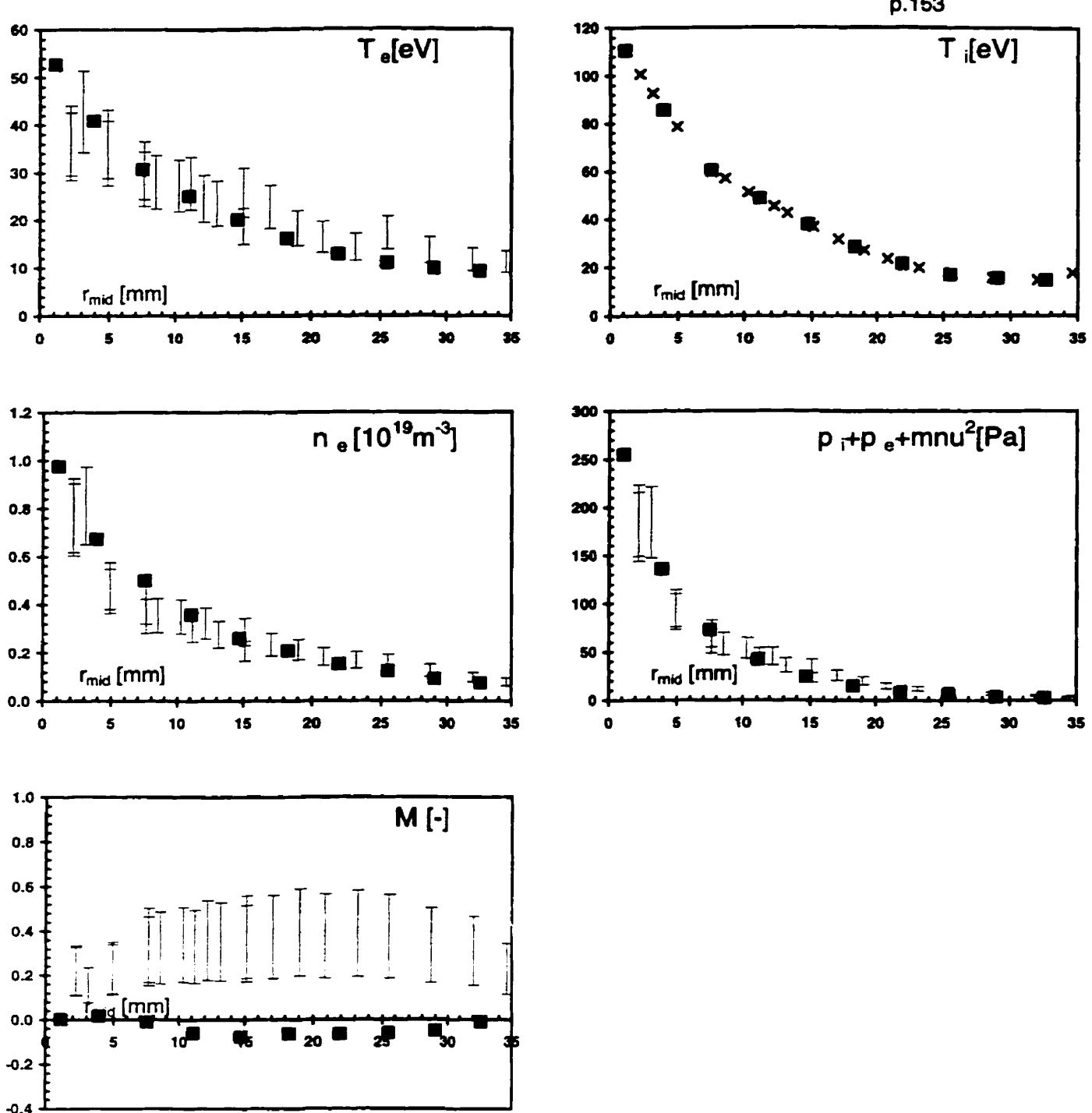


Fig.4.4.7: JET shot 45791,  $t = 63$  sec (L-mode). Radial profiles of plasma variables measured by the upstream reciprocating probe (RCP) and calculated using OSM2/NIMBUS (squares) plotted as a function of the radial distance away from the separatrix at the outer midplane. Radial shift, 20 mm.  $T_i^{\text{RCP}} = T_i^{\text{OSM}}$  assumed.

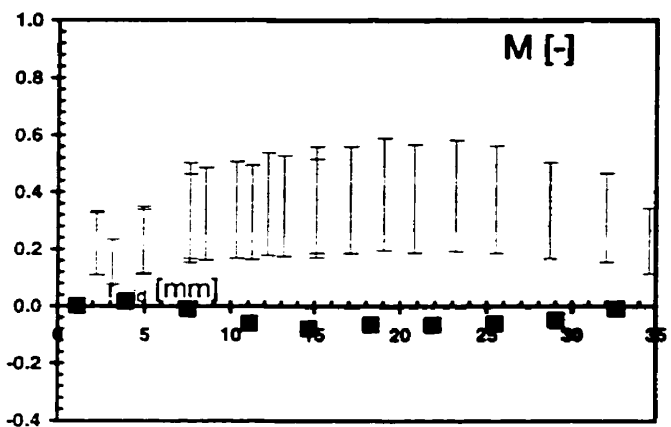
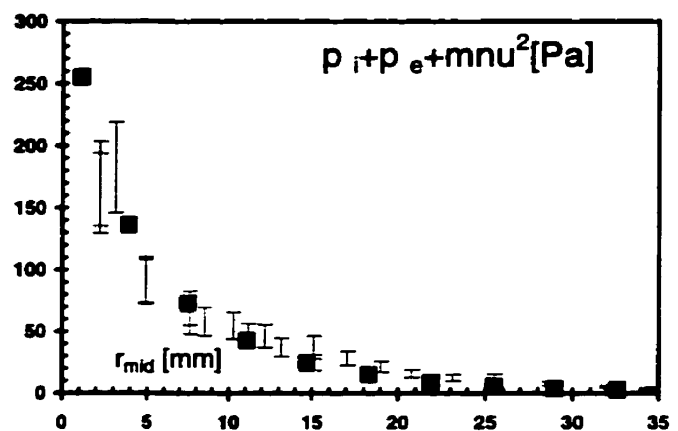
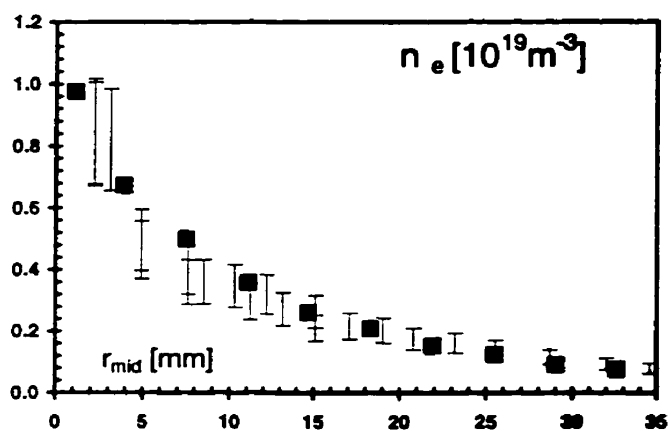
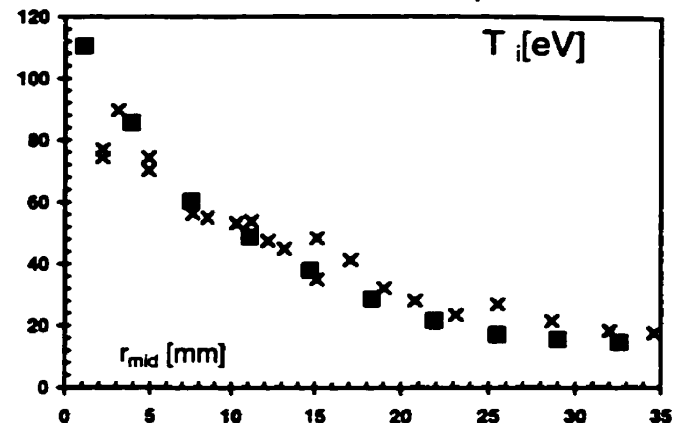
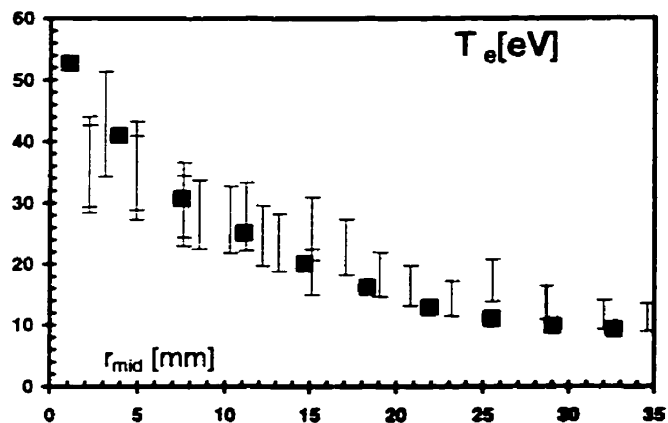


Fig.4.4.8: JET shot 45791,  $t = 63$  sec (L-mode). Same comparison as in Fig.4.4.7, except  $T_i^{RCP} = T_i^{OSM} * (T_i^{OSM}/T_e^{OSM})$ .

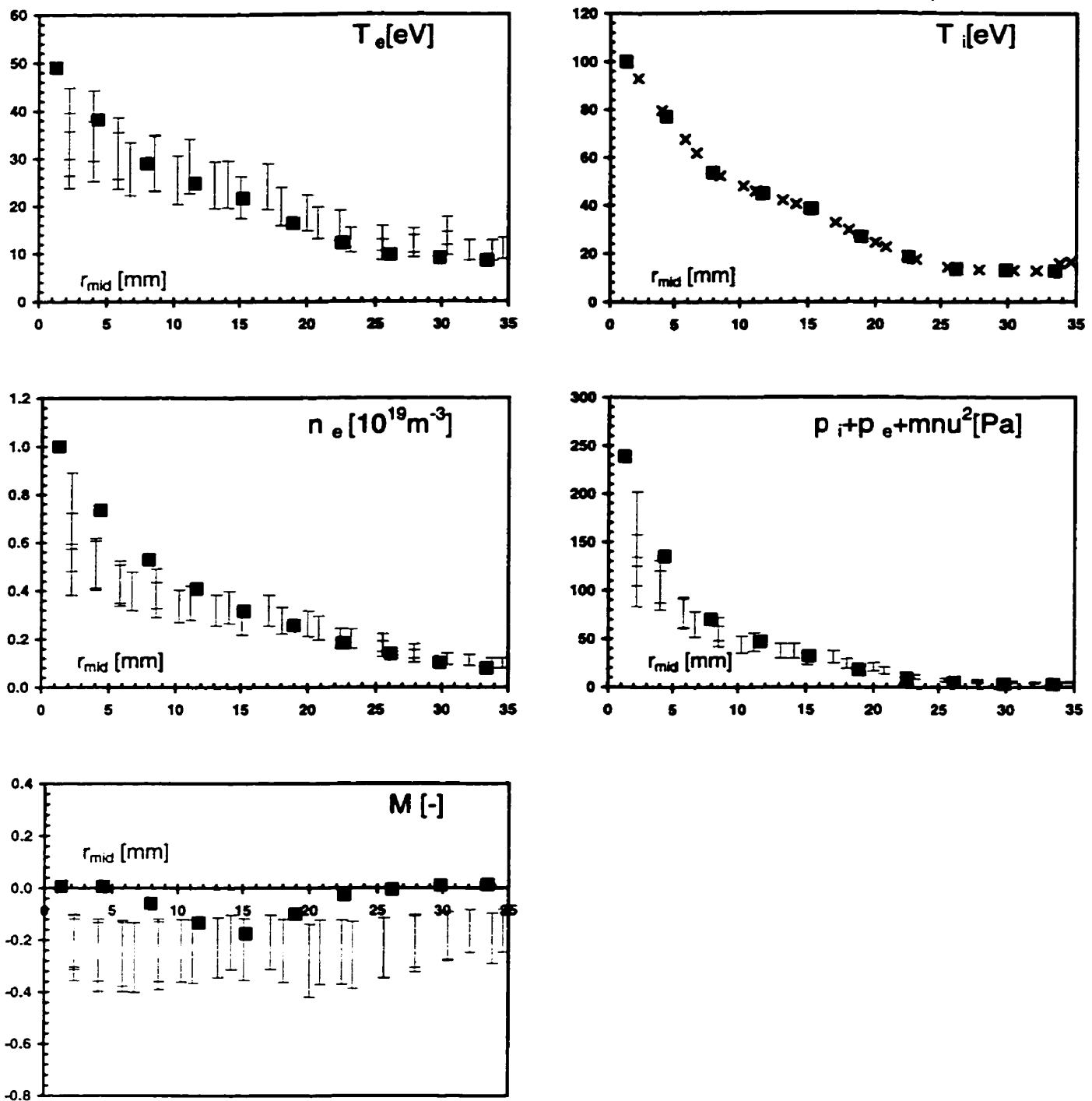


Fig.4.4.9: JET shot 45798,  $t = 63$  sec (L-mode). Radial profiles of plasma variables measured by the upstream reciprocating probe (RCP) and calculated using OSM2/NIMBUS (squares) plotted as a function of the radial distance away from the separatrix at the outer midplane. Radial shift, 20 mm.  $T_i^{\text{RCP}} = T_i^{\text{OSM}}$  assumed.

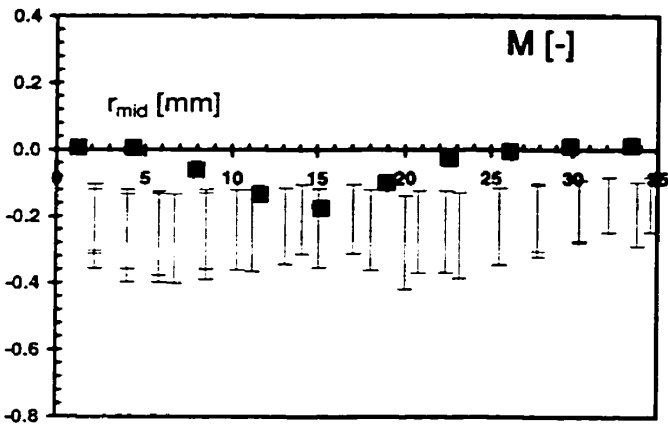
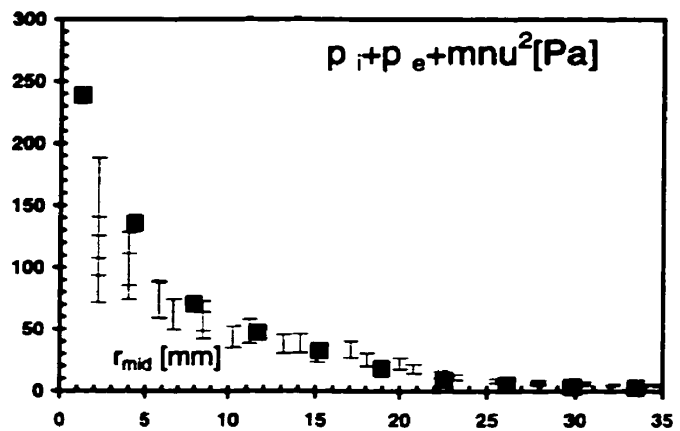
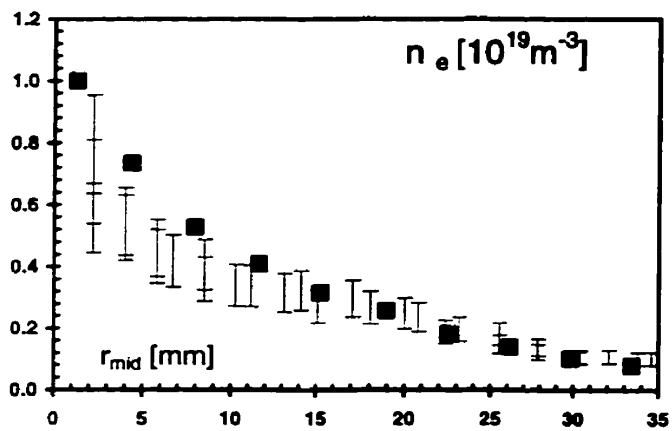
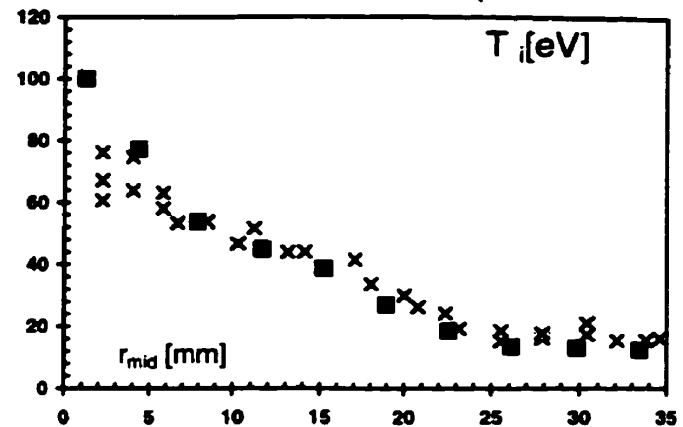
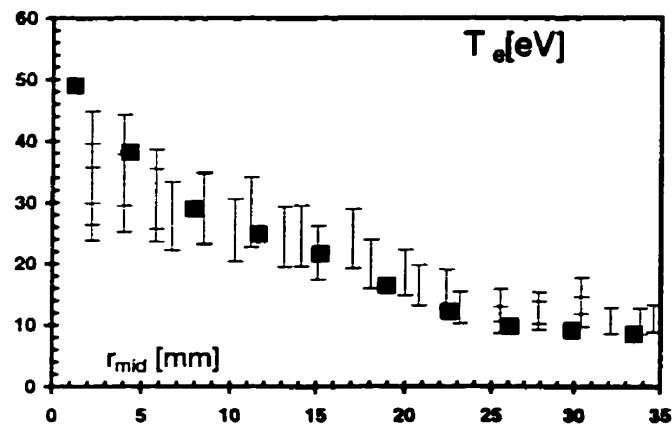


Fig.4.4.10: JET shot 45798,  $t = 63$  sec (L-mode). Same comparison as in Fig.4.4.9, except  $T_i^{RCP} = T_i^{OSM} \approx (T_i^{OSM}/T_e^{OSM})$ .

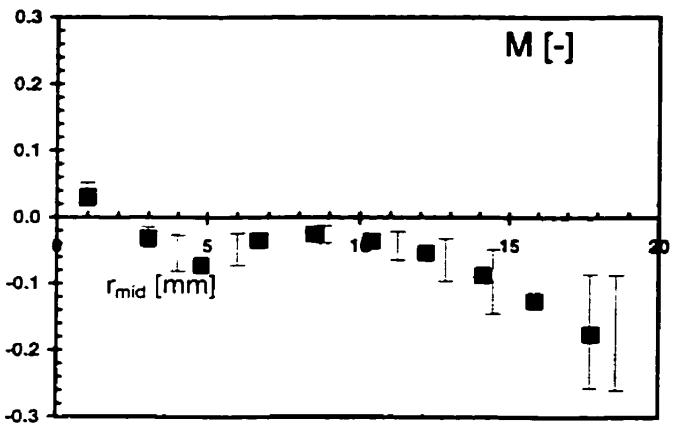
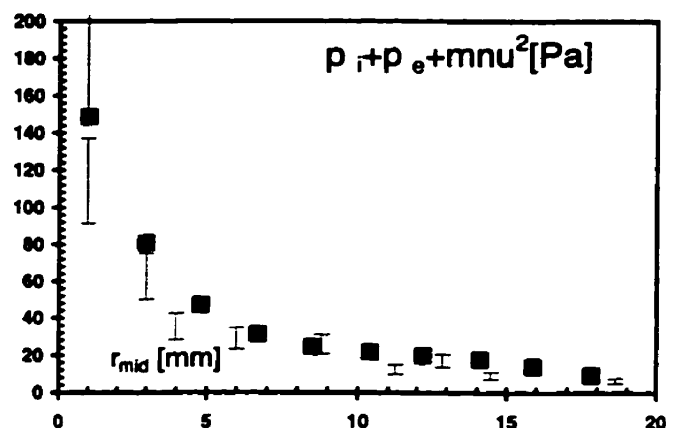
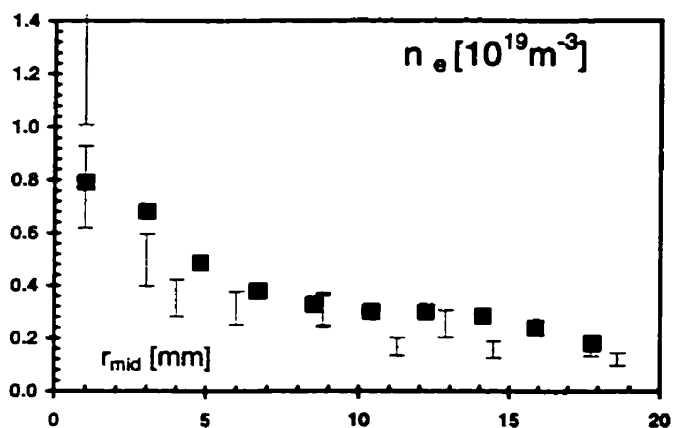
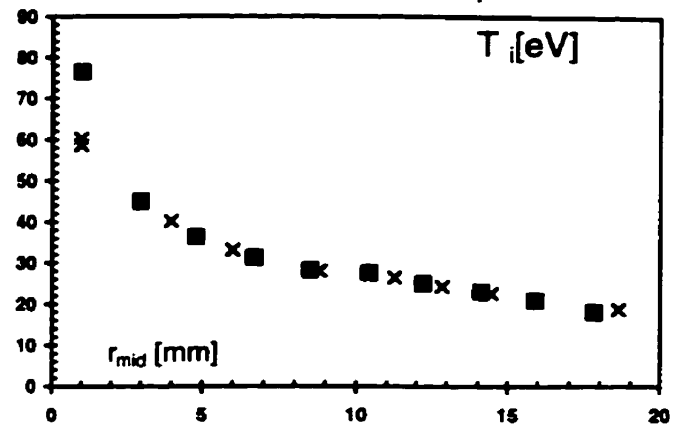
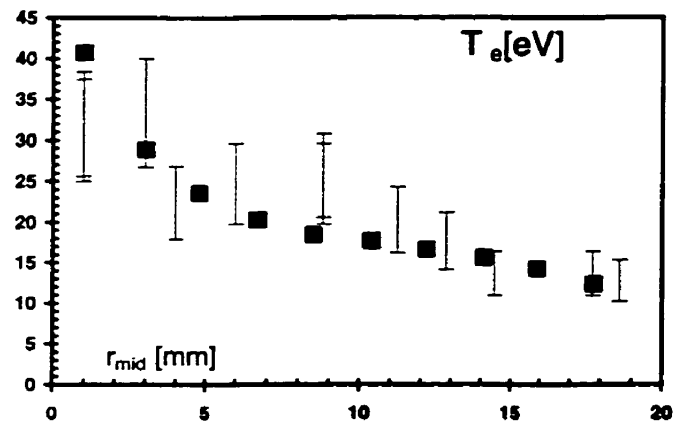


Fig.4.4.11: JET shot 47734,  $t = 61$  sec (H-mode). Radial profiles of plasma variables measured by the upstream reciprocating probe (RCP) and calculated using OSM2/NIMBUS (squares) plotted as a function of the radial distance away from the separatrix at the outer midplane. Radial shift, 8 mm.  $T_i^{\text{RCP}} = T_i^{\text{OSM}}$  assumed.

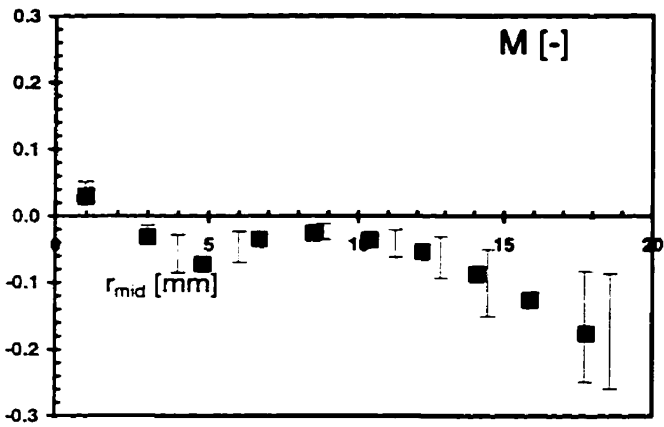
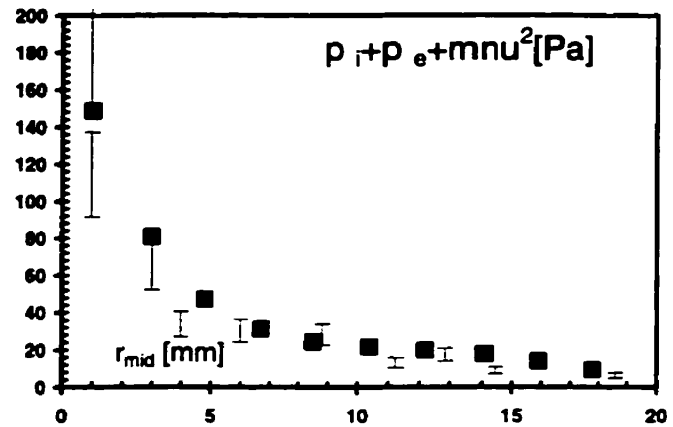
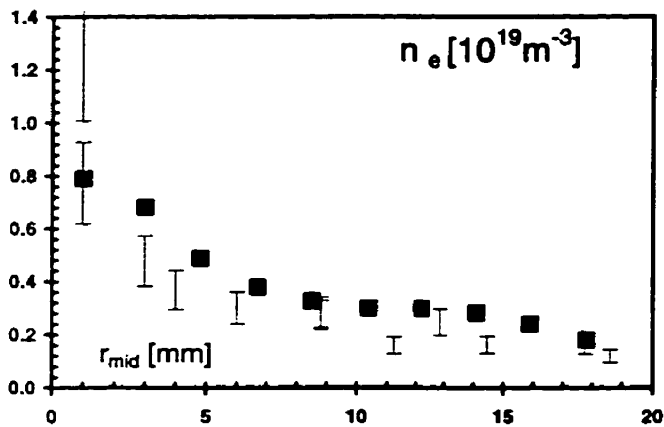
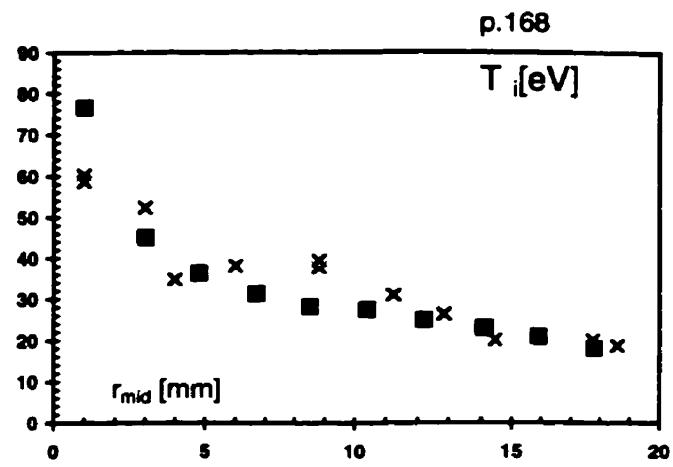
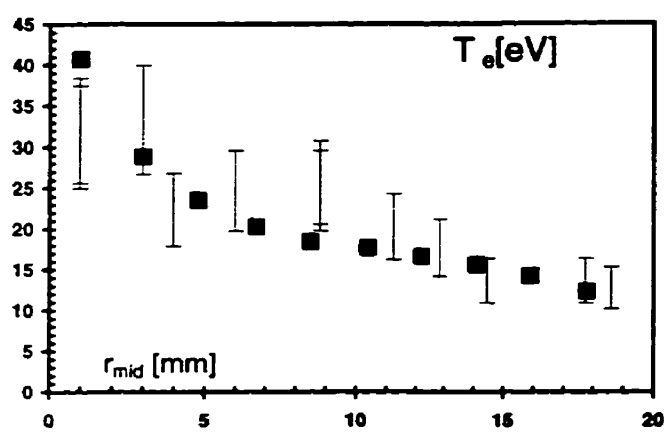


Fig.4.4.12: JET shot 47734,  $t = 61$  sec (H-mode). Same comparison as in Fig.4.4.11, except  $T_i^{\text{RCP}} = T_i^{\text{OSM}} * (T_i^{\text{OSM}}/T_e^{\text{OSM}})$ .

### A.1 Energy in the XXI Century and Nuclear Fusion

The millenium may be viewed as a turning point in humankind's energy usage. Up to now technology of energy production evolved in complexity; with the retreat of the nuclear fission industry and gradual return to fossil fuels, this trend is about to end.

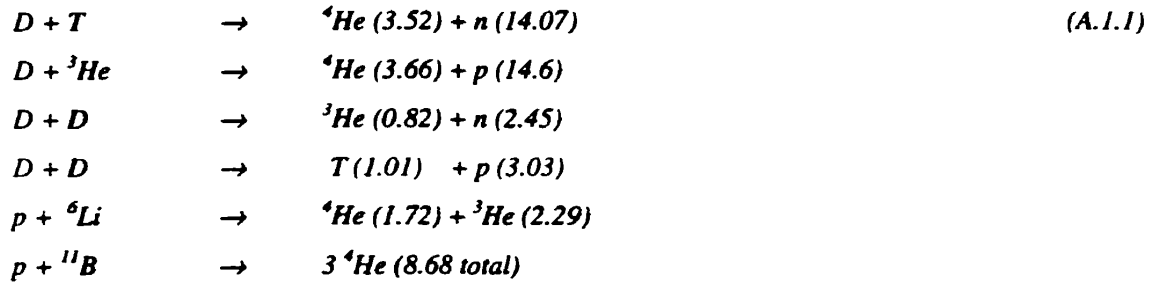
The earth's lithosphere is rich in organic fuels created over millions of years from animal and plant remains. Humans began exploring these non-renewable fossil deposits only in the comparatively recent past (currently roughly two fifths of the world's energy are produced from crude oil, another two fifths each from coal and natural gas, and the remaining fifth from nuclear and hydroelectric power<sup>[Gib89]</sup>), and have not yet had to face the consequences of their eventual and inevitable exhaustion. Based on current estimates of known resources and present world energy consumption, we may expect a fossil energy crisis within the next century<sup>[Gib89]</sup>. However, the moment of crisis may come much sooner, if the hypothesis linking the observed global warming to CO<sub>2</sub> release from fossil fuel combustion was substantiated, and if carbon emission limits were imposed to prevent the anticipated consequences of global warming (erratic weather patterns, drastic climatic changes, rising sea level, desertification<sup>[Gra89, Sch89]</sup>). Although validation of the causal link between CO<sub>2</sub> emission and global warming will require at least a couple of decades, present evidence seems to support a correlation between the two.

In the second half of the XX century, nuclear fission was seen by most as the logical antidote to this future energy crisis, and indeed, from a technological perspective it still appears as a viable option for many centuries via the <sup>232</sup>Th cycle<sup>[Lam83]</sup>. Nonetheless, public apprehension about the health hazards of nuclear exposure in case of an accident has led to the gradual decline of support for the fission alternative. It is the author's opinion that although the dangers of fission reactor operation, as portrayed by the media, are typically exaggerated by factual ignorance or deliberate partisanship, the still serious and long-term hazards posed by spent fuel disposal have not been met with a satisfactory strategy to contemplate a world energy economy based on nuclear fission alone.

The remaining alternative of sufficient magnitude to become the main energy source of our planet (soon to contain nearly five billion inhabitants in rapidly expanding industrial economies), which regrettably excludes such 'renewable' energy sources as solar, wind, geo-thermal or tide power, is the process of nuclear fusion. The universe is full of fusion reactors in the form of stars (fossil fuels themselves are remnants of solar fusion energy, indirectly captured by floral photosynthesis). Fusion energy reserves vary from large to virtually inexhaustible depending on the fuel cycle utilized (the deposits in units of 1985 world energy use<sup>[Fun92]</sup>: crustal <sup>6</sup>Li ~ 10<sup>4</sup>, oceanic <sup>6</sup>Li ~ 10<sup>8</sup>, oceanic D ~ 10<sup>10</sup>, lunar <sup>3</sup>He ~ 10<sup>3</sup>, jovian <sup>3</sup>He ~ 10<sup>17</sup>). Unlike fission, the reaction products are not radioactive, although structural irradiation by neutrons would produce a radioactive inventory; with a proper choice of low activation materials or neutron-scarce fusion fuel cycles (eg. D-<sup>3</sup>He), one could expect total onsite radioactivity many orders of magnitude smaller than in a fission reactor<sup>[Fun92]</sup>. The caveat a propos fusion is twofold: first, both physics and technology required for designing a fusion reactor are not yet at our disposal and require further research (read ~ \$10<sup>10</sup>); secondly, the abundance of fossil fuels on today's

markets (crude oil at \$10 a barrel) undermines the incentive to develop this sophisticated and probably more expensive alternative.

Nuclear fusion refers to a category of nuclear reactions in which two nuclei produce a nucleus of greater mass, such as<sup>[Miy78]</sup>,



where p, D, T are short for  $^1H$ ,  $^2H$ ,  $^3H$ , and the values in brackets are average energy yields in MeV. Most of the energy released in a fusion reaction is carried away by the less massive product, usually a proton or a neutron, according to the ratio of product masses. Since fusion reactions are governed by the short-ranged nuclear force, nuclei must approach each other to within a few fm ( $10^{-15}$  m) for significant wave function overlap. Although such encounters are frequent between neutral particles (eg. neutron scattering), the electrostatic repulsion between like charges reduces the interaction probability by a factor exponential in relative velocity<sup>[Sch49]</sup>.

$$\frac{\sigma_{ab}^{fus}(Z>0)}{\sigma_{ab}^{fus}(Z=0)} = \exp\left(-\frac{2\pi Z_a Z_b e^2}{\hbar} \sqrt{\frac{m_{ab}}{2\varepsilon}}\right) \quad (A.I.2)$$

where  $\sigma_{ab}^{fus}$  denotes a cross section for a fusion reaction between species 'a' and 'b',  $\varepsilon = m_{ab} v^2/2$  the energy in the center of mass frame,  $Z_a e$  and  $Z_b e$  the nuclear charges, and  $m_{ab}$  the reduced mass. This barrier is smallest when the charge-mass product  $Z_a Z_b m_{ab}^{1/2}$  in the numerator of the exponential is minimized, that is for hydrogen isotopes (for which it still amounts to hundreds of keV). As can be seen from Fig. A.I.1, D-T is by far the most reactive fusion mixture. Averaging the product of the fusion cross section  $\sigma_{ab}^{fus}(v)$  and the relative velocity  $v = v_a - v_b$ , over the velocity distributions of both products  $f_a(v)$ ,  $f_b(v)$ , assumed Maxwellian with a single ion temperature  $T_i$  (in energy units), we obtain the thermal fusion reactivity,

$$\langle \sigma v \rangle_{ab}^{fus} = \int dv_a dv_b \cdot \sigma_{ab}^{fus}(v) v \cdot f(v_a) f(v_b) \quad (A.I.3)$$

The integrand peaks at  $\varepsilon \sim 5T_i$ , in the tail of the Maxwellian  $f(\varepsilon)$ <sup>[Mil74]</sup>. The fusion power density becomes

$$P_{ab}^{fus} = \frac{1}{1+\delta_{ab}} n_a n_b \langle \sigma v \rangle_{ab}^{fus} E_{ab}^{fus} \quad (A.I.4)$$

where  $\delta_{ab}$  is the Kronecker delta function,  $n_a$  is the number density of species 'a', and  $E_{ab}^{fus}$  is the energy released per fusion reaction.

The goal of a fusion reactor is to sufficiently confine the reacting species such that the energy released by fusion reactions is sufficient to sustain the reaction (ignition criterion). A milestone on the road towards ignition, is the so called energetic breakeven, for which the heating power is equal to the fusion power produced. Introducing a net reactor efficiency  $\eta_{net}$  which includes both the heating and thermal-to-electric efficiencies, energetic breakeven may be stated as an inequality involving fusion, radiative and convective-conductive (loss) power densities<sup>[Dol82]</sup>,

$$\eta_{net} > \frac{P^{rad} + P^{loss}}{P^{fus} + P^{rad} + P^{loss}} \quad P^{rad} = \sum_{b \in \{ions\}} \alpha_{br} Z_b^2 n_e n_b T_b^{1/2} \quad P^{loss} = \frac{\frac{3}{2} \left( n_e T_e + \sum_{b \in \{ions\}} n_b T_b \right)}{\tau_E} \quad (A.1.5)$$

where we have also defined the global energy confinement time  $\tau_E$ , and assumed that radiative losses are dominated by bremmstrahlung radiation. Inserting the expression for fusion power density and assuming the same  $T_i$  for all ions species, we arrive at the energetic break-even (Lawson) criterion<sup>[Law57]</sup>,

$$n_e \tau_E > \frac{\frac{3}{2} (T_e + T_i Z_{eff}^{-1})}{\frac{\eta_{net}}{\eta_{net} - 1} \cdot \frac{<\sigma v>^{fus} E^{fus}}{4 Z_{eff}^2} - \alpha_{br} Z_{eff} T_e^{1/2}} \quad n_e = \sum_{b \in \{ions\}} Z_b n_b = Z_{eff} \cdot \sum_{b \in \{ions\}} n_b \quad (A.1.6)$$

Ideally, the reactor would become ignited, that is the fusion power absorbed by the plasma would be sufficient to compensate for all power losses, and external heating could be turned off. Since only a fraction  $\mu_+$  of the fusion power is deposited in the plasma (for a D-T mixture, 80% escapes in the form of neutrons), the ignition criterion may be expressed as

$$\mu_+ P^{fus} > P^{rad} + P^{loss} \quad \mu_+ \equiv \frac{E_+^{fus}}{E_+^{fus} + E_0^{fus}} \quad (A.1.7)$$

In terms of the energy multiplication factor  $Q = P^{fus} / P^{heat}$ , the point of energetic break-even is defined as  $Q=1$ , and that of ignition as  $Q \rightarrow \infty$ .

Many different fusion reactor schemes have been conceived over the years<sup>[Gla60, Dol82, Gie90]</sup>.

- a) dual ion beam collision scheme proved ineffective due to space charge losses,
- b) multidirectional laser heating of frozen hydrogen pellets followed by shock wave implosion, so called inertial confinement fusion (ICF), has demonstrated proof of principle in a series of classified tests, but remains plagued by spherical Rayleigh-Taylor instabilities and technological problems linked to the pulsed nature of pellet implosions,

- c) catalyzation of fusion reactions by short-lived muons, whose larger mass decreases the nuclear separation, proved ineffective due to parasitic muon capture by alpha particles,
- d) cold fusion has at best revealed a new multi-body nuclear process, but of insufficient magnitude to prove useful for energy production,
- e) magnetic confinement of ionized fusion fuel is to date the most widely developed method. A number of magnetic configurations have been investigated<sup>[Gie90]</sup> (among them the Z-pinch in the 50's, magnetic mirror in the 60's, stellarator and tokamak starting in the 60's), and although the verdict is far from complete, the toroidal tokamak concept has emerged as the clear leader among the experimental designs, and the most promising candidate for a first generation fusion reactor. The nearly two decades of experiments on a number of large tokamaks (TFTR, D-III, JT-60, JET) and many smaller ones, has greatly extended our understanding of the basic physics of magnetized plasmas, and provided us with the database for extrapolating to reactor relevant regimes<sup>[Wes97]</sup>. At the moment the best results (JET '97) hover about the energetic breakeven point expressed by the Lawson criterion. The next generation experiment (International Thermonuclear Experimental Reactor, or ITER), which has been designed jointly over the last decade by the USA, EU, Russia and Japan, is expected to reach ignition<sup>[Par97]</sup>, a point at which no external heating would be required to sustain the fusion reactions. Recently doubts have arisen concerning the construction of this experiment, due to its multi-billion dollar price tag and a low price of crude oil.

The eventual development of commercial fusion energy seems inevitable: it offers a virtually unlimited, efficient, safe, non-polluting energy source, based on a technology which is already within our grasp. However, this development may be driven either by economic incentives or by political impetus; consequently, the first fusion reactor could see the light of day as early as 2020, if international political commitment to fusion persists, or as late as the end of the coming century, if its future is abandoned to economic factors alone.

## A.2 Plasma Physics

*Let the nature of a fluid be assumed to be such that, of its parts which lie evenly and are continuous, that which is under the lesser pressure is driven along by that under the greater pressure.*

ARCHIMEDES

By the term plasma (*πλασμα [anc.gr.]: shape, creature, phantom, fiction*) we shall mean a large ensemble of charged particles undergoing strong collective interactions<sup>[Ch60]</sup>. We thus begin the discussion of plasma physics by considering how a single charged particle behaves within this ensemble.

### A.2.1 Charged Particle Dynamics

The classical motion of a particle with kinetic energy  $\Theta$  and potential energy  $\Phi$  can be described by Hamilton's equations<sup>[Lan76]</sup>,

$$\frac{\partial \mathbf{q}}{\partial t} = \frac{\partial}{\partial \mathbf{p}} H(\mathbf{q}, \mathbf{p}, t) \equiv \nabla_{\mathbf{p}} H \quad \frac{\partial \mathbf{p}}{\partial t} = -\frac{\partial}{\partial \mathbf{q}} H(\mathbf{q}, \mathbf{p}, t) \equiv -\nabla_{\mathbf{q}} H \quad H(\mathbf{q}, \mathbf{p}, t) = \Theta(\mathbf{p}) + \Phi(\mathbf{q}, \mathbf{p}) \quad (A.2.1)$$

where  $\mathbf{q}$  and  $\mathbf{p}$  are its canonical co-ordinates (position and momentum). For a non-relativistic particle of mass  $m$  and charge  $Ze$  in the presence of an electromagnetic field, the Hamiltonian  $H(\mathbf{q}, \mathbf{p}, t)$  becomes<sup>[Lan89]</sup>

$$H(\mathbf{q}, \mathbf{p}, t) = \frac{\tilde{\mathbf{p}}^2}{2m} + Ze\phi(\mathbf{q}) = \frac{1}{2m} \left( \mathbf{p} - \frac{Ze}{c} \mathbf{A}(\mathbf{q}) \right)^2 + Ze\phi(\mathbf{q}) \quad \mathbf{p} = \tilde{\mathbf{p}} + \frac{Ze}{c} \mathbf{A} \quad \tilde{\mathbf{p}} = m\mathbf{v} \quad (A.2.2)$$

which leads to the equation of motion,

$$m \frac{d\mathbf{v}}{dt} = Ze(E + \frac{1}{c} \mathbf{v} \times \mathbf{B}) \quad (A.2.3)$$

In the above,  $\phi$  and  $\mathbf{A}$  are the potentials of the net fields ( $\mathbf{E} = \nabla\phi - \partial\mathbf{A}/\partial t$ ,  $\mathbf{B} = \nabla \times \mathbf{A}$ ), which we will divide into contributions due to external sources ( $\mathbf{E}_{\text{ext}}$ ,  $\mathbf{B}_{\text{ext}}$ ) and due to microscopic interactions between charged particles ( $\mathbf{E}_{\text{int}}$ ,  $\mathbf{B}_{\text{int}}$ ). The fields evolve according to Maxwell's equations<sup>[Jac75]</sup> (for a plasma  $\epsilon \approx 1$ ,  $\mu \approx 1$ ).

$$\nabla \times \mathbf{E} + \frac{1}{c} \frac{\partial \mathbf{B}}{\partial t} = 0 \quad \nabla \times \mathbf{B} = \frac{4\pi}{c} \mathbf{j} + \frac{1}{c} \frac{\partial \mathbf{E}}{\partial t} \quad (A.2.4)$$

$$\nabla \cdot \mathbf{E} = 4\pi\rho_+ \quad \nabla \cdot \mathbf{B} = 0,$$

where  $\rho_+$  and  $\mathbf{j}$  denote net charge and current densities (CGS units throughout §A.2). In the case of a uniform magnetic field ( $\nabla \cdot \mathbf{B} = 0$ ) and vanishing electric field ( $\mathbf{E} = 0$ ), we find from (A.2.3) that the  $\mathbf{B}$ -field only alters

the velocity perpendicular to  $\mathbf{B}$ ,  $v_{\perp} = v_{\perp}(\cos\varphi \mathbf{i}_x + \sin\varphi \mathbf{i}_y)$ ,  $\varphi = \omega_c t$ , causing the particle to gyrate about the  $\mathbf{B}$ -axis with frequency  $\omega_c$  and radius  $r_L$ , normally called the Larmor radius,

$$\omega_c = \frac{ZeB}{m} \quad r_L = \frac{v_{\perp}}{\omega_c} = \frac{mv_{\perp}}{ZeB} \quad (\text{A.2.5})$$

Note that the electrons gyrate much faster ( $\omega_{ce} \gg \omega_{ci}$ ), in tighter orbits ( $r_{Le} \ll r_{Li}$ ), and in the opposite direction to the ions. The final trajectory is a helix of radius  $r_L$  and pitch angle  $\tan^{-1}(v_{\parallel}/v_{\perp})$ , with the helical axis of the orbit, or its guiding centre, following the magnetic field line, Fig. A.2.1. In the presence of additional non-uniform or varying  $\mathbf{B}$  and  $\mathbf{E}$  fields, sufficiently weak to be treated as a perturbation to the helical solution, that is satisfying the so-called adiabatic invariants<sup>[Miy78]</sup>,

$$\delta_{\psi} \ll 1 \quad L_{\nabla\psi} \equiv \left| \frac{\nabla\psi}{\psi} \right|^{-1} \quad \tau_{\partial\psi} \equiv \left| \frac{I}{\psi} \frac{\partial\psi}{\partial t} \right|^{-1} \quad \delta_{\psi} \equiv \max\left( \frac{r_L}{L_{\nabla\psi}}, \frac{I}{\omega_c \tau_{\partial\psi}} \right) \quad \psi \in (E, B) \quad (\text{A.2.6})$$

the guiding center of the gyrating particle, found by averaging (A.2.3) over a gyration period  $\int_0^{2\pi} d\phi/2\pi$ , acquires a transverse drift velocity due to a non-uniformity of the orbit caused by: a) a transverse  $\mathbf{E}$ -field, b) a transverse gradient of the  $\mathbf{B}$ -field, c) a curvature of the  $\mathbf{B}$ -field, d) a time varying  $\mathbf{E}$ -field. Its along- $\mathbf{B}$  velocity,  $v_{\parallel}$ , changes with the parallel  $\mathbf{B}$  gradient to preserve the magnetic moment of the orbit<sup>[Miy78]</sup>.

$$v_{\perp}^{\text{drift}} = \frac{\mathbf{E} \times \mathbf{B}}{B^2} + \left( \frac{\frac{I}{2} v_{\perp}^2}{\omega_c} + \frac{v_{\parallel}^2 + \frac{I}{2} v_{\perp}^2}{\omega_c} \right) \frac{\mathbf{B} \times \nabla B}{B^2} + \frac{I}{\omega_c B} \frac{dE}{dt} \quad \frac{dv_{\parallel}}{dt} = \frac{v_{\perp}^2}{B} \nabla_{\parallel} B \quad (\text{A.2.7})$$

In the presence of strong  $\mathbf{B}$  and  $\mathbf{E}$  gradients, the trajectory is no longer helical but follows a complicated path dependent on the local field strengths, and the guiding center description ceases to be useful.

Since charged particles in a plasma interact via the long range Coulomb force, we expect the ensemble to exhibit strong collective behaviour. Solving the Poisson equation for an ion test charge in a single ion-species plasma<sup>[Kra80]</sup>,

$$\nabla^2 \phi = -4\pi Ze \delta(x) - 4\pi e (n_{oe} \exp(-e\phi/T_e) - Zn_{oi}) \quad (\text{A.2.8})$$

with the assumption of Boltzmann distribution for the electrons and unperturbed ions, we find that the Coulomb potential is reduced exponentially by the mobile electron population with a scale length  $\lambda_D$ , called the Debye length,

$$\phi(x) = \frac{Ze}{|x|} \exp\left(-\frac{|x|}{\lambda_D}\right) \quad \lambda_D = \left( \frac{T_e}{4\pi e^2 n_e} \right)^{1/2} \quad (\text{A.2.9})$$

This means that electric fields can only penetrate into the plasma a distance on the order of the Debye length before they are shielded; as a consequence, average charge density over dimensions  $L \gg \lambda_D$  is vanishingly small, i.e. the plasma is quasi-neutral,  $|n_e - n_i| \ll n_e$ , and  $n_e \approx n_i$ ; the characteristic response time of this process may be estimated as  $1/\omega_{pe}$ ,

$$\omega_{pe} = \frac{c_e}{\lambda_D} = \left( \frac{4\pi e^2 n_e}{m_e} \right)^{1/2} \quad c_e = \left( \frac{T_e}{m_e} \right)^{1/2} \quad (A.2.10)$$

where  $c_e$  is the thermal electron velocity and  $\omega_{pe}$  the electron plasma frequency. Collective behaviour dominates when the number of particles in a sphere of radius  $\lambda_D$  is large<sup>[Kra80]</sup>,

$$\frac{1}{\Delta} = \frac{4\pi}{3} n \lambda_D^3 \gg 1 \quad (A.2.11)$$

Inserting the expression for  $\lambda_D$  into the above, we find that  $\Delta$ , often called the discreteness parameter, is also the ratio of potential to kinetic energy of particles in the plasma. This leads us to believe that the standard methods employed in kinetic theory of gases, namely an expansion in the discreteness parameter, should remain applicable for plasmas as well, with the collective Coulomb interactions replacing discrete scattering events.

### A.2.2 Statistical Mechanics

An ensemble of  $N$  particles,  $N \gg 1$ , can be described by a phase-space density  $\rho(q_j, p_j, t | j = 1, \dots, N)$ , such that any microscopic quantity  $\psi$  gives rise to a macroscopic quantity  $\Psi = \langle \psi \rangle$ , defined as an average over phase-space with the weight function  $\rho$ <sup>[Lan82, Hua87]</sup>,

$$\langle \psi \rangle = \frac{\int d^N q d^N p \cdot \rho \psi}{\int d^N q d^N p \cdot \rho} \quad (A.2.12)$$

The time evolution of  $\rho$  is governed by the Liouville equation<sup>[Lan82, Hua87]</sup>,

$$\frac{\partial \rho}{\partial t} = \{H, \rho\} \equiv \frac{\partial H}{\partial q} \frac{\partial \rho}{\partial p} - \frac{\partial H}{\partial p} \frac{\partial \rho}{\partial q} = \nabla_q H \cdot \nabla_p \rho - \nabla_p H \cdot \nabla_q \rho \quad (A.2.13)$$

where  $\{ \dots \}$  is the Poisson bracket of classical mechanics, and  $H$  the Hamiltonian of the ensemble. In quantum mechanics,  $H$  and  $\rho$  become operators and  $\{ \dots \}$  a commutator. We are justified in neglecting quantum effects as long as the thermal electron deBroglie wavelength is smaller than the average inter-particle spacing<sup>[Lan82]</sup>. Likewise, we can neglect relativistic effects if the thermal electron velocity  $c_e = (T_e/m_e)^{1/2}$ , is sufficiently

smaller than the velocity of light  $c^{[Lan89]}$ . We may therefore consider the region of validity of classical mechanics to be  $\hbar/m_e c_e < n_e^{-1/3}$  and  $c_e/c < 0.1$ .

For a single ion-species plasma the phase-space density and the non-relativistic Hamiltonian (for which the interaction potential is purely electrostatic,  $\nabla \times \mathbf{E} = 0$ ) can be written<sup>[Kra80]</sup>

$$\rho(\mathbf{q}_{a,j}, \mathbf{p}_{a,j}; t \mid a \in \{i, e\}; j \in \{1, \dots, N\}) \quad (A.2.14)$$

$$H = \frac{1}{2} \sum_{j=1}^N \left( \frac{\mathbf{p}_{i,j}^2}{m_i} + \frac{\mathbf{p}_{e,j}^2}{m_e} \right) + \frac{1}{2} \sum_{j \neq k} \left( \frac{Z^2 e^2}{|\mathbf{q}_{i,j} - \mathbf{q}_{i,k}|} + \frac{e^2}{|\mathbf{q}_{e,j} - \mathbf{q}_{e,k}|} \right) - \sum_{j,k} \frac{Ze^2}{|\mathbf{q}_{i,j} - \mathbf{q}_{e,k}|}$$

where we removed fields generated by external sources from the Hamiltonian of the ensemble, so that  $\mathbf{p} = m\mathbf{v}$  in (A.2.2); the external field Hamiltonian will be added to the final Liouville operator at a later stage. The extension to multi-ion species is straightforward, once we note that  $\sum_a (Z_a N_a) = 0$  in a neutral mixture.

In thermal equilibrium  $\partial \rho / \partial t = \{H, \rho\} = 0$ , and  $\rho$  relaxes to the canonical distribution<sup>[Hua87]</sup>,

$$\rho = \frac{1}{h^{6N} (N!)^2 \zeta} e^{-\beta H} \quad \zeta = \frac{1}{h^{6N} (N!)^2} \int \int d^N \mathbf{q}_i d^N \mathbf{p}_i d^N \mathbf{q}_e d^N \mathbf{p}_e e^{-\beta H} \quad (A.2.15)$$

where  $\beta = 1/T$ , and  $\zeta$  is the partition function. The link to thermodynamics is provided by the expression for the free energy,  $F = -(\beta/\hbar) \ln \zeta$ , from which all other thermodynamic quantities may be obtained using the well established formalism. In evaluating  $\zeta$ , we may perform a cluster expansion in terms of the Mayer functions  $g_{jk} = \exp(-\phi_{jk}) - 1$ , which transforms integrals of the form  $\int d^N \mathbf{q} \exp(-\beta \sum_{j,k} \phi_{jk})$  into  $\int d^N \mathbf{q} \prod_{j,k} (1 + g_{jk})$ . The problem then reduces to evaluating cluster integrals of  $g_{jk}$ , a task less daunting than the original. We will not dwell on the results of these calculations<sup>[Kch92]</sup>, except to note that the departure from the ideal gas law is of the order of the discreteness parameter,  $p_a = n_a T_a + O(\Delta_a)$ ,  $a \in \{i, e\}$ .

### A.2.3 Plasma Kinetic Theory

We would like to predict the probability of finding a particle of a given species in a single ion-species plasma,  $a \in \{i, e\}$ , at position  $\mathbf{q}_a$  with momentum  $\mathbf{p}_a$ ; this probability is given by the one-particle distribution function  $f^a(\mathbf{q}, \mathbf{p}, t)$  defined by integrating the phase-space density  $\rho$  over all but one pair of co-ordinates<sup>[Kra80]</sup>, which we denote by a common  $j$  index,  $j = 1, \dots, N$  with  $N = N_i + N_e$ ,

$$\begin{aligned} f^a(\mathbf{q}_1, \mathbf{p}_1; t) &\equiv N_a \int d^{N-1} \mathbf{q} d^{N-1} \mathbf{p} \cdot \rho \\ f^{ab}(\mathbf{q}_1, \mathbf{p}_1; \mathbf{q}_2, \mathbf{p}_2; t) &\equiv N_a N_b \int d^{N-2} \mathbf{q} d^{N-2} \mathbf{p} \cdot \rho \\ f^{abc}(\mathbf{q}_1, \mathbf{p}_1; \mathbf{q}_2, \mathbf{p}_2; \mathbf{q}_3, \mathbf{p}_3; t) &\equiv N_a N_b N_c \int d^{N-3} \mathbf{q} d^{N-3} \mathbf{p} \cdot \rho \end{aligned} \quad (A.2.16)$$

Here we have also defined the two and three particle distributions,  $f^{ab}$  and  $f^{abc}$ , with each species index spanning over both ions and electrons,  $a,b,c \in \{i,e\}$ ; for like-particle distributions, it is useful to consider the first particle, with indexes ‘a’ and ‘1’, as a test particle, and the following particles, ‘b’, ‘2’, and ‘c’, ‘3’, as field or background particles. Using the mentioned cluster expansion<sup>[Kra80]</sup>, these can be recast in terms of the two and three particle correlation functions  $g^{ab}$  and  $g^{abc}$ ,

$$f^{ab}(\mathbf{q}_1, \mathbf{p}_1; \mathbf{q}_2, \mathbf{p}_2; t) = f^a(\mathbf{q}_1, \mathbf{p}_1; t) f^b(\mathbf{q}_2, \mathbf{p}_2; t) + g^{ab}(\mathbf{q}_1, \mathbf{p}_1; \mathbf{q}_2, \mathbf{p}_2; t) \quad (A.2.17)$$

$$f^{abc} = f^a f^b f^c + f^a g^{ab} + f^b g^{ac} + f^c g^{bc} + g^{abc}$$

where we expect  $g^{ab}/f^a f^b \sim \Delta$  and  $g^{abc}/f^a f^b f^c \sim \Delta^2$ , with the discreteness parameter  $\Delta \ll 1$ . Next, we expand the Poisson bracket in the Liouville equation and express the result in terms of the propagation and interaction operators<sup>[Lch92, Gil81]</sup>,  $\mathbf{L}^a$  and  $\mathbf{L}^{ab}$ ,

$$\left[ \frac{\partial}{\partial t} + \sum_{j=1}^N L_j^a - \sum_{j=1}^N \sum_{k=1}^{j-1} L_{jk}^{ab} \right] \rho = 0 \quad L_{jk}^{ab} = \frac{1}{m_a} \frac{\partial \varphi_{jk}^{ab}}{\partial \mathbf{q}_j} \cdot \frac{\partial}{\partial v_j} \quad (A.2.18)$$

$$L_j^a = \mathbf{v}_j \cdot \frac{\partial}{\partial \mathbf{q}_j} + \frac{Z_a e}{m_a} (\mathbf{E}_{ext} + \frac{1}{c} \mathbf{v}_j \times \mathbf{B}_{ext}) \cdot \frac{\partial}{\partial v_j} \quad \varphi_{jk}^{ab} = \frac{Z_a Z_b e^2}{|\mathbf{q}_j - \mathbf{q}_k|}$$

The effect of external fields is included in the propagation operator  $\mathbf{L}^a$ . Integrating (A.2.18) over  $d^{N-1}\mathbf{q} d^{N-1}\mathbf{p}$  and inserting the cluster expanded  $f^{ab}$ , we obtain<sup>[Spe90]</sup>

$$\left[ \frac{\partial}{\partial t} + L_1^a \right] f^a = \sum_{b \in \{i,e\}} \int d\mathbf{q}_2 d\mathbf{p}_2 L_{12}^{ab} (f^a f^b + g^{ab}) \quad (A.2.19)$$

A similar integration of (A.2.18) over  $d^{N-2}\mathbf{q} d^{N-2}\mathbf{p}$  yields

$$\begin{aligned} \left[ \frac{\partial}{\partial t} + L_1^a + L_2^b \right] g^{ab} &= (L_{12}^{ab} + L_{21}^{ba}) f^a f^b + \\ &\sum_{c \in \{i,e\}} \int d\mathbf{q}_3 d\mathbf{p}_3 [L_{13}^{ac} f^a g^{bc} + L_{23}^{bc} f^b g^{ac} + (L_{13}^{ac} + L_{23}^{bc}) f^c g^{ab}] \end{aligned} \quad (A.2.20)$$

where we have expanded the time derivative, used the previous result for  $\partial f^a / \partial t$  and  $\partial f^b / \partial t$ , and neglected terms of order  $\Delta^2$  to close the BBGKY hierarchy; taken together (A.2.16-20) represent the kinetic equation we set out to find. Since the choice of the test particle is arbitrary, we can recast this equation into a more familiar form by switching to cartesian co-ordinates ( $\mathbf{q}_1 = \mathbf{x}$ ,  $\mathbf{p}_1 = m\mathbf{v}$ ), bringing the microscopic field term  $(\mathbf{L}^{ab} + \mathbf{L}^{ba}) f^a f^b$  onto the left side and adding the external and the microscopic contributions to form the net fields,

$$\left[ \frac{\partial}{\partial t} + \mathbf{v} \cdot \frac{\partial}{\partial \mathbf{x}} + \frac{Z_a e}{m_a} (\mathbf{E} + \frac{\mathbf{v}}{c} \times \mathbf{B}) \cdot \frac{\partial}{\partial \mathbf{v}} \right] f_a(\mathbf{x}, \mathbf{v}, t) = \sum_{b \in \{i, e\}} C_{ab} = \sum_{b \in \{i, e\}} \int d^3 \mathbf{x}' d^3 \mathbf{v}' \mathbf{L}^{ab} g^{ab} \{ f(t') \} \quad (A.2.21)$$

$$\mathbf{E}(\mathbf{x}, t) = \mathbf{E}_{ext}(\mathbf{x}, t) - \sum_{b \in \{i, e\}} Z_b e \frac{\partial}{\partial \mathbf{x}} \int d\mathbf{x}' d\mathbf{v}' \frac{f_b(\mathbf{x}', \mathbf{v}', t)}{|\mathbf{x} - \mathbf{x}'|} \quad \mathbf{B}(\mathbf{x}, t) = \mathbf{B}_{ext}(\mathbf{x}, t)$$

The remaining terms on the right hand side,  $\mathbf{C}_{ab}$ , are normally referred to as the collision terms. Explicit time dependence appearing in  $g^{ab}$  refers to the physical assumption that pair correlation functions relax much faster than the single-particle distribution functions; it allows us on the one hand, to neglect the time-history of the correlation in calculating  $\mathbf{C}_{ab}$ , and on the other, to treat  $f^a$  as constant over the time needed for correlation  $g^{ab}$  to relax. These arguments are referred to as Bogoliubov's characteristic time hierarchy.

The morphology of kinetic equations corresponds to different assumptions used in evaluating  $\mathbf{C}_{ab}$ . The simplest, namely  $g^{ab} = 0$ , leads to the well known Vlasov equation<sup>[Vla38]</sup> for which  $\mathbf{C}_{ab} = 0$  (it is a slight misnomer to call this approximation collisionless, since Coulomb interactions are present in the microscopic field  $\mathbf{E}_{int}$ ; the usage refers to the fact that  $\mathbf{E}_{int}$  does not increase plasma entropy nor generate plasma transport; it can however dissipate field-energy as demonstrated by the 'collisionless' (Landau) damping of E-M waves<sup>[Lan46]</sup>; bowing to common usage, we use the term 'collisionless' to mean  $\mathbf{C}_{ab} = 0$ ). The standard approach of gas dynamics is to retain terms on the order of the discreteness parameter  $\Delta$ ; the calculations have been carried out independently by Balescu<sup>[Bal60]</sup>, Guernsey<sup>[Gue60]</sup>, and Lenard<sup>[Len60]</sup> (1960). There are a number of ways to proceed of which we will adopt the Green's function approach. First, we notice that only the first term on the right hand side of (A.2.20) is not-homogenous with respect to  $g^{ab}$ , and so only this term acts as a forcing function to the evolution of  $g^{ab}$ . We can thus express  $g^{ab}(t)$  as an integral of the forcing function and an unknown propagator  $\mathbf{W}$  over all previous times<sup>[Icb92, Bal88]</sup>,

$$g^{ab}(a, b; t) = \int da' \int db' \int_{-\infty}^t dt' [\mathbf{L}^{a'b'} + \mathbf{L}^{b'a'}] f^{a'}(t') f^{b'}(t') \times \mathbf{W}(a, a'; t - t') \mathbf{W}(b, b'; t - t') \quad (A.2.22)$$

where for conciseness we abandoned the particle index, which will be linked to a and b; thus,  $a = (\mathbf{q}_1, \mathbf{p}_1)$ ,  $b = (\mathbf{q}_2, \mathbf{p}_2)$  with either particle being an ion or electron. Direct substitution of the above into (A.2.20), with no external fields and  $f^a$  constant in time, yields a time-evolution equation for the propagator  $\mathbf{W}$ .

$$\left[ \frac{\partial}{\partial t} + \mathbf{v}_a \cdot \frac{\partial}{\partial \mathbf{x}_a} \right] \mathbf{W}(a, a'; t) = \int db \mathbf{L}^{ab} f^a \mathbf{W}(b, a'; t) \quad \mathbf{W}(a, a', 0) = \delta(a - a') \quad (A.2.23)$$

The propagator  $\mathbf{W}$  may easily be obtained in  $(\mathbf{k}, \omega)$  space by effecting a Fourier transform with respect to  $\mathbf{x}_a - \mathbf{x}_a'$  and a Laplace transform with respect to  $t > 0$ ,

$$W_k(v_a, v'_a; \omega) = \frac{i}{\omega - \mathbf{k} \cdot \mathbf{v}_a} \left[ i\delta(v_a - v'_a) - \frac{\omega_p^2 \mathbf{k}}{k^2} \cdot \frac{\partial}{\partial v_a} f(v_a) \int dv_b W_k(v_a, v'_a; \omega) \right] \quad (A.2.24)$$

Integrating over  $v_a$  gives an expression for the interaction integral<sup>[Ich92]</sup>,

$$\int dv_a W_k(v_a, v'_a; \omega) = \frac{i}{(\omega - \mathbf{k} \cdot \mathbf{v}_a) \epsilon(\mathbf{k}, \omega)} \quad \epsilon(\mathbf{k}, \omega) = 1 + \frac{\omega_p^2}{k^2} \int dv \frac{\mathbf{k}}{\omega - \mathbf{k} \cdot \mathbf{v}} \cdot \frac{\partial f}{\partial \mathbf{v}} \quad (A.2.25)$$

Inserting the above into (A.2.24), we have the final form of the propagator,

$$W_k(v_a, v'_a; \omega) = \frac{i}{\omega - \mathbf{k} \cdot \mathbf{v}_a} \left[ i\delta(v_a - v'_a) - \frac{\omega_p^2}{k^2} \frac{\mathbf{k}}{(\omega - \mathbf{k} \cdot \mathbf{v}'_a) \epsilon(\mathbf{k}, \omega)} \cdot \frac{\partial f(v_a)}{\partial v_a} \right] \quad (A.2.26)$$

The first term is simply a free-particle propagator, while the second is a propagator due to the Coulomb interaction, including the effect of exponential shielding contained in the Vlasov dielectric function  $\epsilon(\mathbf{k}, \omega)$ .

Armed with  $W_k$  we are ready for the collision term  $C_{ab}$ . We carry out the same Fourier-Laplace transform on  $g^{ab}$  as we have on  $W$  and integrate over the time variable,

$$g_k^{ab}(v_a, v_b) = i \frac{\omega_p^2}{2\pi} \int dv'_a \int dv'_b \int d\omega \frac{\mathbf{k}}{k^2} \left[ \frac{\partial}{\partial v'_a} - \frac{\partial}{\partial v'_b} \right] f(v'_a) f(v'_b) \cdot W_k(v_a, v'_a; \omega) W_{-k}(v_b, v'_b; -\omega) \quad (A.2.27)$$

The collision term  $C_{ab}$  may now be constructed from the Fourier components  $g_k^{ab}$  by an integration over  $\mathbf{k}$  that is over the scattering collision parameters,

$$C_{ab} = -i \omega_p^2 \int \frac{d\mathbf{k}}{k^2} \frac{\partial}{\partial \mathbf{v}} \int dv' g_k^{ab}(v, v') \quad (A.2.28)$$

The final steps after combining the last three equations require extensive use of contour integrals and the analytic properties of the transformed propagator; we present the final result without further delay<sup>[Ich92]</sup>.

$$C_{ab} = \int dv' Q(v, v') \left[ \frac{\partial}{\partial v} - \frac{\partial}{\partial v'} \right] f_a(v) f_b(v') \quad Q(v, v') = \pi \omega_p^4 \int \frac{d\mathbf{k} \cdot \mathbf{k}}{k^4} \frac{\delta(k \cdot (v - v'))}{|\epsilon(\mathbf{k}, k \cdot v)|^2} \quad (A.2.29)$$

In the process of integration over  $\mathbf{k}$ , the presence of the dielectric function removes the singularity encountered at long range, since  $\epsilon(\mathbf{k}, \mathbf{k} \cdot \mathbf{v}) \propto 1/k^2$ , for  $k \ll 1$ . A short range limit on the order of the DeBroglie length or the 90° scattering distance must still be assumed,  $k_{\max} \sim \max(m_a v_a / \hbar, 3 T_a / Z_a Z_b e^2)$ , since cluster expansion breaks down at such small distances<sup>[Kra80]</sup>; this limit usually appears as the so called Coulomb logarithm,  $\ln \Lambda_{ab} = \ln$

$(k_{\max} \lambda_D)$ . Symmetry consideration reveal a number of general properties of the BGL collision term which we can summarize as follows: it is symmetric with respect to  $\mathbf{v}$ ; it conserves the average density, velocity and kinetic energy of  $f(\mathbf{v})$ ; it relaxes the  $f(\mathbf{v})$  towards an equilibrium Maxwellian distribution, for which it is identically zero.

The same form of the collision term but without electron shielding,  $\epsilon(\mathbf{k}, \mathbf{k} \cdot \mathbf{v}) = 1$ , was first obtained by Landau<sup>[Lan37]</sup> (1937), who introduced a long-range limit,  $k_{\min} \sim 1 / \lambda_D$ , in integration over  $\mathbf{k}$ . The BGL and Landau terms clearly agree for  $\epsilon(\mathbf{k}, \mathbf{k} \cdot \mathbf{v}) \sim 1 + 1 / k^2 \lambda_D^2$ . It is noteworthy that Landau initially arrived at this expression not by a cluster expansion, but by looking for a collision term of the Fokker-Planck type, appropriate for grazing collisions<sup>[Shk66]</sup>.

$$C_{ab} = -\frac{\partial}{\partial v} \cdot A_{ab} f_a(v) + \frac{1}{2} \frac{\partial}{\partial v \partial v} : B_{ab} f_a(v) \quad (A.2.30)$$

and by including the kinematics of binary, unshielded Coulomb scattering; it is reassuring that both methods give identical results. Integrating by parts we can transform (A.2.29) into the Fokker-Planck form, which we will find useful in evaluating plasma relaxation times. Introducing the Rosenbluth (Trubnikov) potentials  $H_{ab}$  and  $G_{ab}$  we obtain<sup>[Ros57]</sup>

$$\begin{aligned} A_{ab} &= \langle \Delta v \rangle_{ab} = K_{ab} \frac{\partial H_{ab}(v)}{\partial v} & B_{ab} &= \langle \Delta v \Delta v \rangle_{ab} = K_{ab} \frac{\partial^2 G_{ab}(v)}{\partial v \partial v} \\ H_{ab}(v) &= \left(1 + \frac{m_a}{m_b}\right) \int dv' \frac{f_b(v')}{|v - v'|} & G_{ab}(v) &= \int dv' f_b(v') |v - v'| & K_{ab} &= \frac{Z_a^2 Z_b^2 e^4 \ln \Lambda_{ab}}{m_b^2} \end{aligned} \quad (A.2.31)$$

The physical meaning of  $A_{ab}$  and  $B_{ab}$ , which we denote by  $\langle \Delta v \rangle_{ab}$  and  $\langle \Delta v \Delta v \rangle_{ab}$  to avoid confusion with magnetic field quantities, becomes apparent if we consider a beam of mono-energetic test particles and Maxwellian field particles with a thermal velocity  $c_b = (T_b / m_b)^{1/2}$ .

$$f_a(v) = \delta(v - v_0) \quad f_b(v) = \frac{n_b}{(2\pi)^{3/2} c_b^3} \exp\left(-\frac{v^2}{2c_b^2}\right) \quad (A.2.32)$$

Inserting these into (A.2.30), we find that  $\langle \Delta v \rangle_{ab}$  and  $\langle \Delta v \Delta v \rangle_{ab}$  determine, respectively, the rates of slowing down and isotropization of the initially mono-energetic test particles by collisions with the background particles; they are often referred to as the coefficients of friction and diffusion in velocity space. Effecting the integrals in (A.2.31) over  $f_b(v)$  of (A.2.32), the Rosenbluth potentials become<sup>[Kra80, Gil82]</sup>

$$\begin{aligned} H_{ab}(v) &= \left(1 + \frac{m_a}{m_b}\right) \frac{n_b}{v} \Phi(\tilde{v}) & G_{ab}(v) &= n_b \left[ \frac{v^2 + c_b^2}{v} \Phi(\tilde{v}) + \frac{c_b}{\sqrt{2}} \Phi'(\tilde{v}) \right] \\ \Phi(y) &= \frac{2}{\sqrt{\pi}} \int_0^y e^{-z^2} dz & \Phi'(y) &= \frac{2}{\sqrt{\pi}} e^{-y^2} & \tilde{v} &\equiv \frac{v}{\sqrt{2}c_b} \end{aligned} \quad (A.2.33)$$

Using these results, we can evaluate the Fokker-Planck coefficients parallel and perpendicular to the test particle velocity  $\mathbf{v}_0$  by evaluating the gradients in (A.2.31) at  $\mathbf{v}=\mathbf{v}_0$ , as required by  $f_s(\mathbf{v})$  of (A.2.32),

$$\begin{aligned}
 <\Delta v_{||}>_{ab} &= K_{ab} \frac{\partial}{\partial v_{||}} H_{ab}(v) \Big|_{v_{||}=v_0} = -n_b K_{ab} \left(1 + \frac{m_a}{m_b}\right) \frac{I}{c_b^2} \Psi(\tilde{v}_0) \\
 <\Delta v_{\perp}>_{ab} &= K_{ab} \frac{\partial}{\partial v_{\perp}} H_{ab}(v) \Big|_{v_{\perp}=0} = 0 \\
 <\Delta v_{||}\Delta v_{||}>_{ab} &= K_{ab} \frac{\partial}{\partial v_{||}\partial v_{||}} G_{ab}(v) \Big|_{v_{||}=v_0} = 2n_b K_{ab} \frac{I}{v_0} \Psi(\tilde{v}_0) \\
 <\Delta v_{\perp}\Delta v_{\perp}>_{ab} &= K_{ab} \left( \frac{\partial}{\partial v^2} - \frac{\partial}{\partial v_{||}\partial v_{||}} \right) G_{ab}(v) \Big|_{v_{||}=v_0} = 2n_b K_{ab} \frac{I}{v_0} [\Phi(\tilde{v}_0) - \Psi(\tilde{v}_0)] \\
 <\Delta v\Delta v>_{ab} &= <\Delta v_{\perp}\Delta v_{\perp}>_{ab} + <\Delta v_{||}\Delta v_{||}>_{ab} = 2n_b K_{ab} \frac{I}{v_0} \Phi(\tilde{v}_0) \\
 \Psi(\tilde{v}) &= \frac{I}{2\tilde{v}_0^2} [\Phi(\tilde{v}_0) - \tilde{v} \Phi'(\tilde{v}_0)]
 \end{aligned} \tag{A.2.34}$$

Plots of  $\Phi$ ,  $\Phi'$  and  $\Psi$  are shown in Fig. A.2.1, and their asymptotic limits are given below,

$$\Phi(\tilde{v}) \rightarrow \frac{2\tilde{v}}{\sqrt{\pi}}, \quad \Psi(\tilde{v}) \rightarrow \frac{2\tilde{v}}{3\sqrt{\pi}}, \quad \tilde{v} \ll 1 \quad \Phi(\tilde{v}) \rightarrow 1, \quad \Psi(\tilde{v}) \rightarrow \frac{I}{\tilde{v}^2}, \quad \tilde{v} \gg 1 \tag{A.2.35}$$

It is useful to normalize the above by defining characteristic times<sup>[Kra80,Gil82]</sup> for slowing down  $\tau^S$ , deflection  $\tau^D$  and energy exchange  $\tau^E$ , which measure the effectiveness of collisions in relaxing the initial test particle distribution,  $f_s(\mathbf{v}, t=0) = \delta(\mathbf{v}-\mathbf{v}_0)$ , towards the equilibrium background distribution  $f_b(\mathbf{v})$ ,

$$\begin{aligned}
 \tau^S &= -\frac{v_0}{<\Delta v_{||}>} \propto \frac{m_b}{m_a + m_b} \cdot \frac{c_b^3}{n_b} \cdot \frac{\tilde{v}_0}{\Psi(\tilde{v}_0)} \\
 \tau^D &= -\frac{v_0^2}{<\Delta v_{\perp}\Delta v_{\perp}>} \propto \frac{c_b^3}{n_b} \cdot \frac{\tilde{v}_0^3}{\Phi(\tilde{v}_0) - \Psi(\tilde{v}_0)} \quad \tilde{v}_0 = \frac{v_0}{\sqrt{2}c_b} = v_0 \left( \frac{m_b}{2T_b} \right)^{1/2} \\
 \tau^E &= -\frac{v_0^2}{<\Delta v\Delta v>} \propto \frac{c_b^3}{n_b} \cdot \frac{\tilde{v}_0^3}{\Psi(\tilde{v}_0)}
 \end{aligned} \tag{A.2.36}$$

Examining the characteristic times with respect to  $v_0$ ,  $n_b$  and  $T_b$ , we can make several observations:

- a) for fixed  $v_0$ , all relaxation processes increase linearly with density  $n_b$ , and decrease with the background temperature as  $T_b^{-3/2}$ ; ∴ hot plasmas approach the collisionless limit.
- b) slowing down is independent of  $v_0$  for  $v_0 \ll c_b$ , falling as  $v_0^{-3}$  for  $v_0 \gg c_b$ .
- c) broadening of the velocity spectrum (isotropization) proceeds slower at higher energies;  $1/\tau^D$  decreases as  $v_0^{-2}$  for  $v_0 \ll c_b$ , and as  $v_0^{-3}$  for  $v_0 \gg c_b$ .
- d) energy exchange decreases as  $v_0^{-2}$  for  $v_0 \ll c_b$ , and as  $v_0^{-5}$  for  $v_0 \gg c_b$

The effect of particle mass on relaxation becomes evident if we define  $\tau_{ab}$  as a relaxation time of test particles of type  $a \in \{i,e\}$  by collisions with field particles of type  $b \in \{i,e\}$ , and relate these to ion and electron characteristic times  $\tau_i$  and  $\tau_e$ , which we write down explicitly for future reference<sup>[Gil82, Boo90]</sup>,

$$\begin{aligned}\tau_e : \tau^D_{ee} : \tau^D_{ei} : \tau^D_{ii} : \tau^D_{ie} &\sim 1 : 1 : 1 : \sqrt{\frac{m_i}{m_e}} : \frac{m_i}{m_e} \\ \tau_e : \tau^E_{ee} : \tau^E_{ii} : \tau^E_{ei} : \tau^E_{ie} &\sim 1 : 1 : \sqrt{\frac{m_i}{m_e}} : \frac{m_i}{m_e} : \frac{m_i}{m_e}\end{aligned}\quad (\text{A.2.37})$$

$$\begin{aligned}\tau_e &= \frac{3\sqrt{m_e} T_e^{3/2}}{4\sqrt{2\pi} e^4 n_e \ln \Lambda_{ee}} & \ln \Lambda_{ee} &= 14.9 - \frac{1}{2} \ln(n_e [10^{20} m^{-3}]) + \ln(T_e [\text{keV}]) \\ \tau_i &= \frac{3\sqrt{m_i} T_i^{3/2}}{4\sqrt{2\pi} Z^4 e^4 n_i \ln \Lambda_{ii}} & \ln \Lambda_{ii} &= 17.3 - \frac{1}{2} \ln(n_i [10^{20} m^{-3}]) + \frac{3}{2} \ln(T_i [\text{keV}])\end{aligned}$$

Clearly, like particle collisions are more effective at transferring momentum and energy, and electrons tend to relax faster than ions. The evolution towards equilibrium proceeds as follows: first, the electrons relax by self-collisions to a Maxwellian  $f_e^M(v; T_e)$  on a timescale  $\tau_e$ ; next, the ions relax by self-collisions to a Maxwellian  $f_i^M(v; T_i)$  on a timescale  $\tau_i \propto (m_i/m_e)^{1/2} \tau_e$ ; lastly, ion-electron collisions relax the two distributions to a common Maxwellian  $f^M(v; T_i = T_e)$  on a timescale  $\tau_{ei}^E \propto (m_i/m_e) \tau_e$ .

### A.3 Braginskii and CGL equations

A complete set of Braginskii transport equations may be found in the NRL Plasma Formulary<sup>[Boo90]</sup>, p.36.

A derivation of the CGL, or double adiabatic, equations may be found in a text by Miyamoto<sup>[Miy78]</sup>, p.141.

#### A.4 Electrostatic Sheath Problem

Historically, the first solution to the problem of plasma-solid contact appears in a now classic paper by Tonks and Langmuir<sup>[Ton29]</sup> (1929). The authors assumed cold, collisionless ions, for which they obtained values  $\phi_s = -0.84$  and  $M_s = 1.14$ .

The case of warm, collisionless ions has been solved analytically by Emmert et al.<sup>[Emm80]</sup> in the limit  $\lambda_D \ll L$ ; we will summarize their results as useful benchmark for further refinements. Their method consists in casting the ion Vlasov equation into kernel form by rewriting the equation in terms of the total energy,  $mv_x^2/2 + eZ\phi(x)$ , which is an integral of motion, and choosing the source kernel so as to produce a Maxwellian  $f(x, v_x)$  in the absence of potential gradients. The Vlasov equation is integrated in space and energy to yield  $n_i(x)$ , which together with  $n_e(x)$  given by (2.2.3), form an integral-differential equation for the potential  $\phi(x)$ . The authors solved this equation analytically, with the result expressed as a transcendental equation for  $\psi_s \equiv e\phi_s / T_e$  and the parameter  $\zeta = ZT_e / T_i > 0$ ,

$$\frac{2}{\sqrt{\pi\zeta}} \exp[-(1+\zeta)\psi_s] D(\psi_s) + \operatorname{erf}(\sqrt{\zeta}\psi_s) - 1 = 0 \quad D(y) = \int_0^y e^{t^2} dt \quad (A.4.1)$$

$$\psi_s \rightarrow 0; \zeta \rightarrow 0 \quad \psi_s(1) \approx 0.4 \quad \psi_s(3) \approx 0.2 \quad \psi_s \rightarrow 0.854; \zeta \rightarrow \infty$$

The normalized sheath voltage  $\psi_s(\zeta)$  was found to increase monotonically with the ratio  $\zeta$  from 0 for cold electrons, to 0.854 for cold ions. The normalized surface potential  $\psi_0$ , the ion particle flux  $\Gamma_0$  and the power flux for ions  $q_{is}$  were expressed in terms of the sheath potential,

$$\psi_0 = -\ln \left[ \sqrt{\frac{m_i Z}{m_e 4\pi}} \frac{1}{Z + T_i / T_e} \frac{\pi}{2 \exp(-\psi_s) D(\psi_s^{1/2})} \right] \quad (A.4.2)$$

$$\Gamma_0 = \frac{n_0}{Z} \left( \frac{T_i}{2\pi m_i} \right)^{1/2} \frac{4}{Z} \sqrt{\frac{\zeta}{\pi}} \left( 1 + \frac{1}{\zeta} \right) \exp(-\psi_s) D(\psi_s^{1/2}) = \frac{n_0}{Z} \left( \frac{T_i}{2\pi m_i} \right)^{1/2} \beta_i$$

$$q_i = T_i \Gamma_0 \left( 2 - \zeta \frac{\psi_s^{1/2}}{\exp(-\psi_s) D(\psi_s^{1/2})} \right) = 2T_i \Gamma_0 \mu_i$$

The asymptotic limits of the dimensionless functions  $\beta_i$  and  $\mu_i$  are given below,

$$\beta_i \rightarrow \infty; \zeta \rightarrow 0 \quad \beta_i(1) \approx 2.3 \quad \beta_i \rightarrow 2.0; \zeta \rightarrow \infty \quad (A.4.3)$$

$$\mu_i \rightarrow \infty; \zeta \rightarrow 0 \quad \mu_i(1) \approx 1.15 \quad \mu_i \rightarrow 1.0; \zeta \rightarrow \infty$$

Comparing the above results with the ion particle and energy fluxes calculated for a half-space Maxwellian, we see that  $\beta$  and  $\mu$  represent enhancement factors due to the presence of the sheath. They are not sensitive to the electron temperature as long as  $T_i > ZT_e$ ; the ion flux is enhanced even when  $T_i \gg ZT_e$ .

The above formulation was extended<sup>[Sch88]</sup> for weakly collisional ions by including a BGK collision operator in the ion kinetic equation,

$$C_{ii} = \frac{f_{i,0} - f_i}{\tau_i} \quad f_{i,0}(x, v_x) = n_0(x) \left( \frac{m_i}{2\pi T_0(x)} \right)^{1/2} \exp \left( -\frac{m_i}{2\pi T_0(x)} (v_x - v_0(x))^2 \right) \quad (A.4.4)$$

Like-particle collisions do not affect the 0<sup>th</sup>, 1<sup>st</sup> and 2<sup>nd</sup> velocity moments of  $f_i(v_x)$ ; by imposing these constraints on the BGK operator, the shifted Maxwellian parameters  $n_0(x)$ ,  $v_0(x)$ ,  $T_0(x)$  were related to the actual ion distribution  $f_i(x, v_x)$ . The ion density  $n_i(x)$  was once again expressed in terms of integrals over space and energy, and consequent quadratures were evaluated numerically (stable solutions were found only for the case of weak collisionality,  $\lambda_i \sim L$ ). The effect of collisions on the potentials and fluxes into the sheath, was minimal. Whether this insensitivity to self-collisions would persist for  $\lambda_i \ll L$  is not clear. However, since self-collisions only effect the shape and not the averages over the distribution, we would expect the lower moments to be less altered than the higher ones; in fact, the only significant difference between the two models was a 10% increase of the ion heat flux  $q_i \sim m <V^2 V_x>$ .

The same authors investigated the effect of strong ion-ion collisionality<sup>[Sch90]</sup>, using a set of fluid-like moment equations equivalent to a simplified form of the drift-kinetic moment equations (2.1.22), with  $\mathbf{V} = \mathbf{v} - \mathbf{u}$  =  $\mathbf{v} - <\mathbf{v}_x>\mathbf{i}_x$ ,  $<\mathbf{v}_y> = <\mathbf{v}_z> = 0$ ,

$$\begin{aligned} \frac{\partial}{\partial x} n u &= S_0 & \frac{\partial}{\partial x} n \left( u^2 + <V_x^2> + \frac{T_e}{m_i} \right) &= 0 & S_0(x) &= n <S(x, v)> & (A.4.5) \\ \frac{\partial}{\partial x} n m_i \left( \frac{1}{2} u^3 + \frac{3}{2} u <V_x^2> + u <V_y^2> + \frac{L}{2} <V_x^3> \right) &= S_e - u \frac{T_e}{m_i} \frac{\partial n}{\partial x} & S_e(x) &= n <\frac{L}{2} m_i v^2 S(x, v)> \end{aligned}$$

where  $<\dots>$  denotes an average over  $f(\mathbf{v})$ . The above equations are not valid in the sheath itself, since quasi-neutrality was assumed in their derivation, but are relatively accurate up to the sheath edge. Two sets of closure relations were proposed: a) in the collisionless limit, perpendicular energy was taken as constant,  $<V_y^2> = T_y / m_i$  and the flow was assumed adiabatic,  $<V_x^3> = 0$ ; the latter condition was supported by a comparison with previous kinetic results from which the contribution of  $<V_x^3>$  to the total ion heat flux was found to be small. b) in the fully collisional limit, the velocity distribution was assumed isotropic in the frame moving with the velocity  $u$ , hence  $<V_y^2> = <V_x^2>$  and once again  $<V_x^3> = 0$ . Using the above relations two sets of moment equations were obtained. Rather than stating these explicitly, we compare their point of sonic transition, that is the singularity in  $du/dx$ . The collisionless and collisional sound speeds are thus found as,

$$c_s = \left( 3 <V_x^2> + \frac{T_e}{m_i} \right)^{1/2} \quad \lambda_i \gg L_u \quad c_s = \left( \frac{5}{3} <V_x^2> + \frac{T_e}{m_i} \right)^{1/2} \quad \lambda_i \ll L_u \quad (A.4.6)$$

indicating that ion collisions reduce the flow velocity at the sheath edge (assumed to be sonic). The moment equations were solved for  $T_y = T_e$  and the two source distributions:  $S_1(x, v; T_e)$ , corresponding to an isotropic

Maxwellian ionization source, and  $S_2 = S_1 v_x$ , which provides no particles with zero velocity. Since stagnant ions must be accelerated to  $u \sim c_s$  by the E-field, the sheath potential for  $S_1$  is larger than for  $S_2$ .

A similar analysis was performed for ion-neutral collisions, by allowing the BGK operator to alter energy and momentum densities<sup>[Sch90]</sup>. In this case, wall and sheath potentials increased, with the potential drop across the sheath remaining fairly constant; particle and energy fluxes into the sheath were reduced. Very strong ion-neutral collisionality was investigated kinetically by Riemann<sup>[Rie94]</sup>, with the assumption of cold ions,  $T_i = 0$ . Similar effect on potentials and fluxes was observed; in addition, the ion velocity distribution at the sheath edge was significantly broadened by neutral collisions, with a width of the order of  $T_n$ .

The various treatments of non-magnetized ion flow into the electrostatic sheath are reviewed in a recent article<sup>[Rie96]</sup>. Comparing the normalized fluxes and potentials, Table.A.4.1, and the shapes of  $f_i(v)$  at the sheath edge, Fig.A.4.1, we note a surprising robustness of the estimated values over a wide range of modeling assumptions; this insensitivity justifies the use of simplified expressions for the heat transmission coefficients (at least in the context of edge plasma modeling).

## A.5 Tokamak Core Plasma

This appendix is intended as a short preface to tokamak physics, in which the basic physical processes, experimental findings, and technical problems are outlined. The idea of a 'short preface' to such an extensive field as tokamak research may strike the reader as both audacious and ludicrous. To appease his anger, we make our aim explicit: certain physical processes play an essential role in our region of interest -- the tokamak edge plasma -- and these are most simply discussed in the context of tokamak physics at large. Those areas which have little bearing on our analysis, such as plasma heating or wave propagation, receive only a passing mention.

### A.5.1 MHD equilibrium

The term *Tokamak* is a Russian acronym for *toroidal-chamber-magnetic-coil*; it refers to a family of toroidal plasma devices in which the toroidal magnetic field, generated by external current carrying coils, is stronger than magnetic fields generated by plasma currents, Fig. A.5.1. A schematic of the dominant tokamak fields and currents may be stated as follows:

$$\begin{array}{lll} \text{poloidal coil current, } j_\theta^{\text{coil}} & \Rightarrow & \text{toroidal magnetic field, } B_\phi \\ \text{toroidal plasma current, } j_\phi & \Rightarrow & \text{poloidal magnetic field, } B_\theta \end{array} \quad (A.5.1)$$

where the  $j_\theta^{\text{coil}}$  is held constant, sometimes in super-conducting coils, while  $j_\phi$  is induced in the plasma either by an external transformer circuit, the traditional method, or by current drive systems based on non-linear wave absorption, neutral beam injection, or self-induced (bootstrap) plasma current<sup>[Wes97]</sup>. Calculation of the equilibrium  $\mathbf{B}$ -field (or rather the field-plasma system) is simplified by treating the ions and electrons as a single fluid. Starting from the Braginskii transport equations (A.3.1), we add the electron and ion equations for mass and momentum transport assuming quasi-neutrality, and replace the energy transport equations by an adiabatic closure relation,  $p \propto \rho^\gamma$ ,  $\gamma = 5/3$ . Combining the above with Maxwell's equations (A.2.4), we arrive at the equations of magneto-hydro-dynamics (MHD)<sup>[Miy78]</sup>.

$$\begin{array}{lll} \frac{dp}{dt} + \rho \nabla \cdot \mathbf{v} = 0 & \nabla \cdot \mathbf{B} = 0 & \nabla \times \mathbf{B} = \mathbf{j} \\ \rho \frac{dv}{dt} + \nabla p = \mathbf{j} \times \mathbf{B} & \nabla \cdot \mathbf{E} = 0 & \nabla \times \mathbf{E} = -\frac{\partial \mathbf{B}}{\partial t} \\ \frac{dp}{dt} + \gamma p \nabla \cdot \mathbf{v} = 0 & \mathbf{E} + \mathbf{v} \times \mathbf{B} = \eta_e \mathbf{j} & \frac{d}{dt} = \frac{\partial}{\partial t} + \mathbf{v} \cdot \nabla \end{array} \quad (A.5.2)$$

If collisions are neglected entirely, the resistivity  $\eta_e$  becomes zero, and the model is known as ideal MHD. The MHD approximation is valid for global plasma behaviour, that is plasma evolution on length and time scales much longer than those characterizing microscopic processes,  $\lambda \gg (\lambda_D, r_L)$ , and  $\omega \ll (\omega_p, \omega_c)$ . In time

dependent form, it may be used to study a variety of plasma waves with  $k = 2\pi/\lambda$  and  $\omega$  in the above range: broadly speaking, electromagnetic waves (highly non-isotropic with respect to  $\mathbf{B}$ , and exhibiting cut-offs and resonances due to particle gyration), pseudo-acoustic waves (differing for ions and electrons due to  $m_i/m_e \gg 1$ ) and field-inertial or drift waves (such as the Alven wave  $\parallel \mathbf{B}$  coupling ion inertia and  $\mathbf{B}$ -field tension)<sup>[St62]</sup>. In steady state form, the MHD approximation may be used to find the equilibrium state of the field-plasma system<sup>[Fri87, Bal85]</sup>.

So far we have worked in generalized co-ordinates; to proceed further we must select a co-ordinate system appropriate to the tokamak geometry. The toroidal-Cartesian co-ordinates ( $R, Z, \phi$ ) may serve as one such reference frame; here  $R$  is the distance from the major axis of the torus,  $Z$  is the vertical distance from the mid-plane, and  $\phi$  is the toroidal angle. Assuming toroidal symmetry at the outset,  $\partial/\partial\phi=0$ , the  $\nabla \cdot \mathbf{B} = 0$  condition allows us to write the poloidal component of  $\mathbf{B}$  as a gradient of some function  $\psi$ ,

$$\mathbf{B} = B_\phi \hat{i}_\phi + \nabla\psi \times \nabla\phi = B_\phi R \nabla\phi + \nabla \times (\psi \nabla\phi) \quad (A.5.3)$$

Magnetic field lines form surfaces of constant  $\psi$ , which is related to the poloidal magnetic flux cutting across an equatorial ring  $\mathfrak{R} = \{Z=0, R_1 < R < R_2\}$  by the integral<sup>[Miy78]</sup>,

$$\psi_\theta = \int_{\mathfrak{R}} \nabla \times (\psi \nabla\phi) \cdot dA = \int_{\partial\mathfrak{R}} \psi \nabla\phi \cdot dl = 2\pi(\psi_2 - \psi_1) \quad (A.5.4)$$

For this reason it is known as the flux function, and the surfaces of constant  $\psi$  as flux surfaces. Examining the components of the pressure equation,  $\mathbf{j} \times \mathbf{B} = \nabla p$ , along  $\mathbf{B}$ ,  $\mathbf{j}$  and  $\nabla\psi$ , we conclude that pressure is constant along a flux surface,  $\mathbf{B} \cdot \nabla p = 0$ , and current flow is co-planar with the flux surface,  $\mathbf{j} \cdot \nabla p = 0$ . We separate the current density into toroidal and poloidal components,

$$\mathbf{j} = \nabla \times \mathbf{B} = \nabla \times (RB_\phi \nabla\phi + \nabla\psi \times \nabla\phi) = \nabla(RB_\phi) \times \nabla\phi + (R^2 \nabla \cdot \frac{\nabla\psi}{R^2}) \nabla\phi \quad (A.5.5)$$

The poloidal current passing the same ring  $\mathfrak{R}$  is related to  $RB_\phi = \Phi$ ,

$$I_\theta = \int_{\mathfrak{R}} \nabla \times (\Phi \nabla\phi) \cdot dA = \oint_{\partial\mathfrak{R}} \Phi \nabla\phi \cdot dl = 2\pi(\Phi(\psi_2) - \Phi(\psi_1)) \quad (A.5.6)$$

Finally, taking a scalar product of  $\mathbf{j}$  and  $\nabla\psi$ , and using  $\mathbf{j} \cdot \nabla p = \mathbf{j} \cdot \nabla\psi = 0$  we obtain a non-linear, elliptic differential (Grad-Shafranov) equation<sup>[Gra59, Sch57]</sup>, relating  $\psi$  and the two flux functions  $p(\psi)$  and  $\Phi(\psi)$ .

$$(R^2 \nabla \cdot \frac{\nabla}{R^2})\psi + R^2 \frac{dp}{d\psi} + \Phi \frac{d\Phi}{d\psi} = 0 \quad (A.5.7)$$

In practice it is useful to transform this equation into flux co-ordinates ( $r, \theta, \phi$ ). Here we choose the first ordinate as a flux-surface minor radius (radial distance away from the poloidal center),  $r = r(\psi)$ , and denote its value at the last closed flux surface (LCFS) by  $r_{LCFS}$ . The second ordinate  $\theta$  is the poloidal angle; alternatively we could have chosen the poloidal distance along a flux surface,  $s$ , or the distance along  $\mathbf{B}$ ,  $s_\parallel$ . Using the generalized variable relations of §A.3, we obtain expressions for the Jacobian  $J$ , metric tensor  $g_{\alpha\beta}$ , line element  $dx^2$  and the gradient operator  $\nabla$  in the new frame<sup>[deB94]</sup>.

$$dx^2 = g_{rr} dr^2 + 2g_{r\theta} dr d\theta + g_{\theta\theta} d\theta^2 + g_{\phi\phi} d\phi^2 \quad J = \frac{R}{|\nabla r|} \frac{ds_\parallel}{d\theta} \quad (A.5.8)$$

$$g_{rr} = \frac{J^2}{R^2} |\nabla \theta|^2 \quad g_{r\theta} = -\frac{J^2}{R^2} \nabla \theta \cdot \nabla r \quad g_{\theta\theta} = \frac{J^2}{R^2} |\nabla r|^2 \quad g_{\phi\phi} = R^2$$

which allow us to write the Grad-Shafranov equation in terms of flux co-ordinates,

$$\frac{R^2}{J} \frac{d\psi}{dr} \left[ \frac{\partial}{\partial r} \left( \frac{g_{\theta\theta}}{J} \frac{d\psi}{dr} \right) - \frac{\partial}{\partial \theta} \left( \frac{g_{r\theta}}{J} \right) \frac{d\psi}{dr} \right] + R^2 \frac{dp}{dr} + \Phi \frac{d\Phi}{dr} = 0 \quad (A.5.9)$$

To solve the Grad-Shafranov equation in either form, additional constraints are required. In practice, a number of alternatives are present<sup>[Wer97]</sup>: a) specifying  $\psi$  on some flux surface, or the poloidal shape of any flux surface, b) taking the coil current distribution as given, and iterating the plasma current distribution with successive solutions, c) taking account of direct measurements of  $B_\theta$  near the edge of the plasma, and similarly iterating the solution. Specialized numerical solvers are routinely employed to generate such magnetic equilibria; the calculated magnetic field  $\mathbf{B}(r, \theta, \phi)$  provides the substrate for plasma transport calculations; typical poloidal contours of  $\mathbf{B}$  and radial profiles of  $B_\theta, j_\theta$  and  $p$  are shown in Fig. A.5.2.

As a final comment, we note that on a given flux surface field lines may not cross each other due to the vanishing divergence of  $\mathbf{B}$ ; the ratio of toroidal to poloidal revolutions of a field line is therefore constant for a flux surface, and we denote this quantity, known as the safety factor due to its importance for global plasma stability<sup>[Miy78]</sup>, by  $q(\psi)$ ,

$$q(\psi) = \frac{I}{2\pi} \int_0^{2\pi} \frac{d\phi}{d\theta} d\theta = \frac{I}{2\pi} \oint \frac{B_\phi}{B_\theta} \frac{ds_\parallel}{R} \quad (A.5.10)$$

Flux surfaces with rational values of  $q$ , that is with  $m = q \cdot n$ , where  $m$  and  $n$  are both integers, are known as resonant surfaces; on these surfaces field lines return to their original poloidal location after  $m$  toroidal and  $n$  poloidal revolutions (we shall retain this convention when discussing plasma instabilities with wave number  $\mathbf{k} = mi_\phi + ni_\theta$ ). Flux surfaces with irrational values of  $q$ , contain field lines ergodically accessing the entire flux surface, returning to their initial location only after an infinite number of revolutions.

### A.5.2 MHD Instabilities

In deriving the Grad-Shafranov equation, steady state was assumed,  $\partial/\partial t = 0$ . Temporal evolution of the resulting equilibria would reveal their stability properties. To this effect, the time-dependent MHD equations are subjected to two types of perturbation analysis<sup>[Bau85]</sup>:

a) variational energy analysis, based on the fact that dynamical systems evolve in such a way as to minimize their potential energy; if a perturbation is found to lower the net potential energy of both field and plasma, as calculated from the MHD equations, the equilibrium is unstable;

b) eigen-mode analysis, in which the linearized MHD equations are treated as an eigen-system, usually separable in the toroidal and poloidal directions with  $\mathbf{k} = m\hat{\mathbf{e}}_\theta + n\hat{\mathbf{e}}_\phi$ , which yields eigen-functions (modes) and their eigen-frequencies; if the imaginary part of the frequency is positive, the mode is expected to grow, destabilizing the equilibrium.

We restrict ourselves to merely summarizing the results of such analysis, which for many years formed the very heart of the fusion effort. Most generally, MHD instabilities are driven either by radial gradients in the current distribution,  $dj(r)/dr$ , or by radial pressure gradients in regions of convex field curvature,  $dp(r)/dr$ ; they are stabilized by the tension and compressibility of the magnetic field lines, in other words by the B-field energy,  $B^2/8\pi$ . The dominant destabilizing modes and the constraints they place on the equilibrium plasma are listed below<sup>[Wes97]</sup>:

- a) ideal kink modes  $\Rightarrow q(0) > 1.0, q(r_{LCFS})/q(0) > 2.0$
- b) resistive kink (tearing) modes  $\Rightarrow q(0) > 1.0, q(r_{LCFS})/q(0) > 2.0$
- c) ballooning (pressure) modes  $\Rightarrow S \equiv (r/q)(dq/dr) > S_{\min}$   
 $\beta \equiv p/(B^2/8\pi) < \beta_{\max} \sim 0.15r_{LCFS}/(Rq(r_{LCFS}))$
- d) vertical mode  $\Rightarrow B_z \text{ adjusted via active feedback}$

Kink modes<sup>[Wes78]</sup> lead to twisting of the plasma column, as defined by the flux surface; they are strongest at long wavelengths (at low mode numbers  $n,m$ ), originate on flux surfaces resonant with the mode, and are driven primarily by  $dj(r)/dr$ . Tearing modes<sup>[Fur73]</sup> are the resistive equivalent of the kink modes, and are driven by the same mechanism; both of these modes grow when  $B_\theta$  is weaker than  $B_\phi$  anywhere in the plasma, or less than twice  $B_\phi$  at the edge (we shall examine the reasons for this shortly). Ballooning modes<sup>[Con78]</sup>, driven by gradients in the plasma pressure  $dp(r)/dr$ , occur locally on the convex side of the field; they are stabilized when the change of magnetic field pitch angle, often termed the magnetic shear,  $S = (r/q)(dq/dr)$ , is sufficient to oppose the interchange instability; they also place a limit on the ratio of plasma to magnetic pressure,  $\beta$ <sup>[Tro84]</sup>. Finally, the vertical or axi-symmetric mode is important for strongly non-circular poloidal cross-sections, but it may be stabilized by a vertical field from external current carrying control coils.

It is worthwhile to explore the consequences of finite plasma resistivity in more detail. In complete analogy to the analysis of invariant tori manifolds in classical mechanics, the resonant surfaces are more susceptible to the onset of chaos<sup>[Arn89]</sup>, Fig. A.5.3; according to the Kolmogorov-Arnold-Moser (KAM) theorem<sup>[Arn89]</sup>, when non-linear perturbations are introduced into a dynamically conservative system, invariant

tori (representing the integrals of motion) initially break up into islands on the resonant surfaces (the number of islands per surface determined by the periodicity of the torus, each island following a helical trajectory around the torus), then into bounded ergodic volumes, which grow with the strength of the perturbation, eventually filling the entire island region as well as linking all the islands into a continuous ergodic volume. Therefore, a region initially composed of a resonant (non-ergodic) surface, bounded on either side by ergodic surfaces, is transformed into a completely ergodic volume; the initial 2-1-2 topology is destroyed in favour of 3-3-3, where spatial degrees of freedom are indicated. The regions in which the volumetric ergodicity first appears are the X-points of the islands and the separatrix which defines them<sup>[Arn89]</sup>. All of the above features apply directly to the magnetic flux surfaces in a tokamak; magnetic islands have indeed been observed in tokamaks using tomographic techniques<sup>[Gr88]</sup>. The non-linear perturbations responsible for topology breaking may be caused by a) finite resistivity, leading to E fields along current flows, hence E×B drifts, b) oscillations due to MHD modes/waves, c) any kinetic process not included in the ideal MHD picture, eg. plasma interaction with neutral beams, pellet injection, fast particles, etc. The resulting changes to the magnetic topology have consequences for both stability and transport, and conspire to make the tokamak plasma one of the most complicated dynamical systems ever studied.

Quasi-linear analysis of MHD equations reveals that islands grow in response to  $d\psi(r)/dr$  and saturate due to magnetic field line diffusion<sup>[Wh77]</sup>. A perturbation in the form of a radial magnetic field  $B_r$  with wave number  $k = mi_\theta + ni_\phi$  leads to an island of width  $\Delta r$ ,

$$\Delta r = 4 \left( \frac{rB_r}{mL_{\nabla q} B_\theta} \right)^{1/2} \quad L_{\nabla q} \equiv \left( \frac{I}{q} \frac{dq(r)}{dr} \right)^{-1} \quad (A.5.11)$$

with the expression evaluated at the location of the fractured magnetic surface; note the inverse scaling with mode number ( $m=2$  is usually dominant). It follows from the MHD equations (A.5.2), that the radial B-field diffuses due to finite resistivity  $\eta_e$ ,

$$\frac{\partial B_r}{\partial t} = 4\pi\eta_e \nabla_r^2 B_r \quad (A.5.12)$$

which allows us to estimate the saturated island width as the solution of the following expression<sup>[Syk81]</sup>

$$\left( \frac{1}{\psi} \frac{d\psi}{dr} \right)_{r_i + \Delta r_i / 2} - \left( \frac{1}{\psi} \frac{d\psi}{dr} \right)_{r_i - \Delta r_i / 2} = \alpha_r \Delta r_s \quad \psi = \frac{irB_r}{m} \quad (A.5.13)$$

where  $\alpha_r$  is constant, and the characteristic growth time as

$$\tau_w \sim 0.1 \left( \frac{\Delta r_s}{r_{LCFS}} \right) \tau_\eta \sim 0.1 \left( \frac{4\pi \cdot \Delta r_s \cdot r_{LCFS}}{\eta_e} \right) \quad (A.5.14)$$

where  $\tau_\eta$  is the characteristic resistive time. At larger perturbations, chaotic behaviour begins, that is field lines are no longer constrained to particular surfaces but access the bordering volume region ergodically; these regions appear first near resonant surfaces and grow as the strength of the perturbation increases.

The change in magnetic topology is believed to play a key role in two tokamak instabilities, known colloquially as sawteeth and disruptions<sup>[Wer97]</sup>. Sawteeth are oscillations of  $n_e$  and  $T_e$  near the center of the plasma; they have been linked to an  $m=n=1$  mode occurring whenever a  $q=1$  surface exists in the plasma. In one sawtooth period,  $j_\phi(r)$ ,  $T_e(r)$ , and  $n_e(r)$  evolve until a  $q=1$  surface is formed and the instability commences, quickly destroying the surface; the effective constraint on the  $q(r)$  profile is that  $q(0) > 1.0$ . The exact process of the fast phase of this instability is still uncertain, but magnetic reconnection leading to the transfer of energy between a hot, inner region and a cold, outer region is the preferred explanation<sup>[Mir93]</sup>.

Sawteeth oscillation are for the most part benign modulations of core density and temperature; disruptions on the other hand are spectacular instabilities leading to complete destruction of equilibrium<sup>[Wer89,97]</sup>. The plasma current is entirely quenched, the plasma pushed onto the vessel wall, causing large heat fluxes, eddy currents and mechanical stresses (via  $j \times B$  forces). Our understanding of disruptive phenomena is still far from complete, but the sequence of events leading to a disruption and the mechanisms involved at each stage are now fairly clear. Briefly, disruptive instabilities begin with a gradual growth of the  $m=2$  resistive kink mode, and terminate with a critical multi-mode island reconnection causing strong ergodization of the core plasma, rapid flattening of  $j(r)$  and complete loss of confinement. The onset of the  $m=2$  resistive kink mode coincides with the overlap between a  $q=2$  surface and a region of steep negative current gradient,  $dj(r)/dr < 0$ , usually near the edge of the plasma. This is brought about by,

- a) an increase in the current which causes the  $q=2$  surface to move outward (the central  $q$  value can not exceed unity due to sawteeth oscillations via the  $m=1$  resistive kink mode),
- b) radiative cooling of the outer core, which increases local resistivity  $\eta_e$ , contracts the current profile  $j(r)$ , and moves the steep current gradient region inward towards the  $q=2$  surface.

The stability limits imposed by the two cases are  $q(r_{LCFS}) > 2$  and  $10^{19}(nR/B) > q(r_{LCFS})$ , respectively; the latter criterion, known as the Greenwald density limit, places a lower limit on edge density  $n(r_{LCFS})$  (despite the fact that it is usually expressed in terms of the flux-average density  $\langle n \rangle = \int n r dr / \int r dr$ ) and constitutes the most important operational incentive for modeling the tokamak edge plasma.

The evolution of the  $m=2$  resistive kink mode involves growth and ergodization of magnetic islands on the  $q=2$  surface; the measured radial magnetic field  $B_r$  allows us to estimate the width of the  $m=2$  islands at the time of current collapse using the expression for the island width  $\Delta r$  (A.5.11). This width is found to reach a value of  $\sim 0.2r_{LCFS}$ . Why the fast phase sets in at this relatively low value is not clear, but an interaction between ergodized islands of different resonant surfaces which grow until the ergodized regions begin to overlap and merge (that is when the island widths are comparable in size to the separation between surfaces), offers a likely explanation; the process may be described as a critical topological phase transition. In the fully ergodized

plasma, radial gradients are removed on the timescale of parallel transport and rapid loss of confinement follows.

### A.5.3 Kinetic Instabilities and Transport $\perp \mathbf{B}$

In the last section, we saw that even a relatively simple (single fluid or MHD) description of the tokamak plasma predicts complicated global behaviour. In reality, local variations of  $f_i(\mathbf{x}, \mathbf{v})$  and  $f_e(\mathbf{x}, \mathbf{v})$  do not conform to the constraints of the MHD model, but evolve according to the kinetic equations, (2.1.1). In this section we will consider phenomena arising from the kinetic equations, in particular modes with  $k$  and  $\omega$  on the order of the microscopic scale and time lengths,  $\lambda \sim \min(\lambda_D, r_L)$  and  $\omega \sim \max(\omega_p, \omega_c)$ .

Kinetic modes, also called micro-instabilities, may be categorized according to the fields involved (electrostatic vs. electromagnetic), the oscillating particles (ions vs. electrons), the particle trajectory in a tokamak geometry (trapped vs. free), the degree of collisionality (collisionless vs. collisional), in short by the type of kinetic wave from which the mode originates<sup>[Tan78]</sup>. Micro-instabilities are typically investigated by subjecting a quasi-linearized kinetic equation to small perturbations; in order to determine the saturation level of a given mode, fully non-linear calculations are required. The reader may find it useful to consult a recent review of tokamak micro-instabilities in order to appreciate the full complexity of the problem<sup>[Con94]</sup>. As an example, we can consider the micro-tearing mode, which is a kinetic analogue of the MHD-tearing (resistive) mode discussed in the previous section. Quasi-linear analysis reveals that high-m resonant surfaces dissociate into small scale magnetic islands in regions of strong  $T_e$  gradients and intermediate collisionality; the island saturation width for  $\Delta r_s > r_L$  is determined by the influence of the island on local transport. The process is a microscopic equivalent to large-scale ergodization, and has been proposed as one explanation for the disruptive collapse.

Micro-instabilities have a dramatic effect upon cross-field plasma transport, which we shall consider briefly. According to classical theory, §A.3, cross-field fluxes arise due to un-like particle collisions  $C_{ab}$  and radial gradients of  $f_i(\mathbf{x}, \mathbf{v})$ , that is  $\nabla_\perp(n, \mathbf{u}, T)$ ; classical cross-field transport coefficients of §A.3 correspond to a diffusive process with radial step  $r_L \propto 1/B$ , (A.2.5), and collision frequency  $\tau_a^{-1}$ , (A.2.37),

$$(\zeta^{a\perp})_{cl} \propto \frac{r_L \omega_a^2}{\tau_a} \quad \left( \frac{\zeta^{a\perp}}{\zeta^{a\parallel}} \right)_{cl} \propto \frac{1}{(\omega_{ca}\tau_a)^2} \propto \frac{1}{B^2} \quad \begin{aligned} \zeta &\in \{D, \eta, \chi\} \\ a &= \{i, e\} \end{aligned} \quad (A.5.15)$$

Since collision frequencies are much smaller than gyration frequencies ( $\omega_{ca}\tau_a \gg 1$ ), we expect cross-field transport to be much slower than transport parallel to  $\mathbf{B}$  ( $\zeta_\perp \ll \zeta_\parallel$ ). In toroidal geometry, for which  $B_\phi \propto 1/R$ , and low collisionality, the CGL equations predict that some of the particles become trapped in elongated, banana shaped orbits<sup>[Miy78]</sup>. The radial width of such an orbit may be considered as the radial diffusive step, leading to the so called neo-classical estimates<sup>[Cha86]</sup>,

$$\frac{(\zeta^a)_\text{neo}}{(\zeta^a)_\text{cl}} \propto q^2 \epsilon_r^{-3/2} > 1 \quad \epsilon_r = \left( \frac{r}{R} \right) < 1 \quad (A.5.16)$$

It should be noted that aside from a geometrical enhancement factor, the dependence on  $\mathbf{B}$  is unaffected. For stronger collisionality, the neo-classical enhancement is less profound since a particle is likely to suffer a collision before completing the banana orbit. Another mechanism leading to an increase in radial transport is particle trapping due to toroidal asymmetries or ripples in the magnetic field, caused by finite spacing between field coils. It leads to an expression<sup>[Kov84]</sup>,

$$\frac{(\zeta^a)_\text{ripple}}{(\zeta^a)_\text{cl}} \propto \left( \frac{v_a \tau_a}{R} \right)^2 \left( \frac{\Delta B}{B} \right)_\text{ripple} \quad (A.5.17)$$

Needless to say, experimentally extracted values of  $\zeta_\perp$ , that is particle ( $D^i_\perp, D^e_\perp$ ) and energy ( $\chi^i_\perp, \chi^e_\perp$ ) diffusivities disagree quite sharply with the above estimates; the inferred cross-field transport appears stronger by as much as two orders of magnitude, with the discrepancy being larger for electrons than for ions. The observed dependence on the magnetic field is much weaker, roughly linear rather than quadratic,  $\zeta_\perp \propto 1/B$ ; this is known as the Bohm scaling<sup>[Cen77]</sup>,

$$(\zeta^a)_\text{Bohm} \propto r_{La} \omega_{ca} \propto \frac{T_a}{Z_a B} \quad (A.5.18)$$

The search for the underlying transport mechanism is complicated by the difficulty of obtaining an expression which would successfully reproduce experimental data under all operating conditions. In fact, the accepted working procedure has been to extract global particle and energy confinement times rather than local transport coefficients. It is now generally believed that plasma turbulence, driven by locally saturated micro-instabilities, is responsible for the greater part of the observed cross-field transport<sup>[Woo90, Con94]</sup>. The strongest evidence for this claim are measured correlations between  $\zeta_\perp$  and plasma-field fluctuations,  $\delta n, \delta T, \delta E, \delta B$ .

Fluctuations in the local electric field give rise to a fluctuating  $\mathbf{E} \times \mathbf{B}$  drift velocity  $\delta \mathbf{v}_\perp$ . If correlated with  $(\delta n, \delta T)$ , that is if  $(n, T)$  fluctuate with the same frequency as  $\delta \mathbf{v}_\perp$ , their relative phase determines the direction and magnitude of the cross-field fluxes ( $\Gamma_\perp, q_\perp$ ); we note that  $(\nabla_\perp n, \nabla_\perp T)$  produce fluctuations  $(\delta n, \delta T)$  correlated in-phase with  $\delta \mathbf{v}_\perp$ , and fluxes ( $\Gamma_\perp, q_\perp$ ) in the direction opposite to the gradients<sup>[Luc85]</sup>. We define these fluxes as averages over some time  $\tau'$  longer than the fluctuation period  $\omega^{-1}$  but shorter than the macroscopic time scale  $\tau_{\partial U}$ .

$$\delta v_{\perp} = \frac{\delta E \times B}{B^2} \cdot \hat{i}_r \quad \left\{ \frac{I}{q_{\perp}} \right\}(t) = \frac{1}{\tau_k} \int_{t-\tau'}^t \delta v_{\perp} \left\{ \frac{\delta n}{\frac{1}{2} T \delta n + \frac{3}{2} n \delta T} \right\} dt' \quad \tau_{\text{av}} \gg \tau' \gg \omega^{-1} \quad (A.5.19)$$

The diffusion coefficient may be estimated in terms of Fourier components of the fluctuations<sup>[Kad65,Wes97]</sup>,

$$\delta v_k = -\frac{k_{\perp} \delta \varphi_k}{B} \quad D_k = \frac{(\delta r_k)^2}{\tau_k} = \frac{(\delta v_k \tau_k)^2}{\tau_k} = \left( \frac{k_{\perp} \delta \varphi_k}{B} \right)^2 \tau_k \quad (A.5.20)$$

where  $\tau_k$  is the correlation time of the  $k$ -th component of the fluctuation. For small amplitudes, the fluctuations are likely to be decorrelated due to parallel thermal motion  $\tau_{k,a} \sim 1/k_{\parallel} c_a$ , drift motion  $\tau_k \sim 1/\omega^{\text{drift}}$ , or collisions  $\tau_k \sim 1/\omega_{ab}$ ; for large amplitudes, decorrelation occurs as a result of cross-field motion itself, with  $\tau_k \sim 1/k_{\perp} \delta v_k$ . In other words, at high amplitude  $D_{\perp}$  exhibits the Bohm-like,  $1/B$ , behaviour,

$$D_{\perp} = \left\{ \begin{array}{ll} \int dk \cdot \left( \frac{k_{\perp} \delta \varphi_k}{B} \right)^2 \cdot \tau_k^{\min} \propto \frac{1}{B^2} & \frac{1}{k_{\perp} \delta v_k} \gg \tau_k^{\min} \equiv \min\left(\frac{1}{k_{\parallel} c_a}, \frac{1}{\omega^{\text{drift}}}, \frac{1}{\omega_{ab}}\right) \\ \int dk \cdot \left( \frac{k_{\perp} \delta \varphi_k}{B} \right)^2 \cdot \frac{1}{k_{\perp} \delta v_k} \propto \frac{1}{B} & \frac{1}{k_{\perp} \delta v_k} < \tau_k^{\min} \end{array} \right\} \quad (A.5.21)$$

Fluctuations in local  $\mathbf{B}$ -field, such as those present around high- $m$ , small scale magnetic islands, redirect parallel fluxes in the cross-field direction<sup>[Ree78,Wes97]</sup>,

$$\delta v_{\perp} = \frac{v_{\parallel} \delta B_{\perp}}{B} \hat{i}_r \quad \left\{ \frac{I}{q_{\perp}} \right\}(t) = \frac{1}{\tau_k} \int_{t-\tau'}^t \delta v_{\perp} \left\{ \frac{\delta n}{\frac{3}{2} T \delta n + n \chi_a (\delta B_{\perp}) \cdot \nabla_{\perp} T} \right\} dt' \quad (A.5.22)$$

where we replaced  $\delta T_a$  by  $\chi_a(\delta B_{\perp}) \nabla_{\perp} T$  with  $\chi_a(\delta B_{\perp})$  some fluctuation dependent heat diffusivity. We can estimate the  $k$ -th component of the diffusion coefficient of the *magnetic field lines* as

$$D_k^B v_{\parallel} = \frac{(\delta r_k^B)^2}{\tau_k^B} = \frac{(\delta v_k^B \tau_k^B)^2}{\tau_k^B} = \left( \frac{\delta B_{\perp}}{B} \right)^2 v_{\parallel}^2 \tau_k^B = \left( \frac{\delta B_{\perp}}{B} \right)^2 v_{\parallel} q(r) R \quad \tau_k^B \sim \frac{\lambda_{\parallel}^B}{v_{\parallel}} \sim \frac{q(r) R}{v_{\parallel}} \quad (A.5.23)$$

where we assumed a weak turbulence approximation for the magnetic correlation time  $\tau_k^B$ . Considering parallel motion of species 'a' along the diffusing field lines, the radial step size depends on the degree of collisionality: if  $\tau_k \gg \tau_k^B$ , then  $\delta r_k \sim (D_k^B v_{\parallel} \tau_k)^{1/2}$  and  $D_k \sim (\delta r_k)^2 / \tau_k \sim D_k^B v_{\parallel}$ ; if  $\tau_k < \tau_k^B$ , then  $\delta r_k \sim (\delta B_{\perp}/B) v_{\parallel} \tau_k$  and  $D_k \sim (\delta r_k)^2 / \tau_k \sim (\delta B_{\perp}/B)^2 v_{\parallel}^2 \tau_k$ . With these assumptions, we find that cross-field transport due to magnetic fluctuations exhibits a weak scaling with  $B$ , which depends on the  $\delta B_{\perp}/B$  relation.

Lastly, large scale magnetic islands may be considered as providing a virtual short circuit for particle and heat flow, and we expect plasma variables, especially  $T_e(r)$ , to be nearly constant across the island region.

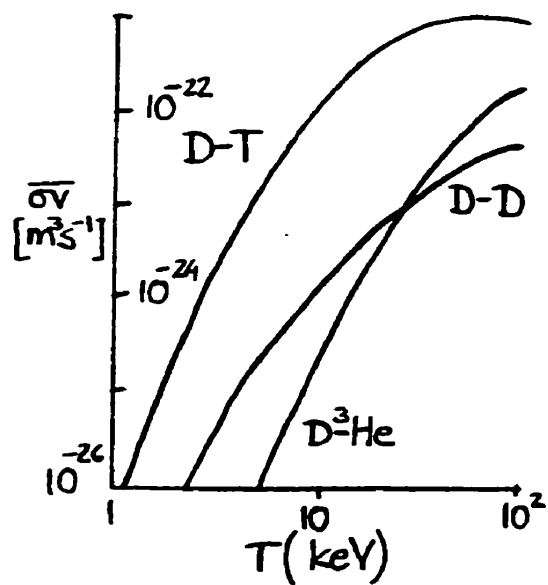


Fig.A.1.1: Fusion reactivities as a function of plasma temperature [Mil74].

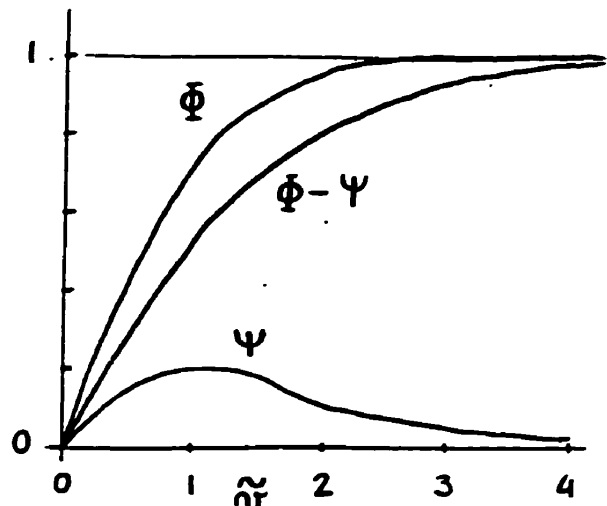


Fig.A.2.2: Rosenbluth (Trubnikov) potentials[Kra80]

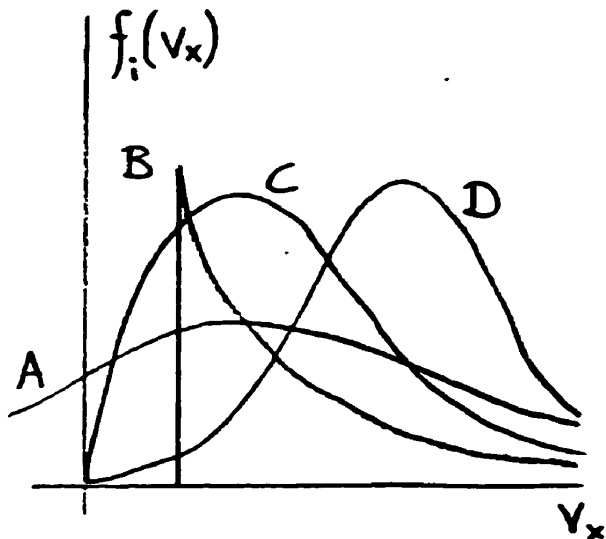


Fig.A.4.1: Ion velocity distributions at the sheath edge as predicted by various kinetic models [Pos84]

	Coll'less fluid	coll'al fluid	coll'less kinetic	coll'al kinetic
$n_e/n_u$	0.5	0.5	0.66	0.43
$M_s$	1.05	1.03	0.95	0.88
$\psi_s$	-0.69	-0.69	-0.41	-0.86
$\psi_0$	-3.13	-3.15	-2.91	-3.45
$\gamma_c$	4.44	4.47	4.83	4.55
$\gamma_i$	2.72	2.75	2.00	2.30
$\gamma_i + \gamma_e$	7.26	7.22	6.83	6.85

Table A.4.1: Values of sheath quantities predicted by various kinetic models [Sta90].

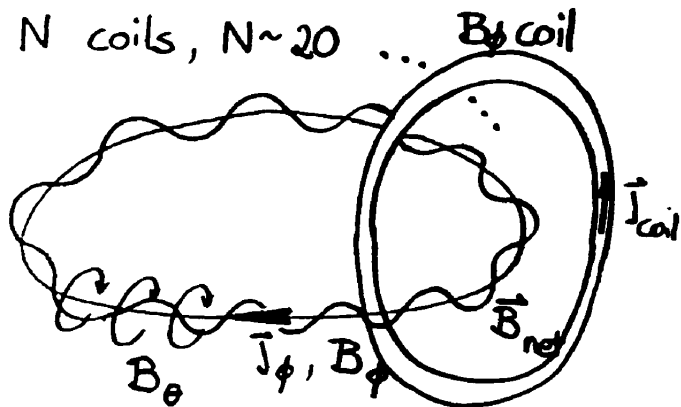


Fig.A.5.1: Schematic of the tokamak concept

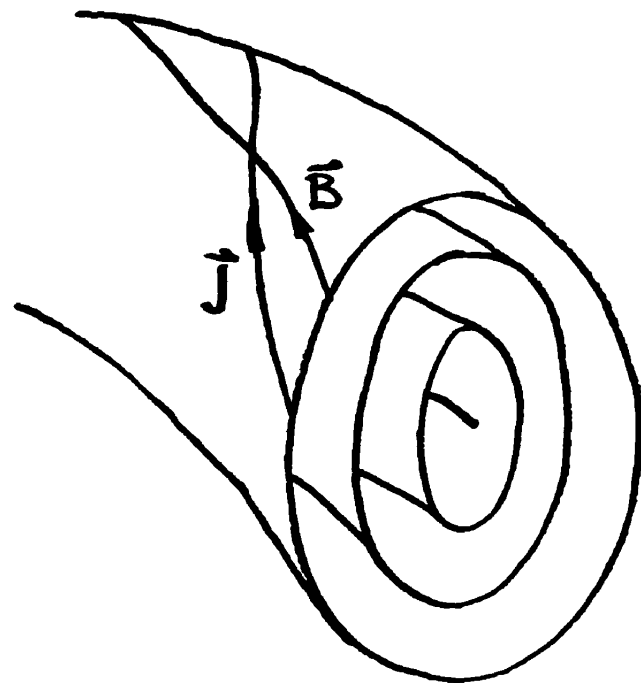


Fig.A.5.2: Tokamak flux-surface geometry

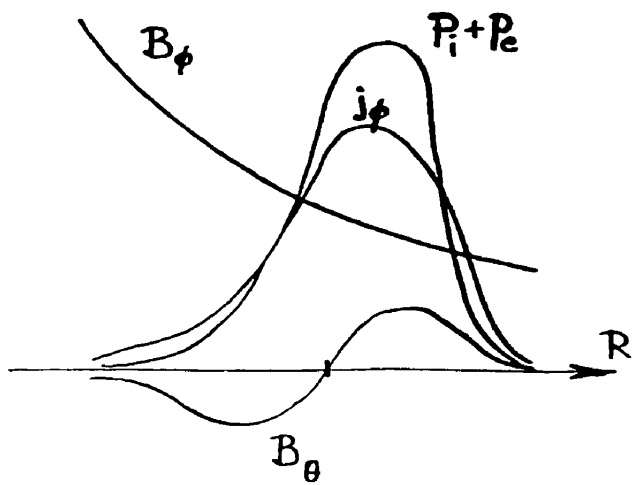
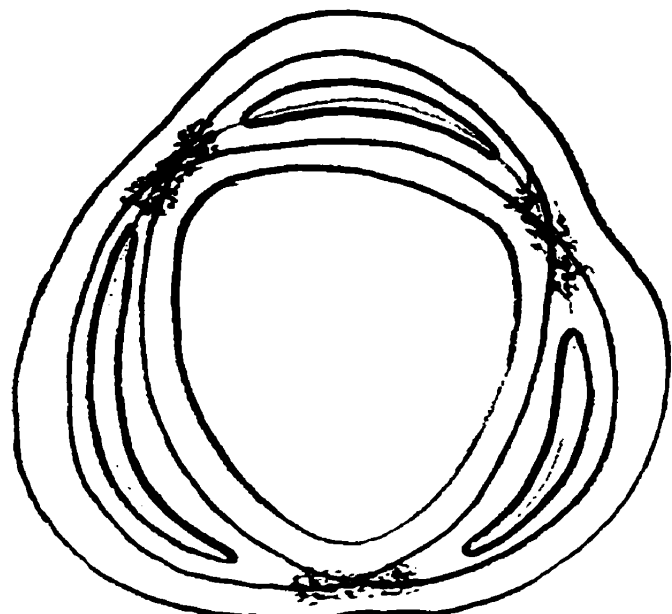


Fig.A.5.3: Typical tokamak fields and currents as a function of the distance from the major axis.

Fig.A.5.4: Magnetic island structure ( $m=3$ ) in poloidal cross-section of a tokamak, showing regions of stochastic behaviour around the X-points.